N73-31841

NASA CR 121235

HYDROGEN FILM COOLING INVESTIGATION

CASE FILE COPY

by

D. C. Rousar and R. L. Ewen

AEROJET LIQUID ROCKET COMPANY
SACRAMENTO, CALIFORNIA 95812

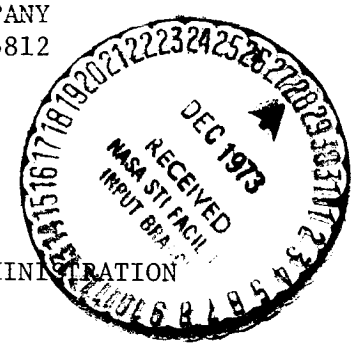

prepared for

NATIONAL AERONAUTICS AND SPACE ADMINISTRATION

NASA Lewis Research Center
Contract NAS 3-15844
D. E. Sokolowski, Project Manager

1. Report No.	2. Government Accession No.	3. Recipient's Catalog No.
NASA CR-121235		

4. Title and Subtitle	5. Report Date
Hydrogen Film Cooling Investigation	August 1973
	6. Performing Organization Code
7. Author(s)	8. Performing Organization Report No.
D. C. Rousar and R. L. Ewen	
9. Performing Organization Name and Address	10. Work Unit No.
Aerojet Liquid Rocket Company Sacramento, California	R3133
	11. Contract or Grant No.
	NAS 3-15844
12. Sponsoring Agency Name and Address	13. Type of Report and Period Covered
National Aeronautics and Space Administration Washington, D. C. 20546	14. Sponsoring Agency Code
	9521

15. Supplementary Notes

Project Manager, D. E. Sokolowski, NASA Lewis Research Center, Cleveland, Ohio

16. Abstract

Effects of flow turning, flow acceleration, and supersonic flow on the effectiveness of film cooling were determined experimentally and correlated in terms of an entrainment film cooling model. Experiments were conducted using thin walled metal test sections, hot nitrogen mainstream gas, and ambient hydrogen or nitrogen as film coolants. The entrainment film cooling model relates film cooling effectiveness to the amount of mainstream gases entrained with the film coolant in a mixing layer. The experimental apparatus and the analytical model used are described in detail and correlations for the entrainment fraction and film coolant-to-wall heat transfer coefficient are presented. Analytical predictions from a spare tug engine and for an APS engine are presented.

17. Key Words (Suggested by Author(s))	18. Distribution Statement
Film Cooling Heat Transfer	Unclassified - Unlimited

19. Security Classif. (of this report)	20. Security Classif. (of this page)	21. No. of Pages	22. Price*
Unclassified	Unclassified	205	$3.00

FOREWORD

The Hydrogen Film Cooling Investigation (Contract NAS 3-15844) was conducted by the Analytical Design Section of the Design and Analysis Department, Aerojet Liquid Rocket Company for the NASA-Lewis Research Center. The period of performance was 12 June 1972 to 4 March 1973. D. E. Sokolowski was the NASA Project Manager. At ALRC the Program Manager was V. H. Ransom, the Project Engineer was D. C. Rousar, and the Program Analyst was R. L. Ewen. Significant contributions to this program were made by the following ALRC personnel:

A. Fink
E. H. Green
R. S. Gross
E. V. Hron
P. M. Loyd
S. L. Munger
K. Y. Wong

TABLE OF CONTENTS

LIST OF TABLES

LIST OF FIGURES

LIST OF FIGURES (cont.)

LIST OF FIGURES (cont.)

I. SUMMARY

The Hydrogen Film Cooling Investigation was an extension of a film cooling study conducted previously by the Aerojet Liquid Rocket Company (Contract NAS 3-14343). The two basic objectives of the program were: (1) to experimentally determine the effects of flow turning, flow acceleration, and supersonic flow on the effectiveness of film cooling, and (2) to establish design correlations for these effects using an entrainment model for film cooling. The major efforts consisted of laboratory film cooling tests with gaseous hydrogen and nitrogen film coolants, correlation of film cooling effectiveness data in terms of an entrainment model, and correlation of film coolant-to-wall heat transfer coefficeints.

The entrainment model approach consists of relating film cooling effectiveness to the quantity of hot mainstream gas entrained by the film coolant gas. An entrainment fraction is defined which relates the entrainment mass flux to the axial mass flux of the mainstream gas. Bulk mixing of the two gases is assumed to occur within a mixing layer. Adiabatic wall temperature and gas composition profiles within the mixing layer are characterized by a shape factor which relates bulk and wall conditions. Film cooling effectiveness is defined on the basis of elemental concentration.

In the laboratory tests, film coolant was injected parallel to the walls of instrumented test sections which simulated rocket engine thrust chambers. Hot nitrogen flowing from an electrical heater at a temperature of 810°K (1000°F) and total pressure of 172 N/cm^2 abs. (250 psia) simulated rocket engine combustion gases. Ambient temperature film coolant was introduced in the subsonic and supersonic regions of the test sections. The subsonic film coolant was injected at film coolant-to-core gas velocity ratios ranging from 0.5 to 1.8. The supersonic film coolant injection conditions were: Mach Number = 1.9, film coolant-to-core gas pressure ratio = 0.45 to 2.0, film coolant-to-core gas velocity ratio=0.5 and 2.0. The core gas Mach Number was 2.5 at

the supersonic injection point and ranged from 2.1 to 4.5 at the outlet of the supersonic test sections.

Adiabatic wall temperatures, effectiveness values, entrainment fractions and heat transfer coefficients were calculated from the test data. Entrainment fraction correlations which are usable for film cooling design calculations were established for accelerating subsonic flow, flow around turns, and for supersonic film cooling. The acceleration data and correlation verify indications obtained in the previous Contract, NAS 3-14343. A completely generalized correlation of the turning effect data was not achieved; however, a graphical correlation was established which is believed sufficient for design purposes. A design correlation for the supersonic entrainment fraction data most applicable to supersonic rocket nozzles was also established. Actual rocket engine data obtained on another NASA program (Contract NAS 3-14354) correlate with the laboratory data. Other effects apparent in the supersonic data such as velocity ratio and constant vs variable mainstream Mach number were not reconciled. Film coolant-to-wall heat transfer coefficients were correlated with a conventional turbulent heat transfer equation by evaluating physical properties at an arithmetic mean temperature and at the wall gas composition.

Other work performed consisted of: (1) a review of previous supersonic film cooling literature, and (2) analytical predictions of film cooling effects in typical O_2/H_2 thrust chambers. Results from the previous supersonic film cooling work were used to define the shape factor and high speed recovery effects for supersonic film cooling. The analytical predictions were made using entrainment fraction and heat transfer coefficient correlations established during the course of the program.

II. INTRODUCTION

The program described in this report was essentially an extension of the work performed under a previous contract, NAS 3-14343, at ALRC which is described in Reference 1. The present program was designed to provide a more extensive evaluation of flow turning effects, flow acceleration effects, and supersonic film cooling effects observed during the previous work. The two basic objectives of the program were: (1) to determine experimentally the effects of flow turning, acceleration, and supersonic injection on the effectiveness of hydrogen film cooling in a simulated rocket thrust chamber, and (2) to establish design correlations for these effects using an entrainment model.

The previous work consisted of film cooling experiments and data correlation. Film cooling data from the literature and from laboratory experiments were correlated in terms of the ALRC entrainment model for film cooling. The literature data were for plane, unaccelerated, subsonic flow conditions, and the laboratory experiments consisted of small scale tests with thin-walled nozzle tests sections which simulated film cooled oxygen/hydrogen rocket thrust chambers. Hydrogen film coolant effectiveness data and film coolant-to-wall heat transfer coefficient data were obtained. The following statements summarize the Reference 1 results which are pertinent to the program described in this report:

(1) The subsonic region effectiveness data indicated that the plane, unaccelerated flow correlation could be applied to rocket engine thrust chambers if adjustments were made in the analytical model to account for turning, acceleration, and axisymmetric flow effects.

(2) Turning effects were more significant than anticipated and a parameter for correlating turning effects was proposed.

(3) A tentative correlation for acceleration effects was established.

(4) The limited film cooling effectiveness data for supersonic flow indicated that the effectiveness decrease in the supersonic region was much smaller than the effectiveness decrease in the subsonic region.

(5) The film coolant-to-wall heat transfer coefficient data in the subsonic region were correlated with a conventional turbulent heat transfer correlation.

The basic testing approach successfully demonstrated during the Contract NAS 3-14343 tests was followed in the present program. Hot nitrogen flowing from an electrical heater into thin-walled test sections simulated rocket engine combustion gases. Ambient temperature hydrogen or nitrogen film coolant was injected to flow along the instrumented test section walls. The test matrix and nominal test conditions are shown in Table I.

Correlations for the effects of acceleration, turning, and supersonic film cooling on entrainment fraction were established from the test data. Analytical predictions for film cooled oxygen/hydrogen thrust chambers were then made using the data correlations. Film coolant-to-wall heat transfer coefficients in the supersonic region were also correlated.

The entrainment model, with which the film cooling data were correlated, has been under development at ALRC during the last 4 years. Mixing of the film coolant and mainstream or core flow gases is assumed to occur within a mixing layer. The mass velocity of mainstream gases into the mixing layer is represented as a fraction of the axial mass velocity of the main stream. This fraction is defined as the entrainment fraction. A description of the entrainment model is given in Section III of this report. Section IV presents an

overview of the program in which the program tasks are summarized. The basic test results and the data correlations established from them are presented in Section V. Analytical predictions are given in Section VI and Conclusions and Recommendations are given in Section VII. Appendices to this report contain analytical derivations which supplement Section III, descriptions of the test apparatus, and cold flow test results.

TABLE I

FILM COOLING TEST MATRIX

Core Gas - N_2 at T_o = 810°K (1000°F) and P_o = 172 N/cm^2 (250 psia)[1]
Ambient Temperature Inlet Film Coolant

Test Setup Number	Flow Region Tested	Film Coolant Injector: Subsonic Injection, Supersonic Injection	Test Assy. Shown in Fig. No.	Nozzle Components: Subsonic Chamber, Supersonic Test Section	Film Coolant	Test[2][3] Flow Rates
101	Subsonic Only	Thin Slot, Cylindrical	B1	30°-1R Cylindrical	N_2	W_o, W_1, W_2, W_3
102	Subsonic Only	Thick Slot, Cylindrical	B1, B9	30°-2R Cylindrical	H_2	W_1, W_2, W_3, W_4
103	A: Subsonic	Thick Slot, Cylindrical	B11, B12	15°-2R Cylindrical	H_2	W_1, W_2, W_3
	B: Supersonic	Cylindrical Supersonic		Cylindrical Supersonic	H_2	W_2+W_5, W_5, W_6, W_7
104	A: Subsonic	Thin Slot, Cylindrical	B11, B18	15°-2R Cylindrical	N_2	W_o, W_1, W_2, W_3
	B: Supersonic	Cylindrical Supersonic		Cylindrical Supersonic	N_2	$W_2+W_5, W_2, W_5, W_6, W_7$
105	A: Subsonic	Thick Slot, Conical	B19, B20	Conical Subsonic	H_2	W_1, W_2, W_3
	B: Supersonic	Conical Supersonic		Conical Supersonic	H_2	$W_2+W_5, W_2, W_5, W_6, W_7$
106	Supersonic Only	Conical Supersonic	B19, B20	Conical Supersonic	N_2	W_5, W_6, W_7

NOTES:

(1) Nominal test conditions, core gas flow rate approximately 1 lb/sec

(2)

Flow Rate	W_o	W_1	W_2	W_3	W_4	W_5	W_6	W_7
Injection Region	← Subsonic →					← Supersonic →		
Nominal Velocity Ratio (u_c/u_e)	0.5	0.75	1.0	1.25	1.8	← See Note (4) →		
Nominal Pressure Ratio (P_c/P_e)	1.0	1.0	1.0	1.0	1.0	1.0	2.0	0.5

(3) Steady-state wall temperature measured at each flow rate condition.
Transient wall temperature data recorded at W_2, W_5, W_6, W_7 flow rates (film coolant on-off-on).

(4) Nominal velocity ratio independent of flow rate for a given coolant.

Coolant	Nominal Velocity Ratio
H_2	2.0
N_2	0.55

III. ENTRAINMENT MODEL FOR FILM COOLING

A. FILM COOLING EFFECTIVENESS

In order to determine the effect of film cooling, it is necessary to describe the region along the wall in which the characteristics of the flow differ from those of the mainstream due to the presence of the film coolant and mixing of the mainstream with it. Since the flow in this mixing layer is greater than the injected coolant flow, the mixing process can be considered to represent entrainment of mainstream flow by the mixing layer as shown schematically in Figure 1. In the present model this entrainment is represented explicitly, but its effect on conditions at the wall is described by means of integral parameters (i.e., without a distributed representation of the transport phenomena within the mixing layer). Therefore, while the model includes the effect of changing enthalpy and concentration profiles within the mixing layer through a profile shape factor, it does not provide a basis for profile calculation.

The film cooling effectiveness used herein is based on element concentration and is defined as

$$\eta = \frac{c_e - c_w}{c_e - 1} \tag{1}$$

in which c is the elemental hydrogen mass fraction. Using an energy transfer - mass transfer analogy, based on a turbulent Lewis number of unity and assuming the viscous sublayer at the wall is thin relative to the mixing layer, the effectiveness also may be written in terms of total enthalpies:

$$\eta = \frac{H_{o_e} - H_{o_v}}{H_{o_e} - H_{o_c}} \tag{2}$$

in which subscript v denotes the edge of the thin viscous sublayer (see Figure 1). The adiabatic wall enthalpy differs from H_{o_v} only because of the imperfect recovery of kinetic energy in the viscous sublayer; this high-speed effect is represented in terms of a conventional recovery factor as

$$H_{o_v} - H_{aw} = (1 - Pr_w^{1/3}) (H_{o_e} - H_e) (\bar{u}/u_e)^2 \quad (3)$$

in which $\bar{u}$ is an effective velocity which is related to the velocity u_v at the edge of the viscous sublayer in the same way as the freestream velocity for a conventional boundary layer. At the coolant injection point $\bar{u}$ should equal the film coolant velocity u_c, while far downstream it becomes u_e since the mixing layer becomes a conventional boundary layer. Combining Equations (2) and (3) gives the adiabatic wall enthalpy as

$$H_{aw} = H_{o_e} - \eta (H_{o_e} - H_{o_c}) - (1 - Pr_w^{1/3}) (H_{o_e} - H_e) (\bar{u}/u_e)^2 \quad (4)$$

For thrust chamber application, the local mixture ratio at the wall is determined by the coolant effectiveness; from Equation (1),

$$MR_w = \frac{1 + MR_e}{1 + \eta\, MR_e} - 1 \quad (5)$$

Therefore, use of the local adiabatic wall enthalpy and wall mixture ratio, Equations (4) and (5), in an equilibrium chemistry model such as Ref. 3 gives the local adiabatic wall temperature. For the laboratory testing reported herein and in Ref. 1, $\eta = c_w$ and

$$H_{aw} = \eta\, H_c\, (T_{aw}) + (1 - \eta)\, H_e\, (T_{aw}) \quad (6)$$

III, A, Film Coolant Effectiveness (cont.)

so that Equation (4) gives the following effectiveness relation in terms of the measured adiabatic wall temperature:

$$\eta = \frac{T_{o_e} - T_{aw} - (1 - Pr_w^{1/3})\ (T_{o_e} - T_e)\ (\bar{u}/u_e)^2}{T_{o_e} - T_{aw} + \frac{C_{p_c}}{C_{p_e}}\ (T_{aw} - T_{o_c})} \tag{7}$$

The cooling effectiveness η is related to the entrainment flow W_E into the mixing layer, the coolant flow and a shape factor describing the elemental hydrogen concentration profile in the mixing layer. A hydrogen mass balance on the mixing layer gives

$$\frac{c_e - c_b}{c_e - 1} = \frac{W_c}{W_c + W_E} \tag{8}$$

from which

$$\eta = \frac{W_c}{\theta\ (W_c + W_E)} = \frac{1}{\theta\ (1 + \frac{W_E}{W_c})} \tag{9}$$

with the profile shape factor θ defined as

$$\theta = \frac{c_e - c_b}{c_e - c_w} = \frac{H_{o_e} - H_{o_b}}{H_{o_e} - H_{o_v}} \tag{10}$$

The present entrainment model is characterized by three regimes: (1) an initial free-jet regime in which the mixing effects have not penetrated to the wall, (2) a transition regime in which both the effectiveness and shape

factor are changing, and (3) a fully-developed regime in which the shape factor is constant. In the initial regime the coolant effectiveness remains at unity, so that Equation (9) gives the shape factor as

$$\theta = \left(1 + \frac{W_E}{W_c}\right)^{-1} \quad \text{(unity effectiveness regime)} \tag{11}$$

It is assumed that θ in the transition region also depends solely on the entrainment flow ratio W_E/W_c.

As indicated in Figure 1, the entrainment mass flux velocity is represented as a fraction k of the axial mass velocity of the mainstream. Thus, the total entrainment flow up to any contour position is

$$W_E = \int_o^x 2\pi \, (r - s \cos \alpha) \, k \, \rho_e \, u_e \, dx \tag{12}$$

A momentum balance on the total nozzle flow should be used to account for the effect of the mixing layer on the freestream mass velocity, $\rho_e u_e$. However, for the sake of simplicity, it is assumed in the present model that the mainstream accelerates as if there were no film cooling. A nozzle mass balance then determines the mixing layer thickness, s, in terms of the entrainment flow and converts Equation (12) into an integral equation (see Ref. 1, Appendix A) whose solution is*

$$\frac{W_E}{W - W_c} = 2 \frac{\bar{x} \, \phi_o}{r_o - s_o} - \left(\frac{\bar{x} \, \phi_o}{r - s_o}\right)^2 \tag{13}$$

*The initial mixing layer thickness s_o is not equal to the slot height s_c when a finite lip separates the core and coolant flows at the injection point. In order to determine s_o, it is assumed herein that the velocity ratio u_c/u_e existing just prior to injection is maintained immediately downstream of the slot.

III, A, Film Coolant Effectiveness (cont.)

in which

$$\bar{x} = \int_{o}^{x} \frac{r_o}{r} \left(\frac{\phi}{\phi_o}\right) k \, dx \qquad (14)$$

The entrainment model described above contains three parameters which remain to be determined: the effective velocity $\bar{u}$ in Equation (3) which characterizes the high-speed effect, the shape factor θ for the transition and fully-developed regions and the entrainment fraction k. These parameters are discussed below in separate sections for film cooling in subsonic and supersonic flow regions. In each case our approach has been to determine $\bar{u}$ and θ a priori from existing results and interpret the test data of the present program in terms of the entrainment fraction.

1. Film Cooling In a Subsonic Flow Region

The subsonic version of the entrainment model used herein is identical to that developed in Ref. 1. In the laboratory tests of both programs high-speed effects are important only after considerable mixing occurs, due to the significant distance between the film coolant injection annulus and the nozzle throat. Therefore, it is assumed that $\bar{u} = u_e$, i.e., the mixing layer is fully developed when the high-speed effects are of any significance. Five groups of existing cooling effectiveness data are correlated in Ref. 1 for plane unaccelerated flow covering wide ranges of injection velocity ratio and density ratio. Figure 2 shows the resultant profile shape factor correlation, with a fully-developed subsonic flow value of 0.758 and a transition regime defined by $0.06 \leq W_E/W_c \leq 1.4$. The corresponding entrainment fractions were found to be independent of axial position and are correlated by

III, A, Film Coolant Effectiveness (cont.)

$$k_o = \frac{0.1\ (u_c/u_e)}{\left(\frac{\rho_c}{\rho_e}\right)^{0.15} f\left(\frac{u_c}{u_e}\right) Re_c^{0.25}} \qquad (15)$$

with $f\ (u_c/u_e)$ defined in Figure 3.

The effectiveness data from the laboratory testing of Ref. 1 were interpreted in terms of the ratio k/k_o; i.e., the multiplier required to account for coolant injection and nozzle geometry effects not present in the plane, unaccelerated flow entrainment fraction, k_o. In a cylindrical section downstream of the film coolant injection annulus, the entrainment fraction was about 1.6 k_o. A large increase in the entrainment fraction was observed in the turn at the start of the convergent section, followed by a large decrease in the throat turn. A large increase in entrainment fraction is indicative of large increases in the entrainment mass velocity and is undesireable since increased mixing of the film coolant and core gas result. Most of the expansion section data in Reference 1 were correlated adequately by assuming no additional mixing ($k = o$) beyond the throat. On the other hand, analysis of the nozzle effectiveness data of Ref. 4 in terms of an entrainment fraction indicated just the opposite turning effects for flow turning when the film coolant is more dense than the core flow.

Data reported in Ref. 1 for a conical chamber indicated flow acceleration decreases the entrainment fraction, consistent with the traditionally observed decrease in Stanton number. Correlation suggested by the work of Deissler (Refs. 5 and 6) correlates the acceleration effect data obtained on this program and the data reported in Reference 1. Therefore, in the present program, the entrainment fraction has been partitioned as

$$k = k_o \left[\frac{\rho_e\ u_e}{(\rho_e\ u_e)_o}\right]^{-n} k_m \qquad (16)$$

with the bracketed term representing the effect of flow acceleration. Evaluation of the exponent n from conical chamber data is discussed in Section V,B. All cylindrical chamber effectiveness data were then interpreted in terms of the multiplier k_m, which accounts for the effects of coolant injection geometry, freestream turbulence and nozzle geometry. With the above entrainment fraction of formulation, Equation (14) for $\bar{x}$ becomes

$$\bar{x} = k_o \int_o^x \left(\frac{r_o}{r}\right)^{1-2n} \left(\frac{\phi}{\phi_o}\right)^{1-n} k_m \, dx \qquad (17)$$

2. Film Cooling In a Supersonic Flow Region

In this case the high-speed effects of Equation (3) are important throughout the test section, so it is necessary to define the axial variation of the effective velocity $\bar{u}$. This has been accomplished, along with formulation of the supersonic mixing layer profile shape factor θ, using existing data and analyses obtained from the supersonic film cooling literature. The following paragraphs contain a review of the supersonic film cooling literature and discussions on the profile shape factor and high speed effects.

a. Review of Supersonic Film Cooling Literature

Comparison of the various literature sources is complicated by lack of a consistent definition for supersonic effectiveness. Since most data have been obtained with air injection into air, simple temperature-based effectiveness definitions have been used; the inconsistency arises in specifying the freestream reference temperature. Three such temperatures have been used and each has disadvantages. Use of the stagnation temperature ignores high-speed recovery effects entirely, so the resultant effectiveness depends

on both coolant and freestream Mach numbers. Use of the local recovery temperature without film cooling accounts for high-speed effects based on the freestream flow, but neglects coolant Mach number effects near the injection point. Use of the local isoenergetic wall temperature, measured with the film coolant injected at the same stagnation temperature as the freestream (Ref. 7), eleminates all high-speed effects from the effectiveness when the latter is obtained with a small coolant-freestream temperature difference. However, this approach is not of general interest since with a large temperature difference the isoenergetic condition changes the coolant injection velocity. Note that the results obtained in the present program are of general utility since the high-speed effects are presented explicitly and are not involved in the effectiveness definition.

References 7-11 provide data for gaseous film cooling injected parallel to a constant Mach number air flow with the coolant slot and lip forming a step discontinuity in the wall. In Ref. 2 gaseous hydrogen coolant was injected in the expansion section of a hydrogen/oxygen rocket nozzle. The following table indicates the pertinent parameters for these studies; corresponding parameters for the present hydrogen and nitrogen coolant tests are shown for comparison.

Ref.	Freestream Mach No.	Coolant Mach No.	Velocity Ratio	Mass Velocity Ratio	Static Pressure Ratio
7	3	1	≤ 0.5	0-0.41	< 1 and > 1
8	6	1	0.39	-	-
9	6	2.3	0.62	-	1
10	6	1	0.29-0.35	0.03-1.6	< 1 and > 1
11	1.5-1.7	1	-	-	-
2	3.1-4.5	2.6	0.6	1.6-2.5	1.2
H_2*	2.5, 2.5-4.5	1.9	1.94	0.14-0.58	0.5-2.0
N_2*	2.5, 2.5-4.5	1.9	0.54	0.47-2.2	0.5-2.0

* Data presented in this report

III, A, Film Coolant Effectiveness (cont.)

Unfortunately, the range of coolant injection conditions covered is not sufficient to determine the relative importance of static pressure matching vs velocity matching. In many cases practical limitations on coolant injection velocity prevent velocity matching; on the other hand, static pressure matching is possible in most applications.

Schlieren studies reported in Refs. 7 and 9 reveal the flow phenomena involved due to the interaction of the two flows and the step discontinuity in the wall. Due to the flow over the edge of the slot lip there is an expansion fan, lip shock, separated region and recompression shock at the reattachment point. However, the recompression shock becomes weaker and disappears as the coolant mass velocity increases. Beyond this mass velocity, the region of unity effectiveness was found in Ref. 7 to increase more rapidly with increasing coolant mass velocity, and the effectiveness decrease beyond this region was less rapid. Thus, a significant change in mixing characteristics was associated with the disappearance of the recompression shock at the reattachment point.

With the coolant static pressure less than that of the free stream, a compression zone at the slot exit was observed in Ref. 9 which increased the wall pressure to about three times the free stream static pressure in some cases. However, this pressure perturbation disappeared within 3-4 slot heights downstream of the slot exit, a distance well within the length of the unity effectiveness region. These results indicate a pressure mismatch at injection may not result in a serious degradation of cooling effectiveness. With the coolant static pressure greater than that of the free stream, the coolant flow was observed in Ref. 7 to expand and then recompress; with larger pressure differentials, expansions and compressions occurred alternately in both streams.

The Mach 6 testing reported in Ref. 8 was repeated using direct adiabatic wall temperature measurements instead of heat flux measurements and the results are given in Ref. 10. This work along with the analyses reported in Ref. 12 demonstrated both experimentally and analytically that the adiabatic wall temperatures inferred from heat flux data and reported in Refs. 8 and 9 are significantly in error due to the effect of film cooling on the local heat transfer coefficient. However, it is of interest to compare the Ref. 9 results in which the coolant flow was also supersonic, with the sonic injection data reported in Ref. 8 for the same freestream Mach number. Longer regions of unity effectiveness were obtained consistently with supersonic injection, and the effectiveness decreased less rapidly downstream. The greater cooling effectiveness with supersonic vs subsonic injection is attributed to the higher velocity ratio and larger slot Reynolds numbers obtained in the supersonic injection tests. In the work of Ref. 10 effectiveness data at a second, lower coolant temperature were also obtained and this lower temperature resulted in a lower injection velocity ratio. Effectiveness values were reduced as in the case of subsonic film cooling, with the magnitude of the reduction accurately predicted by the boundary layer computer program described in Ref. 12. The Ref. 11 film coolant slot had a very thick lip (2-9 slot heights) and produced effectiveness data considerably lower than the comparable results of Ref. 7.

The existing data most pertinent to this program are the ALRC data (Ref. 2), the data of Goldstein and co-workers (Ref. 7), and the data of Cary and Hefner (Ref. 10). Adiabatic wall temperature data from Ref. 2 have been reprocessed using the shape factor and kinetic energy recovery formulations adopted herein. Since the isoenergetic wall temperature was used in the effectiveness definition used by Goldstein, and the difference between coolant and freestream stagnation temperatures was small, the effectiveness results reported in Ref. 7 can be interpreted as identical to the concentration effectiveness of interest herein. Unfortunately, the effectiveness defined by Cary and Hefner is based on freestream stagnation temperature and cannot be compared with the

other data. However, the NASA-Langley boundary layer analyses (Ref. 12) for a pressure ratio of unity are in excellent agreement with the Cary and Hefner data and include a species concentration calculation. Figure 4 shows the resultant concentration effectiveness as a function of the correlating parameter used by Cary and Hefner, with the Goldstein results shown for comparison. Since a different correlating parameter (x/mh) was used by Goldstein, his effectiveness correlation has been shifted based on the average mass velocity ratio and average slot height associated with that data. The rates of effectiveness decay are the same, although the Ref. 12 result implies a lower entrainment fraction and includes a transition region between the free-jet region of unity effectiveness and the power-law decay. These curves imply an increase in entrainment fraction with increasing axial distance, whereas comparable subsonic data were correlated in Ref. 1 using an entrainment fraction which is independent of axial position. Figure 4 also shows some of the variable Mach number data from Ref 2, which indicate a reduction in entrainment fraction with axial distance. Actual entrainment fraction values inferred from Refs. 2 and 7 are compared with the data obtained here in Section V,B,3. Note that the success of the correlating methods such as shown in Figure 4 over a wide range of coolant flow rates for a fixed hardware design indicates that pressure matching between the core and film coolant streams may not be critical.

b. Mixing Layer Profile Shape Factor

The mixing layer profile shape factor formulation used in the present model was developed from the analytical results of Ref. 12. Appendix A provides the details of this development, and the resulting correlation with entrainment flow ratio is shown in Figure 2. The transition regime between the initial free-jet regime, Equation (11), and the fully-developed regime is defined by $0.5 \leq W_E/W_c \leq 2.2$. The data reported in Refs. 7-10 indicate much longer regions of unity effectiveness compared with correlations for subsonic freestream flow, and this is reflected in Figure 2 in terms of entrainment flow ratio since

the transition regime for supersonic flow starts at $W_E/W_c = 0.5$ compared with 0.06 for the subsonic case. The shape factor analyses of Appendix A also yield the entrainment fractions for Refs. 7 and 12 in the fully-developed regimes.

c. High Speed Effects

The effective velocity $\bar{u}$ used to account for kinetic energy recovery, Equation (3), has been defined in terms of a velocity mixing function $V\ (W_E/W_c)$:

$$\bar{u} = u_e + (u_c - u_e)\ V\ (W_E/W_c) \qquad (18)$$

This function was derived from Goldstein's isoenergetic wall temperature data and partially confirmed by the NASA-Langley analytical results (Ref. 12), as described in Appendix A. The resultant correlation is shown in Figure 5; two points from Ref. 12 are shown for comparison.

The role which imperfect recovery of kinetic energy plays in determining the film cooling effectiveness for the constant Mach number tests is shown in Figures 6 and 7. Equation (7) is plotted as effectiveness vs a dimensionless adiabatic wall temperature for typical test conditions, along with the corresponding result (dashed curves) for low-speed flow. Figure 6 is for Test Setup 103B data (hydrogen film coolant); in this case the injection velocity ratio is near two, so the high-speed effect is large initially and then decays. Figure 7 is for Test Setup 104B data (nitrogen film coolant); in this case the injection velocity ratio is only 0.54, so the initial high-speed effect is small. At small values of effectiveness the difference between the two curves in Figure 7 is constant and equal to 0.1. For both tests at an effectiveness of unity the dimensionless adiabatic wall temperature is near -0.03, which corresponds to an actual adiabatic wall temperature 27°F lower than the coolant stagnation temperature.

III, Film Cooling Model (cont.)

B. HEAT TRANSFER

The convective heat flux to a non-adiabatic wall with film cooling is represented herein as

$$q = G\ St\ (H_{aw} - H_w)\ \rho_{ref}/\rho_e \qquad (19)$$

in which H_{aw} is the adiabatic wall enthalpy defined by the cooling effectiveness and H_w is the enthalpy of the local gas mixture at the wall at the non-adiabatic wall temperature. The gas composition at the wall is also defined by the cooling effectiveness. Use of H_{aw} as the driving enthalpy is based on the assumption that the thermal boundary layer due to wall cooling or heating is small relative to the mixing layer.

The Stanton number is correlated by a modified turbulent pipe flow equation

$$St = C_g(x)\ Re_D^{-0.2}\ Pr_{ref}^{-0.6} \qquad (20)$$

in which

$C_g(x)$ = position dependent correlation coefficient

Re_D = Reynolds number based on flow diameter, $\rho_{ref}\ GD/\rho_e \mu_{ref}$

Pr = Prandtl number

The reference properties (ρ, μ and Pr) are evaluated for the gas composition at the wall defined by the cooling effectiveness and at a reference temperature. The reference temperature, selected on the basis of data from Ref. 1, is the arithmetic mean of the adiabatic and non-adiabatic wall temperatures.

It was found in Ref. 1 that the above formulation would allow the same correlation coefficients to be used with and without film cooling, except near the injection point when the coolant and freestream velocities are not equal.

IV. PROGRAM APPROACH

The program consisted of the following tasks: Task I - Preliminary Analysis and Design, Task II - Hardware Fabrication and Facility Preparation, Task III - Testing, and Task IV - Model Development, Data Correlation, and Analytical Predictions. The scope of each of these tasks is explained in the following sections.

A. TASK I - PRELIMINARY ANALYSIS AND DESIGN

1. Analysis and Test Planning

The Analysis and Test Planning work consisted of finalizing test plans, establishing the necessary component design parameters, reviewing the existing supersonic film cooling literature, performing preliminary supersonic model development analyses, and modifying existing computer programs. The preliminary supersonic model development consisted of defining the mixing layer profile shape factor and the effective velocity characterizing kinetic energy recovery; this effort is described completely in Section III and Appendix A. The finalized test plan is the test matrix shown in Table I.

In actual thrust chamber applications, the velocity ratio[1] with supersonic film coolants ranges from 0.2 to 0.7. The ALRC supersonic film coolant injector utilized on APS thrust chambers with hydrogen film coolant (Ref. 2) operated at about 0.5 velocity ratio. In the tests conducted on this program with hydrogen and nitrogen, the velocity ratios were approximately 2.0 and 0.55, respectively. The low nitrogen velocity ratio (0.55) is desirable for a laboratory test program because it is within the range of actual thrust chamber applications. The high velocity ratio for hydrogen film cooling (2.0) is acceptable, but tests at an additional velocity ratio near 1.0 are desirable because they would provide a useful supersonic film cooling reference condition. A unity velocity ratio is probably more efficient than a non-unity velocity ratio because a velocity mismatch may enhance turbulent mixing effects. This certainly has been found to be the case with subsonic film cooling.

[1] velocity ratio = $\frac{u_c}{u_e}$

During the course of finalizing the program test plans, testing with a hydrogen/nitrogen mixture as film coolant in the supersonic region was considered because this allows injection of the film coolant at a velocity ratio of 1.0. The velocity ratio for supersonic film coolant is given by the following equation.

$$\frac{u_c}{u_e} = \text{velocity ratio} = \frac{M_c}{M_e} \left(\frac{MW_e}{MW_c}\right)^{1/2} \left(\frac{T_c}{T_e}\right)^{1/2}$$

For the core gas conditions employed on this program, it was determined that a mixture of 21.3% hydrogen and 78.7% nitrogen (by weight) would result in a velocity ratio of 1.0. Testing with such a H_2/N_2 mixture appears feasible and could be accomplished using a gas mixer unit installed upstream of the supersonic film coolant injector. Furthermore, it appears that a cold flow injector element design whose hydrogen/nitrogen mixing efficiency has been characterized experimentally at ALRC (Ref. 13) could be utilized in establishing a mixing device design.

It was determined that testing with a hydrogen/nitrogen mixture film coolant was beyond the scope of this program and consequently no supersonic film cooling data with velocity ratio of 1.0 were obtained. Testing at this condition is recommended for future work.

2. Component Design

Component design consisted of the mechanical design of the film cooling test components and preparation of fabrication drawings. Descriptions and drawings of the components are given in Appendix B. A summary of the designs established is given below.

1 modification of a Contract NAS 3-14343 conical subsonic test section

1 modification of a Contract NAS 3-14343 cylindrical subsonic test section

2 cylindrical subsonic test sections

1 subsonic film coolant injector

2 supersonic flow film coolant injectors

2 supersonic test sections

1 diffuser tube

3 adapter sleeves

B. TASK II - COMPONENT FABRICATION AND FACILITY PREPARATION

This task consisted of fabricating the components designed during Task I and assembling the film cooling test system. Photographs of the completed test components and a schematic drawing of the test system are presented in Appendix B.

C. TASK III - TESTING

The testing task consists of cold flow tests and film cooling tests. The scope of these tests is described in the following two sections.

1. Cold Flow Tests

Cold flow tests of the newly fabricated subsonic and supersonic film coolant injectors were performed prior to the film cooling tests. The objectives of the cold flow tests were to verify the integrity of these units and to establish the circumferential distribution of the film coolant at the injector outlet. The test procedure consisted of flowing ambient temperature

N_2 through the film coolant injectors (no core flow) and measuring total pressures within the coolant slot and at the coolant slot exit with a total pressure probe. The cold flow test results are presented in Appendix C.

2. Film Cooling Tests

a. Testing Approach

The basic testing approach successfully demonstrated by ALRC during the Contract NAS 3-14343 tests was followed. Test facilities and test components developed under Contract NAS 3-14343 were used as much as possible. The film cooling tests were conducted using thin-walled circular test sections which simulated the environment of a film cooled oxygen/hydrogen thrust chamber. Hot nitrogen flowing from an electrical heater into the tube at approximately 810°K (1000°F) and 172 N/cm^2 abs (250 psia) total pressure simulated the core combustion gases. The use of hot nitrogen core gas provided an evaluation of film cooling effectiveness without the super-imposed effects of the mainstream or propellant injector and of the combustion process. Tests were conducted to evaluate both the subsonic and supersonic flow regions. In the subsonic testing, film coolant was introduced upstream of the throat. The supersonic testing was performed using both supersonic core flow and supersonic coolant injection. Ambient temperature hydrogen or nitrogen film coolant was injected through film coolant slots to flow along the instrumented test section walls. Supersonic injectors and test sections were attached downstream of the throats of the subsonic test sections. In addition to evaluating subsonic and supersonic film cooling independently, "carry over" effects were evaluated by monitoring supersonic region thermocouples when the film coolant was injected simultaneously in the subsonic and supersonic regions and when film coolant was injected in the subsonic region only.

The subsonic and supersonic test sections were instrumented with thermocouples attached to the outside wall. Two distinct types

of test section wall temperature data were obtained: steady-state wall temperature data for effectiveness and transient wall temperature data for heat transfer coefficients. The steady-state wall temperature data were recorded for each film coolant flow rate. Transient wall temperature data were recorded at selected film coolant flow rates after steady-state wall temperatures had been recorded. A wall heating transient was obtained by abruptly shutting off the film coolant flow. After the wall had achieved steady-state with no film cooling, the film coolant flow was rapidly re-established.

b. Test Matrix

A total of 34 tests were conducted with 6 hardware setups designated as Test Setups 101, 102, 103, 104, 105, and 106. A test is defined as one combination of film coolant flow rate, film coolant injector, instrumented test section, and core gas flow conditions. The test matrix is shown in Table I. Subsonic and supersonic test components were combined in three of the test setups (103, 104, and 105). Different wall temperatures were recorded in the subsonic and supersonic tests with these combined setups; consequently, the combined setups are referred to in this report as either Setup A (subsonic tests) or Setup B (supersonic tests). The test instrumentation consisted of approximately 20 wall temperatures, 4 film coolant temperatures and pressures (1 each at both flowmeters, 1 each at both film coolant injector manifolds), 1 core gas temperature, and 1 core gas inlet pressure.

The specific effects investigated with each test setup are listed below. The results obtained are presented in Section V,A and correlations of the data are discussed in Section V,B.

(1) Acceleration Effects: The effect of acceleration without turning was investigated in Test Setup 105A (hydrogen film coolant).

IV, C, Task III - Testing (cont.)

(2) Turning Effects: Flow turning effects in the subsonic region were investigated in Test Setups 101, 102, 103A, and 104A using hydrogen and nitrogen film coolants.

(3) Supersonic Flow Effects: Film cooling with supersonic film coolant and supersonic core gas was investigated in Test Setups 103B, 104B, 105B, and 106. Film cooling at nearly constant core gas Mach number was tested in Setup 103B with hydrogen film coolant, and in Setup 104B with nitrogen film coolant. Supersonic film cooling with variable core Mach number was investigated in Test Setup 105B with hydrogen film coolant and in Test Setup 106 with nitrogen film coolant.

c. Test Procedures

The testing procedures were based on those developed during the NAS 3-14343 work. In tests conducted with Test Setups 101 and 102 (subsonic injection only), and Test Setup 106 (supersonic injection only), the test procedure was virtually identical to that followed previously: the hot nitrogen core flow was established, then the film coolant flow for the initial test was established and adiabatic wall temperature data were recorded when steady conditions had been achieved. Similar data were then obtained for the other tests. Wall heating and cooling transient data also were recorded in certain tests (see Table I). The test procedure for the combined test setups was somewhat different. Part A (subsonic injection) was performed following the foregoing procedure, then testing was stopped temporarily while thermocouple cables were switched from the subsonic test section to the supersonic test section. Part B testing (supersonic injection) was then performed following the same test procedure as in Part A.

D. TASK IV - MODEL DEVELOPMENT, DATA CORRELATIONS AND ANALYTICAL PREDICTIONS

1. Model Development and Data Correlations

The Task IV model development and data correlations work consisted of: (1) reducing the steady state and transient wall temperature measurements into adiabatic wall temperature and heat transfer coefficient data, (2) interpreting these data within the context of the entrainment model, and (3) establishing design correlations for entrainment fraction and heat transfer coefficient.

a. Data Reduction

Data reduction consisted of three parts:

(1) Obtaining heat transfer coefficients and the corresponding correlation coefficients, Equation (20), from wall temperature transients using the wall as a calorimeter.

(2) Correcting steady-state wall temperatures with film cooling for external heat losses to obtain the adiabatic wall temperature and calculating the corresponding film cooling effectiveness from Equation (7).

(3) Calculating from these effectiveness values the average entrainment fraction between successive pairs of thermocouples in each axial row.

Details of Items (1) and (2) have been given in Appendix B of Reference 1 and evaluating entrainment fractions follows directly from the model of Section III. Effectiveness values for the nitrogen film cooled

test setups (101, 104A, 104B, and 106) were based on a film coolant injection temperature which was corrected for preheating effects inside the film coolant annulus. The correction for subsonic injection was based on the measurements made with Test Setup 104A (measurements tabulated in Section V. A.) while the correction for supersonic injection was obtained analytically. It was found that only the initial entrainment fraction, i.e., the value between the injection point and the first thermocouple, was affected by the inlet temperature correction, and even this effect was usually small. It was determined that no corrections were necessary for the hydrogen inlet temperature, consequently the hydrogen effectiveness values were calculated using the film coolant injector manifold temperature as the inlet temperature (this is consistent with Reference 1).

The data reduction sequence was as follows: the heating transient in each test was analyzed first to determine simultaneously the core gas-to-wall heat transfer coefficients (no film cooling) and the external heat loss coefficients; the latter were then used in analyzing the cooling transients and the steady-state wall temperatures with film cooling to determine effectiveness and film coolant-to-wall heat transfer coefficients.

b. Data Interpretation and Correlation

Interpretation and correlation of the entrainment fractions and heat transfer correlation coefficients are discussed below.

(1) Subsonic Film Cooling

Data from the conical chamber (Test 105A) were processed first in order to determine the acceleration exponent n in Equation (16), the subsonic entrainment fraction model. In processing subsonic effectiveness data, n is specified and the entrainment fraction multiplier k_m is calculated. Conical chamber data were processed with n = o, so that a fictitious k'_m was

generated with acceleration effects included. Assuming the flow is one dimensional, Equation (16) yields

$$k'_m = k_m \left(\frac{r}{r_o}\right)^{2n} \tag{21}$$

Since there are no turns in this chamber, entrainment fraction changes are caused solely by acceleration; i.e., k_m is constant and k'_m data give the acceleration exponent n directly from Equation (21). The resultant value of n was then used to process all other subsonic effectiveness data; some data from References 1 and 4 were reprocessed in this manner for use in correlating turning effects.

Data from the cylindrical chambers were interpreted in terms of entrainment fraction multipliers for turning effects by defining a turning multiplier as

$$k_{turn} = \frac{(k_m) \text{ in turn or after turn}}{(k_m) \text{ before turn}} \tag{22}$$

Correlation of these factors using the turning parameter developed in Reference 1 was then investigated.

(2) Supersonic Film Cooling

Absolute values of the entrainment fraction k were determined from the supersonic effectiveness data since no general reference correlation was available. A general correlation of these results was not possible within the scope of this program, however, a correlation of the variable Mach number entrainment fractions with nitrogen coolant and the data of Reference 2 was obtained using a dimensionless axial coordinate similar to those used in References 7 to 10. This correlation provides a basis for nozzle applications over a narrow range of injection velocity ratio.

IV, D, Task IV - Model Development, Data Correlation and Analytical Predictions (cont.)

Heat transfer correlation coefficients were checked to determine if values without film cooling could be used with film cooling at some distance downstream of the injection point, as was the case with the present model in the subsonic case, and to investigate coolant flow effects near the injection point.

2. Analytical Predictions

Analytical predictions of film cooling requirements for a completely film cooled thrust chamber, and for the effect of film cooling on the wall temperature of a regeneratively cooled thrust chamber were made using entrainment fraction and heat transfer coefficient correlations developed on this program. These predictions are described in Section VI of this report. The film cooling requirement predictions were made for the subsonic region of a typical Space Shuttle APS thrust chamber. A range of thrust, chamber pressure, mixture ratio, and film coolant inlet temperature operating conditions were considered. The wall temperature predictions were made for the subsonic and supersonic regions of a proposed O_2/H_2 Space Shuttle Tug thrust chamber. A range of film coolant flow rates and thrust levels were considered.

V. EXPERIMENTAL RESULTS AND DATA CORRELATIONS

A. EXPERIMENTAL RESULTS

The direct experimental results of the film cooling tests are presented in this section. The test conditions for all tests are summarized in Table II. The adiabatic wall temperatures, effectiveness values, and local heat transfer coefficients are presented in Figures 8 to 33. Heat transfer correlation coefficients for the supersonic test sections are given in Table III. Experimental Mach numbers for the supersonic tests are shown in Table IV. The test conditions and components utilized with each test setup are briefly summarized in the following paragraphs. Details of the test components and the test system are given in Appendix B.

Test Setup 101

(Figures 8, 9, 10)

During the testing with Test Setup 101, experimental adiabatic wall temperature distributions were measured downstream of the film coolant slot where ambient temperature N_2 film coolant was injected at four velocity ratios (0.62, 0.87, 1.12, 1.41). The thin slot subsonic injector and 30°-IR[1] subsonic test section were major components in this test assembly (both components residual from NAS 3-14343). The adiabatic wall temperature distributions determined from the Test Setup 101 data have the same general appearance of the distributions obtained with cold hydrogen film coolant and the thin slot injector on the previous test program (Ref. 1).

Test Setup 102

(Figures 11, 12, 13)

The Test Setup 102 assembly consisted of the 30°-2R[2] subsonic test section fabricated on this program, and the thick slot height subsonic injector (residual from NAS 3-14343). Testing was accomplished using ambient hydrogen

---

[1] 30° convergence angle, reference turn radii as shown in Figure B1.

[2] 30° convergence angle, turn radii increased by a factor of two.

film coolant. Steady-state wall temperature data were obtained at three velocity ratios(0.81, 1.12 and 1.8). Heating transient and cooling transient data also were obtained at the 1.12 velocity ratio. The nitrogen core gas temperature was about 883°K (1130°F) which is higher than planned; however this does not compromise the value of the data.

Test Setups 103A and 103B

(Figures 14, 15, 16 (Part A), and Figures 17, 18, 19 (Part B))

Ambinet temperature hydrogen film coolant was used with test Setups 103A and 103B which were the first combined subsonic and supersonic test setups. The hardware consisted of the thick slot subsonic injector, the 15°-2R subsonic test chamber, the cylindrical supersonic injector, and the cylindrical supersonic test section. In the Test Setup 103A tests, wall temperatures on the subsonic test section were measured at steady state with subsonic film coolant injeetion at three velocity ratios of 0.785, 1.03, and 1.30. Heating and cooling transient data also were recorded at 1.03 velocity ratio.

Prior to Test 103B, thermocouple connectors were rearranged so that thermocouples attached to the cylindrical supersonic test section would be recorded. Tests were conducted in which steady-state wall temperature distributions along the supersonic test section were measured at the following conditions:

(a) Simultaneous subsonic and supersonic injection (subsonic injection at 1.03 velocity ratio and supersonic injection at 0.88 static pressure ratio);

(b) Supersonic injection at 0.94 static pressure ratio;

(c) Supersonic injection at 1.87 static pressure ratio;

(d) Supersonic injection at 0.5 static pressure ratio.

V, A, Experimental Results (cont.)

Heating and cooling transient data also were recorded at the (b), (c), and (d) conditions noted above. The core flow Mach number at the injection point was 2.5. The Mach number near the test section exit ranged from 2.44 (no supersonic injection) to 2.23 (Condition (c)).

Test Setups 104A and 104B

(Figures 20, 21, 22 (104A), and Figures 23, 24, 25 (104B))

Ambient temperature nitrogen film coolant was used with Test Setups 104A and 104B. The test assembly was the same as in Setups 103A and 103B except that the thin slot subsonic injector (tested previously as part of Test Setup 101) replaced the thick slot subsonic injector. Subsonic test chamber wall temperatures were measured in tests with Test Setup 104A. Four velocity ratios were tested, 0.62, 0.87, 1.13, and 1.4. Steady-state wall temperatures were measured at each velocity ratio, and heating and cooling transient data were obtained at 1.13 velocity ratio.

During the tests conducted with the 104A Test Setup, nitrogen film coolant outlet temperatures were measured using a 0.0127cm(0.005-in.) diameter sheathed chromel alumel thermocouple. The thermocouple was installed in a thin copper ring which was positioned downstream of the film coolant injector outlet. The thermocouple junction protruded into the film coolant slot about 0.025cm(0.010-in.) and did not touch the walls of the film coolant slot. The measured outlet temperatures and corresponding measured manifold temperatures are listed below.

Subsonic Nitrogen Film Coolant Flow Rate		Nitrogen Manifold Temperature		Outlet Temperature	
kg/sec	lbm/sec	°K	°F	°K	°F
0.035	0.077	298	76	346	162
0.052	0.1145	292	66	328	130
0.069	0.1525	288	59	318	111
0.086	0.1899	287	56	315	107

V, A, Experimental Results (cont.)

Supersonic nitrogen film cooling tests were conducted using Test Setup 104B (supersonic test section instrumented) at the following conditions:

(a) Simultaneous subsonic and supersonic injection (carryover data);
(b) Subsonic injection only at velocity ratio = 1.13 (carryover data);
(c) Supersonic injection at 0.95 static pressure ratio;
(d) Supersonic injection at 1.8 static pressure ratio;
(e) Supersonic injection at 0.45 static pressure ratio.

Steady-state wall temperatures were measured at all of these conditions. Heating and cooling transient data were obtained at conditions (c), (d), and (e). Core Mach number near the test section outlet ranged from 2.45 (no supersonic injection) to 2.31 (condition (d)) as shown in Table IV.

Test Setup 105A and 105B

(Figures 26, 27, 28 (Part A) and Figures 29, 30, 31 (Part B)

This test assembly consisted of all the conical components fabricated on this program (subsonic test section, subsonic injector, supersonic test section, supersonic injector). The aft end of the hardware assembly was attached to a cylindrical tube diffuser so that a static pressure of about 0.7 N/cm^2 abs (1.0 psia) could be maintained at the supersonic test section outlet. Testing was accomplished using ambient temperature nitrogen film coolant.

In the three tests conducted with Test Setup 105A, steady-state wall temperatures were measured in the subsonic chamber with subsonic hydrogen film coolant injected at three velocity ratios (0.76, 1.0 and 1.27). Heating and cooling transient data also were obtained at the 1.0 velocity ratio. The Test 105A data are considered quite adequate for evaluating acceleration effects.

V, A, Experimental Results (cont.)

In the 105B tests, steady-state, heating transient, and cooling transient wall temperature measurements were made on the conical supersonic test section when hydrogen was injected through the supersonic injector at core-gas-to-film coolant static pressure ratios of about 1.0, 2.0 and 0.5. In addition, steady-state wall temperatures in the supersonic test section were measured with subsonic film coolant carryover (with and without supersonic injection).

The heating and cooling transient data adequately describe the heat transfer coefficients with and without film cooling. However, the hydrogen film coolant was so effective that the increase in adiabatic wall temperature along the nozzle length was quite small. The measured wall temperature increase ranged from about 17°K (0.5 pressure ratio) to about 3°K (2.0 pressure ratio).

Test Setup 106

(Figures 32, 33)

After a review of the test data obtained with Test Setup 105B, it was determined that sufficiently large axial wall temperature gradients could be obtained by repeating the 105B tests with nitrogen supersonic film coolant instead of hydrogen. This was done in Test Setup 106. Steady-state wall temperatures were measured at 0.55, 1.04, and 2.0 pressure ratios. The axial temperature gradient in these tests ranged from 55 to 100°K (100 to 180°F).

V, Experimental Results and Correlation (cont.)

B. DATA CORRELATIONS

1. Acceleration Effects

Flow acceleration effects were found to decrease the entrainment fraction. Data from the conical chamber, Test Setup 105A, were used to determine the acceleration exponent n in the entrainment fraction formulation of Equation (16). As described previously in Section IV,D,1, the artificial entrainment fraction multiplier k'_m obtained with n = 0 was plotted vs $(r/r_o)^2$; a linear fit on log-log coordinates represents the proposed acceleration model, with the slope equal to the exponent n. Figure 34 shows the Test 105A data plotted in this manner, along with the conical chamber data of Ref. 1. The first entrainment fractions downstream of the injection point are omitted for the data of Ref. 1 since they are influenced by a turn. The two sets of data are in reasonably good agreement, and are well represented by the linear relationship of the proposed model. An acceleration exponent of 0.65 was obtained from the correlating line of Figure 34. This is in good agreement with the value of 0.59 indicated by Deissler, (Refs. 5 and 6), for turbulent transport phenomena in a homogeneous fluid. The value of 0.65 from Figure 34 was used in interpreting all remaining subsonic data.

2. Turning Effects

Entrainment fraction multipliers, k_m in Equation (16), were calculated from the appropriate subsonic effectiveness data. These multipliers account for film coolant injector perturbations, turning effects and any other phenomena not represented by the above acceleration correlation and the entrainment fraction k_o for plane, unaccelerated flow with continuous injection slots and thin slot lips. Figures 35 and 36 give the resultant multipliers for Setups 102 and 103A, respectively, which extend the hydrogen cooling data of Ref. 1 to new

convergent section geometries. Cylindrical section multiplers are consistent with the results of Ref. 1. Figure 35 indicates an entrainment fraction in this region equal to about 1.5 k_o, while Figure 36 gives a slightly larger value; the effectiveness data of Ref. 1 were correlated by 1.6 k_o. The significant increase in entrainment multipler in the turn at the start of convergence, which motivated the additional subsonic testing of the present program, is clearly evident in both figures. Figure 36 shows a very large reduction in entrainment in the 15° throat turn, while Figure 35 indicates a small reduction in the 30° throat turn. Correlation of turning effects is considered later in this section. Entrainment fractions in the supersonic transition section of Setup 103A, Figure 36, are approximately equal to those in the subsonic cylindrical section.

Figures 37 and 38 give the entrainment fraction multipliers for Setups 101 and 104A, respectively, which utilized nitrogen film coolant with the 0.038 cm (0.015-in.) slot coolant injector. Both figures show much higher multipliers in the cylindrical section than those noted above for hydrogen with a 0.153 cm (0.060-in.) slot height. This is attributed to the coolant injector lip which separates the two flows; it is 0.051 cm (0.020-in.) thick in each case, so that the ratio of lip thickness to slot height is much greater for the nitrogen data. A lip which is thick relative to the slot height is known to decrease the effectiveness (increase entrainment) for plane, unaccelerated flow, Ref. 14. The initial entrainment fraction multipliers of Figure 37 are higher than those in the rest of the cylindrical section; this may be the result of underestimating the preheating of the coolant. Figure 38 shows a large reduction in entrainment fraction in the 15° turn at the start of convergence, consistent with the data of Ref. 4 and the hypothesis of Ref. 1. This hypothesis attributes the turning effects to imbalances in centrifugal forces resulting from density differences between the coolant and core flows. Since the nitrogen coolant is heavier than the core flow, while the hydrogen

coolant of Setups 102 and 103A is lighter, the opposing turning effects exhibited by Figures 36 and 38 (same hardware) are to be expected. Figure 37 shows a smaller reduction in entrainment fraction in the 30° turn at the start of convergence compared with the 15° turn of Figure 38.

Analysis of individual thermocouple rows and test conditions for the results of Figures 37 and 38 does not reveal a consistent trend due to the throat turns. This results from an accuracy problem with the basic nitrogen data which is most acute in the convergent section. Part of the problem is the much higher wall temperature obtained compared with hydrogen for a given effectiveness. These high temperatures result in greater external heat losses, so that any error in correcting for these losses to obtain the adiabatic wall temperature is more significant. In addition, the reduction in entrainment in the turn at the start of convergence, as noted above, results in very little change in effectiveness in the convergent section as illustrated in Figures 9 and 21. Since each entrainment fraction is related to the difference in two adjacent effectiveness values, any error in effectiveness is greatly magnified in terms of the entrainment fraction in such a situation. Therefore, the throat data from Test Setups 101 and 104A have not been used in the turning correlation effort described below.

A parameter for correlating turning effects was proposed in Ref. 1, and its use has been continued herein. This parameter is based on the ratio of the differential centrifugal force resulting from the density difference across the mixing layer to the turbulent shear in the mixing layer; it is

$$2\left(\frac{\rho_e - \rho_w}{\rho_e + \rho_w}\right)\frac{s}{R} \qquad (23)$$

in which s is the mixing layer thickness at the start of the turn and R is the turn radius of curvature. R is taken to be positive at the start of convergence

and negative in the throat. Turning multipliers for the entrainment fraction were defined by dividing the overall multipliers of Figures 35 - 38, either in the turn or after the turn, by the multiplier immediately upstream of the turn as noted in Equation (22). All throat values except those from Ref. 4 are based on the average k_m multipliers in the turn. This definition is of greatest interest for application purposes and was a necessity considering the nature of the data. However, most multipliers for the turn at the start of convergence are based on the k_m value after the turn, i.e., the average in the cone; again, this definition is the one of most practical interest. In some cases the nature of the data necessitated alternate definitions at the start of convergence, with the numerator of Equation (22) based on the average k_m in the turn, turn plus cone or turn plus half the cone (cold hydrogen data of Ref. 1). Table V summarizes all data considered in the turning correlation study, including those from Refs. 1 and 4.

Figure 39 shows the turning multipliers as a function of the above turning parameter*. Since four groups of results are obtained, it is apparent that the proposed parameter is not sufficient to correlate turning effects. Each group of results is discussed below, with the group number corresponding to that shown on Figure 39.

(1) These results represent a broad range of conditions. Most are for hydrogen coolant in the turn at the start of convergence, but with both 15° and 30° turn angles. However, nitrogen data in both types of turns are included also. Since the throat turn results of Ref. 4 are defined

*Average values from the two thermocouple rows are presented for the current tests unless different definitions were used for each row.

on a local basis, all but two points in this group are defined consistently. For positive values the correlation parameter accomplishes its desired goal of correlating turning effects independent of turn angle and of the sign of $\rho_e - \rho_w$.

(2) All points in this group are for hydrogen in a 30° throat turn.

(3) This group is similar to the second in turning multiplier definition and turn angle; however, it is for nitrogen at the start of convergence. Therefore, Groups 2 and 3 indicate that for negative values of the proposed correlation parameter, it is necessary to distinguish between positive and negative values of $\rho_e - \rho_w$.

(4) This group indicates that it also is necessary to add a turn angle effect when the correlation parameter is negative, since this group is for a 15° turn. Although both hydrogen throat turn and nitrogen convergent turn data are represented, it cannot be concluded that these results would be correlated by the same curve. The hydrogen data are shown schematically since all but one in six were actually negative; additional points for Tests 104A (⊡) were also negative. The nitrogen data of Ref. 4 shed some light on the turn angle situation, since three results are included in Figure 39 for the turn at the start of convergence. Local results at approximately 15° are lowest and well below unity. Continued turning then increases the local entrainment fraction since the average value over a 35° turn is higher and the local value after 35° is still higher.

It should be remembered that turning effects are being interpreted here solely in terms of the entrainment fraction; it is possible that the mixing layer shape factor is also altered in a turn.

V, B, Data Correlations (cont.)

3. Supersonic Flow Effects Data

a. Supersonic Effectiveness

(1) Constant Mach Number

Data were obtained with the constant Mach number test section for both hydrogen and nitrogen coolants thereby obtaining injection velocity ratios of about 1.94 and 0.54, respectively. In each case three static pressure ratios were run (approximately 0.5, 1.0, and 1.8); six different entrainment fraction characteristics resulted. The most interesting comparison with existing effectiveness data is between the hydrogen data for a pressure ratio of 0.50 and the correlation from Ref. 7. This comparison is shown in Figure 40. Except for the first axial position the hydrogen data parallel the correlation of Ref. 7, although falling slightly below it. These are the only data from the present program which exhibit the effectiveness decay characteristics of existing data. The results of Ref. 12 show this same type of decay, although Figure 41 shows that these effectiveness values are considerably above the present hydrogen data. Both figures include the present nitrogen data for a pressure ratio of 0.45 for comparison purposes; the nitrogen data approximate the injection velocity ratio of Ref. 7.

Data for other pressure ratios were not shown on Figures 40 and 41 since they do not collapse into a single correlation. This is apparent for the hydrogen data from Figure 42, which shows a decreasing slope with increasing pressure ratio; the corresponding entrainment fractions are shown in Figures 43-45. For a pressure ratio of 0.50 the entrainment fraction increases axially similar to the result inferred in Appendix A for Ref. 7, which is included in Figure 43 for comparison. With approximate pressure matching, Figure 44, the entrainment fraction decreases slightly with axial position, starting from a value close to that for a pressure ratio of 0.50. Figure 45 is for a pressure ratio of 1.87; entrainment fractions are initially similar to

those for the previous pressure ratios, but then show a significant increase followed by an abrupt drop to values equal to or less than the corresponding pressure-matching entrainment fractions. The trendlines shown on Figures 43-45 were used to calculate entrainment flows in order to show the effect of entrainment fraction data scatter on effectiveness prediction. Figure 46 shows the hydrogen effectiveness data as a function of the resultant entrainment flow ratios; the curve shown is the model of Section III.

Some of the entrainment fraction characteristics of Figures 43-45 are consistent with the flow phenomena which would be expected as the two supersonic flows interact. Entrainment fractions in the first few inches are lowest with pressure matching, and in this case there is little variation throughout the length of the test section. It is of interest to note that these entrainment fractions are about equal to those obtained in the cylindrical section for subsonic injection with velocity matching using the 0.060-in. slot coolant injector (hydrogen data). The increase in entrainment fraction starting about 40 slot heights from the injection point for both cases with static pressure differences is presumably caused by expansion of the high pressure flow and its resultant interaction with the other flow. This effect must penetrate to the wall and thus is not seen in the initial entrainment fractions. Cause of the sharp reduction in entrainment fraction after about 150 slot heights with high pressure coolant, Figure 45, is not clear.

Figures 47-49 give the entrainment fractions for the nitrogen data of Test 104B; Figure 47 includes the values inferred from Ref. 7 for comparison. Only one row of data is shown, since a number of thermocouples in the other row were not operational for this test; these other entrainment fractions indicate the same trends but are slightly greater in magnitude. Initial entrainment fractions increase slightly with pressure ratio and are roughly double the values for the hydrogen data discussed above. The latter may

V, B, Data Correlations (cont.)

be due to the different injection velocity ratios in each case: 0.54 for nitrogen compared with 1.94 for hydrogen. For each nitrogen coolant pressure ratio the entrainment fraction is approximately constant for 120-150 slot heights, decays to about half the initial value at 250-300 slot heights and finally undergoes a rapid increase. Thus, the pressure ratio and axial position characteristics have nothing in common with the hydrogen data.

(2) Variable Mach Number

Figure 50 shows the entrainment fractions for all three of the setup 105B pressure ratios which used hydrogen coolant in the variable area supersonic test section. Results for all three pressure ratios are about the same. Initial values are slightly lower than the corresponding results for constant Mach number, Figures 43-45. However, a rapid decay follows to a level about one-third the initial value, except for an increase at the 0.71 cm (1.8 in.) axial position.

Setup 106 with nitrogen coolant approximates the injection velocity ratio of the hot firing data of Ref. 2. Figure 51 compares all effectiveness data from Setup 106 with ambient hydrogen data from Ref. 2 using the axial coordinate $\overline{X}_1/m\ s_c$; $\overline{X}_1$ accounts for core mass velocity variations and is derived from Equation (14) with an entrainment fraction of unity. It is noted that the data of Setup 106 for various pressure ratios collapse into a single curve fairly well using this coordinate. In addition, all results except for the last two or three locations for a pressure ratio of 0.56 are consistent with the data of Ref. 2, which were obtained with a pressure ratio slightly greater than unity.

Figures 52-54 give the entrainment fractions for Setup 106. For a pressure ratio of 0.56, Figure 52, the entrainment fraction is approximately constant and only slightly lower than the initial value for the corresponding

constant Mach number case, Figure 47. For static pressure matching, Figure 53, the entrainment fraction decreases gradually with axial position. Initial values are somewhat lower than for the constant Mach number case, Figure 48, but are slightly higher than for a pressure ratio of 0.56. Initial entrainment fractions for a pressure ratio of 2.01, Figure 54, are again slightly lower than in the constant Mach number case, Figure 49, and are slightly higher than for pressure matching. At this pressure ratio the initial entrainment fraction is maintained for about 0.6 cm (1.5 in.)., followed by a significant decay; this trend is similar to the first part of Figure 49 and covers about the same entrainment fraction range. The trendlines in Figures 53 and 54, along with a constant entrainment fraction of 0.027 for the data of Figure 52, were used to predict entrainment flow ratios; the resultant effectiveness correlation is shown on Figure 55, with the curve representing the supersonic model of Section III.

As noted above, Setup 106 with a pressure ratio of unity approximates the injection conditions of Ref. 2. Figure 56 shows a correlation of the corresponding entrainment fractions using the dimensionless coordinate of Figure 51. The results of Ref. 2 represent an excellent continuation of the Test 106B data. Since some of the present data for other pressure ratios are also in reasonable agreement with Figure 56, this correlation is recommended for nozzle design purposes when the coolant injection velocity ratio is 0.5-0.6. Based on extrapolating a linear version of Figure 56 to an axial coordinate of zero, the following correlation is recommended for small values of $\bar{x}_1/m\, s_c$:

$$k = \frac{0.038}{1 + 0.0176\, \dfrac{\bar{x}_1}{ms_c}} \; ; \quad \frac{\bar{x}_1}{ms_c} \leq 13.4 \qquad (24)$$

V, B, Data Correlations (cont.)

(3) Carryover Effects

The effects of using subsonic and supersonic film cooling simultaneously were studied in Setups 103 and 104. Test Setup 104 also included data in the supersonic test section when the only coolant was from the subsonic injector. An essentially constant effectiveness resulted, as shown in Figure 57. Also shown in Figure 57 are the effectiveness values with supersonic cooling only and with both coolant flows. These results show that the carryover from subsonic coolant can significantly increase the effectiveness in the supersonic section. A similar result was obtained in Setup 103 as shown in Figure 58, although the increase due to carryover is smaller since the effectiveness upstream of the supersonic injection was smaller.

Since the subsonic injection effectiveness was constant in the supersonic test section, a simple model for synthesizing carryover effects was investigated. This model postulates that the effectiveness for supersonic cooling only still applies with carryover provided the freestream species concentration is replaced by that obtained at the wall when only the subsonic coolant is utilized. Such an approach was first proposed in Ref. 15; the resultant effectiveness with carryover is

$$\eta = \eta_2 + \eta_1 (1 - \eta_2) \tag{25}$$

in which subscript 1 refers to subsonic cooling only and subscript 2 refers to supersonic cooling only. Figures 57 and 58 include the synthesized effectiveness predictions; in the latter case the effectiveness just upstream of the supersonic coolant injector was assumed to apply throughout the supersonic test section for subsonic cooling only. In both cases the synthesized effectiveness is in excellent agreement with the data for 1.2-1.6 cm (3-4 inches), after which the synthesized values are a little higher.

V, B, Data Correlations (cont.)

b. Heat Transfer Coefficient

(1) Correlation Approach

Heat transfer coefficients with and without film cooling in the supersonic nozzle region were correlated during this program. Heat transfer coefficients in the subsonic region were correlated previously (Ref. 1). In this previous work, it was found that the data for film cooled walls and for the case of no film cooling both are correlated by Equation (20) when the arithmetic mean of the wall and adiabatic wall temperatures was the reference temperature for evaluating physical properties. An additional effect of injection velocity was also observed. This previous correlation is a convenient analytical tool for analyzing non-adiabatic film cooled walls because it allows the calculation of heat transfer coefficients without film cooling if the heat transfer coefficients, or more specifically the C_g values, without film cooling are known and the composition of the mixing layer is evaluated from the entrainment model. Consequently, the same correlation approach was evaluated with the supersonic data obtained on this program.

(2) Constant Core Mach Number Data (Cylindrical Supersonic Test Section)

Values of the C_g factor calculated from the constant core Mach number test data are plotted as a function of axial position from the injection slot in Figures 59 and 60. These C_g values were from Equation (20) calculated using a Stanton number based on average test section mass flux (core gas flow rate and film coolant flow rate divided by total test section cross sectional area). Physical properties in Equation (20) were evaluated for the gas composition at the test section wall which was indicated by the effectiveness data, and at two reference temperatures: (1) the arithmetic mean of the wall

and adiabatic wall temperatures, and (2) the adiabatic wall temperature. The Figure 59 values are based on the arithmetic mean reference temperature and the Figure 60 values are based on the adiabatic wall reference temperature. These plots demonstrate that: (1) there are injection effects in the hydrogen data but not in the nitrogen data, and (2) that the arithmetic mean reference temperature provides a more concise grouping of the data. It is therefore concluded that the heat transfer correlation established previously for subsonic film cooling (Ref. 1) is also applicable for supersonic film cooling. As in the subsonic case, injection effects exist in certain of the data near the injection point.

The nitrogen film cooling C_g values are independent of the film-coolant-to-core-gas static pressure ratio and are about the same as the nitrogen core gas C_g values along the entire length of the cylindrical test section. The only significant difference exists within 3 cm (1.2-in.) of the injection point where the core gas data is slightly higher. The maximum observed difference is 20% at 1.5 cm (0.6-in.) axial distance. These higher core gas C_g values appear to be a "step effect" produced by the slight flow disturbance which occurs when the core gas flow expands across the 0.1 cm (0.04-in.) flow step formed by the film coolant injection slot and lip (no film coolant flow). Disregarding this "step effect", the nitrogen film coolant and core gas C_g values are practically constant along the test section length and range from 0.026 to 0.023 which is the traditional range for fully developed turbulent flow heat transfer.

The hydrogen supersonic heat transfer data are characterized by relatively large C_g values within about 10 cm (4-in.) of the injection point. The hydrogen C_g values are a function of pressure ratio and the highest values were observed at the highest pressure ratio. These hydrogen film cooling C_g values demonstrate that a significant difference existed in the

hydrogen film coolant and nitrogen film coolant wall heat transfer mechanisms near the injection point. A fundamental explanation of this behavior has not been established. It is possible that these high C_g values are related to supersonic shock phenomena. In terms of the injection conditions, it appears to be a velocity ratio effect since the coolant-to-freestream velocity ratio was about 2.0 with hydrogen film cooling and about 0.55 in the nitrogen film cooling case. Another possible explanation is that the unusual velocity profile downstream of the film coolant annulus at $u_c/u_e = 2.0$ (high velocity along walls) was unstable and tended to promote wall turbulence until a more regular profile was established at some distance downstream of the injection point.

(3) Variable Core Mach Number Data (Conical Supersonic Test Section)

The C_g values obtained with hydrogen film cooling in the conical supersonic test section are similar to the cylindrical supersonic results, and are plotted on Figure 61 and tabulated in Table V. However, these data are more difficult to interpret because it appears that shock phenomena at the entrance of the supersonic diffuser tube produced unusually large wall conduction effects which influenced the adiabatic wall temperature results.

The data near the film coolant injection point (upstream end) indicate the same general characteristics as the constant Mach number data. The hydrogen film cooling C_g's are relatively high, increase with pressure ratio, and decrease with axial distance, while the core gas nitrogen values are about the same as in the constant Mach number test section. However, towards the downstream end of the test section, the axial distribution of the hydrogen C_g data indicates a reversal of the initial decay characteristic and a trend toward increased C_g's. The core gas C_g values also tend to increase in this region. This trend of increasing C_g with axial distance appears invalid. It appears that shock-boundary layer interaction produced a

relatively high heat transfer coefficient on the ID of the nozzle exit flange where the conical nozzle ends abruptly and the cylindrical diffuser geometry begins. Furthermore, it appears that the effect of this high coefficient was to produce excess wall heating during the heating transient and excess wall cooling during the cooling transient. This leads to erroneously high C_g values for the core gas heating and the hydrogen film cooling transients. An additional factor here is that the conical supersonic test section transients were relatively long due to the low heat transfer coefficients which occur at high Mach number and consequently a longer time period existed for flange effects to influence the data. The transient periods were 10-20 seconds compared to 2-3 seconds in the subsonic and cylindrical supersonic test sections.

(4) Recommended Correlations

Two heat transfer correlations are recommended, one for film-coolant-to-core velocity ratios less than one and another for velocity ratios greater than one. For velocity ratio less than one, the recommended correlation is Equation (20) with $C_g = 0.026$ and with physical properties evaluated using the local wall fluid properties and the arithmetic mean reference temperature. This equation provides a good correlation of the nitrogen film cooling data obtained at 2.5 core Mach number and about 0.55 velocity ratio.

For velocity ratio greater than one, the hydrogen data indicate that injection effects are significant near the injection point. The foregoing correlation for velocity ratio less than unity but modified by injection effect factors is recommended for heat transfer from supersonic film coolant injected at a velocity ratio greater than one. Injection effect factors established from the hydrogen data are shown in Figure 62 as a function of pressure ratio and axial position, and in Figure 63 as a function of axial position and mass flux ratio.

TABLE II

FILM COOLING TEST CONDITIONS

Test Setup Number	Core N_2 Flow Rate, kg/sec	(lb/sec)	Core N_2 Temperature, °K	(°F)	Core N_2 Total Pressure, N/cm^2	(psia)	Film Coolant Gas	Coolant Flow Rate, kg/sec	(lb/sec)	Film[4] Coolant Temperature, °K	(°F)	Velocity Ratio, u_c/u_e	Density Ratio, ρ_c/ρ_e	Pressure Ratio, P_c/P_e	Slot Height, cm	(in.)	Coolant Reynolds Number
101	0.437	(0.962)	820	(1016)	174	(243)	N_2[1]	0.0345	(0.0761)	341	(155)	0.617	2.4	1.0	0.038	(0.015)	18263
	0.434	(0.955)	822	(1019)	171	(248)	N_2[1]	0.0513	(0.113)	320	(116)	0.866	2.57	1.0	0.038	(0.015)	28388
	0.427	(0.940)	819	(1014)	173	(251)	N_2[1]	0.0671	(0.148)	312	(102)	1.12	2.62	1.0	0.038	(0.015)	37825
	0.423	(0.932)	816	(1010)	174	(253)	N_2[1]	0.083	(0.183)	311	(100)	1.41	2.63	1.0	0.038	(0.015)	46887
102	0.397	(0.875)	880	(1130)	172	(250)	H_2[1]	0.0165	(0.0364)	310	(98)	0.812	0.205	1.0	0.152	(0.060)	19734
	0.386	(0.851)	886	(1138)	173	(252)	H_2[1]	0.0222	(0.0488)	311	(101)	1.12	0.205	1.0	0.152	(0.060)	26362
	0.373	(0.822)	884	(1135)	172	(250)	H_2[1]	0.0278	(0.0613)	308	(96)	1.45	0.206	1.0	0.152	(0.060)	33313
	0.355	(0.781)	887	(1140)	172	(250)	H_2[1]	0.0332	(0.0731)	307	(93)	1.8	0.208	1.0	0.152	(0.060)	39870
103A	0.444	(0.979)	816	(1009)	170	(267)	H_2[1]	0.0168	(0.0369)	305	(90)	0.785	0.192	1.0	0.152	(0.060)	20199
	0.444	(0.978)	814	(1007)	189	(275)	H_2[1]	0.0222	(0.0489)	302	(85)	1.03	0.194	1.0	0.152	(0.060)	26931
	0.444	(0.979)	814	(1007)	193	(280)	H_2[1]	0.0282	(0.062)	300	(80)	1.30	0.195	1.0	0.152	(0.060)	34357
103B	0.398	(0.876)	834	(1038)	172	(250)	H_2[2]	0.0226	(0.0497)	288	(60)	1.03	0.194	1.0	0.038	(0.015)	--
								0.00899	(0.0198)	290	(63)	1.93	0.142	0.88	0.051	(0.02)	
	0.466	(1.026)	817	(1011)	171	(248)	H_2[3]	0.0885	(0.0195)	291	(65)	1.98	0.140	0.938	0.051	(0.020)	14353
	0.469	(1.033)	814	(1007)	171	(249)	H_2[3]	0.0180	(0.0396)	290	(63)	1.95	0.287	1.87	0.051	(0.020)	29620
	0.469	(1.032)	813	(1005)	171	(249)	H_2[3]	0.00463	(0.0102)	293	(69)	2.02	0.071	0.498	0.051	(0.020)	7321
104A	0.450	(0.991)	915	(1008)	176	(255)	N_2[1]	0.0350	(0.077)	345	(162)	0.619	2.36	1.0	0.038	(0.015)	18334
	0.448	(0.987)	817	(1012)	179	(260)	N_2[1]	0.0658	(0.1145)	327	(130)	0.874	2.50	1.0	0.038	(0.015)	28287
	0.448	(0.987)	814	(1007)	182	(265)	N_2[1]	0.0692	(0.1525)	317	(111)	1.13	2.57	1.0	0.038	(0.015)	38545
	0.448	(0.987)	816	(1010)	187	(271)	N_2[1]	0.0862	(0.19)	315	(107)	1.40	2.59	1.0	0.038	(0.015)	48260
104B	0.418	(0.921)	820	(1016)	172	(250)	N_2[2]	0.0695	(0.153)	317	(111)	1.13	2.57	1.0	0.038	(0.015)	--
								0.0351	(0.0773)	295	(72)	0.527	2.03	0.93	0.051	(0.02)	
	0.417	(0.919)	829	(1030)	172	(250)	N_2[1]	0.0695	(0.153)	317	(111)	1.13	2.57	1.0	0.038	(0.015)	--
	0.465	(1.025)	818	(1012)	172	(250)	N_2[3]	0.0351	(0.077)	311	(100)	0.541	1.96	0.953	0.051	(0.02)	33557
	0.475	(1.046)	814	(1007)	174	(253)	N_2[3]	0.0690	(0.152)	290	(62)	0.524	3.94	1.79	0.051	(0.02)	69573
	0.473	(1.041)	816	(1009)	173	(252)	N_2[3]	0.0158	(0.0347)	354	(178)	0.578	0.818	0.454	0.051	(0.02)	13807

TABLE II (cont.)

Test Setup Number	Core N_2 Flow Rate, kg/sec	(lb/sec)	Core N_2 Temperature, °K	(°F)	Core N_2 Total Pressure, N/cm^2	(psia)	Film Coolant Gas	Coolant Flow Rate, kg/sec	(lb/sec)	Film[4] Coolant Temperature, °K	(°F)	Velocity Ratio, u_c/u_e	Density Ratio, ρ_c/ρ_e	Pressure Ratio, P_c/P_e	Slot Height, cm	(in.)	Coolant Reynolds Number
105A	0.449	(0.988)	817	(1012)	183	(265)	H_2(1)	0.0153	(0.0338)	305	(89)	0.758	0.193	1.0	0.152	(0.06)	18524
	0.446	(0.983)	817	(1012)	187	(272)	H_2(1)	0.0218	(0.0457)	301	(83)	1.02	0.195	1.0	0.152	(0.06)	25231
	0.447	(0.986)	817	(1012)	194	(282)	H_2(1)	0.026	(0.0573)	300	(80)	1.27	0.196	1.0	0.152	(0.06)	31753
105B	0.406	(0.895)	823	(1020)	172	(250)	H_2(2)	0.0208	(0.0458)	290	(63)	1.02	0.195	1.0	0.152	(0.06)	--
								0.00900	(0.0198)	290	(63)	1.92	0.149	0.961	0.051	(0.02)	
	0.406	(0.894)	817	(1012)	171	(249)	H_2(1)	0.0208	(0.0458)	289	(61)	1.02	0.195	1.0	0.152	(0.06)	--
	0.473	(1.042)	812	(1003)	172	(250)	H_2(3)	0.00901	(0.0201)	289	(62)	1.97	0.147	0.995	0.051	(0.02)	17586
	0.469	(1.035)	817	(1012)	171	(249)	H_2(3)	0.0183	(0.0404)	284	(53)	1.93	0.304	1.97	0.051	(0.02)	36197
	0.469	(1.035)	816	(1009)	171	(249)	H_2(3)	0.00471	(0.0104)	286	(56)	1.99	0.076	0.523	0.051	(0.02)	8957
106	0.469	(1.035)	814	(1007)	171	(248)	N_2(3)	0.0176	(0.0388)	346	(163)	0.564	1.00	0.556	0.051	(0.02)	15463
	0.469	(1.036)	814	(1007)	171	(249)	N_2(3)	0.0350	(0.0772)	310	(99)	0.534	2.09	1.044	0.051	(0.02)	33185
	0.468	(1.033)	814	(1007)	171	(248)	N_2(3)	0.0698	(0.154)	288	(59)	0.515	4.35	2.014	0.051	(0.02)	69719

NOTES: (1) Subsonic Injection Only

(2) Subsonic and Supersonic Injection, Subsonic Data Listed First

(3) Supersonic Injection Only

(4) N_2 Values Adjusted for Preheating

TABLE III

SUPERSONIC C_g VALUES

$$C_g = St\ Pr^{0.6}\ Re^{0.2}$$

$(C_g)_{aw}$: Reference Temperature = Adiabatic Wall Temperature (T_{aw})

$(C_g)_{am}$: Reference Temperature = $\frac{T_{wall} + T_{aw}}{2}$

Test Setup 103B

H_2 Film Coolant, S_c = .051 cm (.02-in.)

	Heating Transient		Pressure Ratio = .94		Pressure Ratio = 1.87		Pressure Ratio = .50	
Z/S_c	$(C_g)_{aw}$	$(C_g)_{am}$	$(C_g)_{aw}$	$(C_g)_{am}$	$(C_g)_{aw}$	$(C_g)_{am}$	$(C_g)_{aw}$	$(C_g)_{am}$
30	.0338	.0300	.0379	.0448	.0560	.0708	.0278	.0328
55	.0324	.0290	.0273	.0320	.0433	.0532	.0220	.0250
92.5	.0286	.0254	.0213	.0243	.0317	.0387	.0193	.0214
130	.0274	.0245	.0199	.0226	.0285	.0340	.0202	.0220
180	.0266	.0238	.0176	.0196	.0236	.0273	.0193	.0207
230	.0275	.0249	.0126	.0195	.0226	.0259	.0206	.0219
280	.0244	.0220	.0163	.0180	.0240	.0240	.0187	.0197
335	.0225	.0248	.0157	.0172	.0198	.0224	.0189	.0197
390	.0228	.0206	.0156	.0176	.0186	.0207	.0186	.0181

TABLE III (cont.)

Test Setup 104B

N_2 Film Coolant, S_c = .051 cm (.02-in.)

Z/S_c	Heating Transient $(C_g)_{aw}$	Heating Transient $(C_g)_{am}$	Pressure Ratio = .94 $(C_g)_{aw}$	Pressure Ratio = .94 $(C_g)_{am}$	Pressure Ratio = 1.87 $(C_g)_{aw}$	Pressure Ratio = 1.87 $(C_g)_{am}$	Pressure Ratio = .50 $(C_g)_{aw}$	Pressure Ratio = .50 $(C_g)_{am}$
30	.0393	.0337	.0211	.0252	.0211	.0257	.0249	.0267
55	.0317	.0286	.0231	.0248	.0208	.0240	.0252	.0258
92.5	.0277	.0257	.0248	.0260	.0228	.0250	.0242	.0246
130	.0279	.0263	.0230	.0261	.0254	.0267	.0252	.0254
180	.0252	.0240	.0227	.0232	.0221	.0229	.0224	.0224
230	.0265	.0254	.0241	.0244	.0243	.0251	.0240	.0240
280	.0253	.0242	.0245	.0247	.0245	.0253	.0248	.0249
355	.0244	.0233	.0220	.0223	.0217	.0233	.0229	.0229
390	.0238	.0227	.0214	.0216	.0216	.0219	.0230	.0227

Test Setup 105B

H_2 Film Coolant, S_c = .051 cm (.02-in.)

33.5	.0368	.0330	.0343	.0403	.0467	.0565	.0490	.0713
56	.0357	.0314	.0326	.0375	.0428	.0513	.0489	.066
78.5	.0366	.0321	.0310	.0356	.0393	.0471	.0479	.0616
101	.0376	.0324	.0294	.0336	.0377	.0447	.0488	.0611
123.5	.0444	.0380	.0310	.0348	.0389	.0461	.0498	.0617

TABLE IV

EXPERIMENTAL TEST SECTION MACH NUMBERS

Test	Subsonic U_c/U_e	Supersonic P_c/P_e	M_{exit} (3)
103A	.75	(1)	2.44
↓	1.0	(1)	2.43
↓	1.25	(1)	2.4
103B	1.0	1.0	2.33
↓	(2)	1.0	2.34
↓	(2)	2.0	2.23
↓	(2)	.5	2.38
104A	.5	(1)	2.45
↓	.75	(1)	↓
↓	1.0	(1)	↓
↓	1.25	(1)	↓
104B	1.0	1.0	2.36
↓	1.0	(1)	2.44
↓	(2)	1.0	2.35
↓	(2)	2.0	2.31
↓	(2)	.5	2.40
105A	.75, 1.0, 1.25	(1)	4.25
105B	1.0	1.0	4.2
↓	1.0	(1)	4.25
↓	(2)	1.0	4.2
↓	(2)	2.0	4.05
↓	(2)	.5	4.15
106	(2)	2.0	4.15
↓	(2)	1.0	4.2
↓	(2)	.5	4.2

(1) - indicates no supersonic injection
(2) - indicates no subsonic injection
(3) - Mach number 1/2-in. from test section exit.

TABLE V

TURNING CORRELATION PARAMETERS

Source	Angle, Degrees	Type*	S/R Range	$\Delta\rho/\bar{\rho}$ Range	Correlation Parameter	Correlation Group
S/R +, $\Delta\rho/\bar{\rho}$ + (H_2 Conv.)						
Ref. 1 (cold)	30	◐	.26 to .32	.056	.015 to .018	1
103A	15	□	.10 to .13	.49 to .73	.060 to .083	1
102A	30	○	.10 to .13	.50 to .81	.061 to .097	1
Ref. 1	30	○	.29	.57 to .60	.16 to .17	1
S/R -, $\Delta\rho/\bar{\rho}$ - (N_2 Throat)						
Ref. 4	27	◢	-.019	-.58	.011	1
S/R - $\Delta\rho/\bar{\rho}$ + (H_2 Throat)						
Ref. 1	30	●	-.47	.46	-.22	2
102A	30	●	-.17 to -.21	.41 to .63	-.085 to -.125	2
103A	15	■	-.15 to -.19	.41 to .55	-.070 to -.099	4
Ref. 1 (cold)	30	●	-.40 to -.50	.078	-.031 to -.039	2
S/R+, $\Delta\rho/\bar{\rho}$- (N_2 Conv.)						
101A	30	○ ◑ ◒	.22 to .37	-.18 to -.40	-.061 to -.099	3
104A	15	□ ◨	.13 to .15	-.18 to -.24	-.025 to -.033	4
Ref. 4	15	⌂	.013	-.87	-.011	4
Ref. 4	35	▲ △				3,1

* See Legend on Figure 39

VI. ANALYTICAL PREDICTIONS

Analytical predictions for hydrogen film cooled hydrogen-oxygen thrust chambers were made with the ALRC entrainment model and certain of the entrainment fraction correlations derived from test data and discussed in Section V,B. Analyses were performed for conditions representative of 2 engine systems: (1) a space shuttle APS engine, and (2) a space shuttle tug engine.

A. APS THRUST CHAMBER PREDICTIONS

The APS predictions were made for the subsonic region only of a typical film cooled thrust chamber. The geometry parameters and the range of operating conditions considered are typical for the Auxiliary Propulsion System for the Space Shuttle (Ref. 2). The thrust chamber geometry was established from data supplied in References 1 and 2 and is shown in Figure 64. The range of operating conditions considered are as follows:

Chamber Pressure:	69 to 207 N/cm^2 (100 to 300 psia)
O_2/H_2 Mixture Ratio:	2 to 6
Vacuum Thrust:	4.45×10^2 to 4.45×10^4 N (100 to 10^4 lb_f)
Inlet Film Coolant Temp:	79 to 300°K (140 to 540°R)
Velocity Ratio (Subsonic Injection):	1.0
Main Injector Propellant Temperatures:	H_2 = 179K (250 R)
	O_2 = 208K (375 R)

The reference design case was: MR = 4,207 N/cm^2 (300 psia) chamber pressure, 6680 N (1500 lb_f) thrust, and 300°K (540°R) H_2 inlet temperature. For other operating conditions, thrust chamber design parameters were changed as follows (geometry defined on Figure 64):

VI, A, APS Thrust Chamber Predictions (cont.)

(a) $R_t \alpha \left(\frac{F}{P_o}\right)^{1/2}$

R_t = 244 cm (0.96 in.) for the reference case.

(b) L' = 8.4 cm (3.3 in.) for F = 445 N (100 lb_f)

= 14.6 cm (5.75 in.) for F = 6,680 N (1500 lb_f)

= 25.4 cm (10.0 in.) for F = 4.45×10^4 N (10^4 lb_f)

(c) R_c/R_t = 1.77

(d) W α F

W = 1.52 kg/sec (3.41 lb_m/sec) for the reference case.

Film coolant flow rate requirements were calculated for an otherwise uncooled thrust chamber in which film coolant is injected parallel to the thrust chamber walls at the main propellant injector. The design criterion governing film coolant flow rate was that a 1090°K (1500°F) maximum adiabatic wall temperature was allowed at the thrust chamber throat. This temperature was established in Reference 1 as representative of the conditions required to meet Space Shuttle APS cycle life requirements. Entrainment fraction values were calculated from the following equation which is based on the Setup 105A data and the acceleration effect correlation given in Section V,B.

$$k = 2.7 \left[\frac{\rho_e U_e}{(\rho_e U_e)_o}\right]^{-0.65} k_o \qquad (26)$$

Predicted adiabatic wall temperatures and slot heights obtained from the ALRC film cooling model are listed in Table VI. Film cooling requirements based on the 1090°K T_{aw} criteria for variable MR and P_c with 300°K (540°R)

film coolant inlet temperature are shown as a percent of the fuel flow rate and as a percent of the total propellant flow rate in Figure 65. The predicted requirement for the reference design case is 28% of the fuel or 5.6% of the total flow rate. The required amount of film cooling decreases with MR and increases with P_o. The MR = 2 film cooling flow rates are slightly optimistic because the corresponding slot height values are on the order of 0.0375 cm (0.015 in.) and a film cooling annulus this thin is difficult to fabricate. Thicker slot heights would yield a velocity ratio less than 1.0 and, because of increased mixing, this leads to less efficient utilization of the film coolant. All other slot heights are greater than 0.0625 cm (0.025 in.).

The effects of inlet temperature and thrust on film cooling requirements are shown in Figures 66 and 67. The predicted film cooling requirement decreases as the thrust increases and the inlet temperature decreases. The indicated decrease with reduced inlet temperature may not be practical to achieve because of the small slot heights required for unity velocity ratio at the lower temperatures.

B. SPACE TUG THRUST CHAMBER PREDICTIONS

Predictions for the effect of hydrogen film cooling on the wall temperatures of a proposed O_2/H_2 space tug engine (Ref. 6) were made using certain of the entrainment fraction correlations and the heat transfer correlation discussed in Section V,B. Predictions were made for both the subsonic and supersonic region of the thrust chamber. The thrust chamber geometry and film coolant annulus slot height were assumed fixed and wall temperature and heat flux values at critical points were calculated as a function of the H_2 film coolant flow rate for operating conditions which yield 100%, 50%, and 17% of rated thrust. Pertinent operating conditions and design parameters provided by D. E. Sokolowski of the NASA Lewis Research Center are listed in Table VII.

VI, B, Space Tug Thrust Chamber Predictions (cont.)

1. Subsonic Region Adiabatic Wall Temperature

Adiabatic wall temperature predictions for the subsonic region of the O_2/H_2 space tug thrust chamber shown in Figure 68 were obtained using the ALRC entrainment model and the entrainment fraction correlation applied in the APS thrust chamber analysis. It was assumed that the hydrogen film coolant was introduced at the main propellant injector. Turning effects in the convergent region were assumed negligible because of the large turn radius and the contour approximates a cone. The coefficient of the entrainment fraction correlation was modified in accordance with the laboratory test results obtained with cylindrical chambers on this program and in previous work (Ref. 1). The following equation was used to calculate the factor which was applied to the plane unaccelerated flow entrainment fraction value.

$$k = 2.0 \left[\frac{\rho_e U_e}{(\rho_e U_e)_o}\right]^{-0.65} k_o \qquad (27)$$

Initial adiabatic wall temperature calculations were made assuming a film-coolant-to-core-gas velocity ratio of 1.0 in order to minimize mixing of the film coolant and core gases. However it was found that this velocity ratio assumption implied film cooling injection annulus slot heights which were too small and not practical to fabricate. Consequently, the slot height was fixed at 0.0635 cm (0.025 in.) and the adiabatic wall temperatures were re-evaluated. The adiabatic wall temperature results, calculated slot heights ($u_c/u_e = 1.0$), and calculated velocity ratios (fixed slot height) are tabulated in Table VIII. Comparison of the adiabatic wall temperature results in Table VIII demonstrates the predicted loss in film cooling efficiency for velocity ratio less than unity.

VI, B, Space Tug Thrust Chamber Predictions (cont.)

2. Supersonic Adiabatic Wall Temperature

The adiabatic wall temperature predictions for the supersonic region of the O_2/H_2 space tug thrust chamber were calculated from the ALRC entrainment model using the entrainment fraction correlation derived in Section V,B for variable Mach number flow at pressure ratio of about one and velocity ratio less than one. This correlation is restated below:

$$k = \frac{0.038}{1 + 0.01757 \frac{\bar{X}_1}{ms_c}}, \quad \left(\frac{\bar{X}_1}{ms_c}\right) < 13.4 \tag{28}$$

$$k = 0.04709 - 0.1449 \log_{10} \left(\frac{\bar{X}_1}{ms_c}\right), \quad 13.4 \leq \left(\frac{\bar{X}_1}{ms_c}\right) \leq 362.8 \tag{29}$$

$$k = 0.01; \left(\frac{\bar{X}_1}{ms_c}\right) > 362.8 \tag{30}$$

The calculated adiabatic wall temperatures and other pertinent results are listed in Table IX. These values were obtained assuming a pressure ratio of 1.0 which implies different slot heights for each film coolant flow rate as shown in the table. Certain of these slot heights are too small (% FFC < 20). If it is assumed that pressure ratio effects on k are small, these T_{aw} values are applicable to a film coolant annulus with fixed slot height but which operates over a range of pressure ratios (k is independent of s_c since $ms_c = W_c\ D/4\ W$).

VI, B, Space Tug Thrust Chamber Predictions (cont.)

3. Gas-Side Wall Temperature and Heat Flux

Gas-side wall temperatures and heat fluxes at the critical locations noted in Table VII were estimated for the regeneratively cooled space tug engine with supplemental hydrogen film cooling applied to the walls. The estimates are shown plotted as a function of the film coolant flow rate in Figures 69 and 70. They were obtained using the following procedure:

a. The thermal resistance, (R_{th}), at each critical point between the gas side wall and the coolant bulk temperatures was calculated from the Table VII data and assumed constant.

b. Heat transfer coefficients with film cooling were calculated from the Table VII values through the use of a ratio derived from Equation 20. The ratio is defined by the following equation.[1]

$$\frac{(h_g)_2}{(h_g)_1} = \frac{\left(\frac{\mu^{0.2} C_p}{Pr^{0.6}}\right)_2}{\left(\frac{\mu^{0.2} C_p}{Pr^{0.6}}\right)_1} \qquad \frac{(MW_{am})_2}{(MW_{am})_1} \frac{(T_{am})_1}{(T_{am})_2} \tag{31}$$

where: μ, C_p, Pr are evaluated at arithmetic mean temperature, T_{am}

Representative wall temperatures were assumed and the above heat transfer coefficient ratio was calculated as a function of wall MR. The calculated ratios are shown in Figure 71.

[1]See footnote at bottom of following page.

VI, B, Space Tug Thrust Chamber Predictions (cont.)

c. Heat flux and gas-side wall temperature values were generated using the following expressions.[2]

$$(q/A)_{\text{gas side}} = \frac{T_{aw} - T_b}{\frac{1}{h_g} + R_{th}} \tag{32}$$

$$T_{wg} = T_{aw} - (q/A)_{\text{gas side}} \left(\frac{1}{h_g}\right) \tag{33}$$

The T_{aw} wall values used are shown in Table VIII (constant slot height results) and Table IX. The coolant bulk temperature values of Table VII were assumed constant.

[2]The gas side heat transfer coefficient shown in Equations 31, 32, and 33 and Figure 71 is based on temperature driving potential rather than enthalpy driving potential as indicated in Section III,B, Equation 19. In Ref. 2 it is shown that for O_2/H_2 propellant at MR values less than 3.0, the difference between hg based on enthalpy and hg based on temperature is less than 5%. Note that with the hg based on temperature, the Stanton Number definition is: St = hg/GCp.

TABLE VI

ADIABATIC WALL TEMPERATURE RESULTS

APS THRUST CHAMBER ANALYSIS

F_{ref} = 4.45 N = 1 lb_f

$(P_o)_{ref}$ = 0.689 N/cm^2 = 1 psia

T_{ref} = 810°K = 1000°R

$(S_c)_{ref}$ = 2.54 cm = 1 inch

F/F_{ref}	$P_o/(P_o)_{ref}$	MR	FFC	$\frac{(T_{aw})tht}{T_{ref}}$	$\frac{s_c}{(s_c)_{ref}}$	$\frac{T_{in}^{(1)}}{T_{ref}}$
1500	100	2	5	2.389	0.012	0.54
			10	1.712	0.0242	
			20	1.102	0.0494	
			30	0.892	0.0767	
		4	10	3.126	0.016	
			20	1.974	0.0337	
			30	1.432	0.0539	
		6	10	4.358	0.0134	
			20	2.948	0.0289	
			30	2.135	0.0472	
1500	300	2	5	2.665	0.0068	0.54
			10	2.051	0.0137	
			20	1.346	0.0279	
			30	1.055	0.0431	
		4	10	3.680	0.0089	
			20	2.516	0.0189	
			30	1.862	0.03	

TABLE VI (cont.)

F/F_{ref}	$P_o/(P_o)_{ref}$	MR	FFC	$\frac{(T_{aw})tht}{T_{ref}}$	$\frac{s_c}{(s_c)_{ref}}$	$\frac{T_{in}}{T_{ref}}$ (1)
		6	20	3.670	-	
			30	2.800	0.0266	
			40	2.238	0.0389	
			50	1.858	0.0543	
1500	500	2	5	2.787	0.0052	0.54
			10	2.213	0.0105	
			20	1.508	0.0213	
			30	1.162	0.0329	
		4	10	3.930	0.0069	
			20	2.818	0.0145	
			30	2.127	0.0232	
		6	30	3.151	0.0204	
			40	2.569	0.0299	
			50	2.160	0.0416	
10,000	300	4	10	2.809	0.0234	0.54
			20	1.681	0.0494	
			30	1.248	0.0793	
100	300	4	30	3.450	0.0074	0.54
			53	2.509	0.0165	
			60	2.321	0.0205	
			66.6	2.180	0.0255	
1500	300	4	10	3.404	0.0056	0.34
			20	2.159	0.0119	
			30	1.500	0.0191	
1500	300	4	10	2.856	0.0022	0.14
			20	1.576	0.0048	
			30	1.008	0.0077	

(1) T_{in} = Film Coolant Inlet Temperature

TABLE VII

SPACE TUG THRUST CHAMBER OPERATING CONDITIONS
AND DESIGN PARAMETERS

% of Maximum Thrust	Chamber Pressure kN/m^2 (psia)	Mixture Ratio O_2/H_2	SUBSONIC REGION WITH NO FILM COOLING				SUPERSONIC REGION WITH NO FILM COOLING			
			Critical Point	T_{wg} °K (°R)	h_{g2} watt/cm^2 °K (Btu/in^2 sec °R	Regen Coolant Temp. °K (°R)	Critical Point	T_{wg} °K (°R)	watt/cm^2 °K (Btu/in^2 sec °R)	Regen Coolant Temp. °K (°R)
100	1310 (1900)	6.5	1.25 cm (0.5 in.) upstream of throat	755 (1360)	4.44 (.015)	103 (186)	A/A_t = 78/1	579 (1041)	.0624 (.000212)	83 (149)
50	655 (950)	6.0	15 cm (6 in.) Upstream of Throat	621 (1120)	0.95 (.00323)	212 (382)	A/A_t = 78/1	464 (835)	.033 (.000122)	83 (149)
17	220 (320)	5.0	15 cm (6 in.) Upstream of throat	494 (888)	0.4 (.00136)	185 (333)	A/A_t = 78/1	328 (590)	.0151 (.0000515)	80 (144)

Film Coolant Inlet Temperature = 90°R

Subsonic Film Coolant Introduced at Main Injector

Supersonic Film Coolant Introduced at A/A_t = 8/1

Subsonic Film Coolant Annulus Slot Height = .0635 cm (.025 in)

Supersonic Film Coolant Annulus Slot Height = .0635 cm (.025 in.)

TABLE VIII

SUBSONIC ADIABATIC WALL TEMPERATURE RESULTS
SPACE TUG THRUST CHAMBER
Film Coolant Injected Parallel to Chamber Wall at Main Injector

% Thrust	Overall MR	% FFC	s_c/s_{ref}	T_{aw} (1) °K	MR at Wall (1)	u_c/u_e	T_{aw} (1) °K	MR at Wall (1)
100	6.5	10	.06	1910	2.09	.06	-	3
		20	.13	1006	.99	.13	2138	2.4
		30	.22	618	.58	.22	1298	1.32
		40	.30	437	.40	.29	804	0.77
50	6.0	5	.03	1778	1.87	.03	-	3
		10	.06	929	.88	.05	2440	2.84
		20	.12	419	.37	.12	1420	1.11
		30	.19	263	.22	.19	570	.52
		40	.29	193	.16	.28	347	.3
		50	.40	156	.17	.40	230	.2
17	5.0	5	.03	1623	1.66	.03	-	3
		10	.06	843	.79	.06	2152	2.38
		20	.14	382	.34	.14	972	.93
		30	.22	241	.21	.22	488	.44
		40	.33	179	.14	.33	297	.26

(1) Conditions at critical points:

% Thrust	Critical Point Location
100	1.25 cm upstream of throat
50	15 cm upstream of throat
17	15 cm upstream of throat

TABLE IX

SUPERSONIC ADIABATIC WALL TEMPERATURE RESULTS
SPACE TUG THRUST CHAMBER
Film Coolant Injected Parallel to Chamber Wall at $A/A_T = 8/1$

% Thrust	Overall MR	% FFC	$\frac{u_c}{u_e}$ (1)	Taw °K (2)	MR at Wall (2)	S_c/S_{ref} or Pressure Ratio (3) (4)
100	6.5	5	.20	1669	2.09	.21
		10	.20	1145	1.37	.42
		20	.21	679	.77	.88
		30	.21	444	.48	1.4
		40	.23	286	.30	1.99
50	6.0	5	.20	1567	1.95	.22
		10	.20	1068	1.27	.46
		20	.21	623	.71	.94
		30	.21	396	.42	1.48
		40	.22	253	.26	2.09
		50	.24	167	.16	2.81
17	5.0	5	.20	1344	1.65	.26
		10	.20	901	1.07	.53
		20	.20	500	.57	1.07
		30	.20	297	.32	1.65
		40	.21	178	.18	2.31

(1) $\frac{u_c}{u_e} = \frac{M_c}{M_e} \left(\frac{T_c}{T_e}\right)^{1/2} \left(\frac{MW_e}{MW_c}\right)^{1/2}$, $\frac{\rho_c}{\rho_e} = \frac{T_e}{T_c} \frac{P_c}{P_e} \frac{MW_c}{MW_e}$

$M_c = 2.0$, $M_e = 2.95$ $(T_c)_o = 90°R$, Core Gas MR $= \frac{\text{Overall MR}}{1 - \frac{\% \text{ FFC}}{100}}$

(2) Conditions at nozzle area ratio = 78/1
(3) Pressure Ratio = 1.0, Slot Height Variable
(4) Slot Height = .0625 cm (.025 in) = S_{ref},
Pressure Ratio Variable
k assumed independent of pressure ratio

VII. CONCLUSIONS AND RECOMMENDATIONS

1. Flow acceleration reduces the entrainment fraction and thus increases cooling effectiveness. This effect is correlated in the convergent section by the mass velocity power-law of Equation (16) with n = 0.65, which is in good agreement with the exponent of 0.59 obtained by Deissler (Refs. 5 and 6) for turbulent transport phenomena in a homogeneous fluid.

2. Turning effects have been partially correlated as shown in Figure 39 using the turning parameter proposed in Ref. 1. The correlation for positive values of this parameter is recommended for design purposes. Although the results for negative values also provide a design guide, the correlation parameter is not sufficient by itself to describe all results. For example, it does not include the turn angle, which is shown to be an important parameter in this region. In addition, the present parameter apparently does not properly distinguish between heavy coolant at the start of convergence and light coolant in a throat turn. Additional studies of turning effects are recommended using larger hardware to improve accuracy and obtain entrainment fraction variations within the turns.

3. Initial entrainment fractions for supersonic film cooling are strongly dependent on injection velocity ratio. Values for a velocity ratio of about 0.5 (nitrogen coolant) are approximately double those for a velocity ratio of about 2.0 (hydrogen data); the latter entrainment fractions are about equal to the lowest values obtained for subsonic film cooling. These initial entrainment fractions are independent of pressure ratio for the higher velocity ratio, but increase slightly with pressure ratio at the lower velocity ratio. The above trends were observed in both the constant and variable Mach number tests.

4. A great diversity of variations in supersonic entrainment fraction with axial distance from the injection point was observed. It is concluded that these variations are related to the expansion, compression and shock phenomena

associated with the interaction of the two flows and that flow visualization studies are required in order to explain specific results. In general, the variable Mach number entrainment fractions decrease significantly with axial distance, starting from initial values close to the corresponding constant Mach number results.

5. Good correlation of the variable Mach number data for a velocity ratio of 0.54 and pressure ratio of unity was obtained using a dimensionless axial coordinate. The film cooled rocket nozzle data of Ref. 2 agree with this correlation. Some of the data for other pressure ratios are also in reasonable agreement with this correlation and it is recommended for rocket nozzle design application when the injection velocity ratio is 0.5-0.6.

6. Supersonic film cooling tests in which the film coolant is hydrogen and nitrogen mixed in the appropriate proportions to provide a unity film coolant-to-core gas velocity ratio are recommended for future supersonic film cooling studies. Such tests would provide a useful supersonic film cooling reference condition and would eliminate any turbulent mixing effects due to the velocity mismatch between the core and film coolant gases.

7. Carryover effects from simultaneous subsonic film cooling can significantly increase supersonic effectiveness values. This increase is accurately predicted by a simple synthesis model using the individual coolant effectiveness values.

8. Heat transfer coefficients with and without film cooling in the supersonic nozzle region are correlated by Equation (20). For a film coolant to core gas velocity ratio of about 0.5, the data correlate with the same C_g factor provided that physical properties are evaluated at the following conditions: (1) the temperature corresponding to the arithmetic mean of the

adiabatic wall and wall temperatures, and (2) the gas composition at the wall. Equation 20 and the foregoing procedure for evaluating physical properties are therefore recommended for design calculations when the velocity ratio is approximately 0.5. If no experimental C_g data are available, a value of 0.026 is recommended. The subsonic heat transfer coefficient data obtained previously indicate that these recommendations are also applicable for the subsonic region except near the injection slot (See Ref. 1). The heat transfer coefficient data obtained at a velocity ratio of about 2.0 indicate a significant injection effect. Possibly this is due to shock phenomena or an inherently unstable velocity profile which promotes turbulence at the wall. The factor shown in Figures 62 and 63 is recommended for evaluating this effect.

9. The entrainment film cooling model developed at ALRC has been designed to account for chemical reactions between the film coolant and entrained core gases through the use of an enthalpy effectiveness definition. However, two aspects of chemical reactions remain to be investigated; (1) the possible effects of core reactions on the entrainment fraction, and (2) reaction kinetics effects. An experimental hydrogen film cooling program with actual rocket engine injectors generating core flow gases with a known chemistry is recommended for future work.

10. Analytical studies using two-dimensional boundary layer computer programs, such as the NASA-Langley program (Ref. 12) developed specifically for film cooling, are recommended to verify the shape factor and high-speed formulations of the present entrainment model. These studies would also provide valuable insight into the correlation of velocity ratio and Reynolds number effects.

REFERENCES

1. Ewen, R. L., "Hydrogen Film/Conductive Cooling, Aerojet Liquid Rocket Company, NASA CR-120926, Contract NAS 3-14343, November 1972

2. Schoenman, L., and LaBotz, R. J., "Hydrogen-Oxygen Auxiliary Propulsion For the Space Shuttle, Volume 1: High Pressure Thrusters", Aerojet Liquid Rocket Company, NASA CR-120895, Contract NAS 3-14354, 30 January 1973

3. Gordon, S. and McBride, B., "Computer Program for Calculation of Complex Chemical Equilibrium Composition, Rocket Performance, Incident and Reflected Shocks, and Chapman - Jouquet Detonations", NASA SP-273, NASA Lewis Research Center, 1971

4. Williams, J. J., "The Effect of Gaseous Film Cooling on the Recovery Temperature Distribution in Rocket Nozzles", PhD. Thesis, University of California at Davis, May 1969. Also ASME Paper No. 70-HT/SpT-42

5. Deissler, R. G., "Weak Locally Homogenous Turbulence in Idealized Flow Through a Cone", NASA TN D-3613, 1966

6. Deissler, R. G., "Weak Locally Homogenous Turbulence and Heat Transfer with Uniform Normal Strain", NASA TN D-3779, January 1967

7. Goldstein, R. J., et al., "Film Cooling with Air and Helium Injection Through a Rearward Facing Slot into a Supersonic Air Flow", AIAA Journal, Vol. 4, No. 6, 1966, pp 981-985; also University of Minnesota, Heat Transfer Laboratory, TR No. 60, February 1965

8. Parthasarathy, K and Zakkay, V., "Turbulent Slot Injection Studies at Mach 6", ARL 69-0066, April 1969

9. Zakkay, V., et al., "An Experimental Investigation of Supersonic Slot Cooling", Proceedings of the 1970 Heat Transfer and Fluid Mechanics Institute, Stanford University Press, pp 88-103

10. Cary, A. M., Jr., and Hefner, J. N., "An Investigation of Film-Cooling Effectiveness and Skin Friction in Hypersonic Flow", AIAA Paper No. 71-599, June 1971

11. Mukerjee, T. and Martin, B. W., "Film Cooling by Air Injection Through a Backward Facing Annular Tangential Slot into a Supersonic Axisymmetric Parallel Diffuser", Proceedings of the 1968 Heat Transfer and Fluid Mechanics Institute, Stanford University Press, pp 221-242

12. Beckwith, J. E., and Bushnell, D. M., "Calculation by a Finite-Difference Method of Supersonic Turbulent Boundary Layers with Tangential Slot Injection", NASA TN D-6221, 1971

REFERENCES (cont.)

13. Calhoon, D. F., "Investigation of GH_2-GO_2 Combustion", Aerojet Liquid Rocket Company, Contract NAS 3-14379, Second Quarterly Report, 15 January 1972

14. Sivasegaram, S., and Whitelaw, J. H., "Film Cooling Slots: The Importance of Lip Thickness and Injection Angle", J. Mech. Engr. Sci., Vol. II, No. 1, 1969, pp 22-27

15. Sellers, John P., Jr., "Gaseous Film Cooling with Multiple Injection Stations", AIAA Journal, Vol. 1, No. 9, 2154-2156, September 1973

16. Advanced O_2/H_2 Thrust Chamber Design and Analysis Program, Design Review Document, Rocketdyne, North American Rockwell, 20 December 1972

17. Fortini, A., "Performance Investigation of a Nonpumping Rocket-Ejector System for Altitude Simulation", NASA TN D-257, December 1959

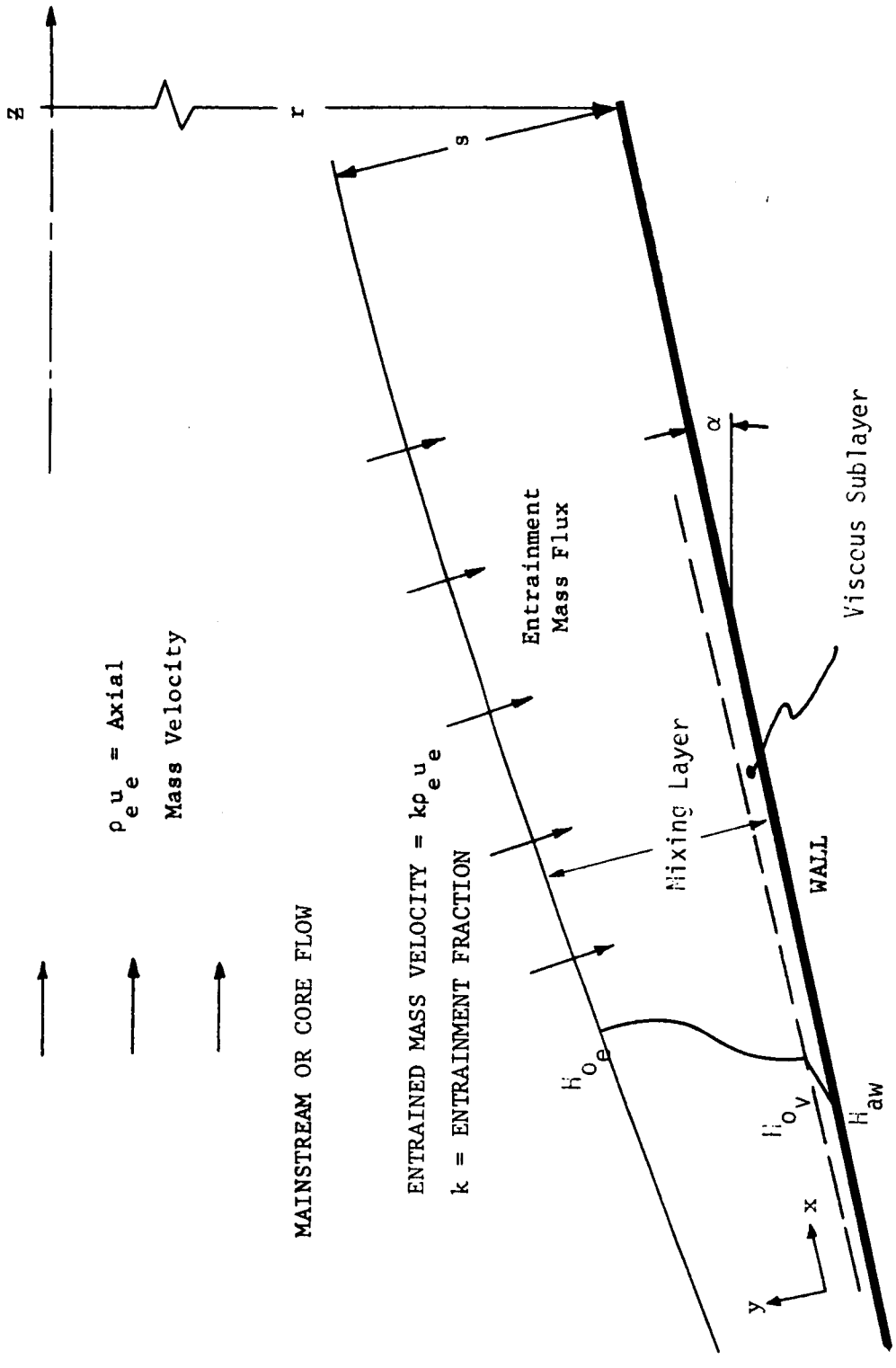

Figure 1. Entrainment Model Schematic

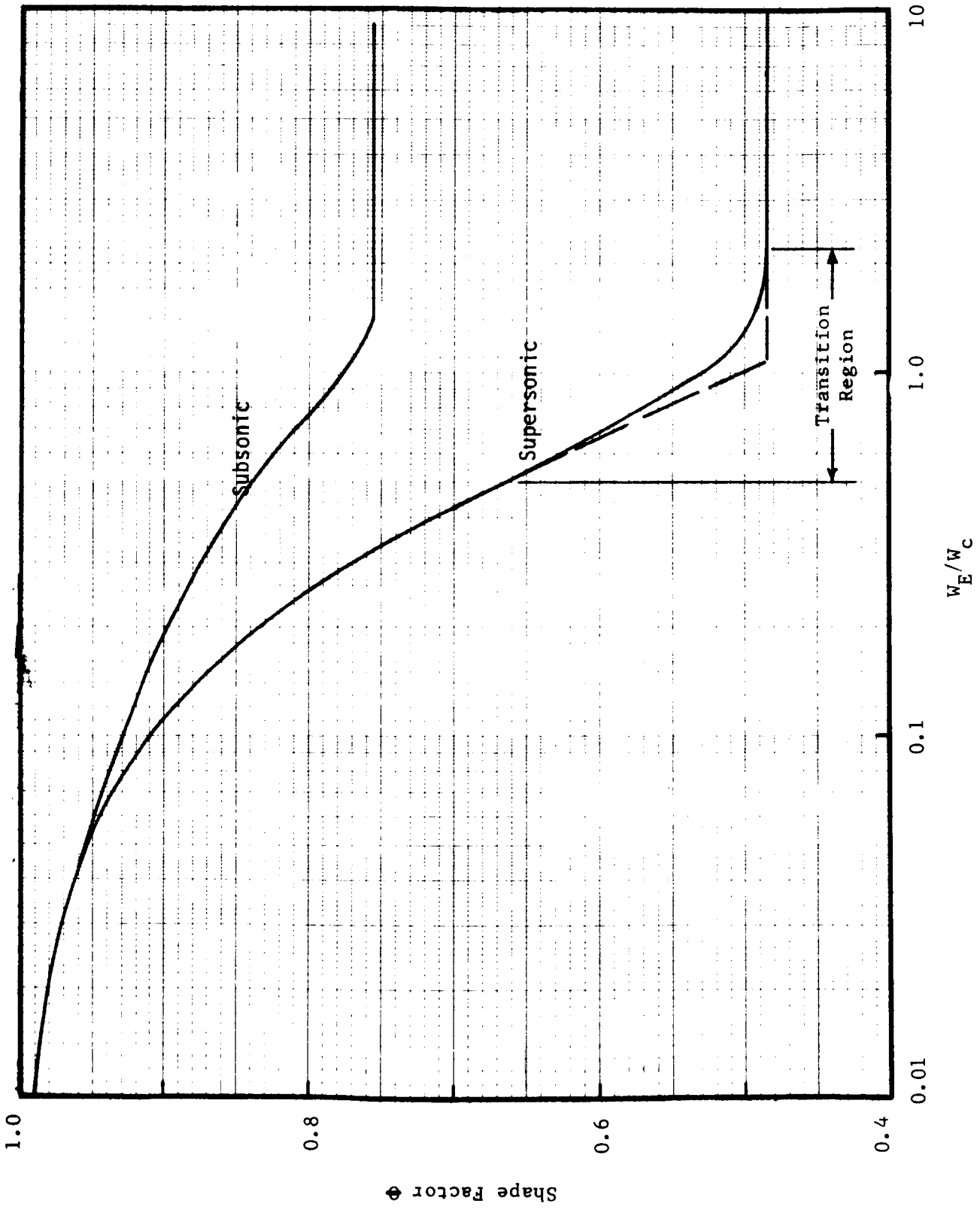

Figure 2. Mixing Layer Profile Shape Factor Correlations

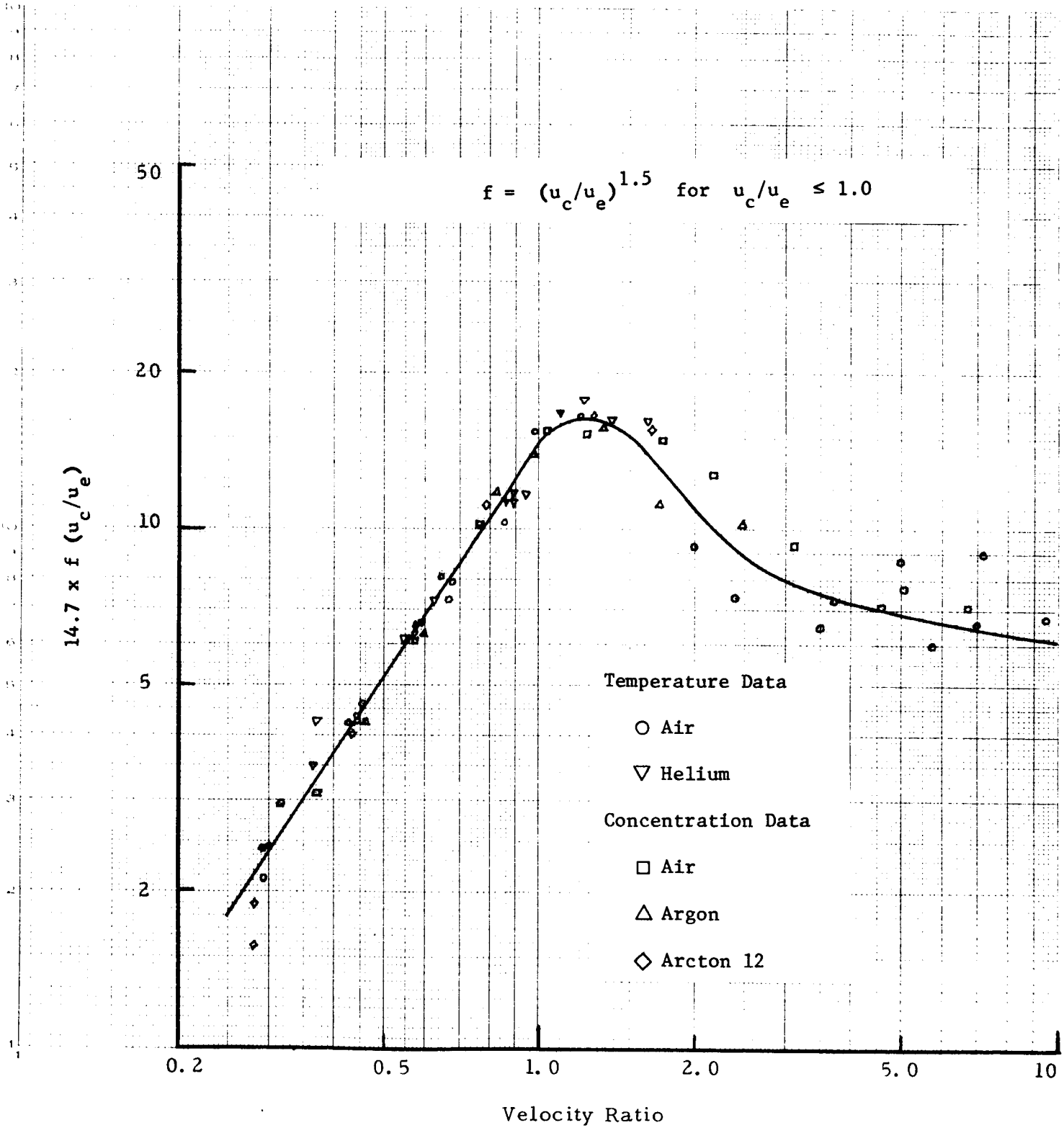

Figure 3. Velocity Ratio Correlating Function

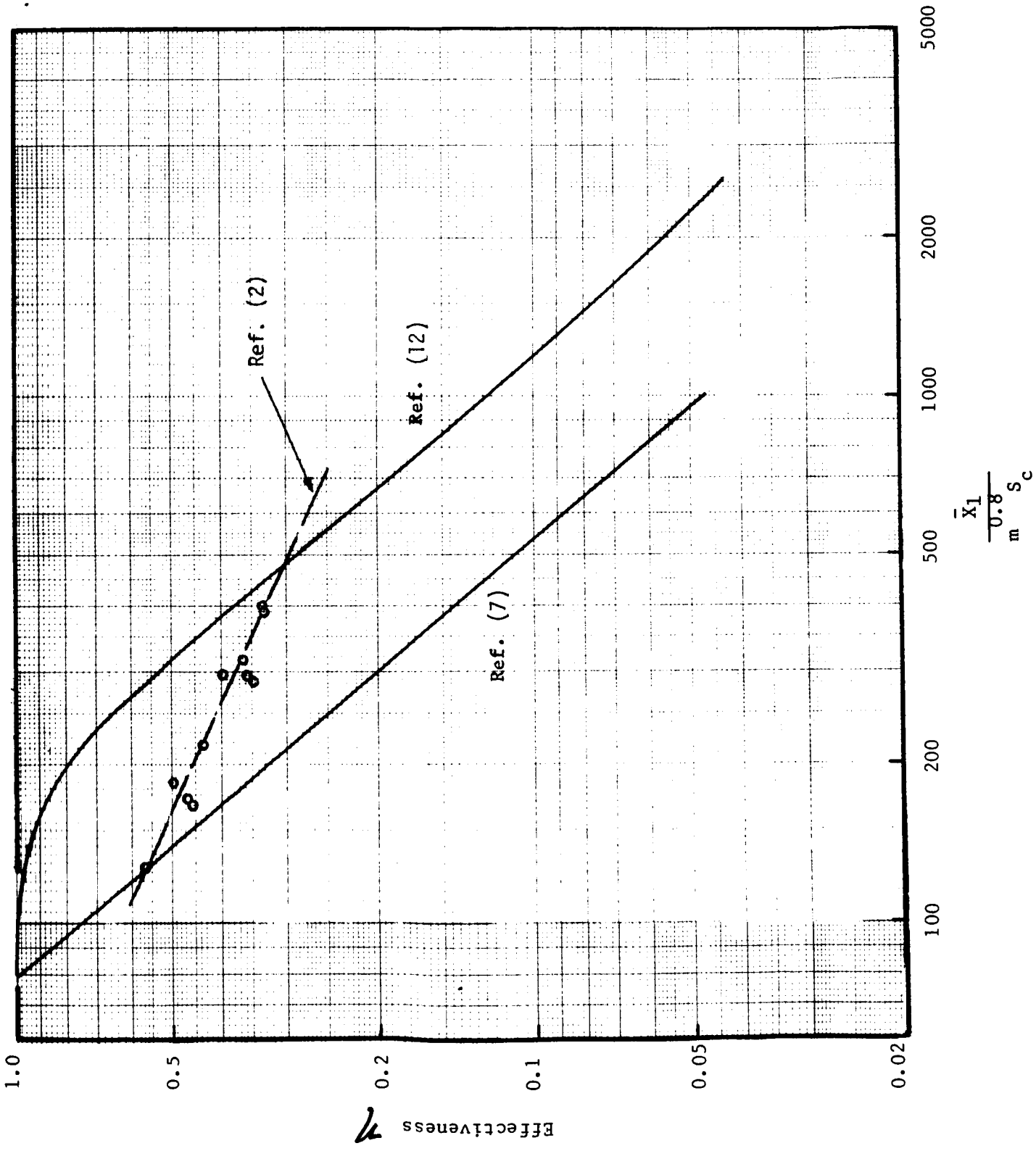

Figure 4. Comparison of Existing Supersonic Effectiveness Results

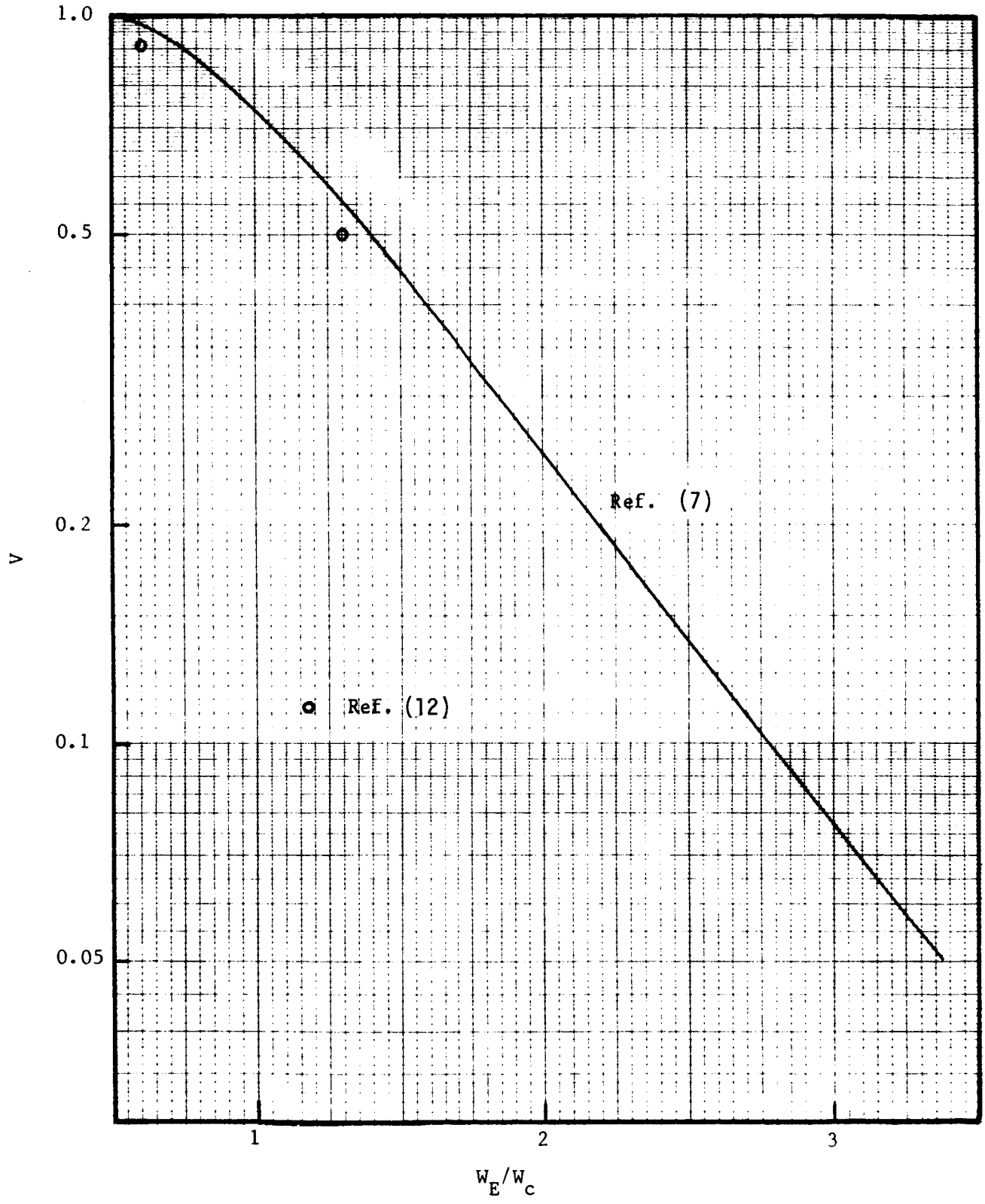

Figure 5. Velocity Mixing Function Correlation

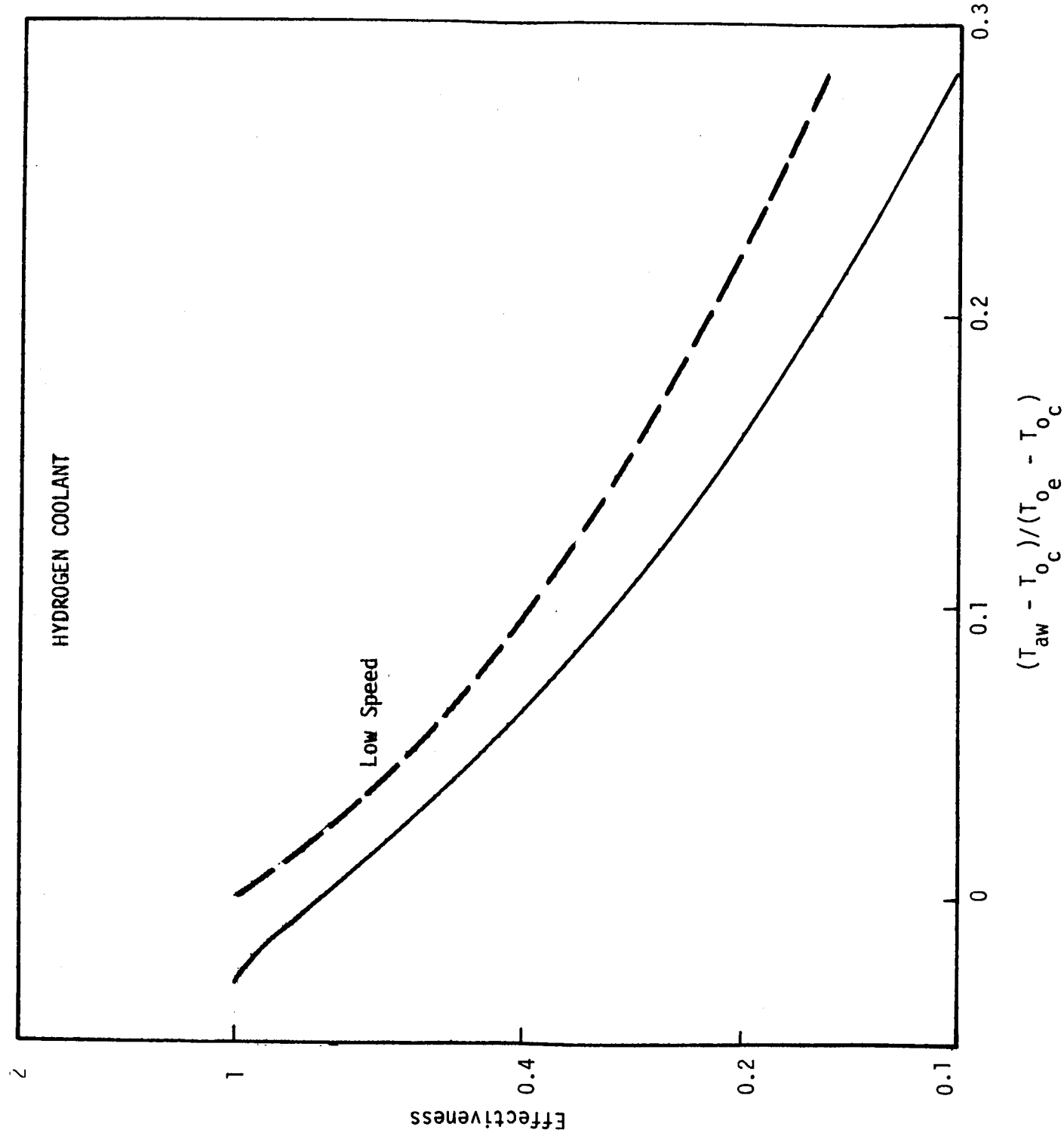

Figure 6. High-Speed Flow Effects in Test 103B

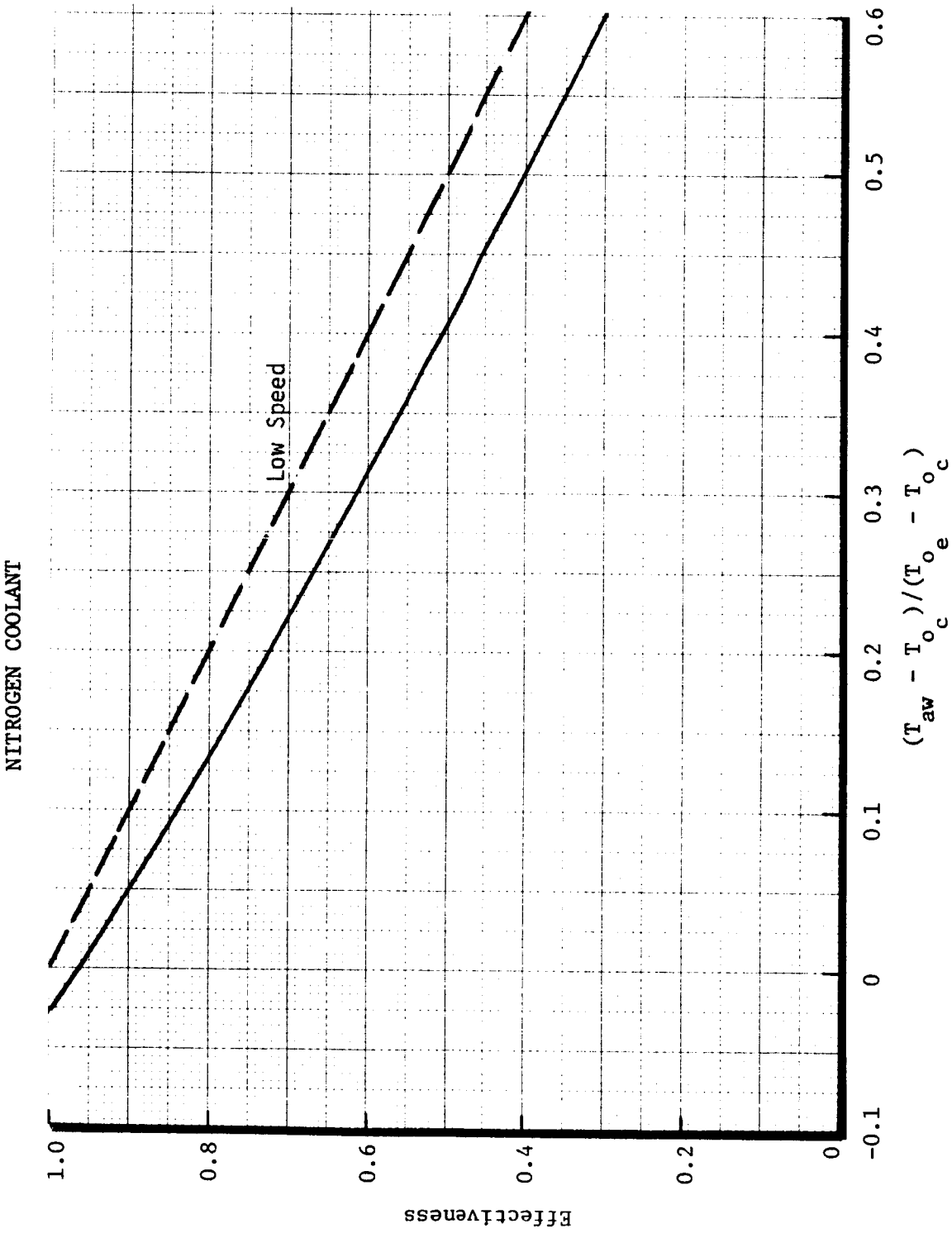

Figure 7. High-Speed Flow Effects in Test 104B

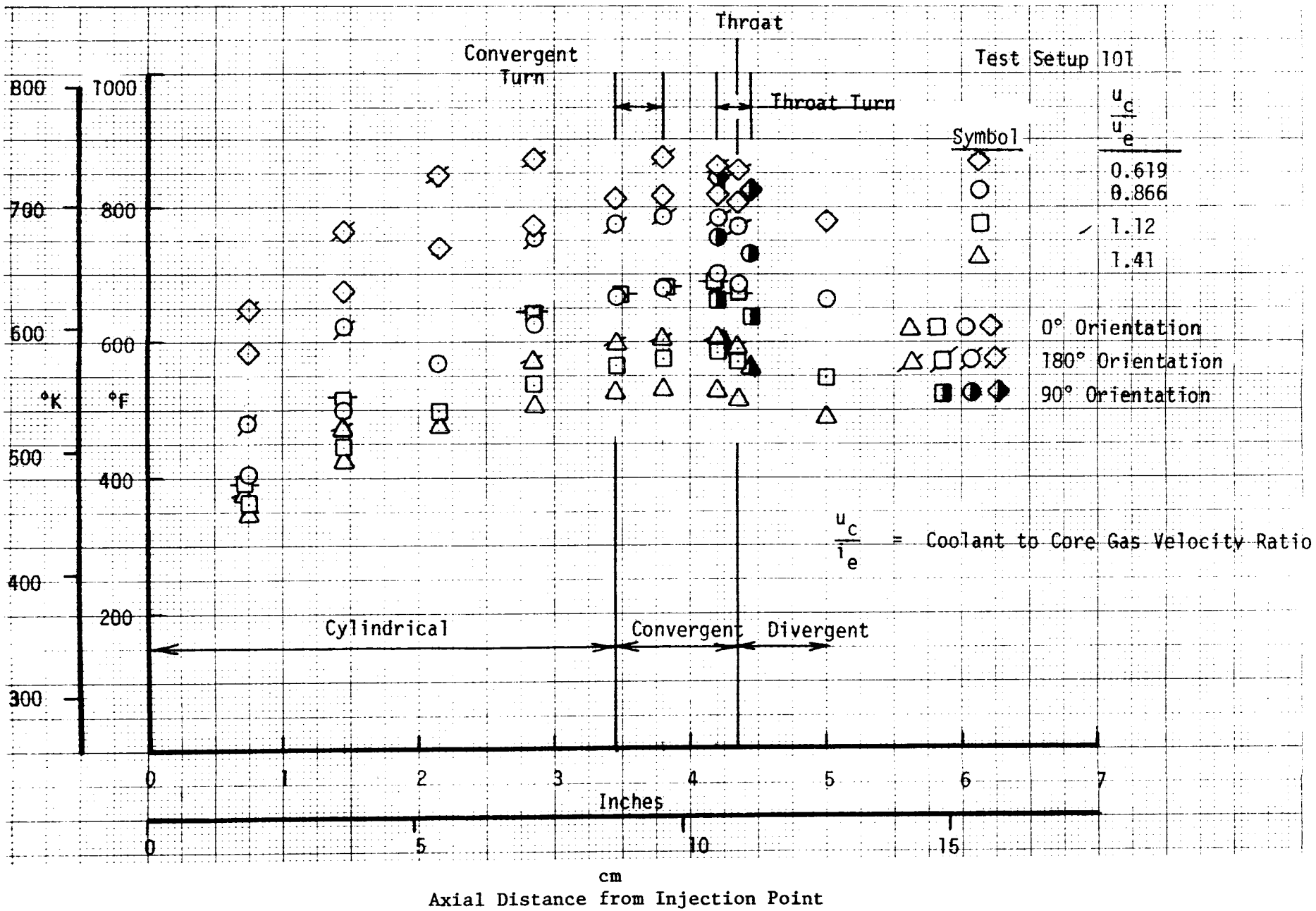

Figure 8. Test Setup 101 Adiabatic Wall Temperatures

T_{aw}, Adiabatic Wall Temperature

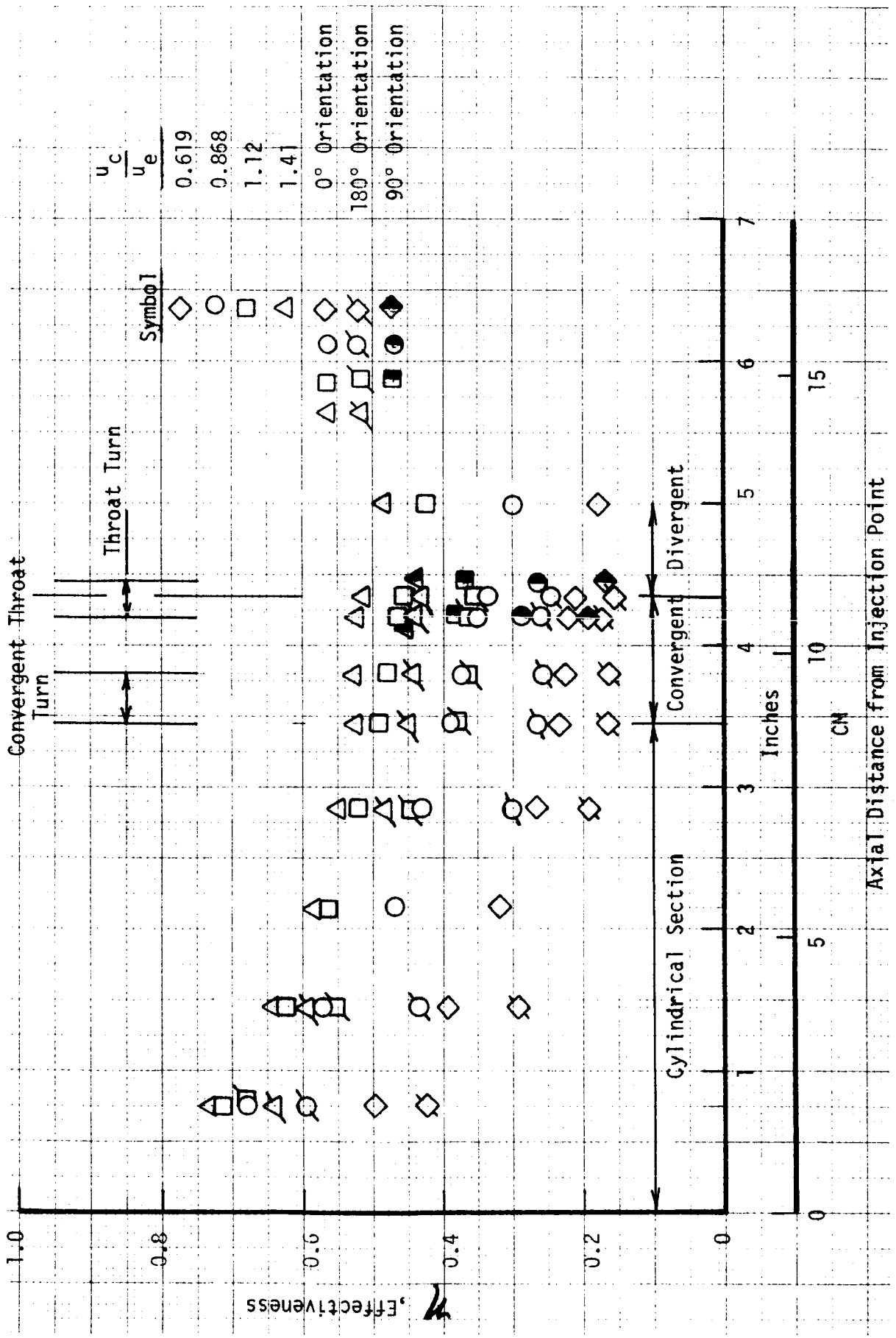

Figure 9. Test Setup 101 Effectiveness Values

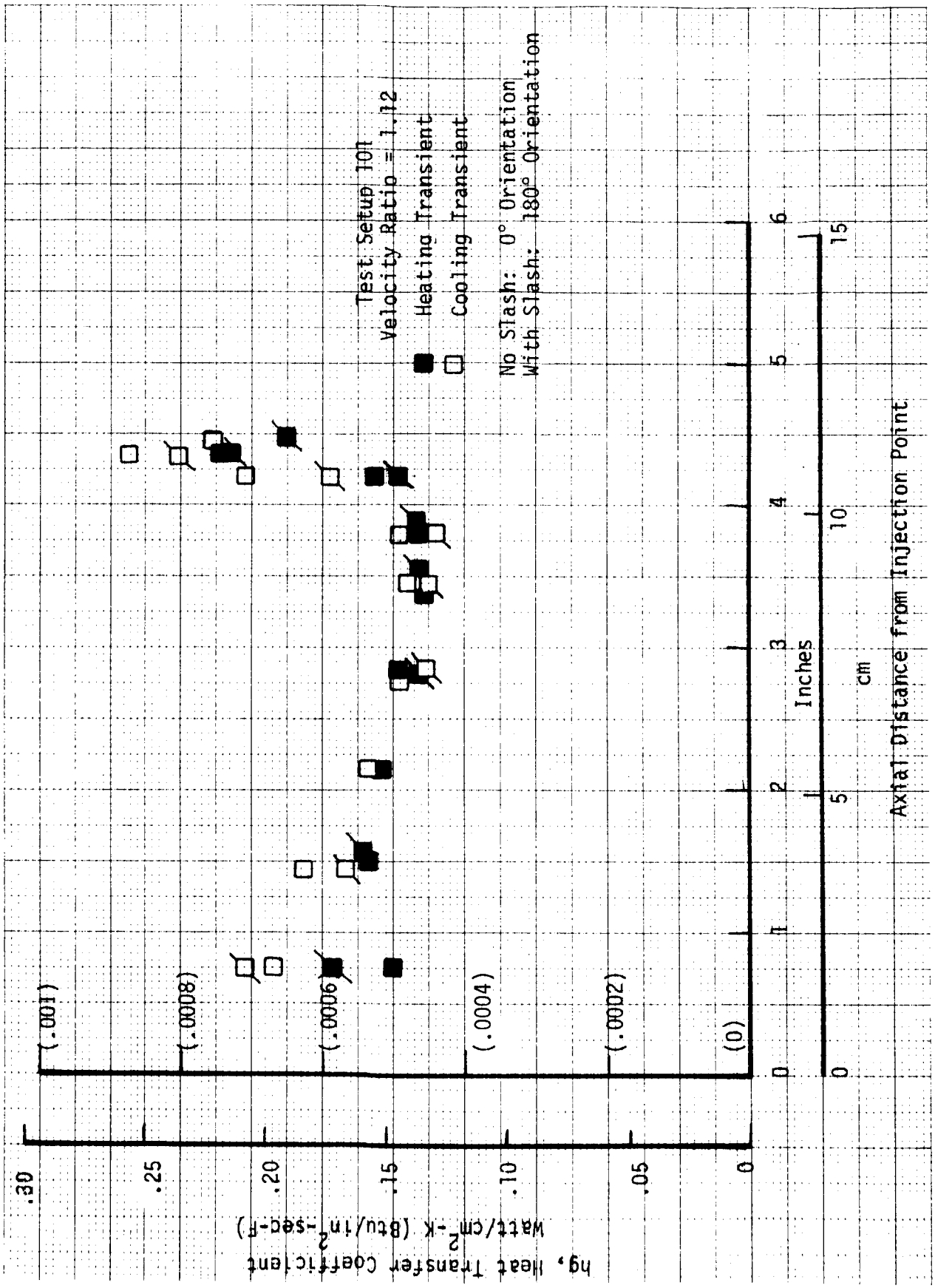

Figure 10. Test Setup 101 Heat Transfer Coefficients

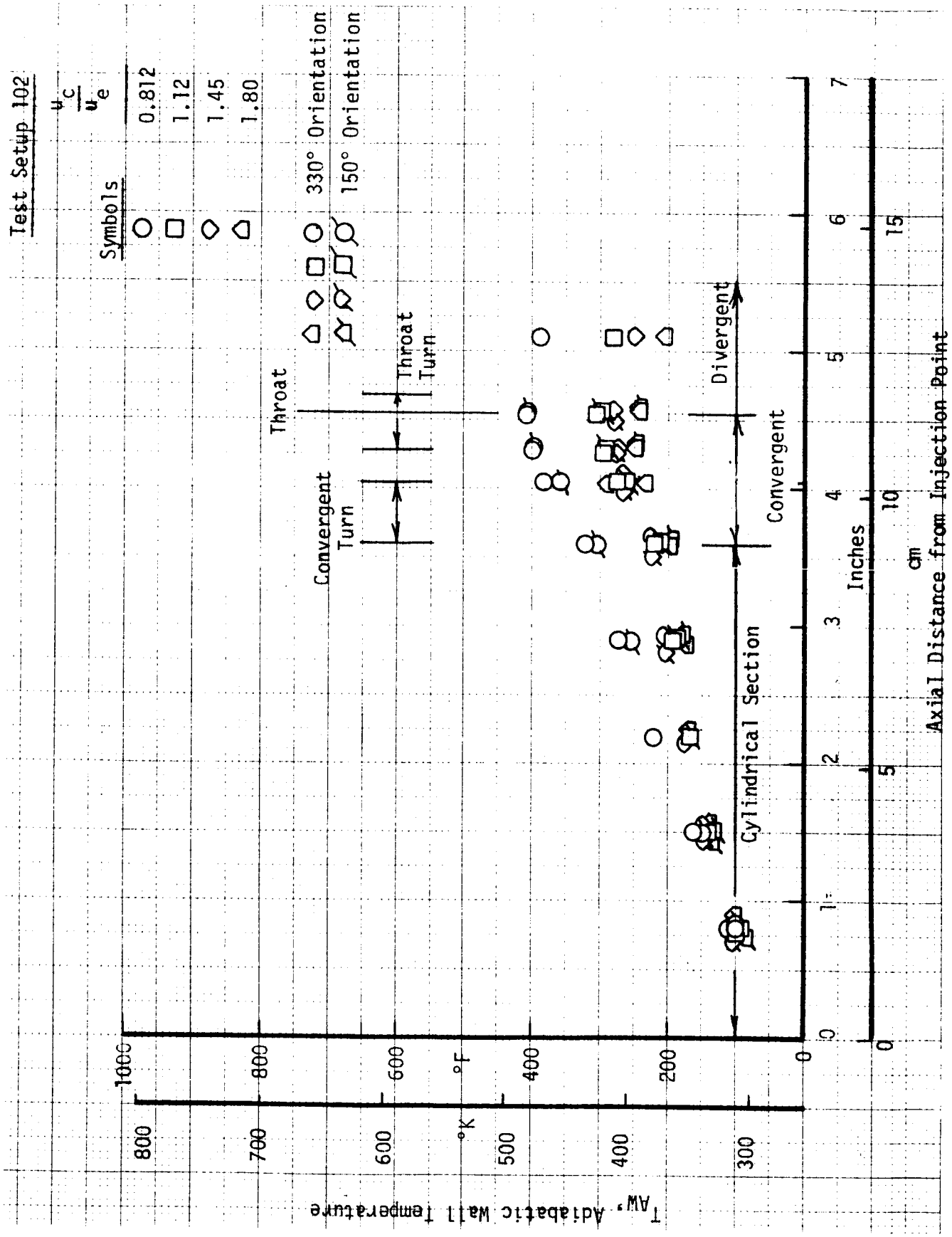

Figure 11. Test Setup 102 Adiabatic Wall Temperatures

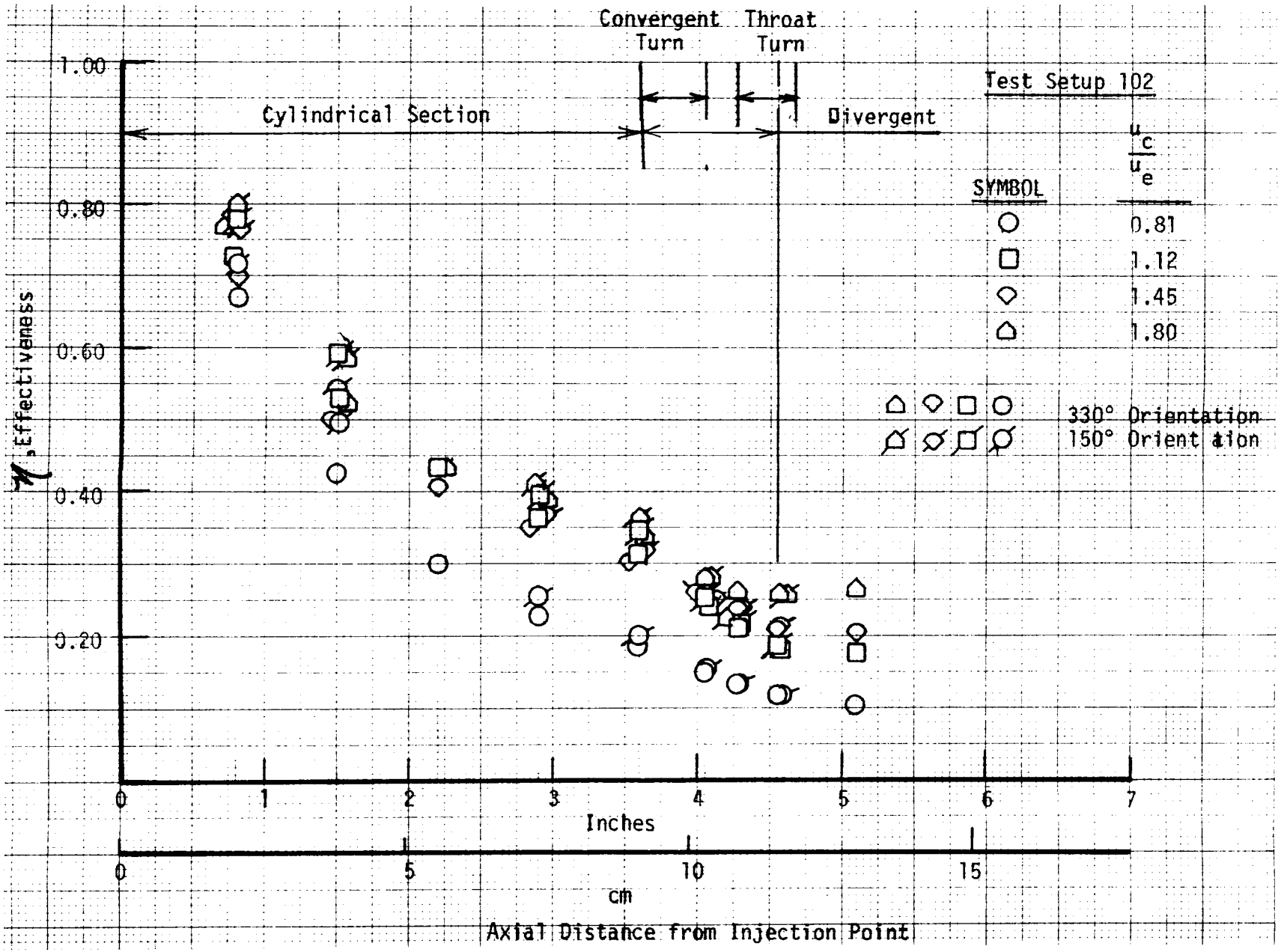

Figure 12. Test Setup 102 Effectiveness Values

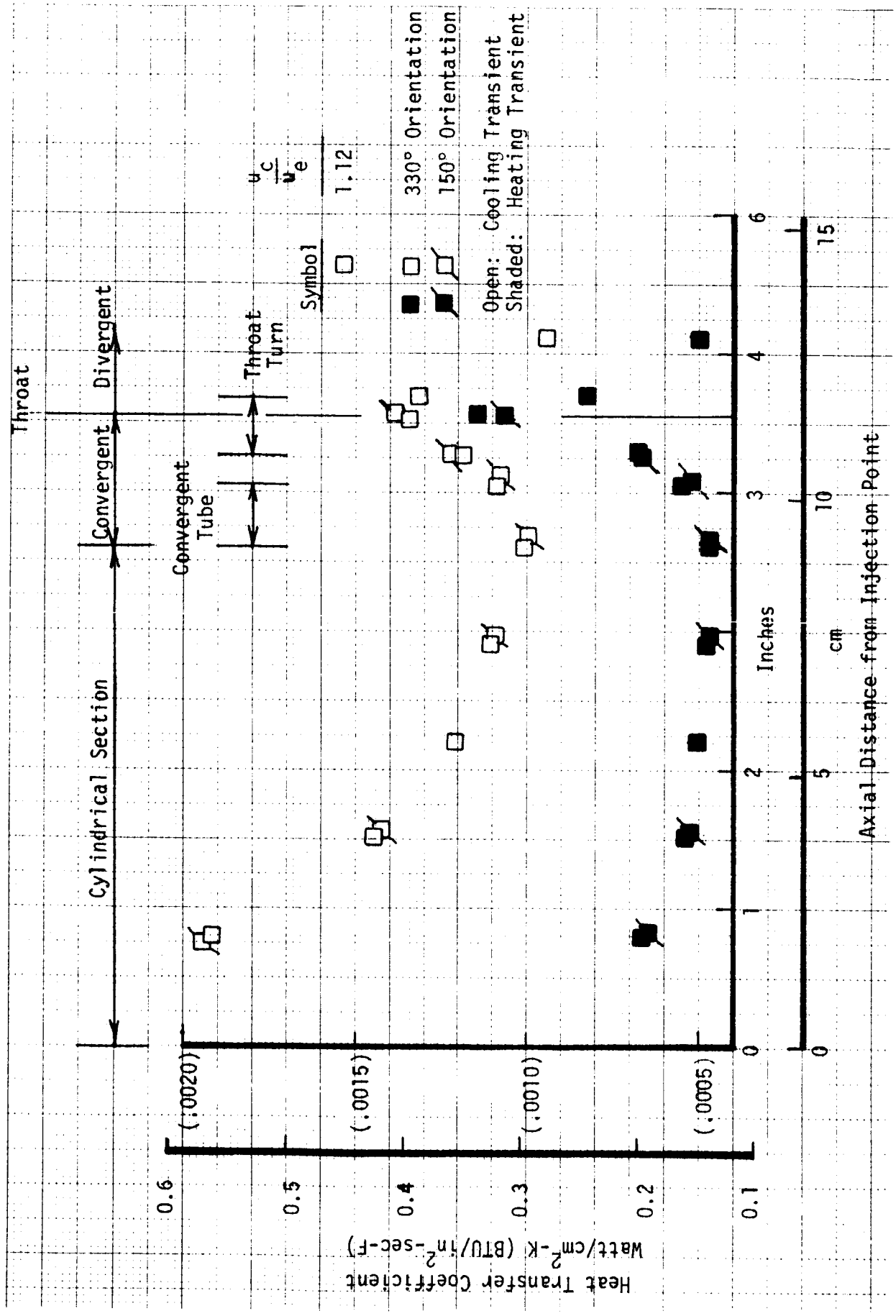

Figure 13. Test Setup 102 Heat Transfer Coefficients

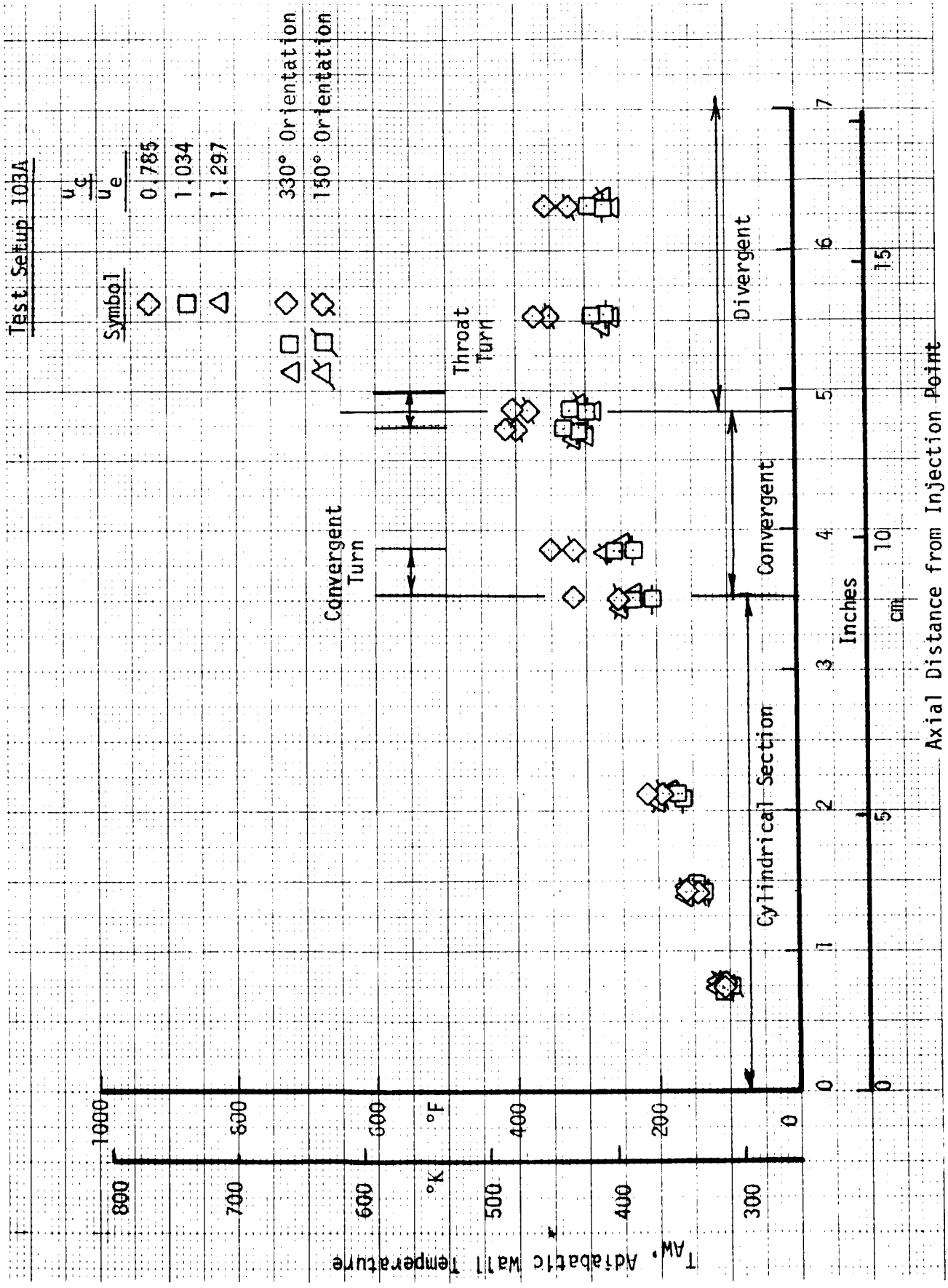

Figure 14. Test Setup 103A Adiabatic Wall Temperatures

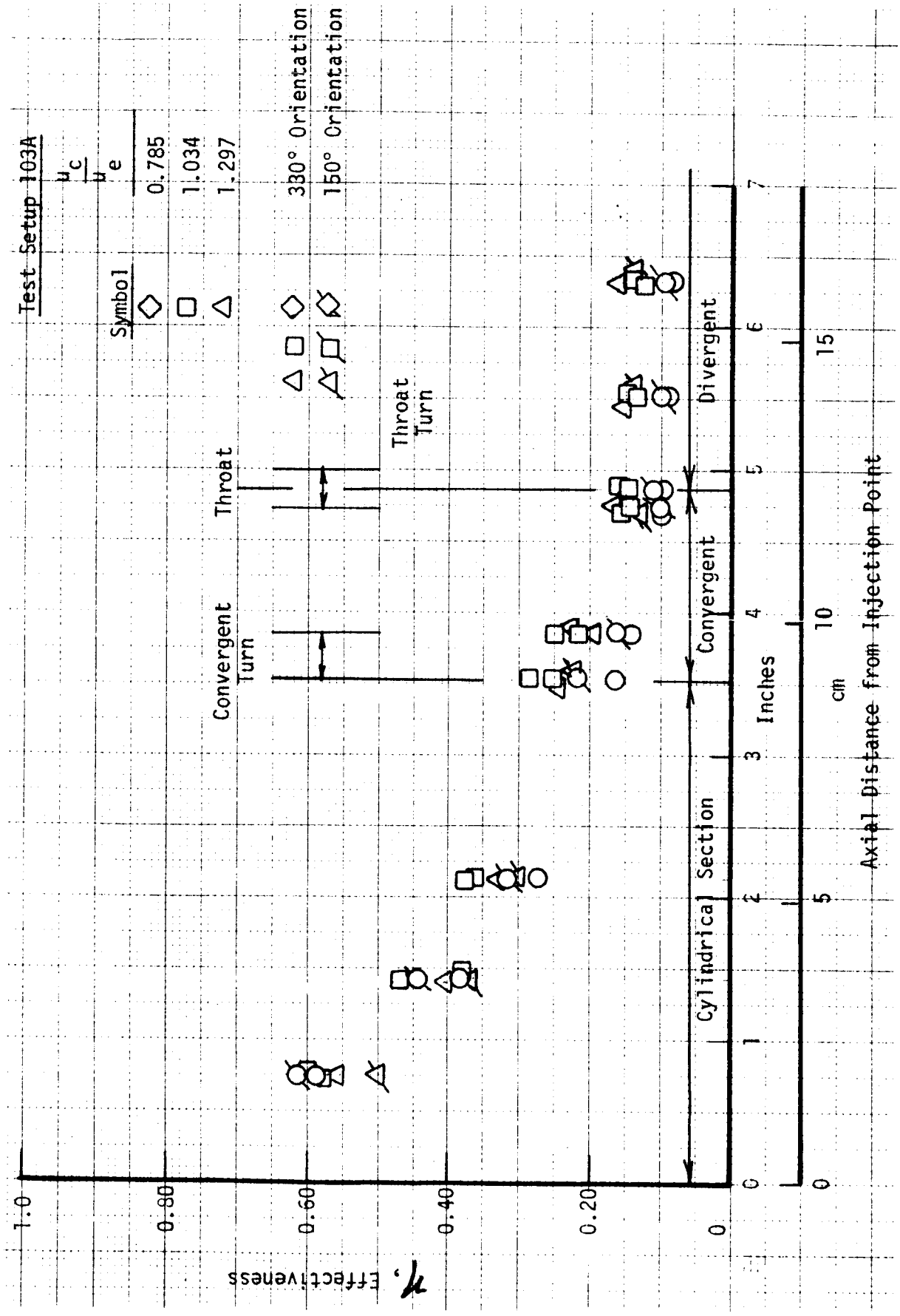

Figure 15. Test Setup 103A Effectiveness Values

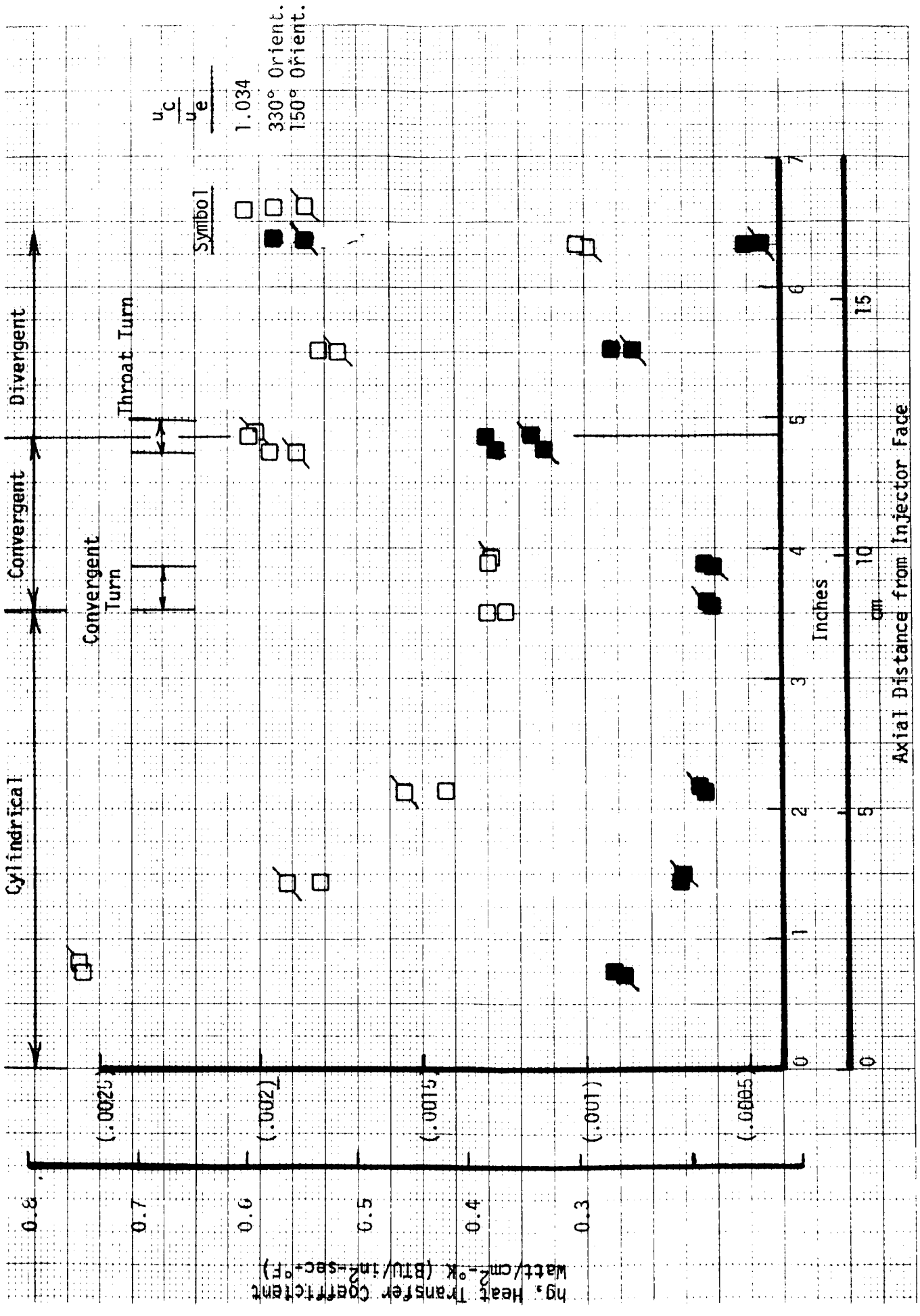

Figure 16. Test Setup 103A Heat Transfer Coefficients

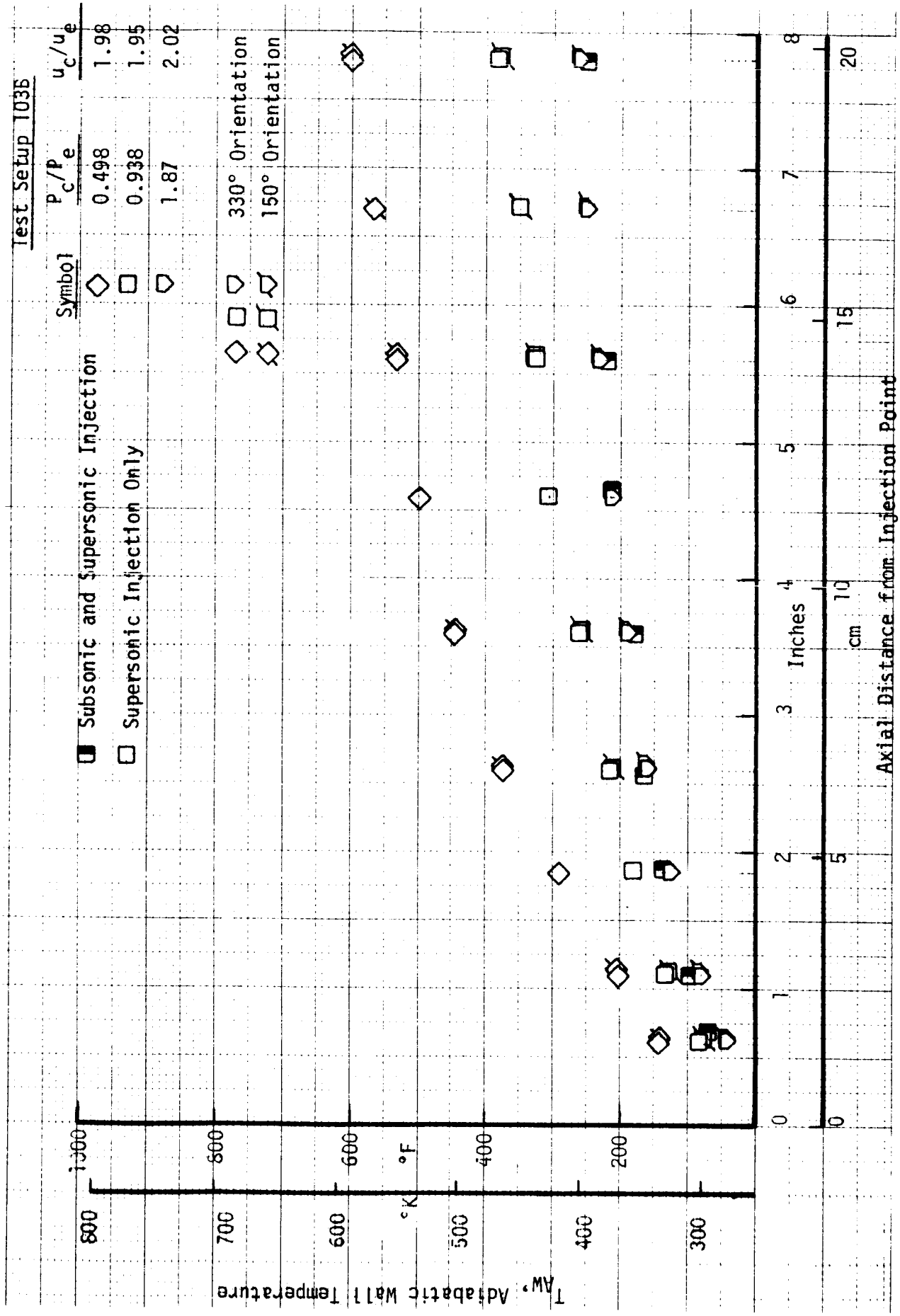

Figure 17. Test Setup 103B Adiabatic Wall Temperatures

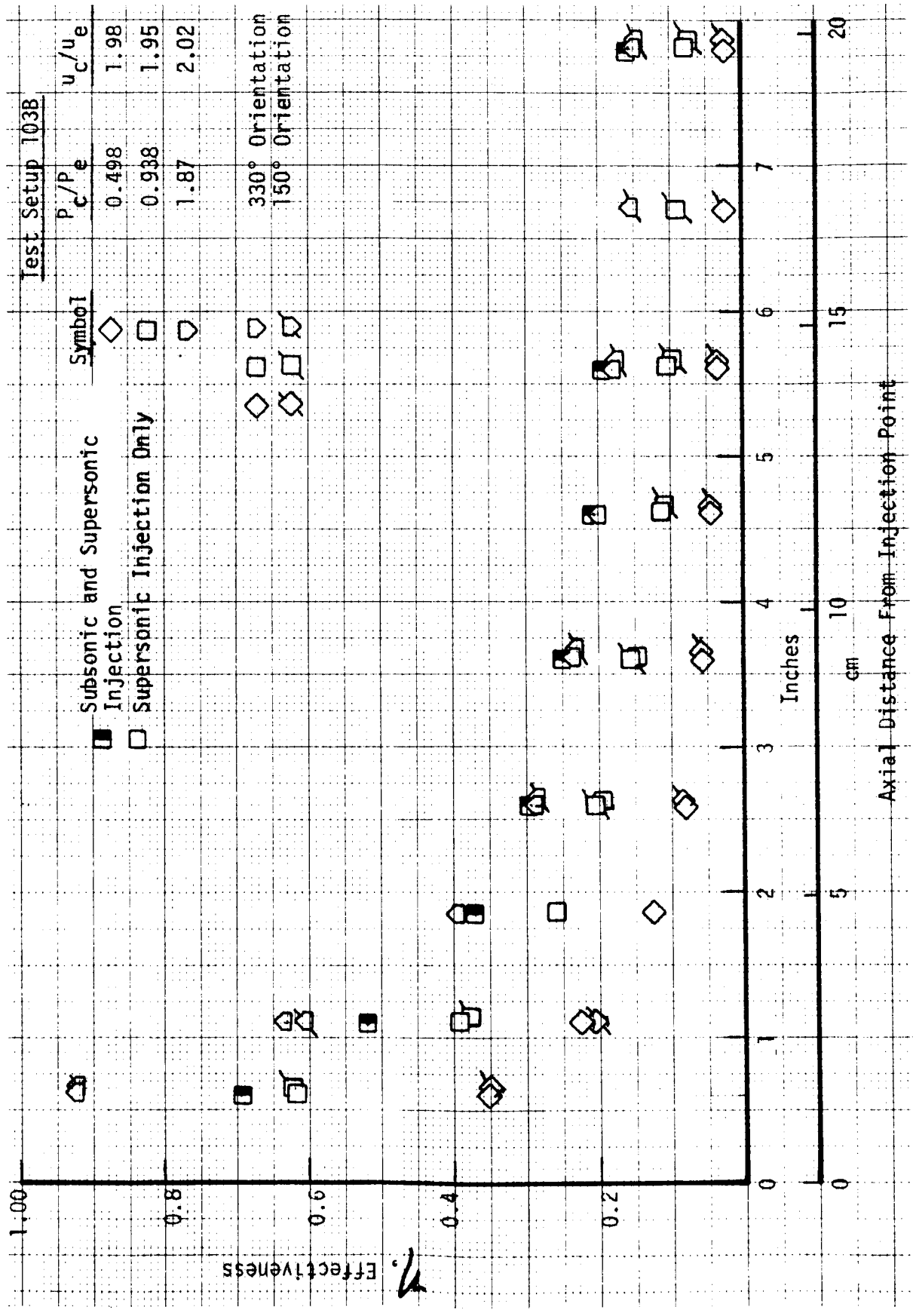

Figure 18. Test Setup 103B Effectiveness Values

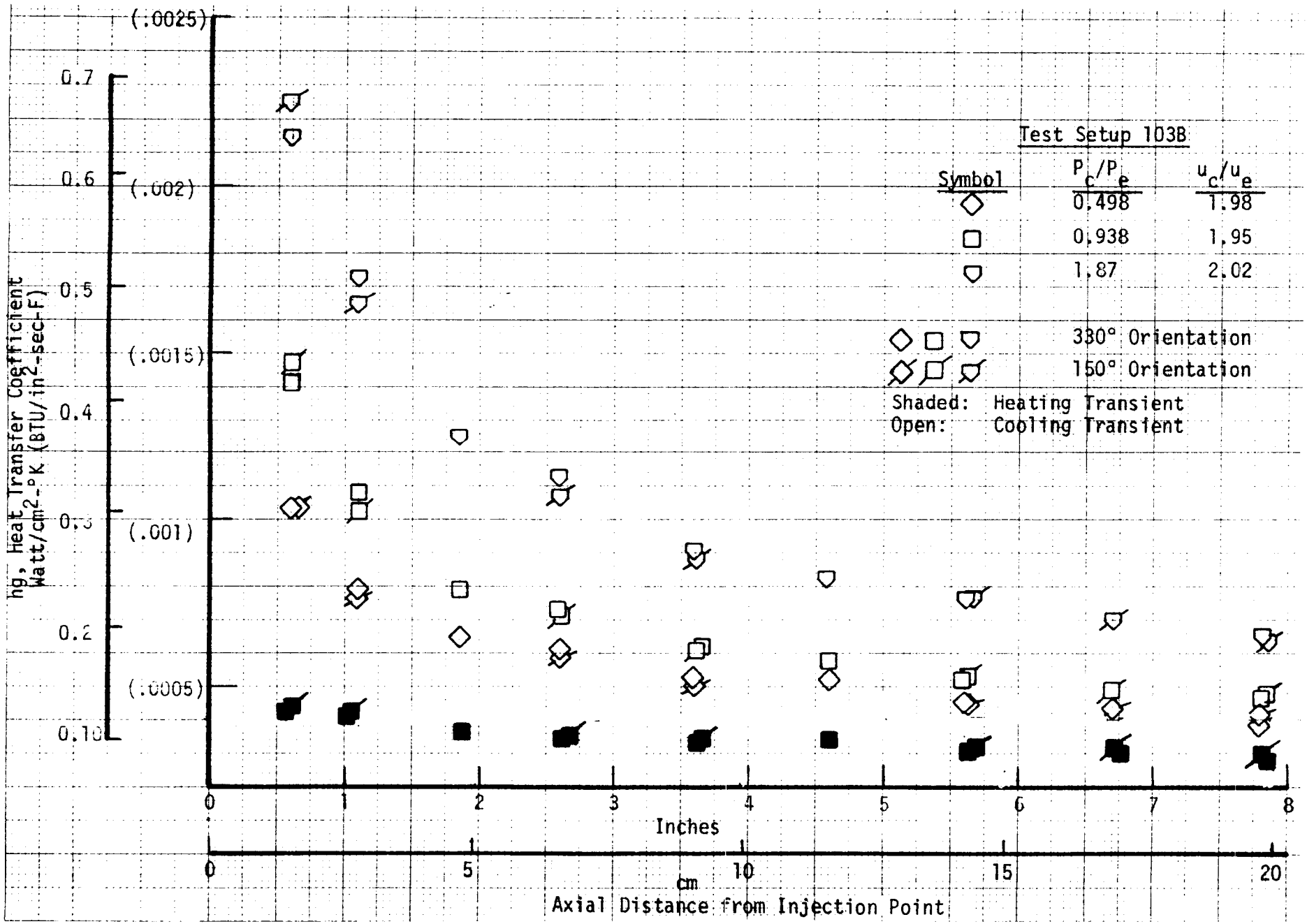

Figure 19. Test Setup 103B Heat Transfer Coefficients

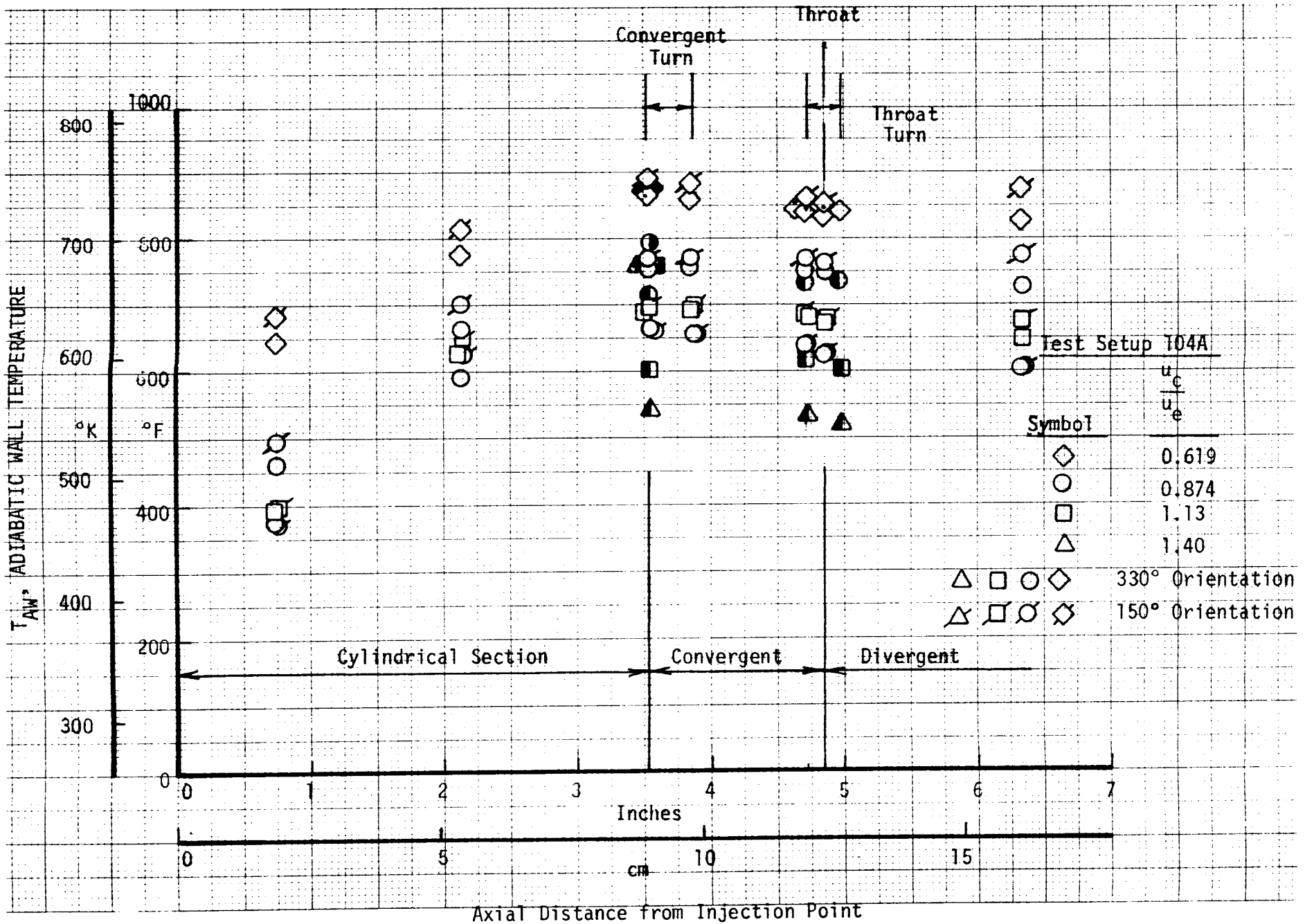

Figure 20. Test Setup 104A Adiabatic Wall Temperatures

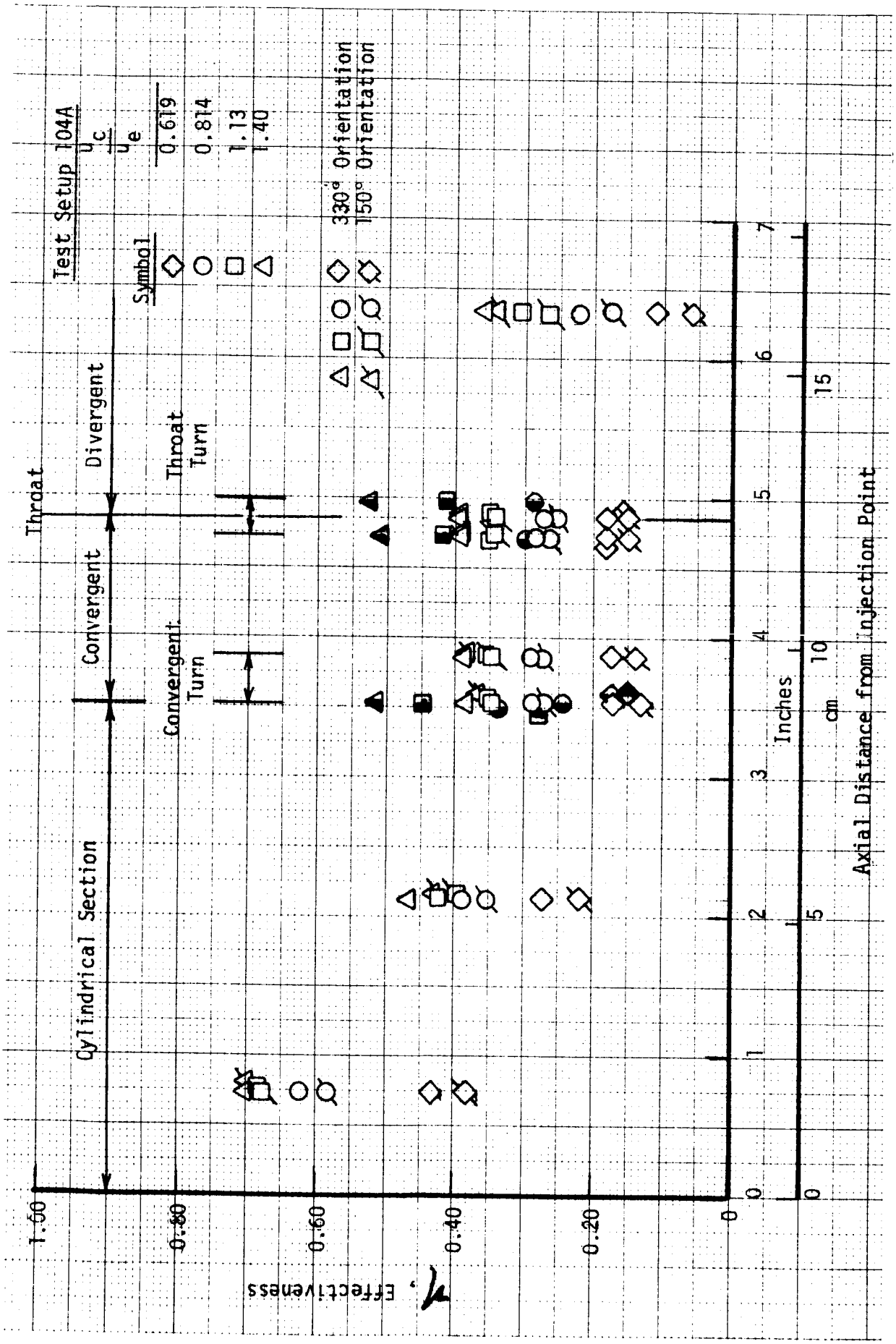

Figure 21. Test Setup 104A Effectiveness Values

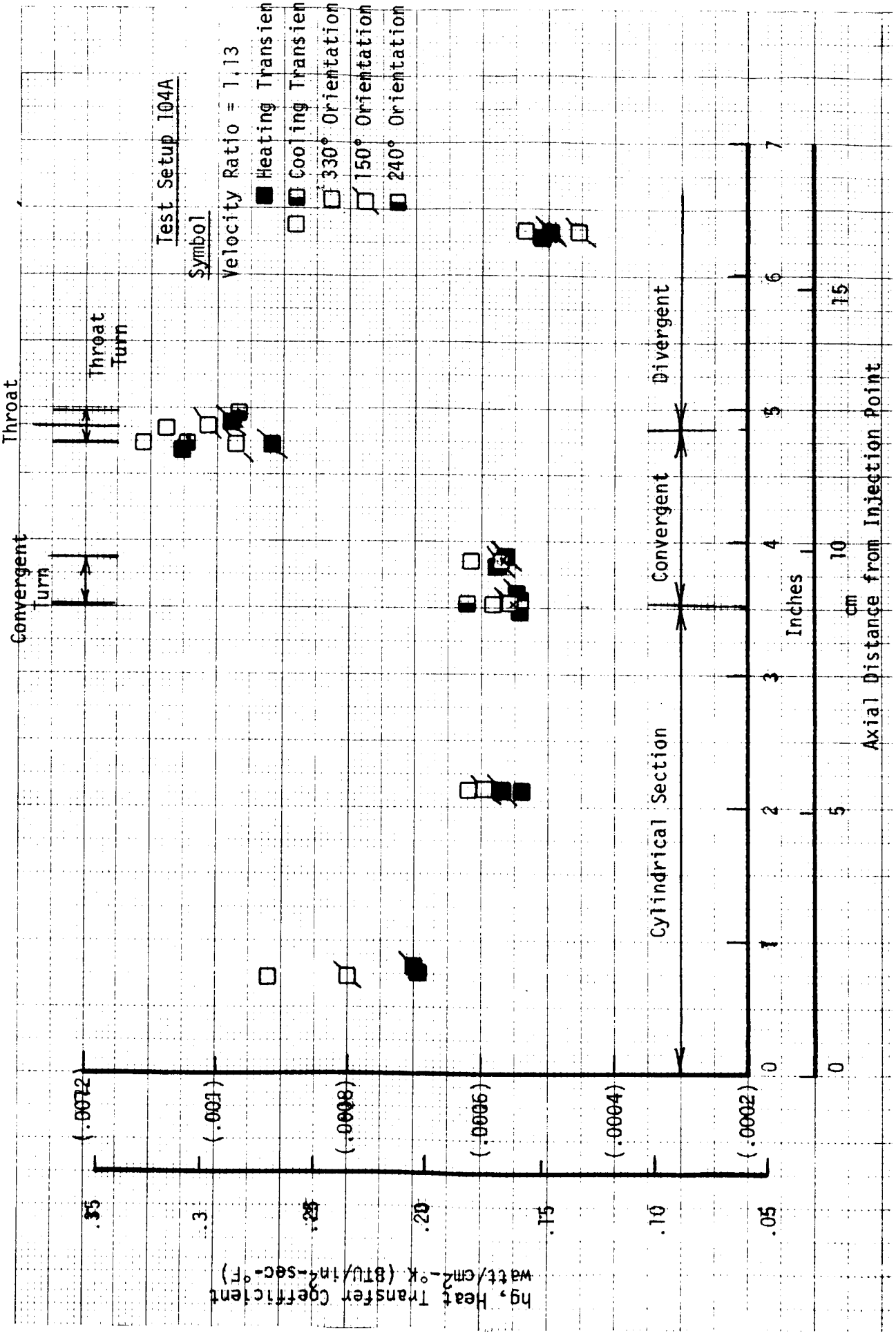

Figure 22. Test Setup 104A Heat Transfer Coefficients

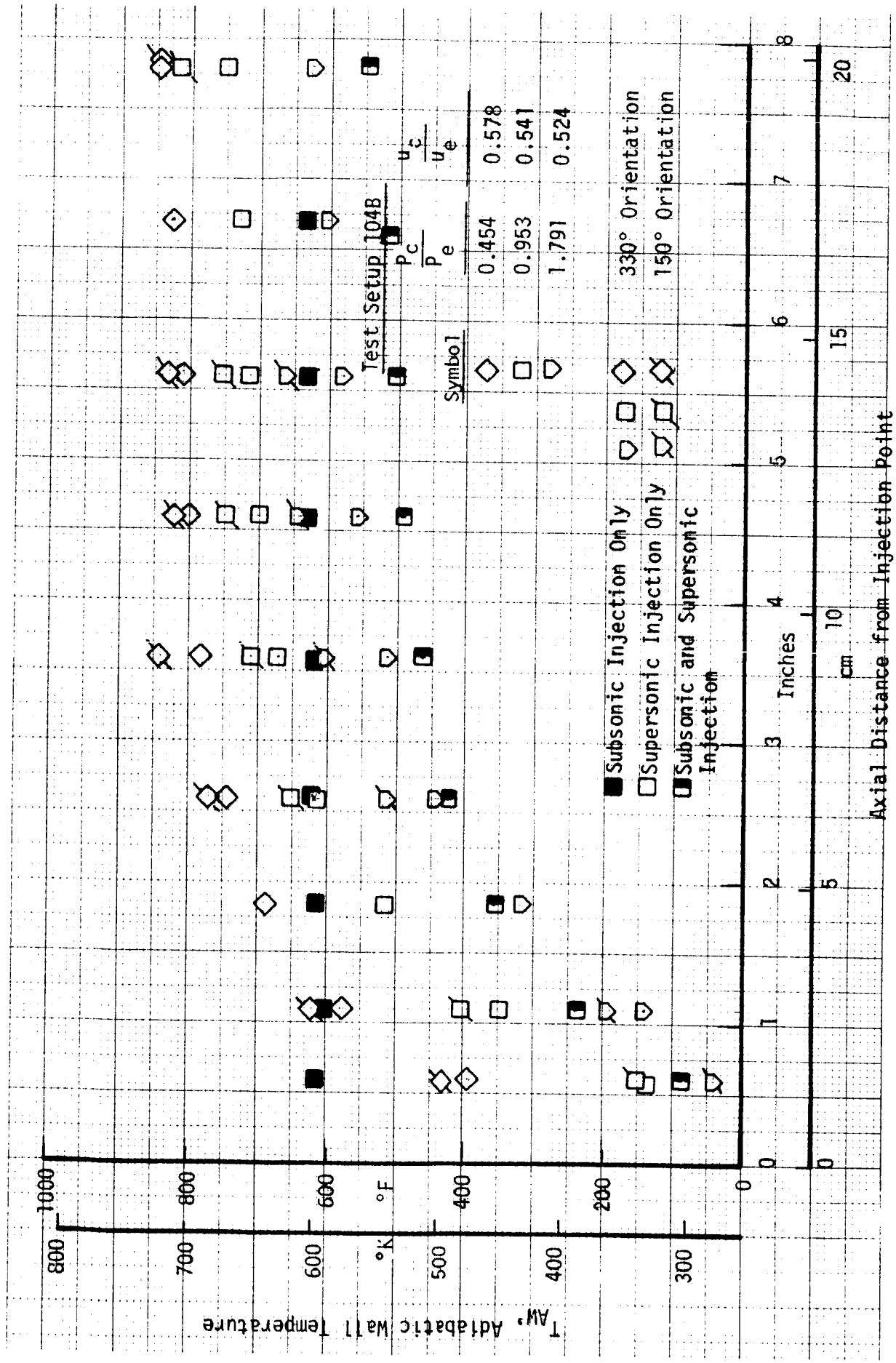

Figure 23. Test Setup 104B Adiabatic Wall Temperature

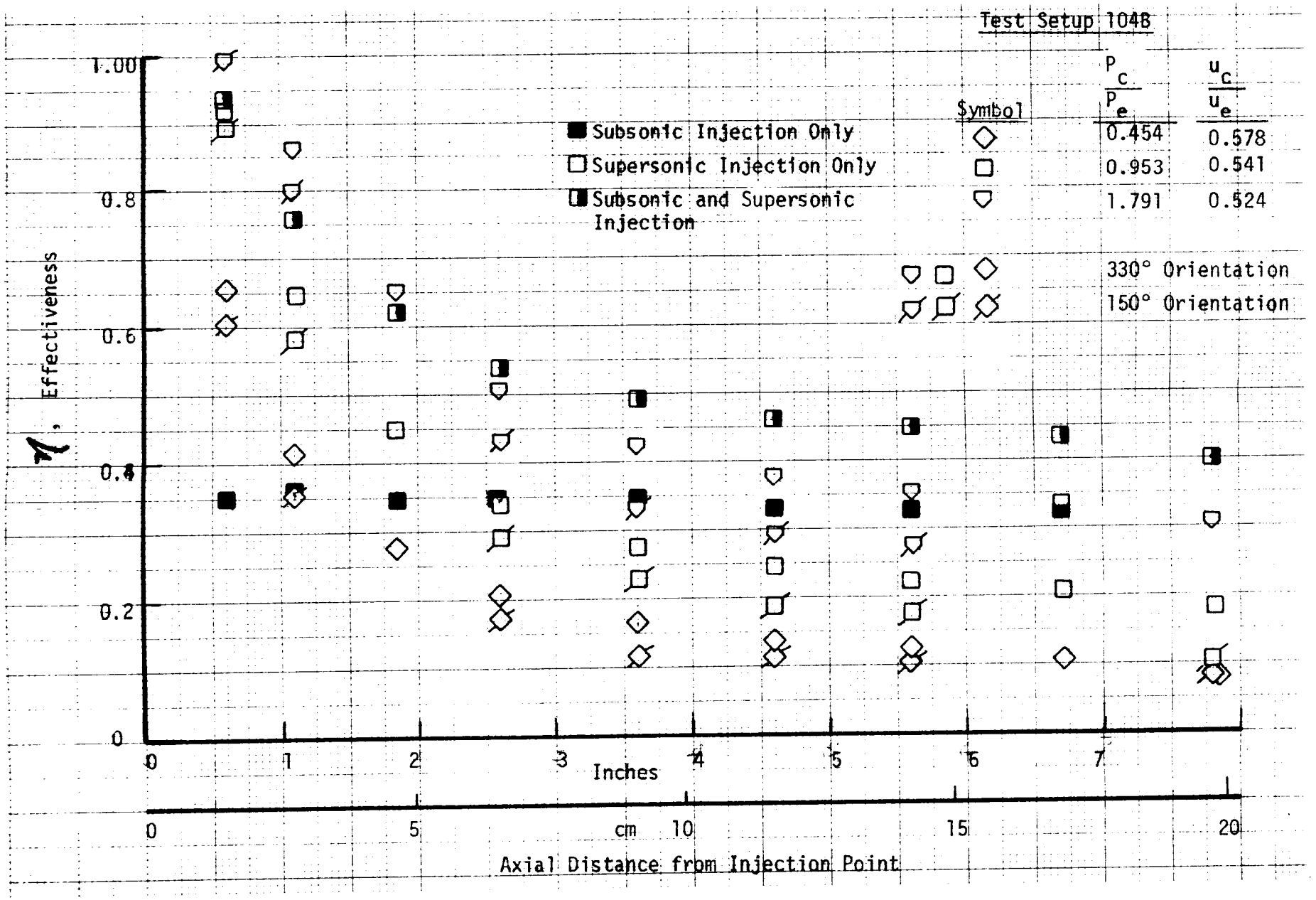

Figure 24. Test Setup 104B Effectiveness Values

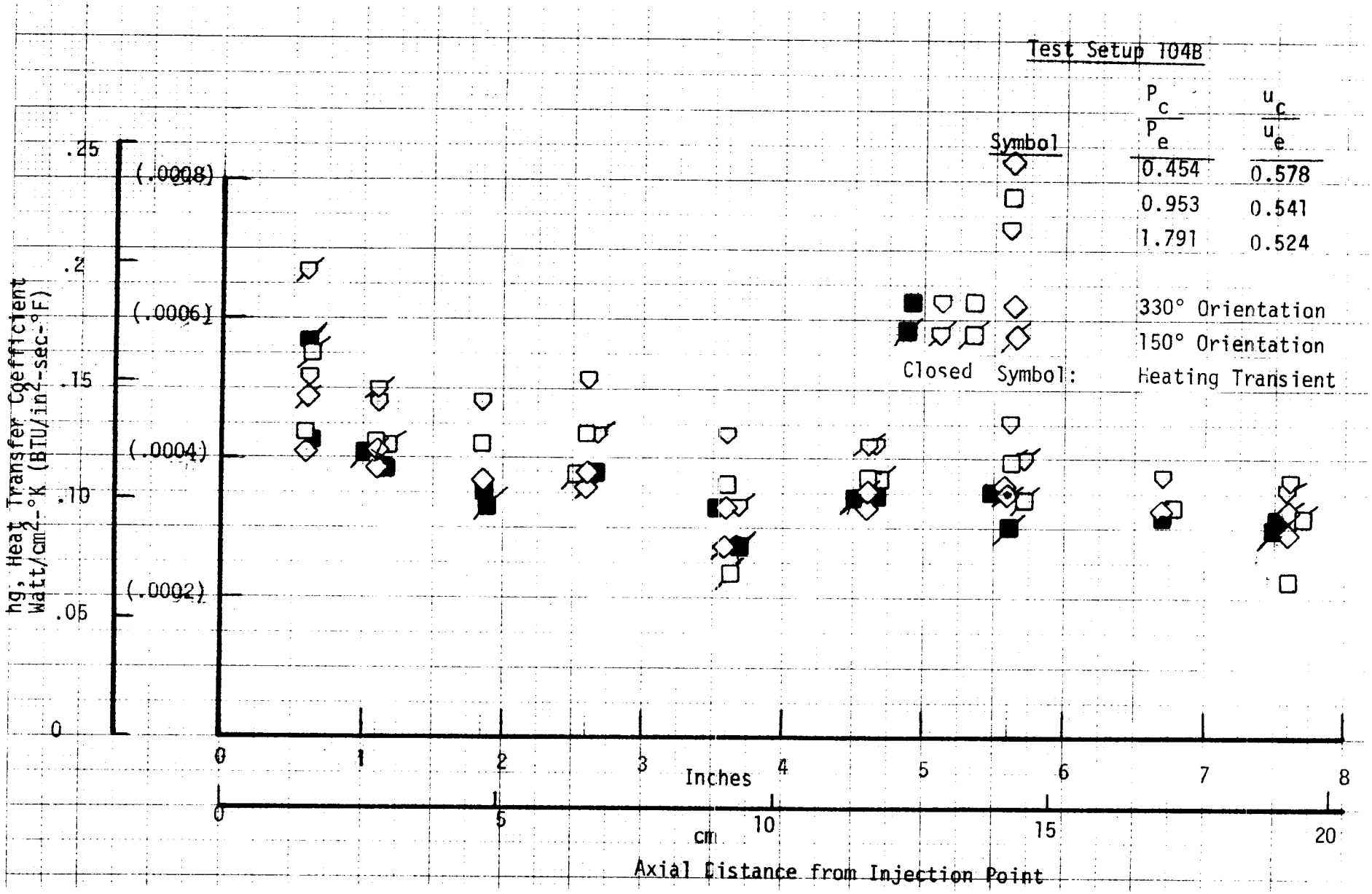

Figure 25. Test Setup 104B Heat Transfer Coefficients

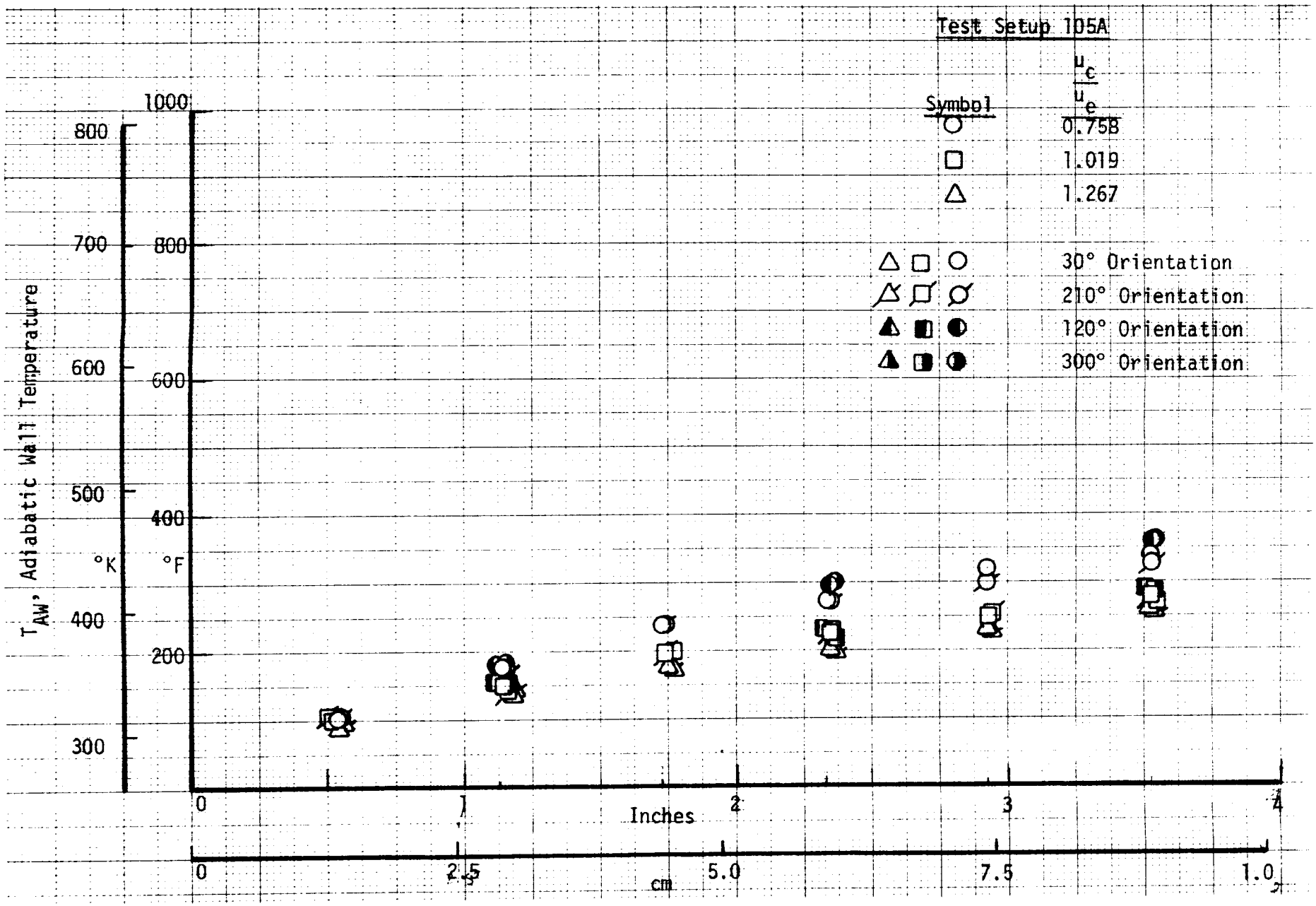

Figure 26. Test Setup 105A Adiabatic Wall Temperatures

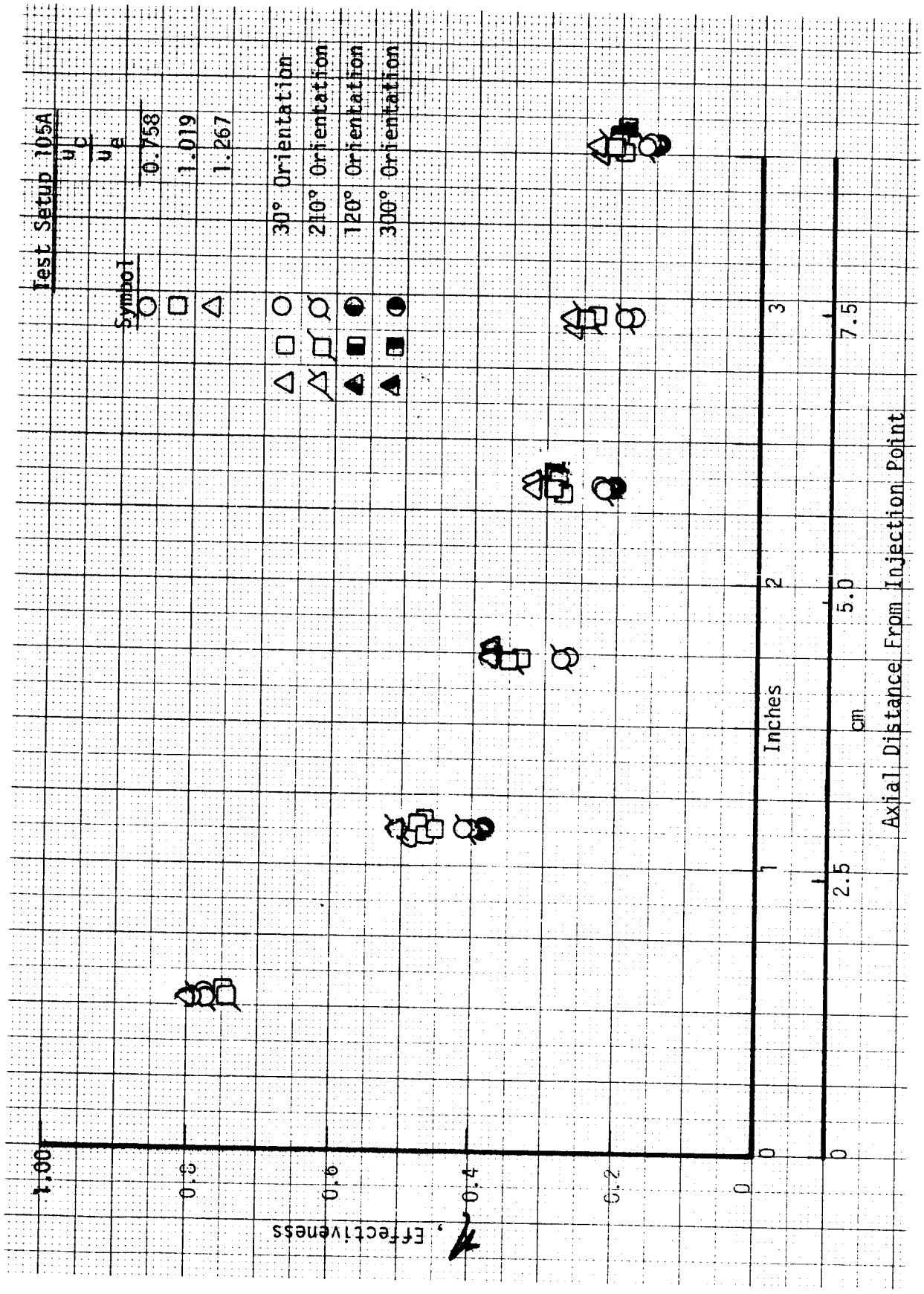

Figure 27. Test Setup 105A Effectiveness Values

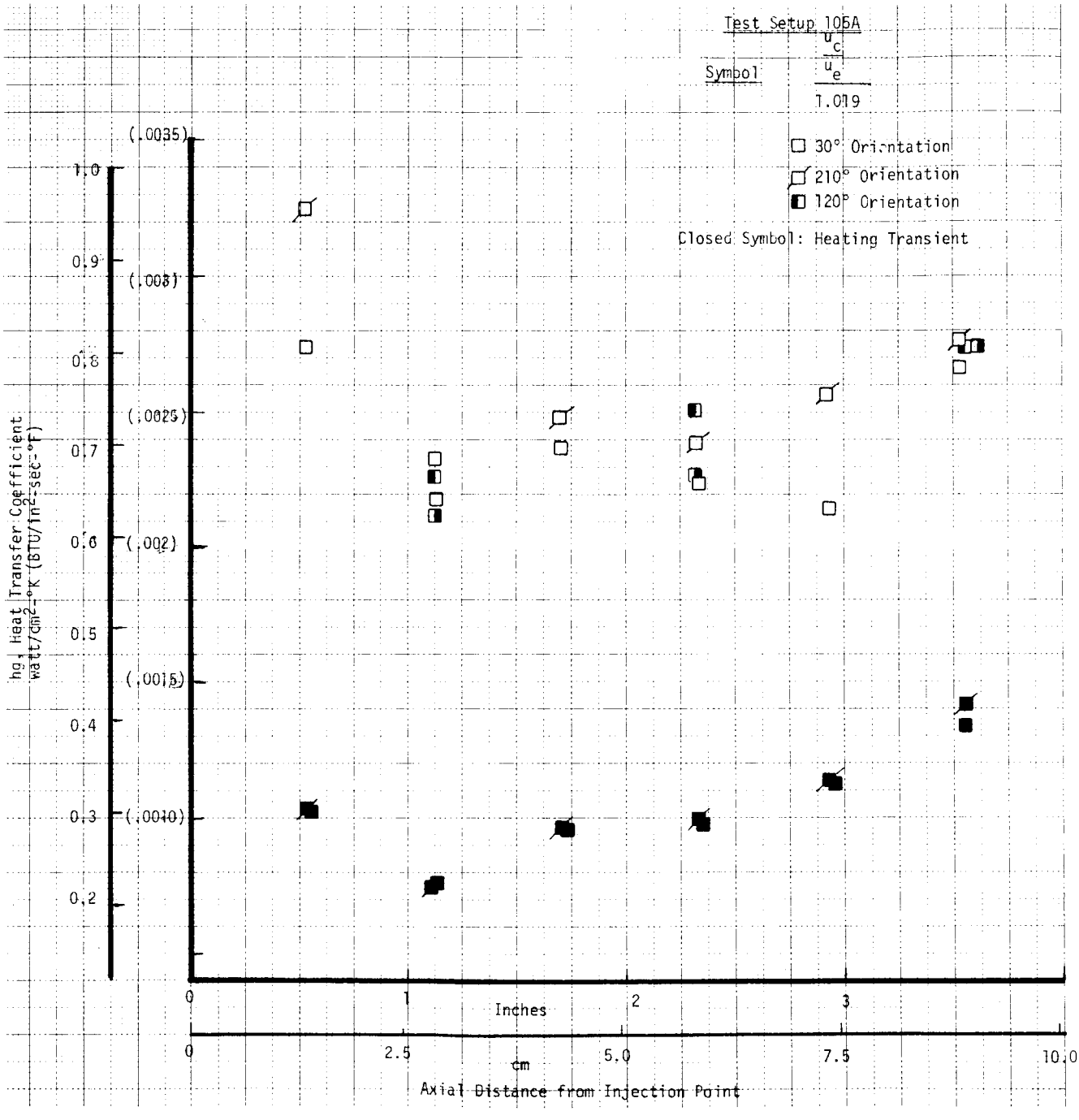

Figure 28. Test Setup 105A Heat Transfer Coefficient

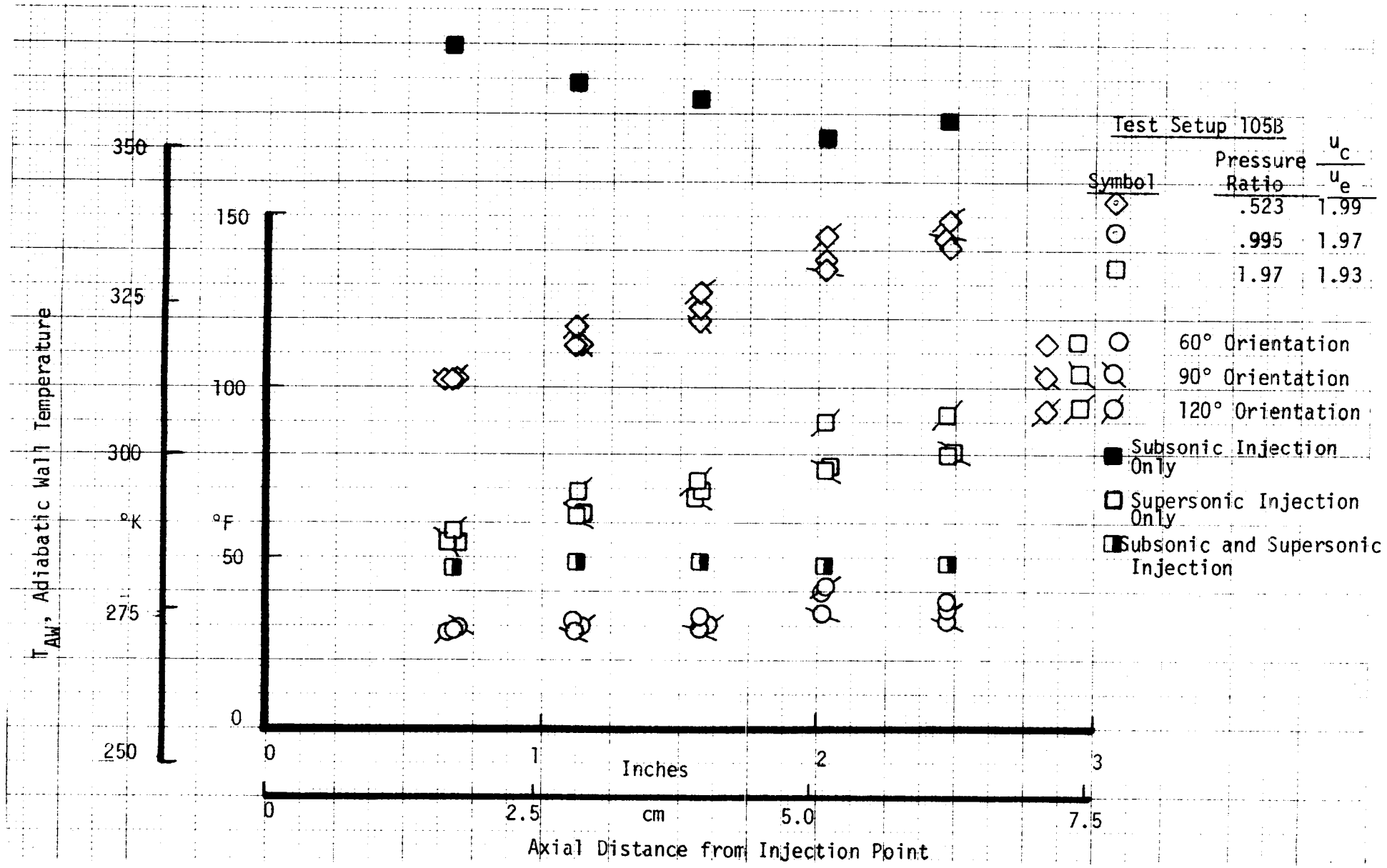

Figure 29. Test Setup 105B Adiabatic Wall Temperature

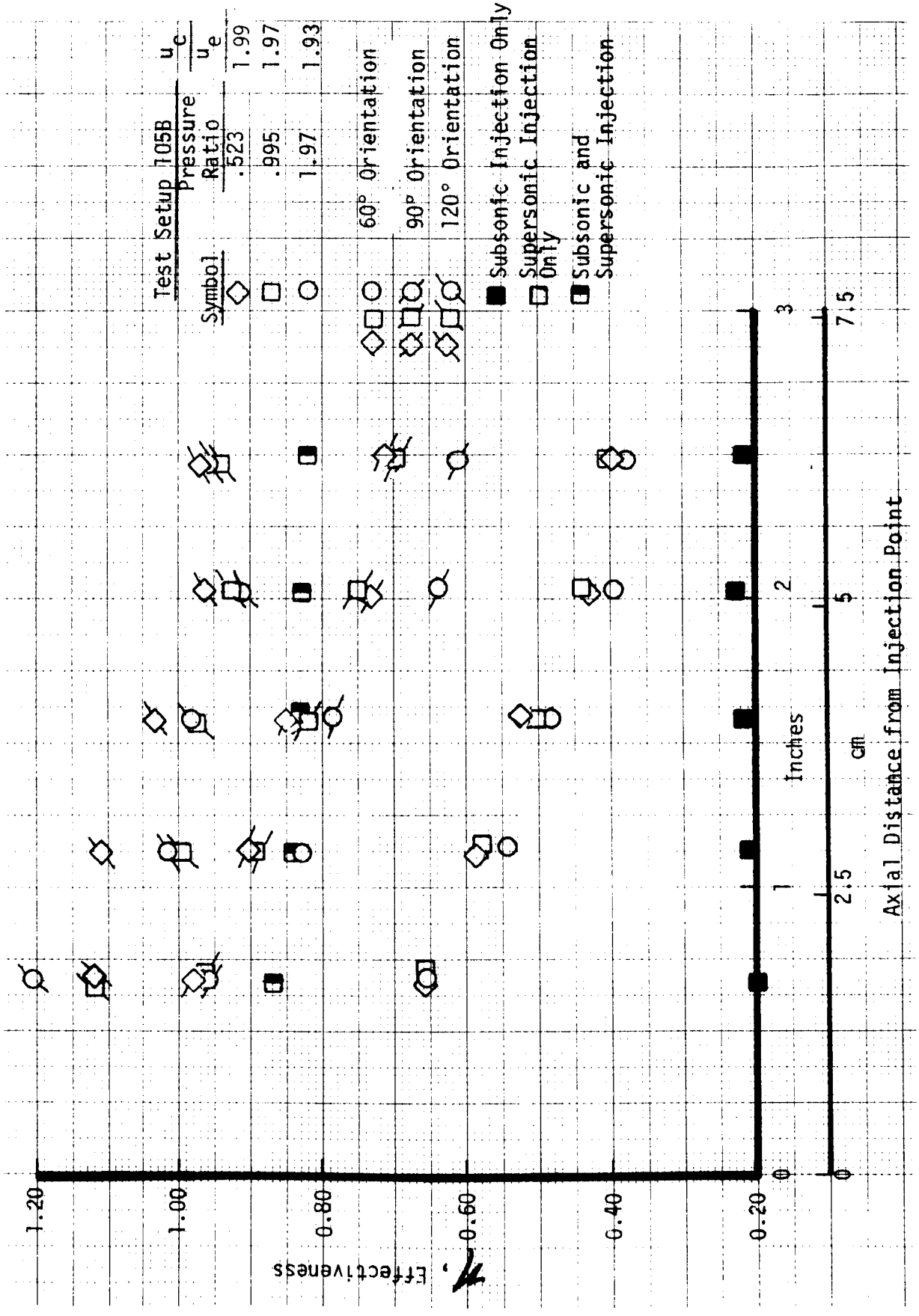

Figure 30. Test Setup 105B Effectiveness Values

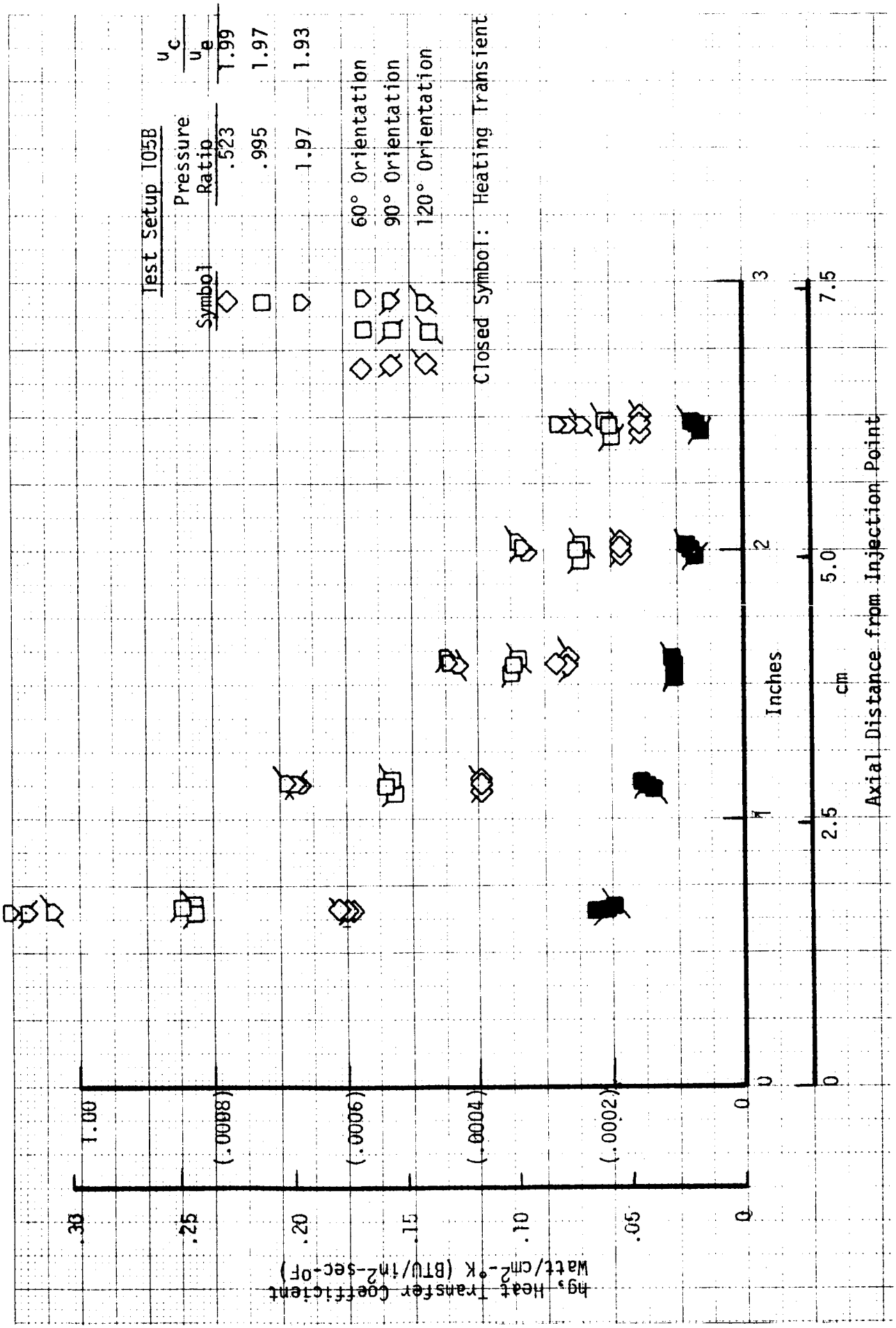

Figure 31. Test Setup 105B Heat Transfer Coefficients

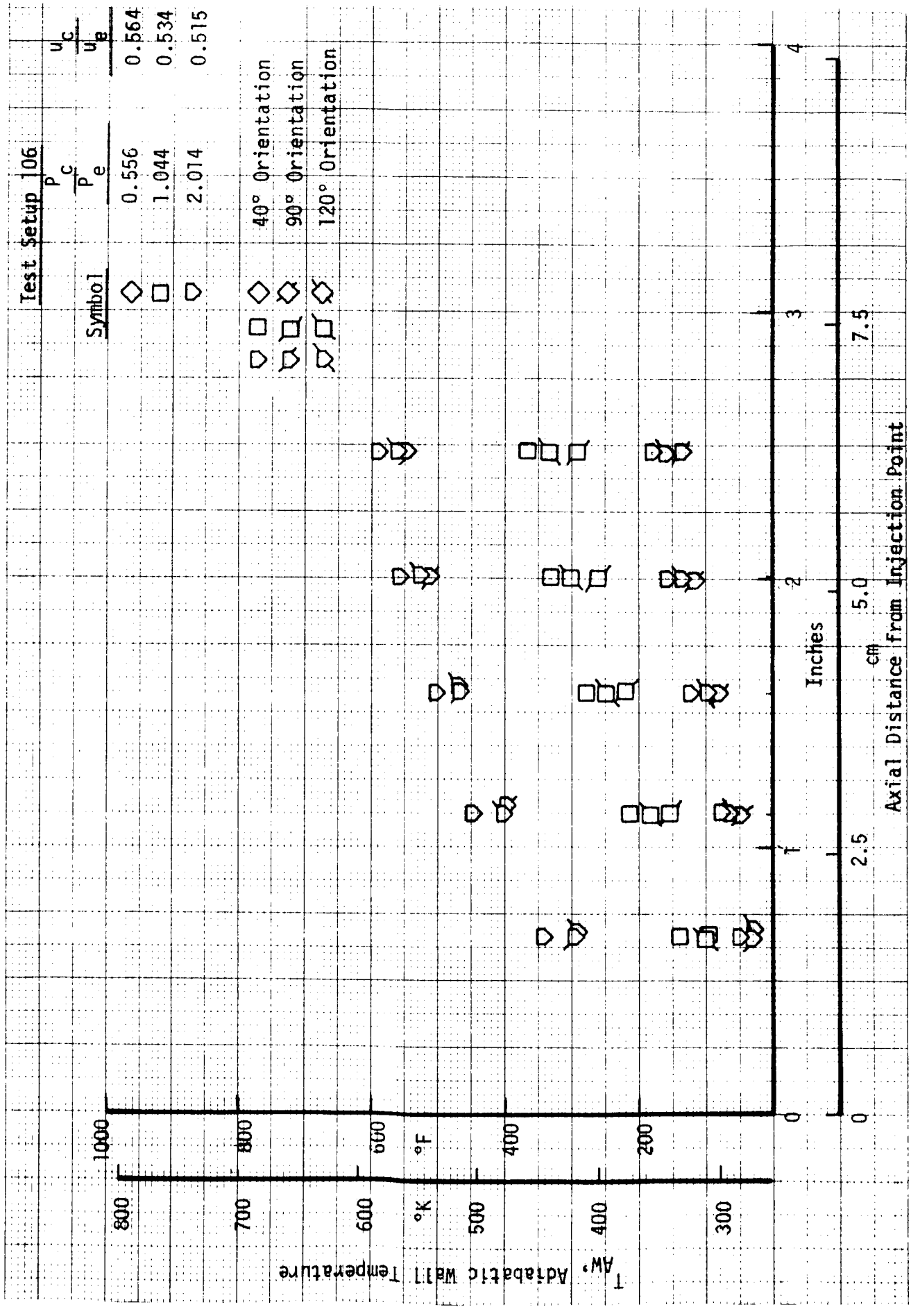

Figure 32. Test Setup 106 Adiabatic Wall Temperatures

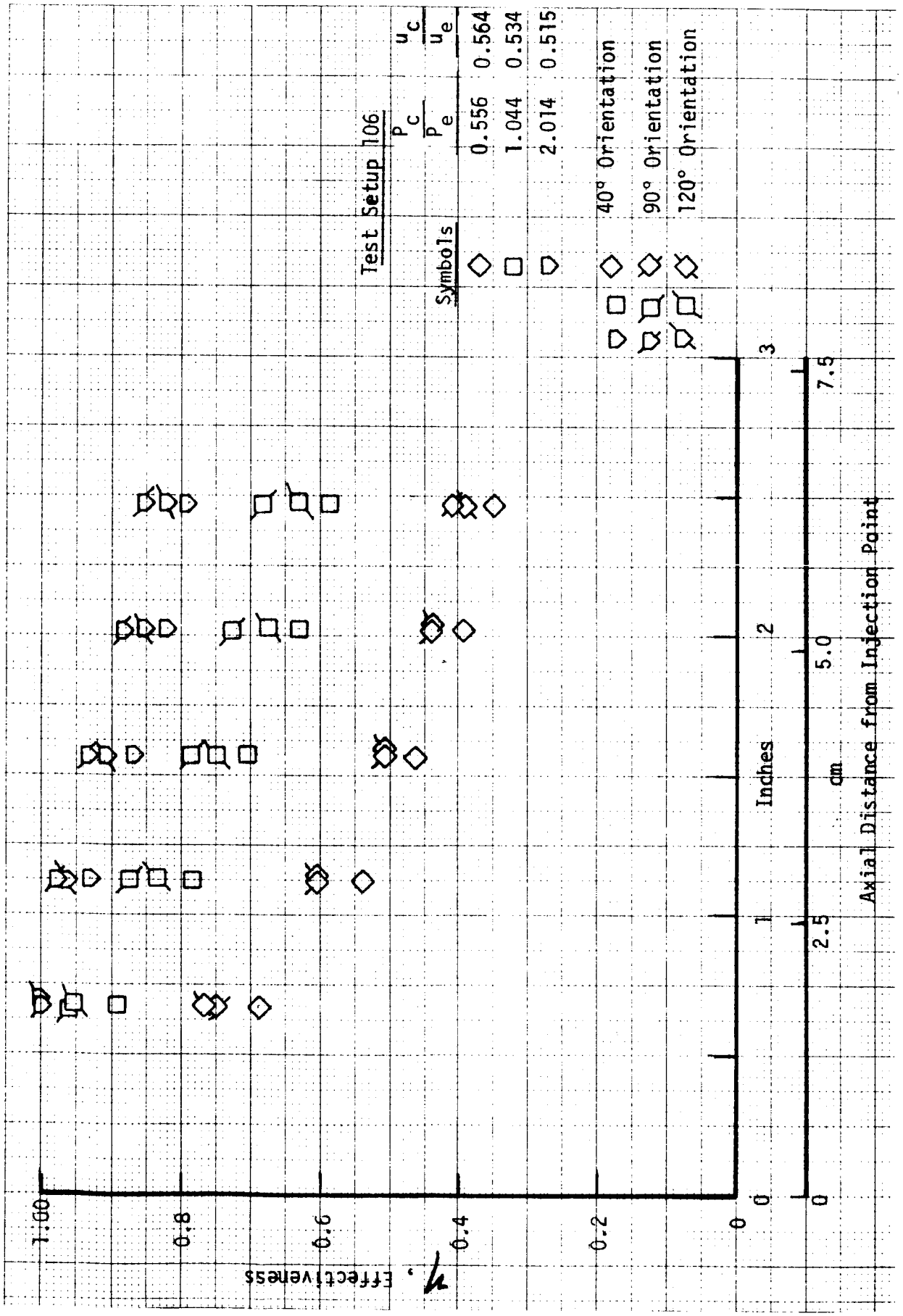

Figure 33. Test Setup 106 Effectiveness Values

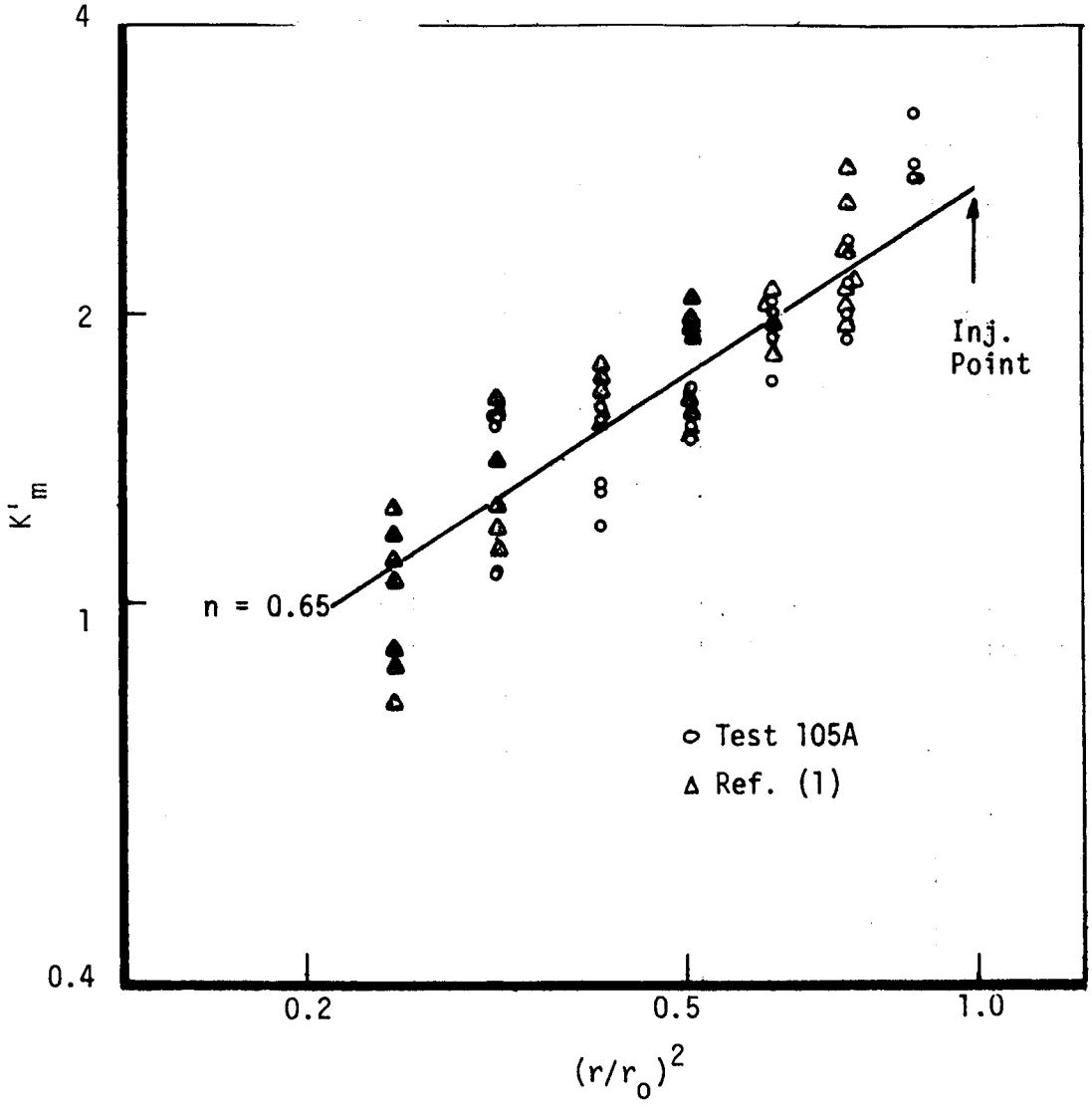

Figure 34. Flow Acceleration Correlation

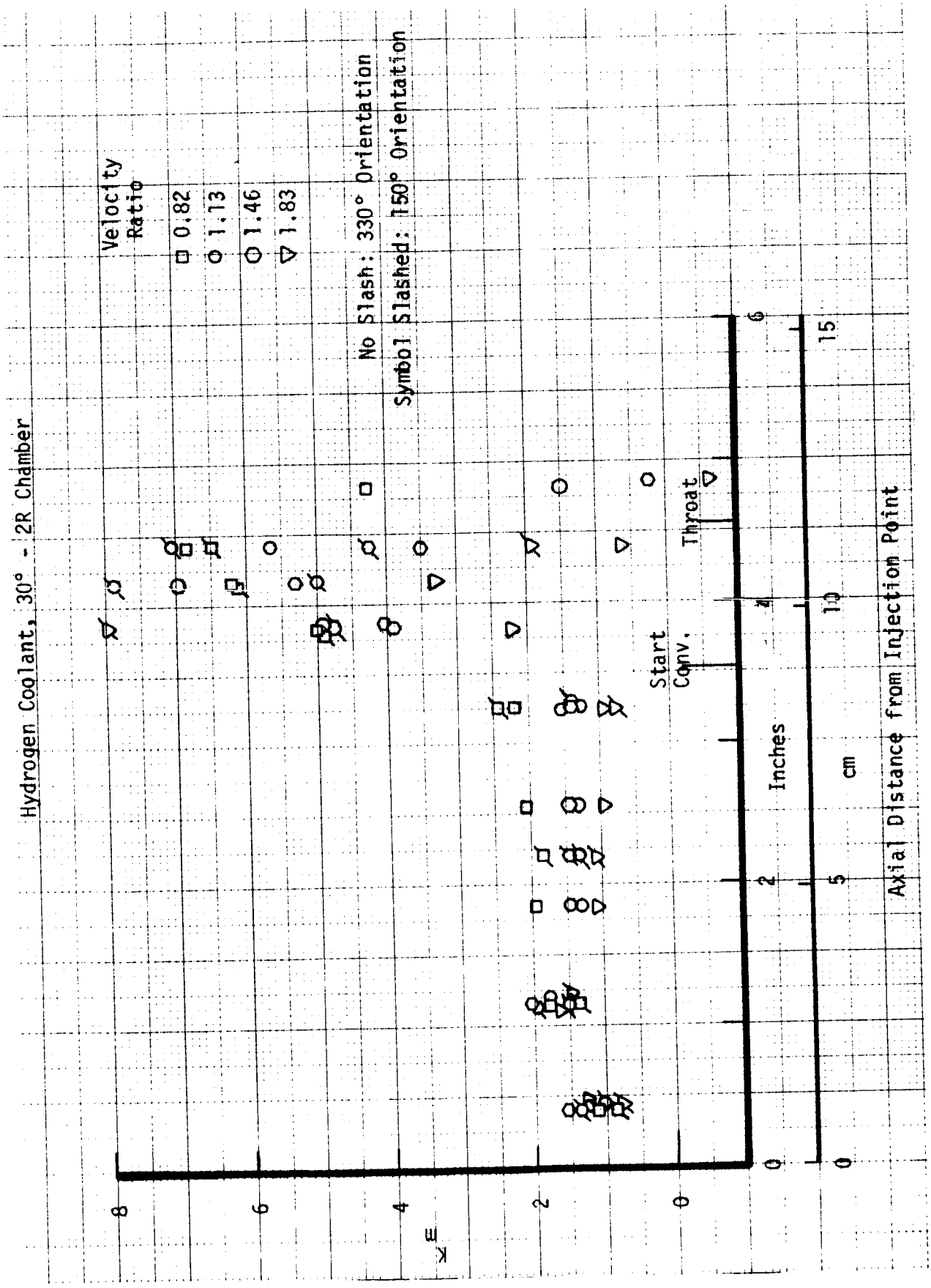

Figure 35. Entrainment Fraction Multipliers for Test 102

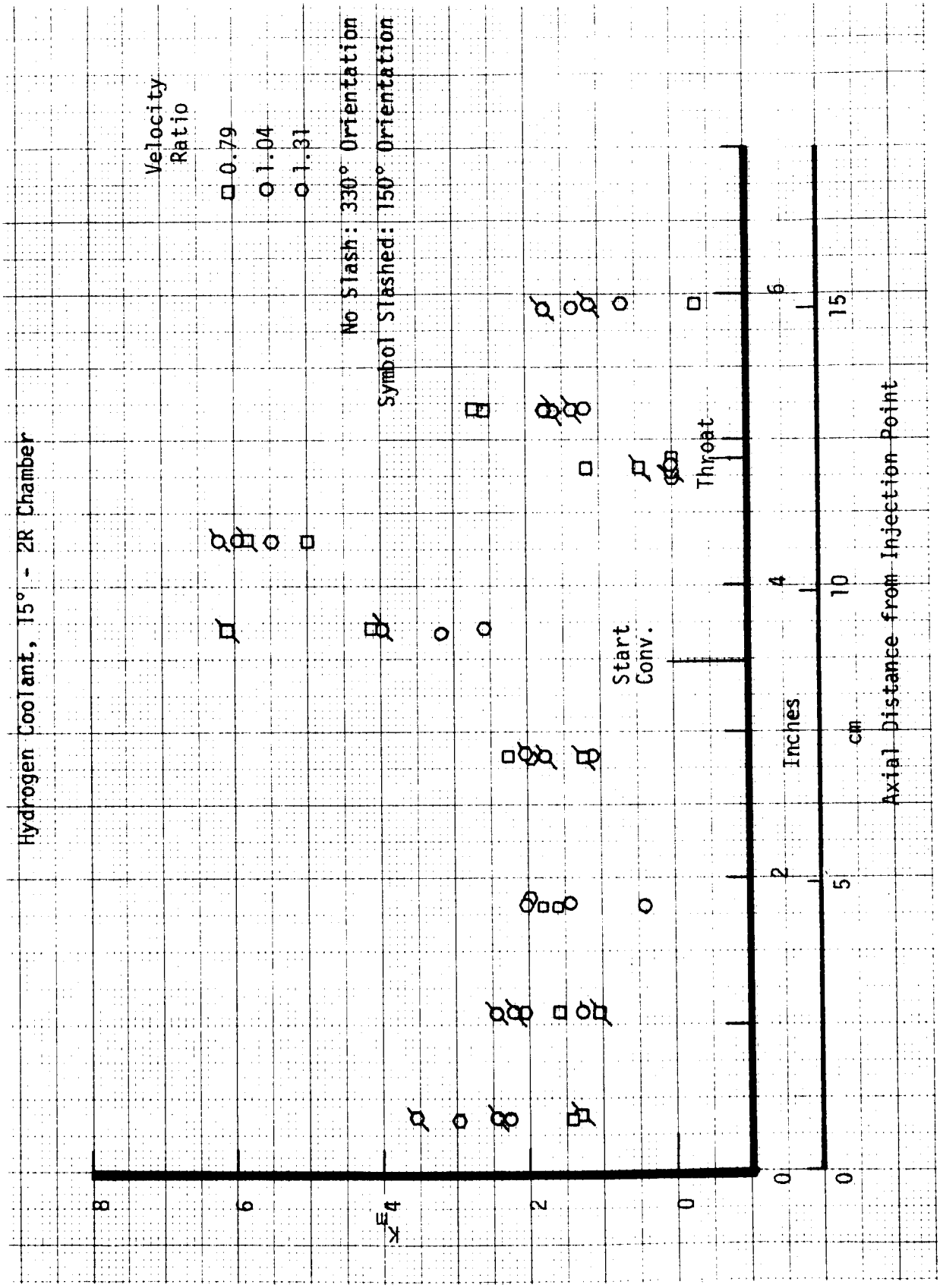

Figure 36. Entrainment Fraction Multipliers for Test 103A

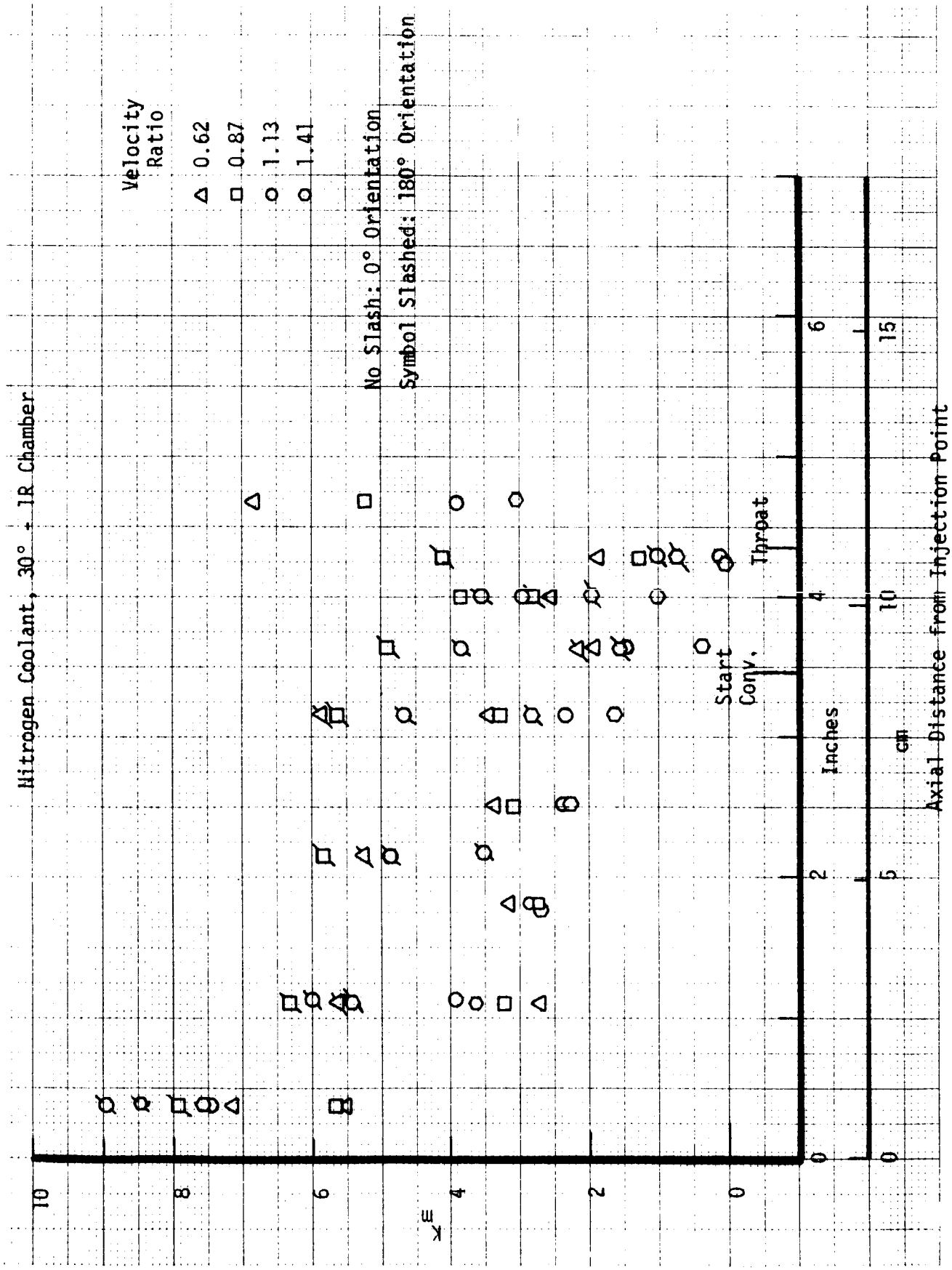

Figure 37. Entrainment Fraction Multipliers for Test 101

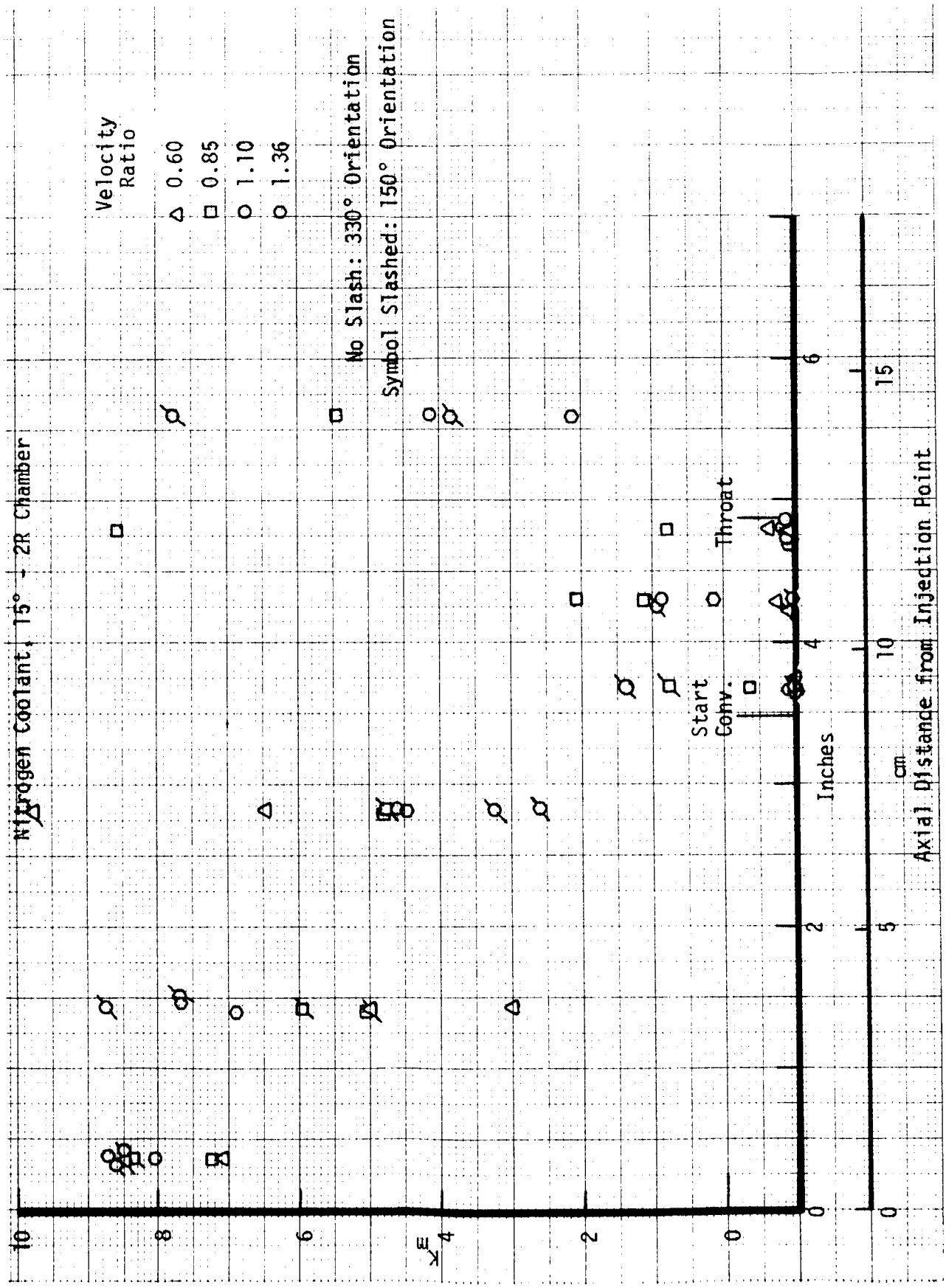

Figure 38. Entrainment Fraction Multipliers for Test 104A

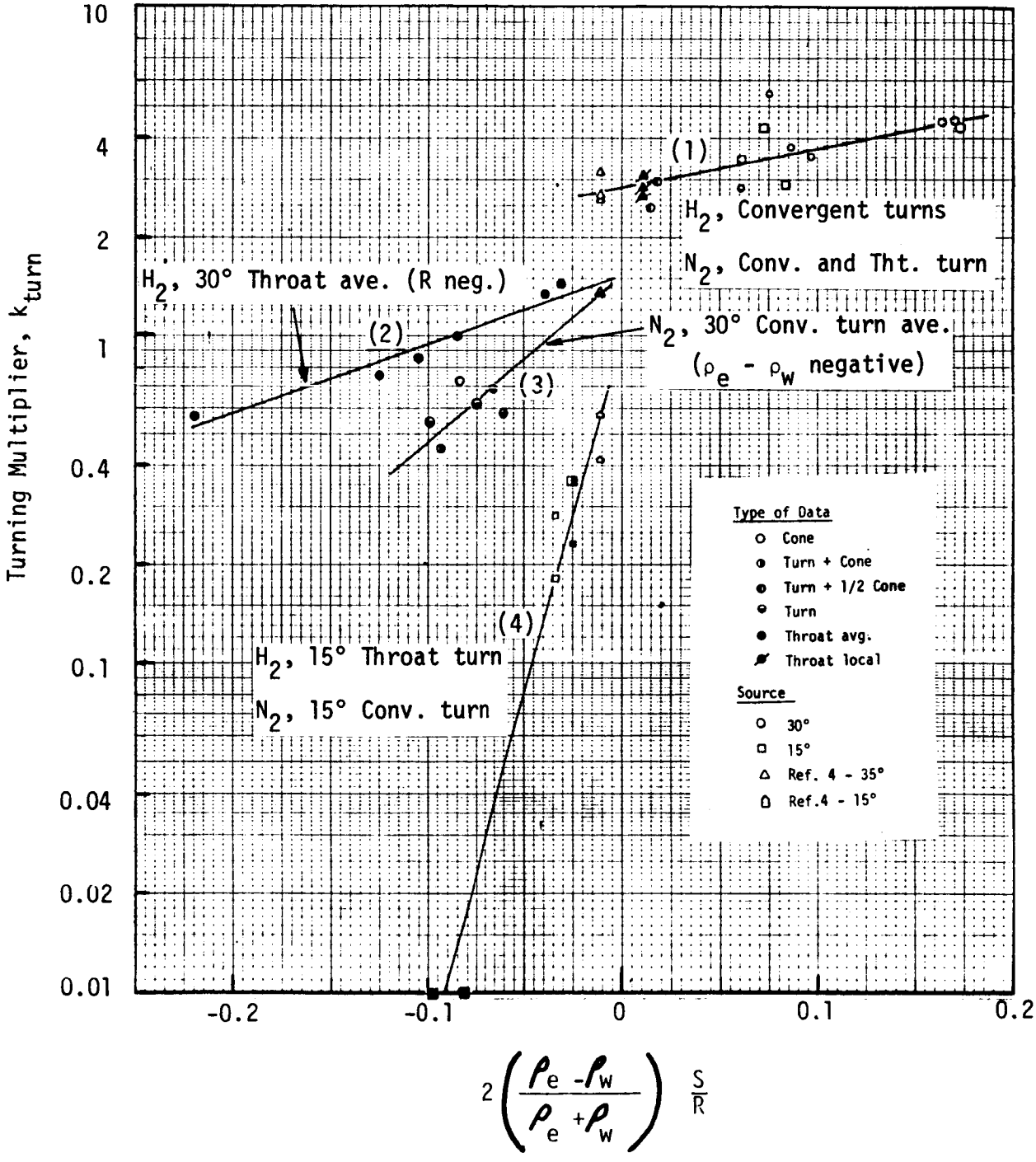

Figure 39. Turning Correlation

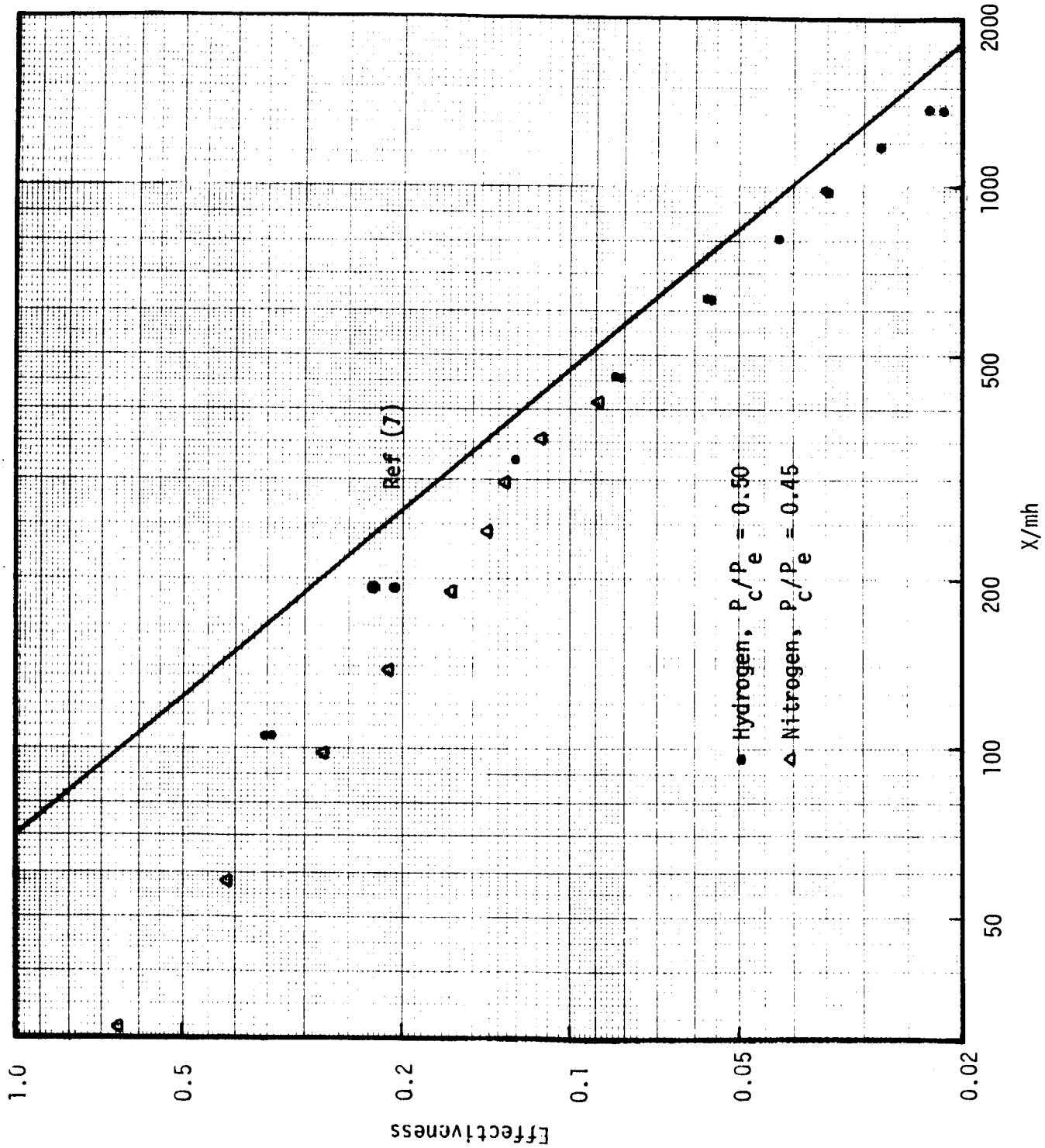

Figure 40. Comparison of Constant Mach Number Effectiveness Data with Ref. (7)

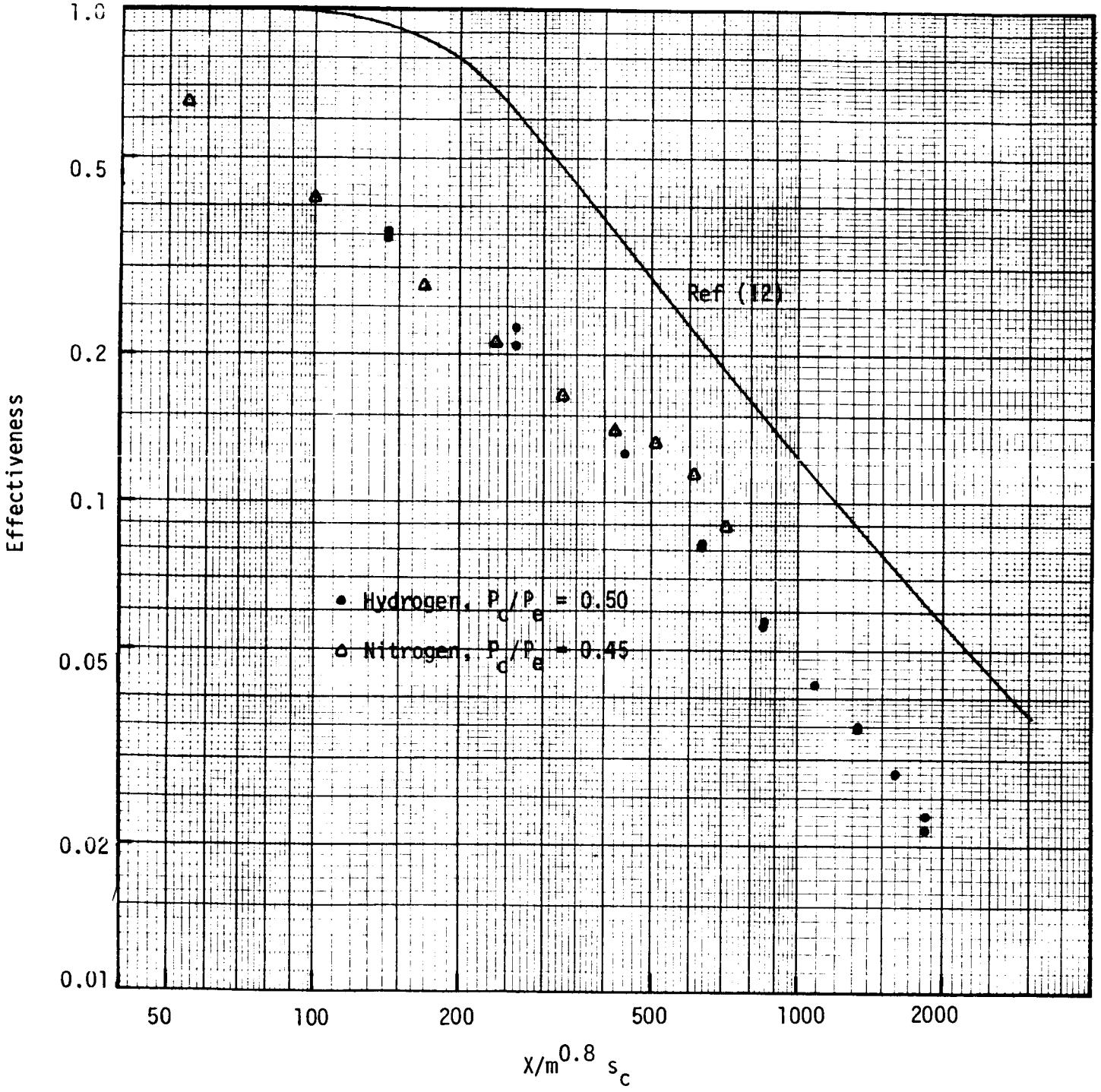

Figure 41. Comparison of Constant Mach No. Effectiveness Data with Ref. (12)

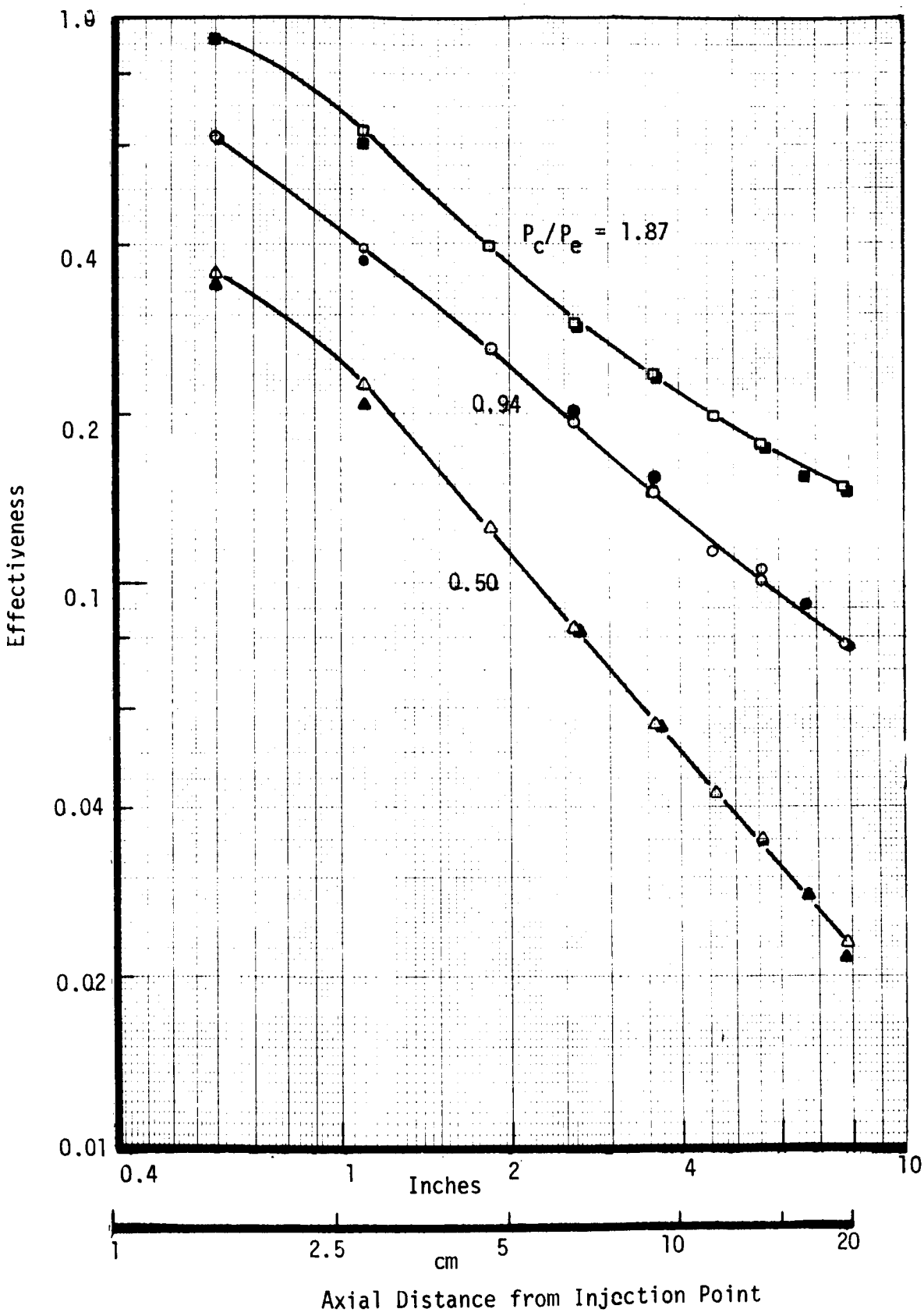

Figure 42. Effect of Pressure Ratio for Test 103B

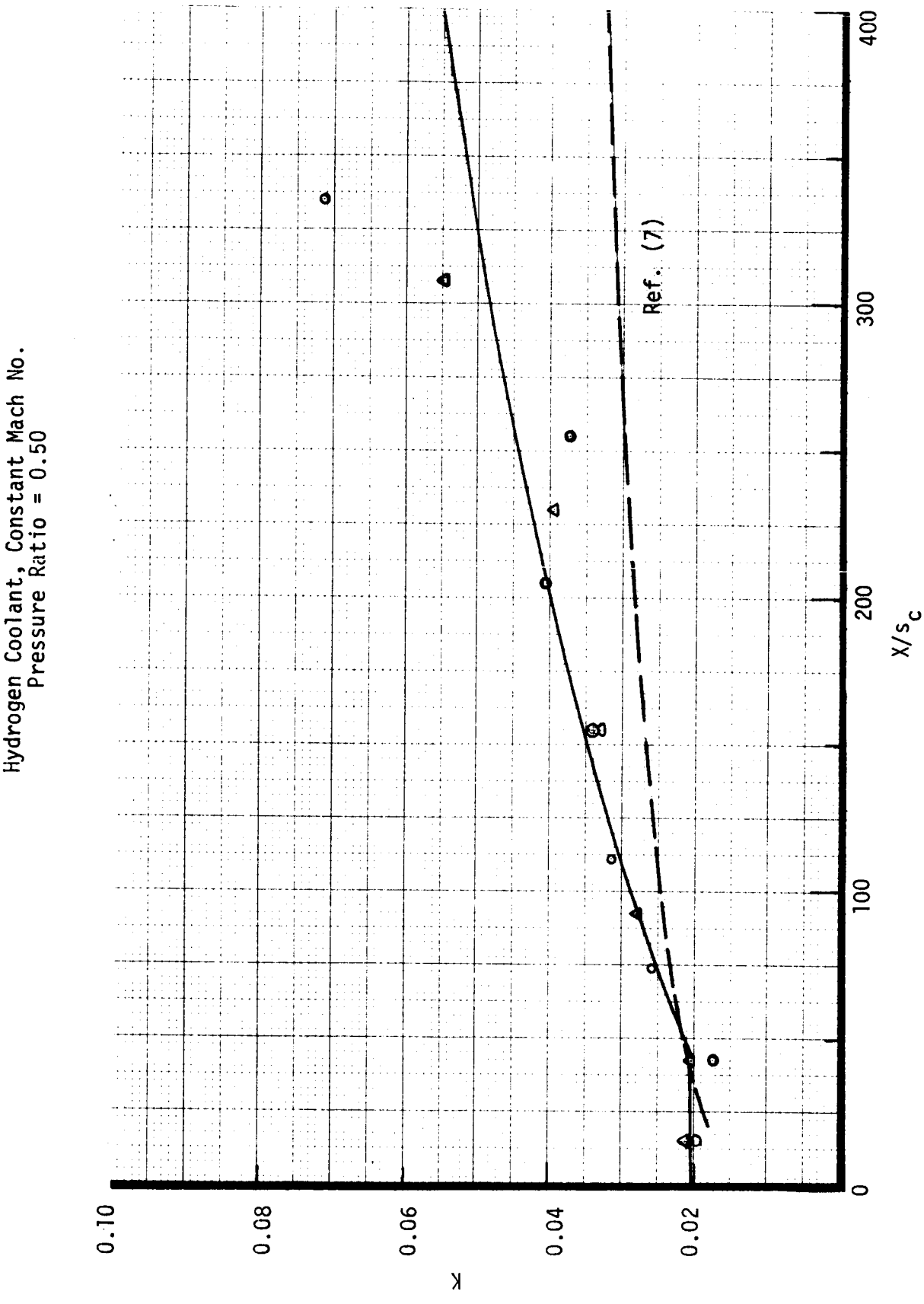

Figure 43. Entrainment Fraction for Test 103B

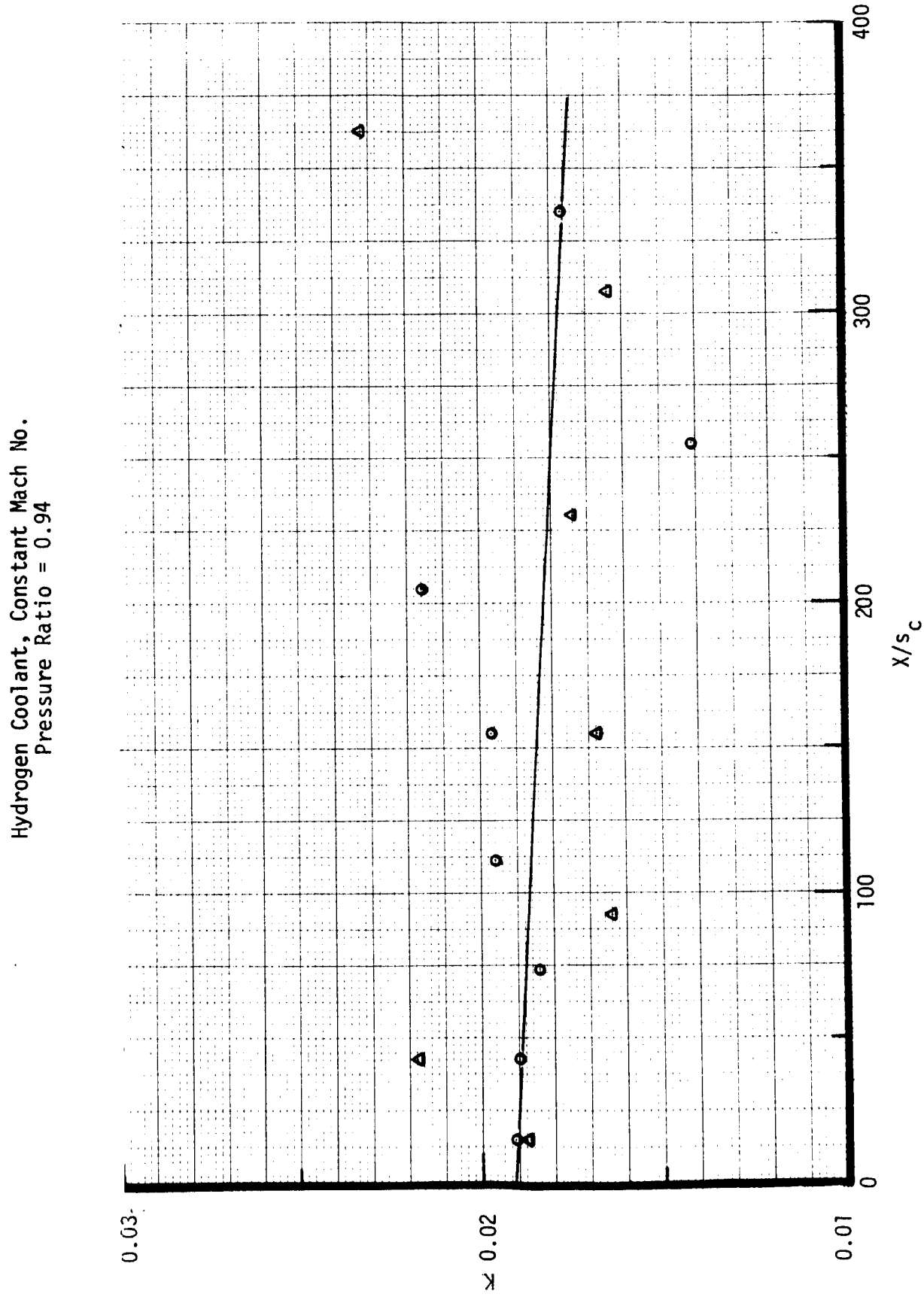

Figure 44. Entrainment Fractions for Test 103B

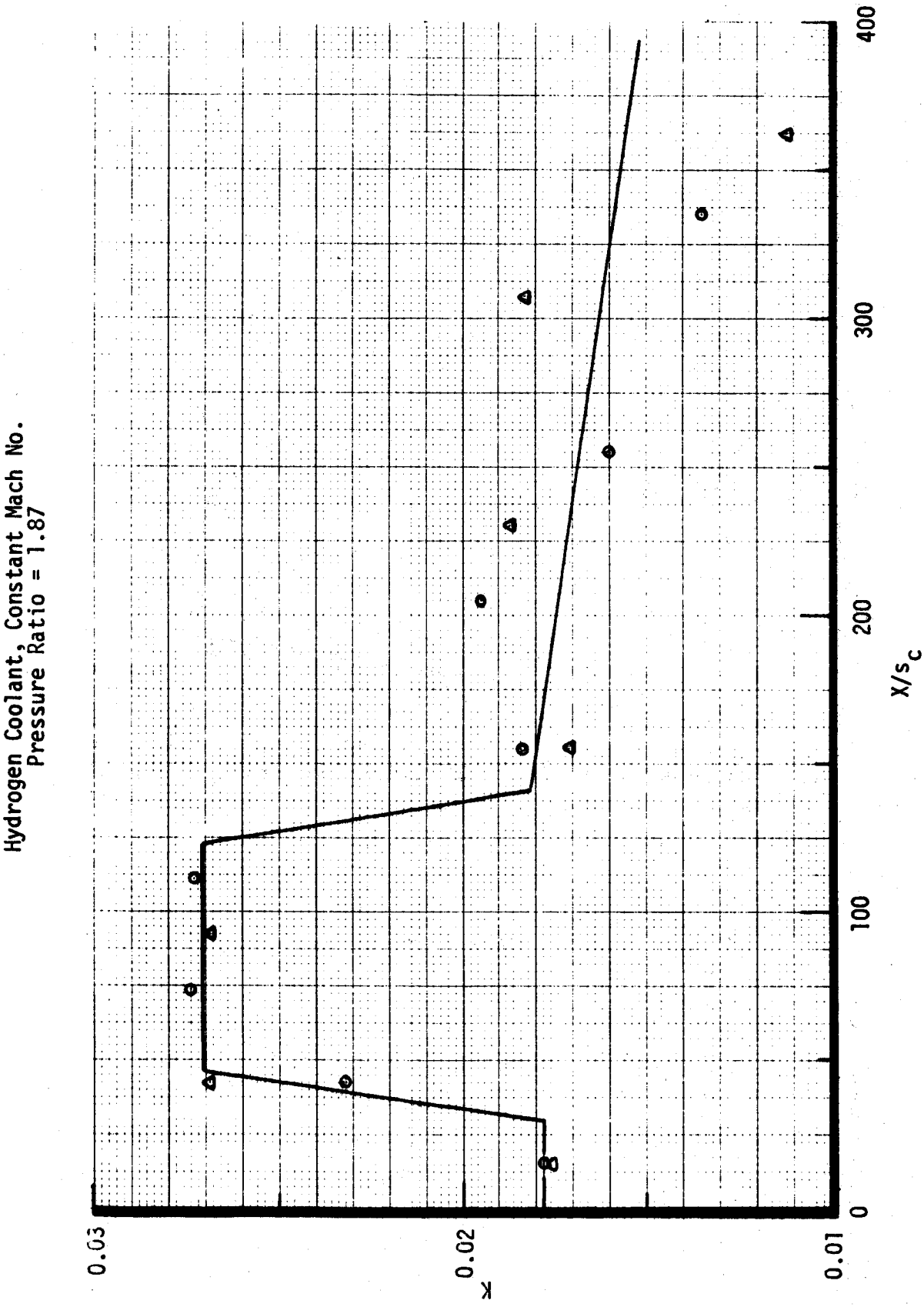

Figure 45. Entrainment Fractions for Test 103B

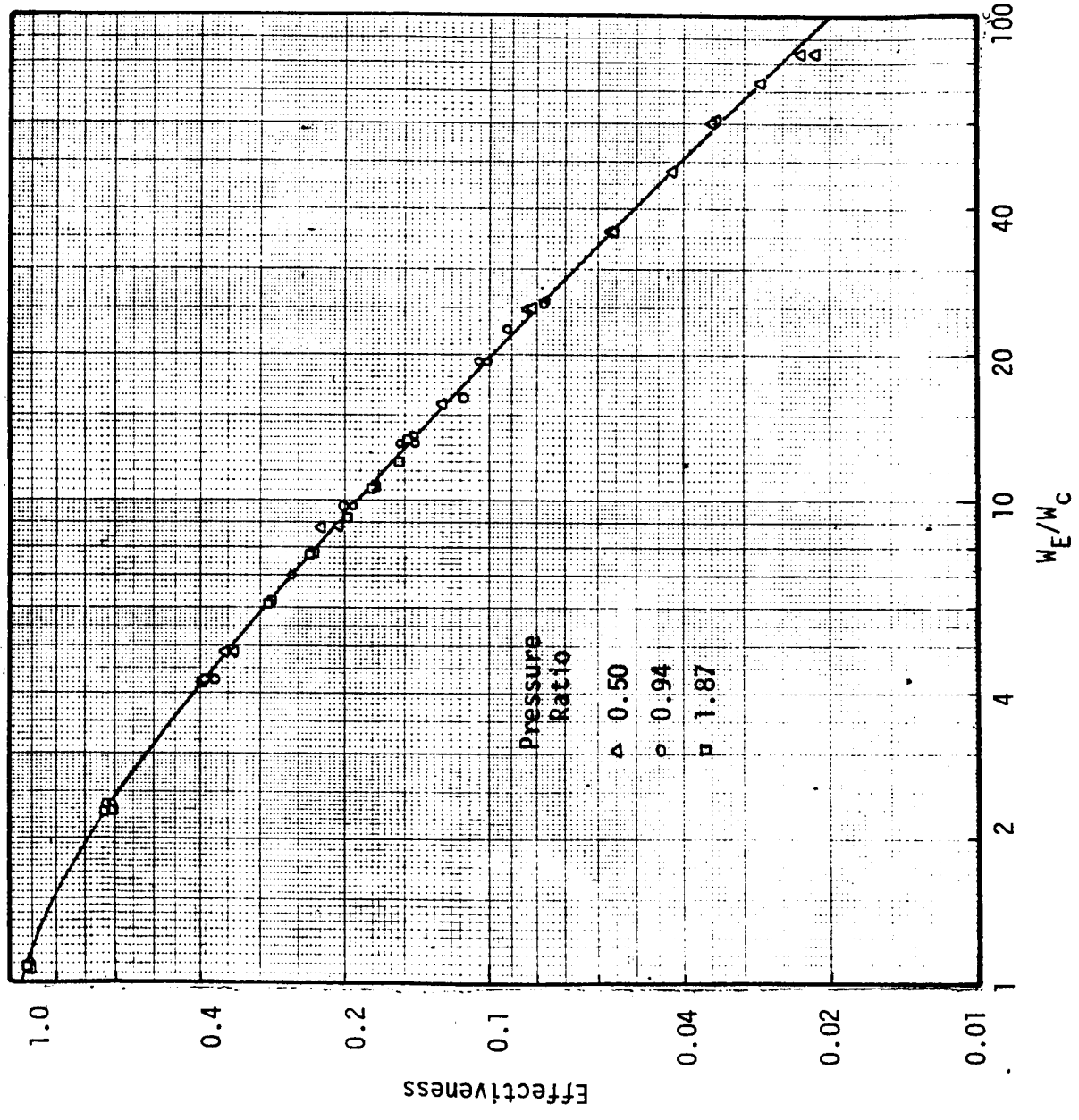

Figure 46. Effectiveness Correlation with Entrainment Flow - Test 103B

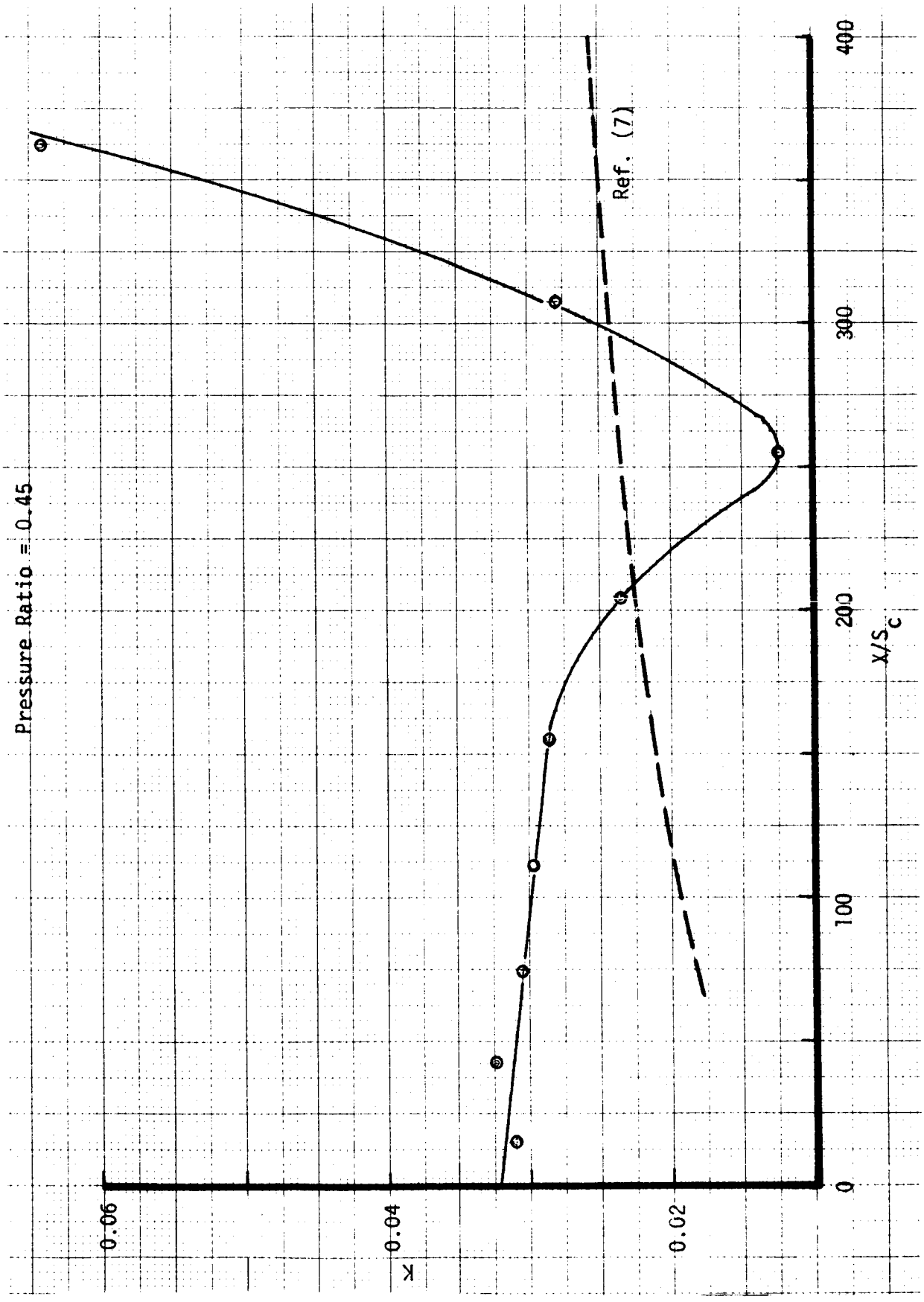

Figure 47. Entrainment Fractions for Test 104B

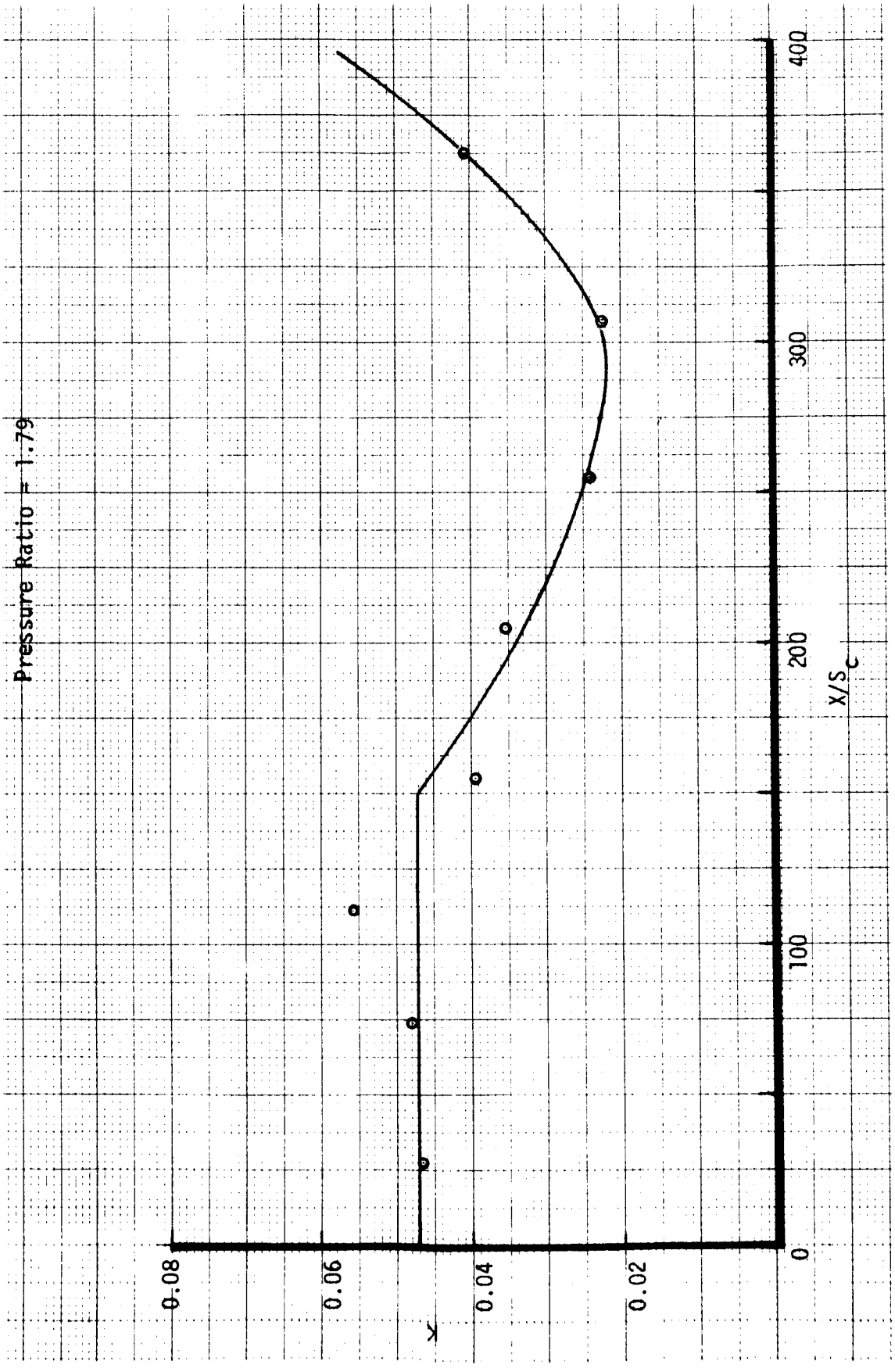

Figure 48. Entrainment Fractions for Test 104B

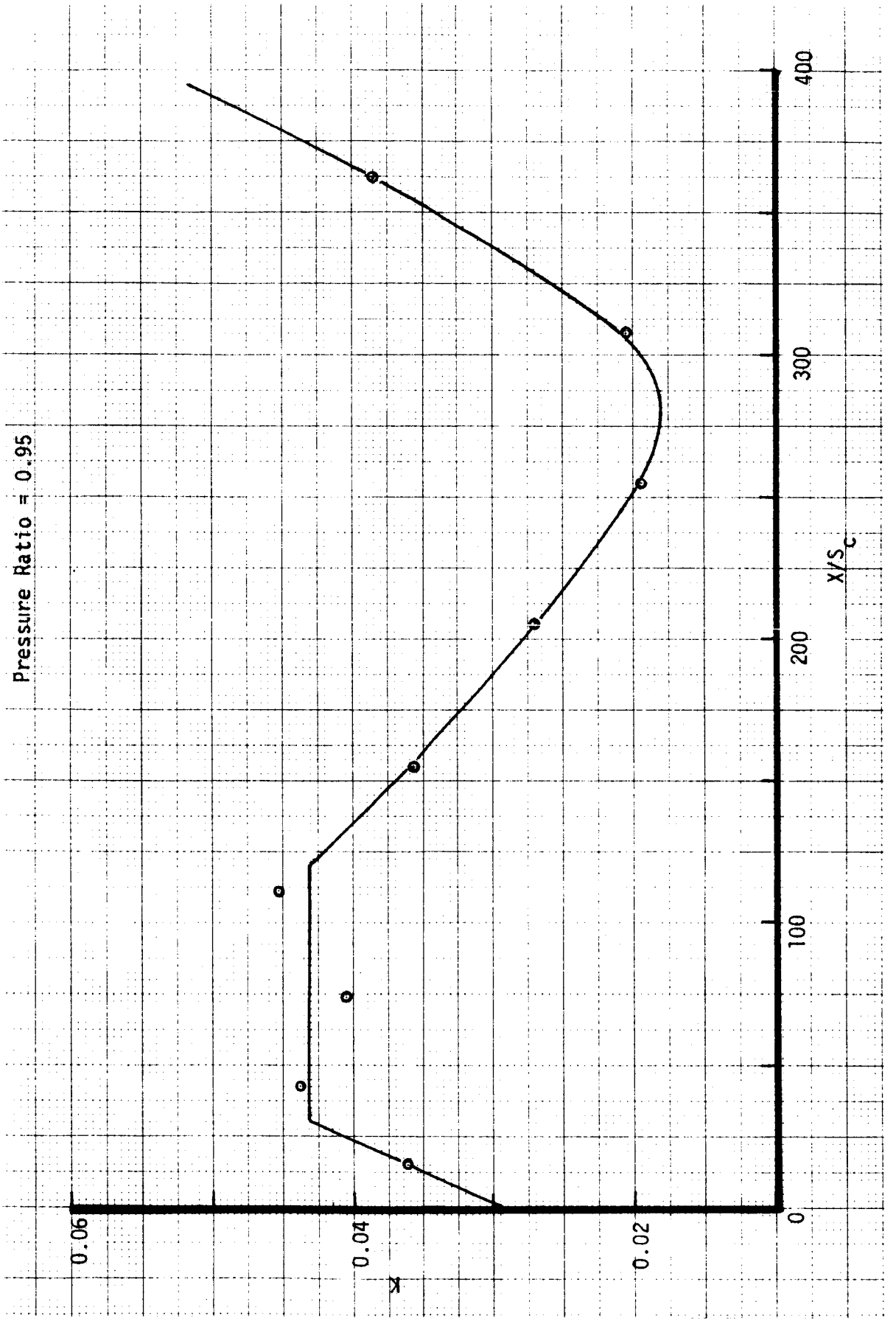

Figure 49. Entrainment Fractions for Test 104B

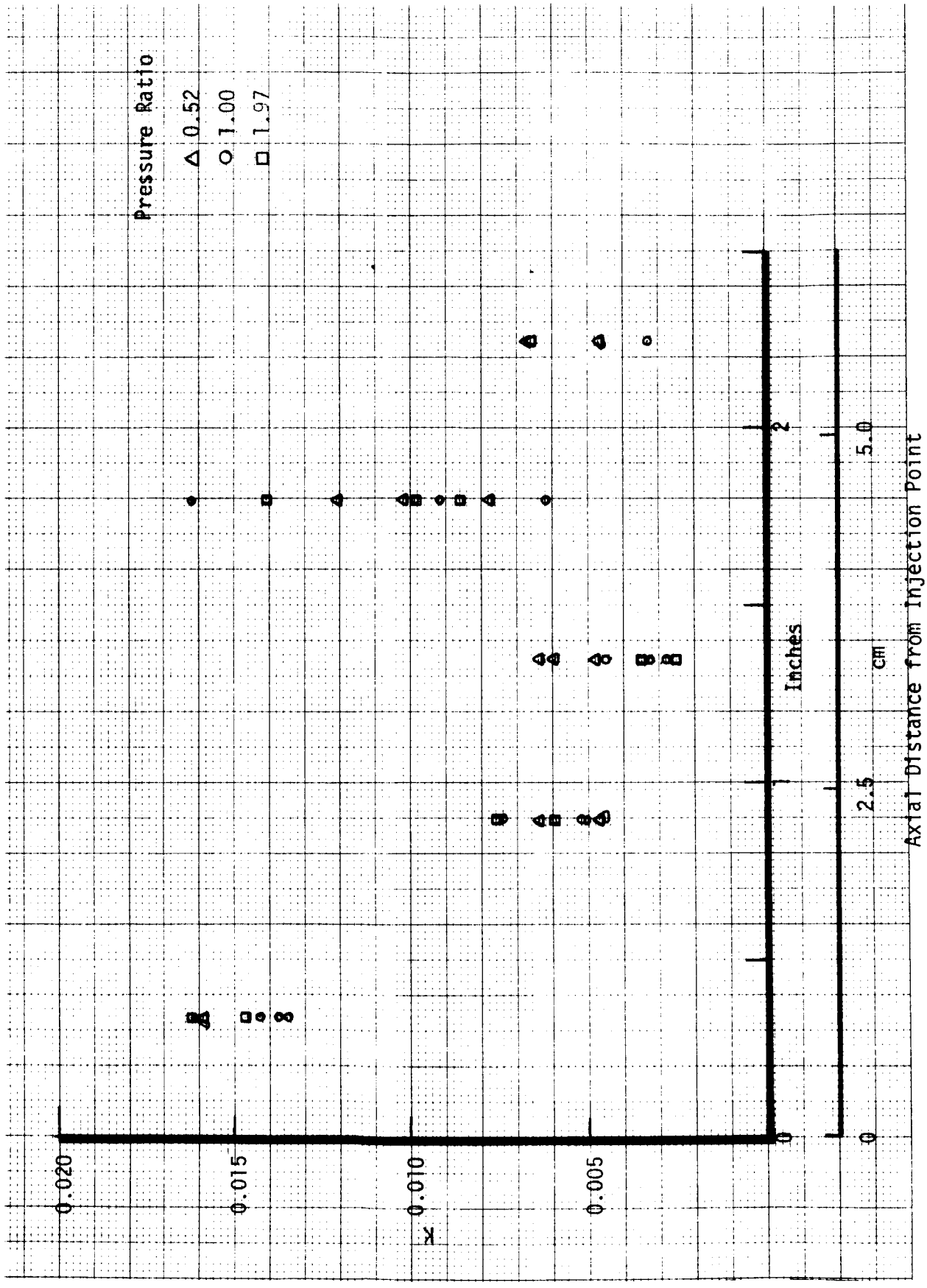

Figure 50. Entrainment Fractions for Test 105B

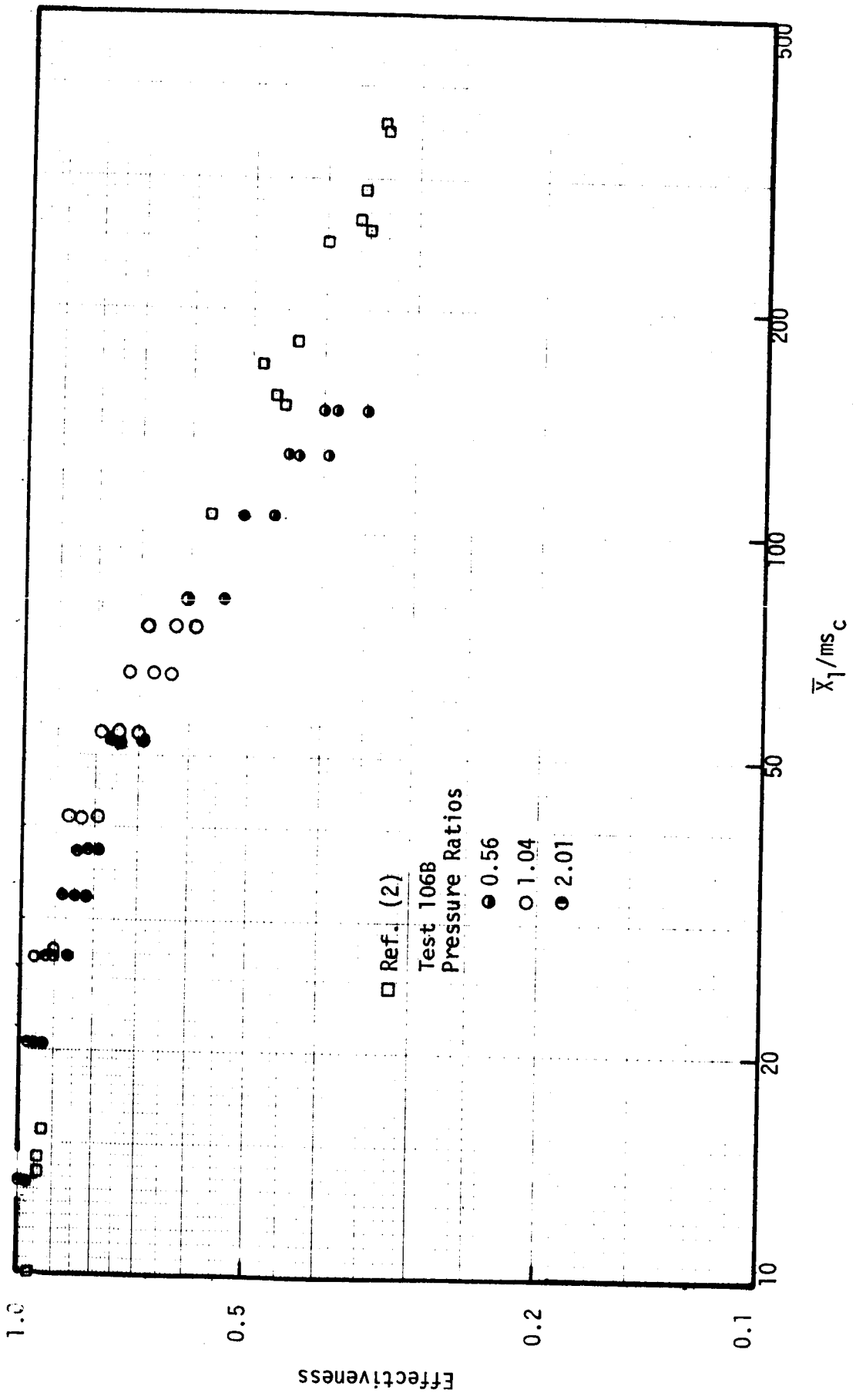

Figure 51. Effectiveness Data for Test 106B and Ref. (2)

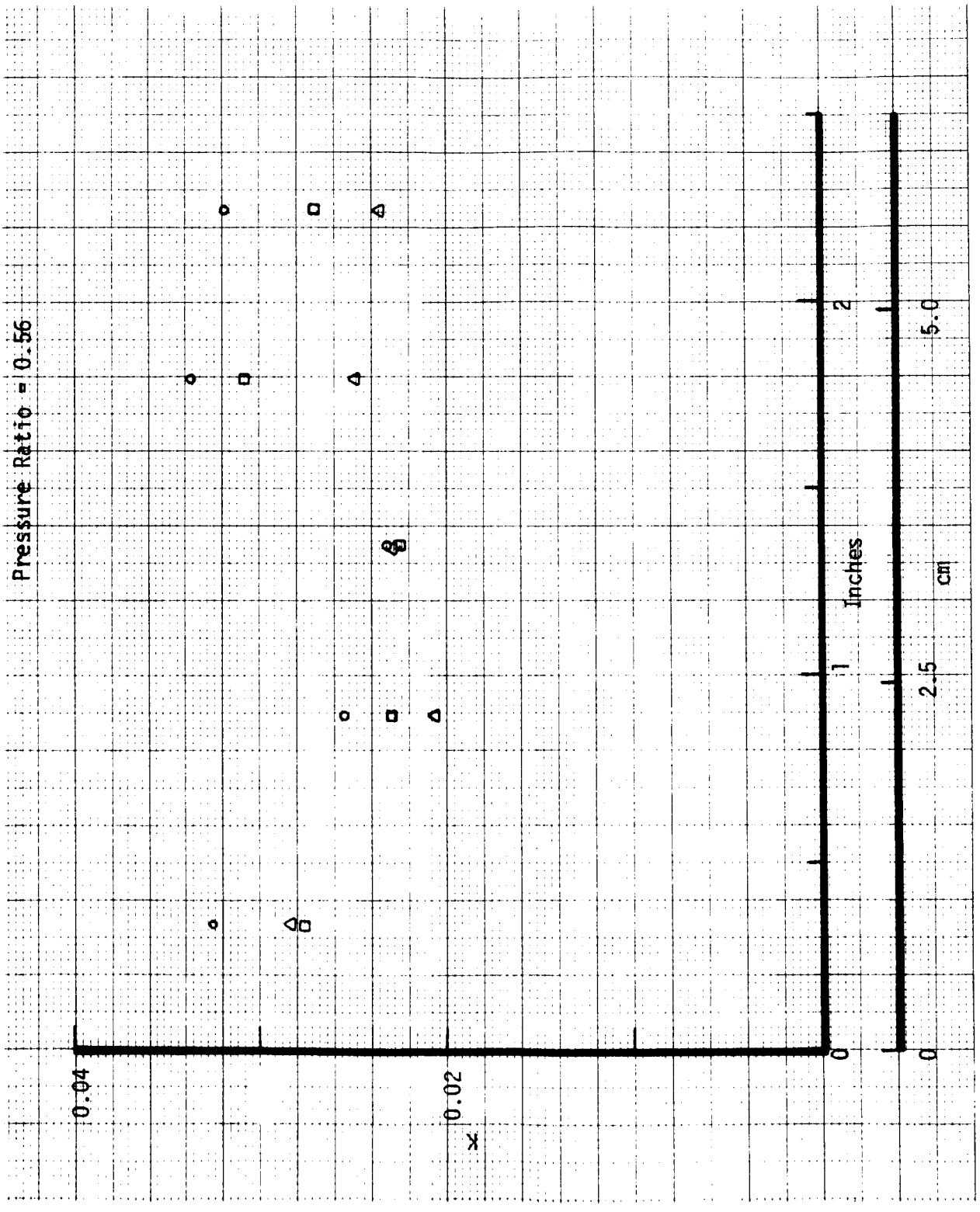

Figure 52. Entrainment Fractions for Test 106B

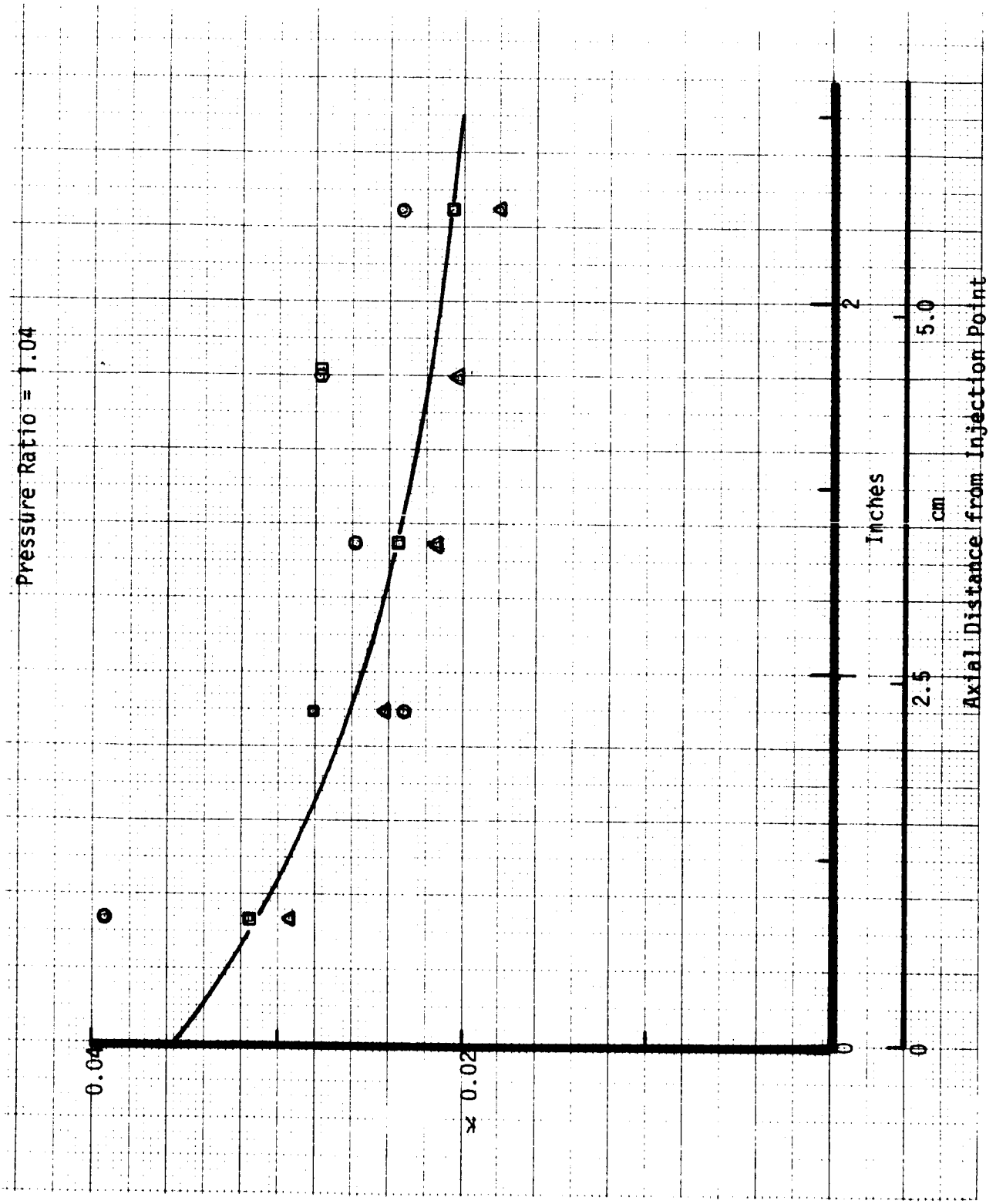

Figure 53. Entrainment Fractions for Test 106B

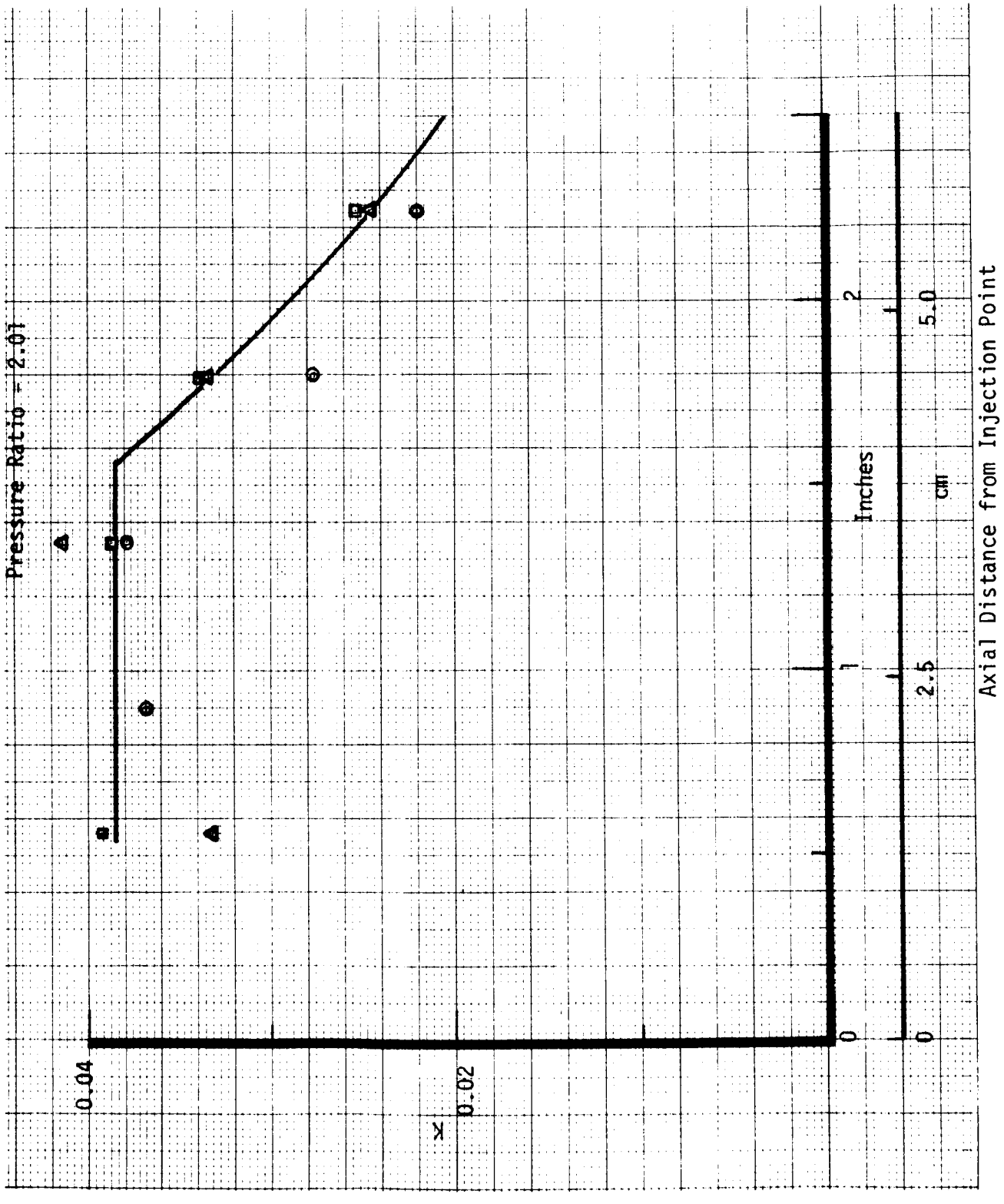

Figure 54. Entrainment Fractions for Test 106B

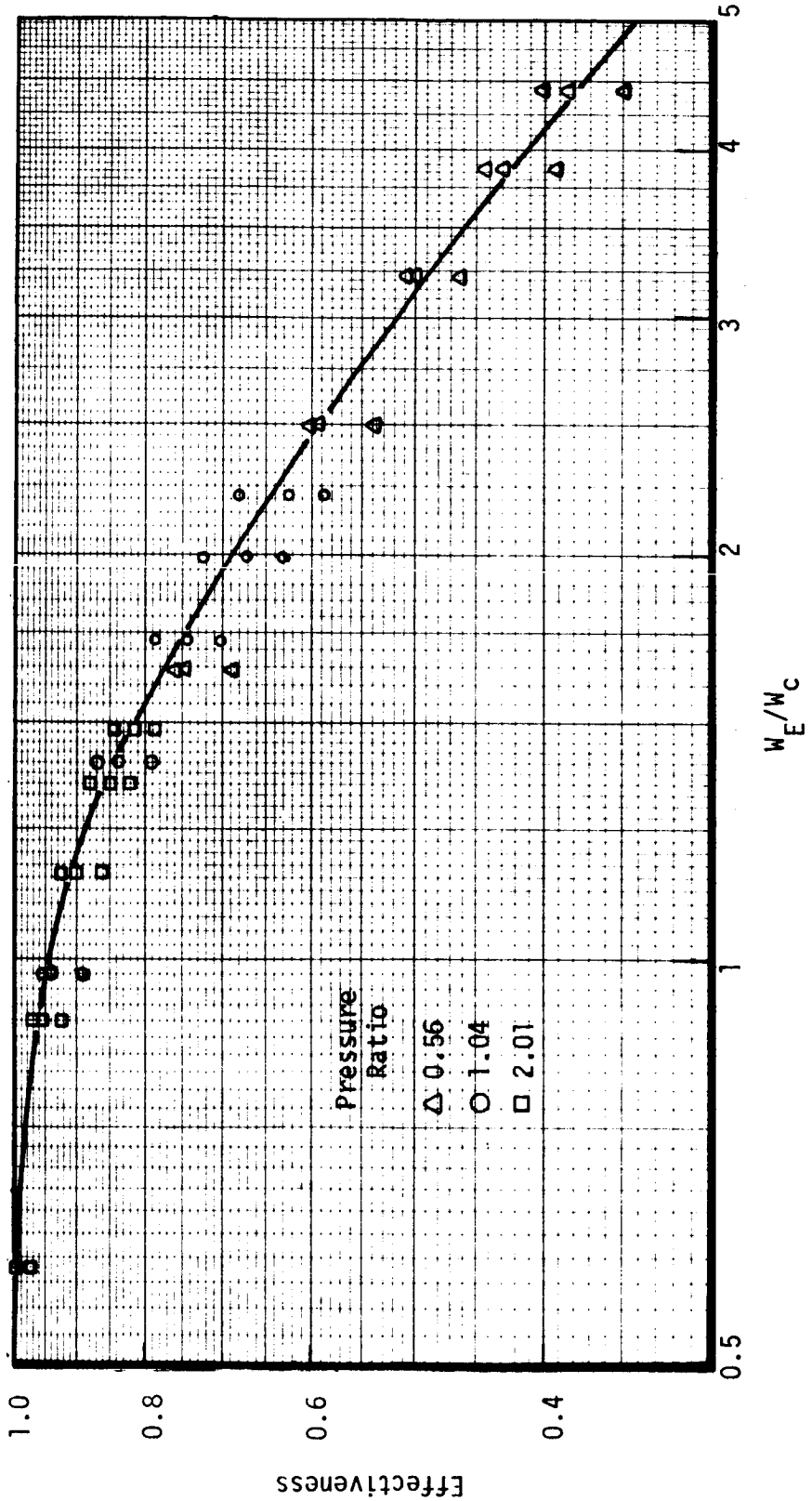

Figure 55. Effectiveness Correlation with Entrainment Flow - Test 106B

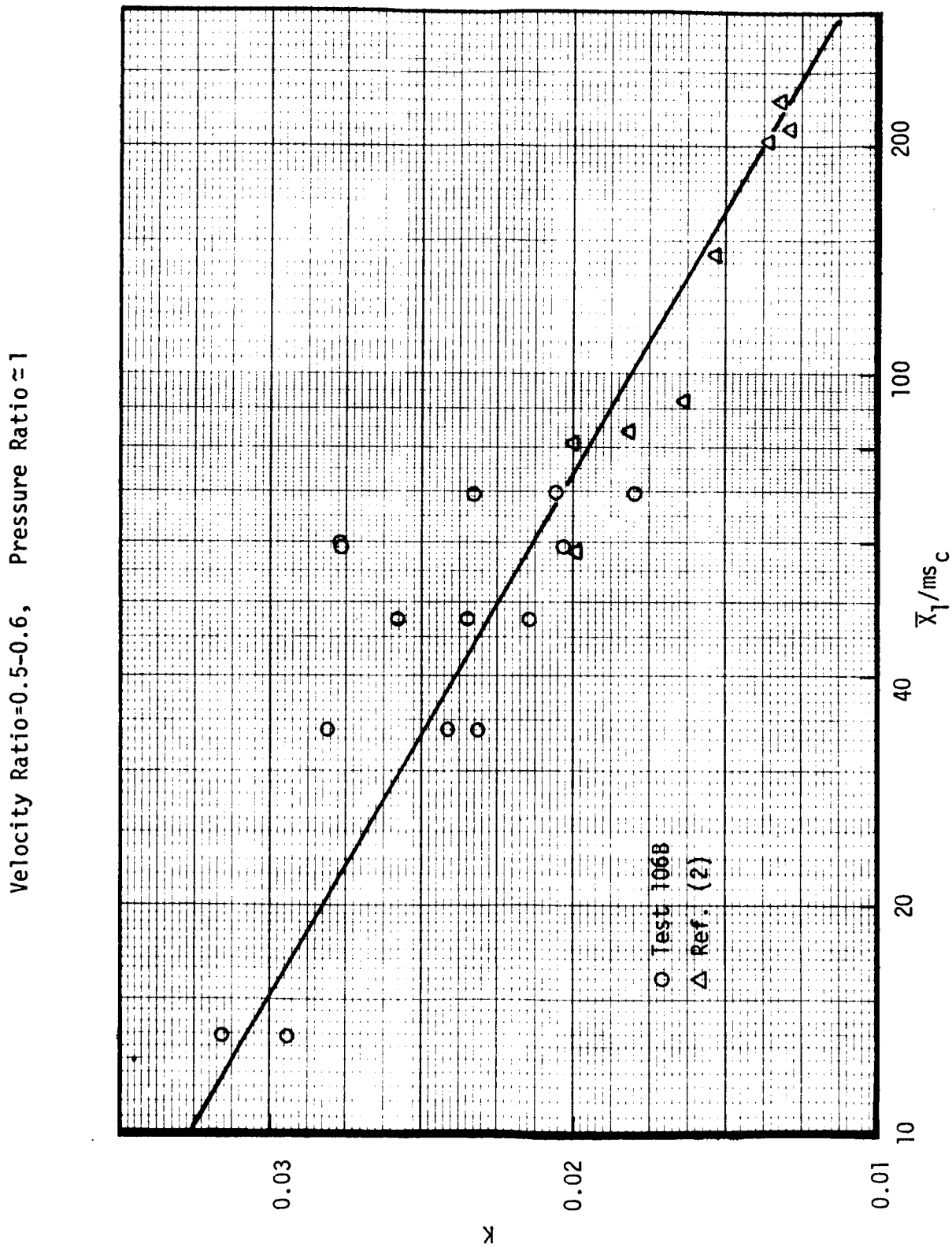

Figure 56. Variable Mach Number Entrainment Fraction Correlation

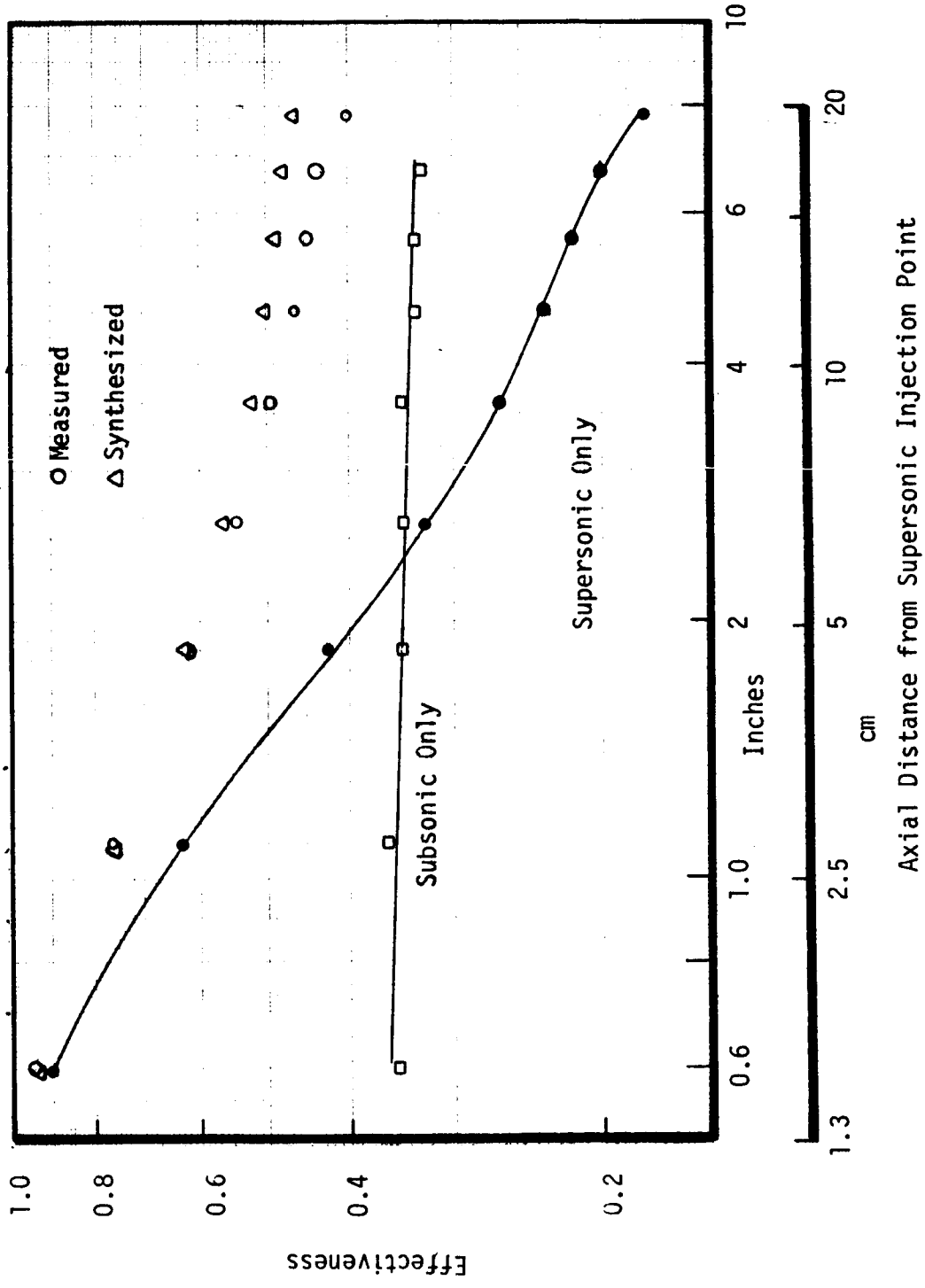

Figure 57. Test 104B Effectiveness Data with Subsonic Injection Carryover

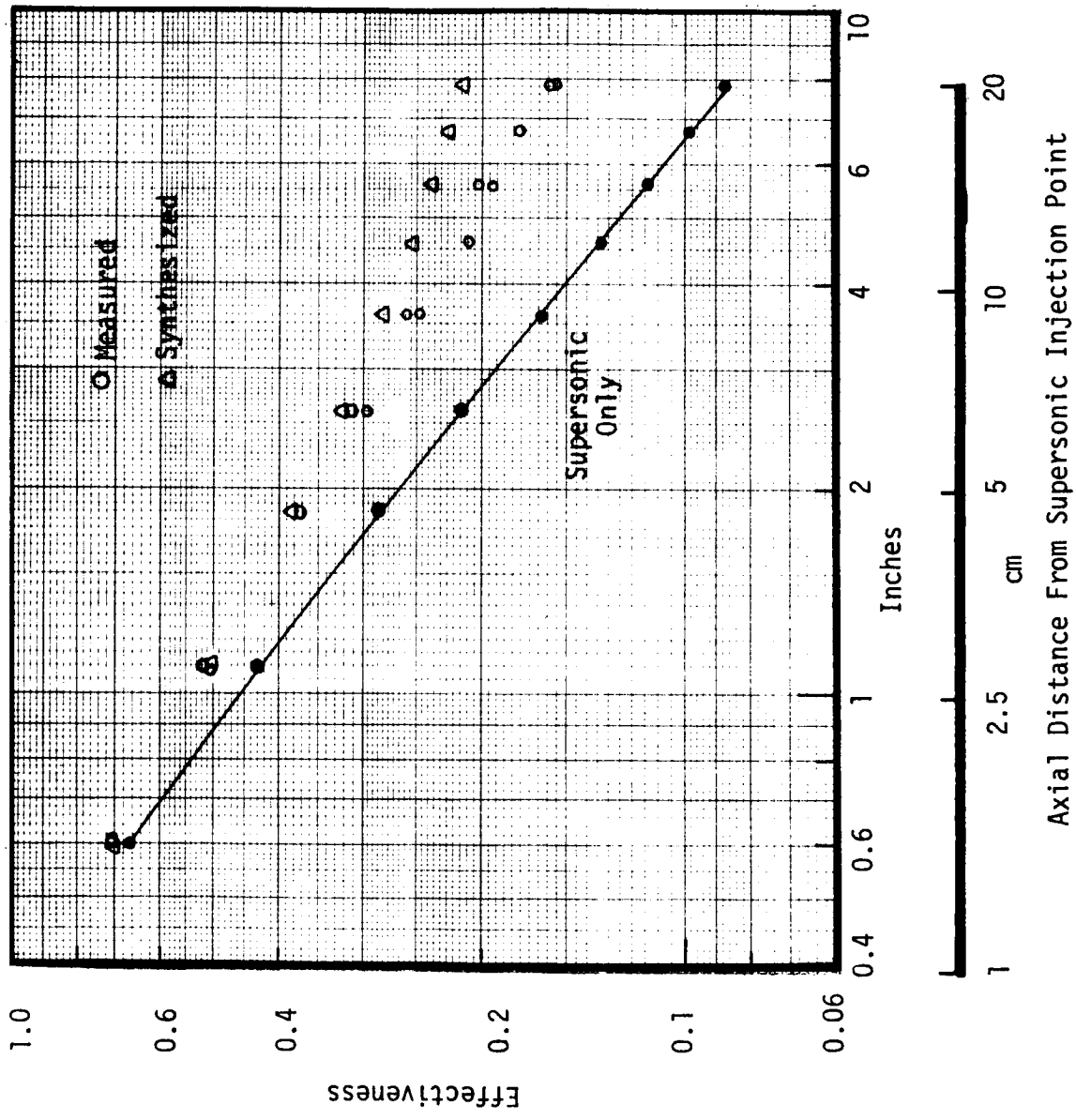

Figure 58. Test 103B Effectiveness Data with Subsonic Injection Carryover

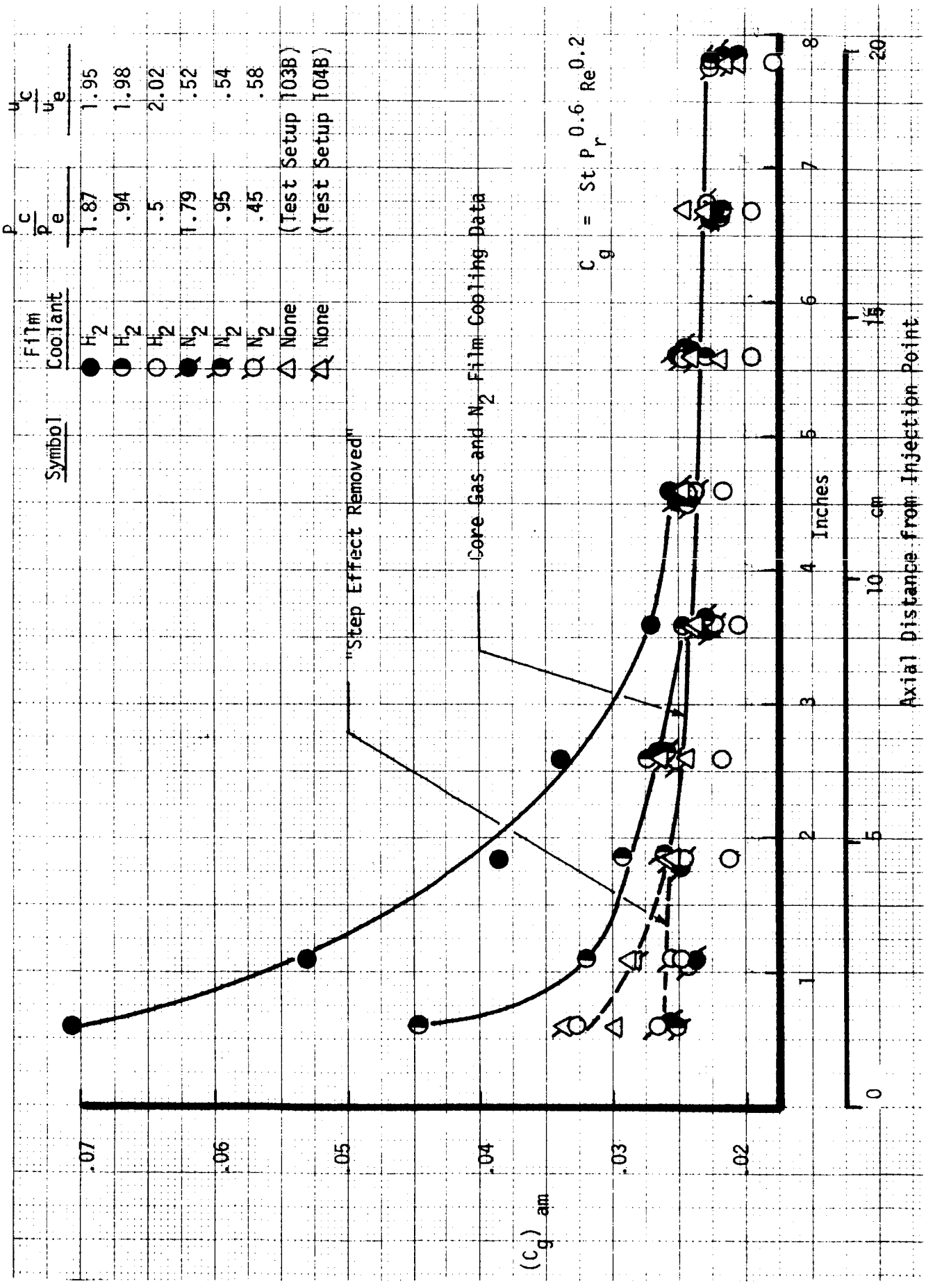

Figure 59. Constant Mach Number C_g Values, T_{am} Reference Temperature

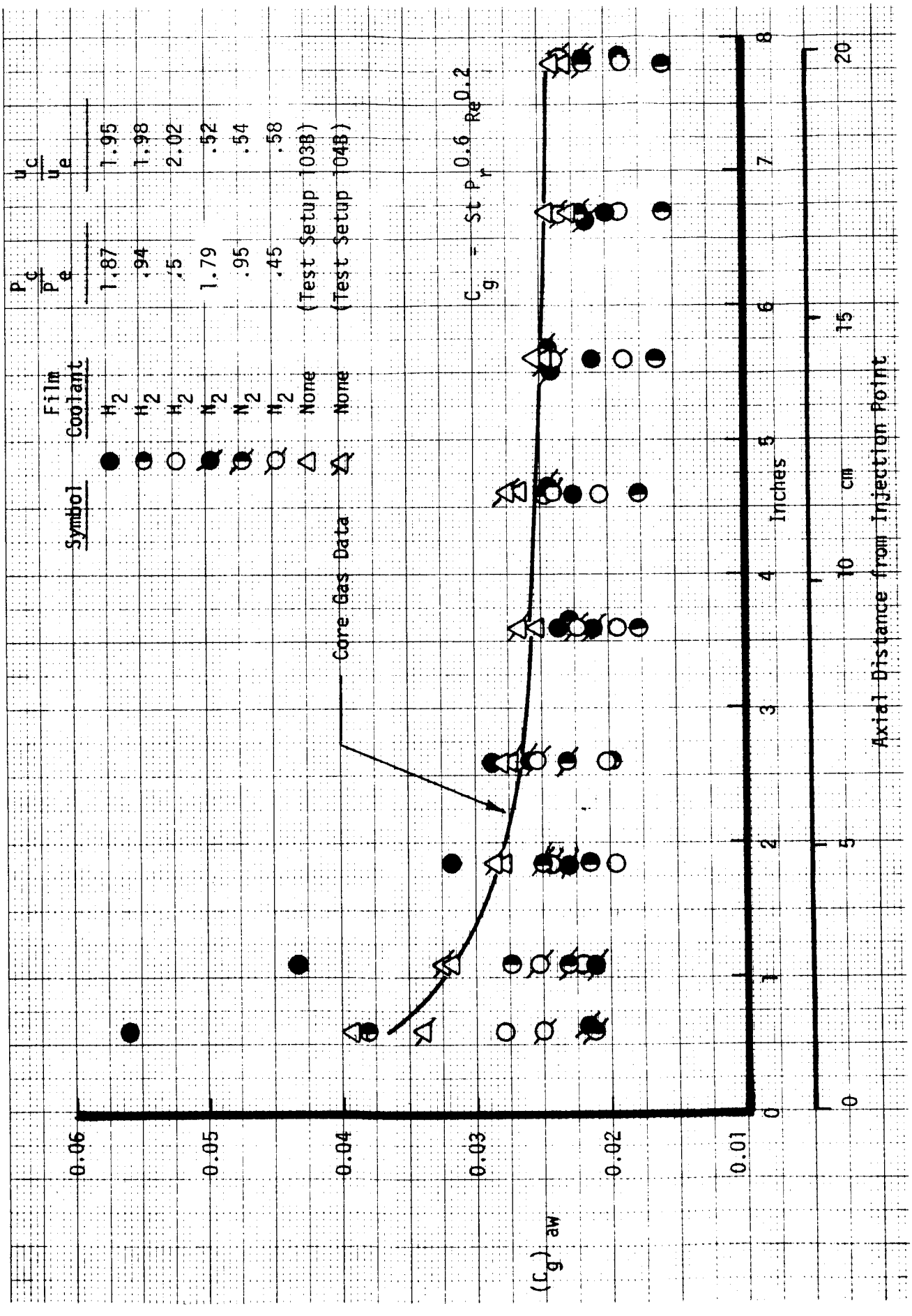

Figure 60. Constant Mach Number C_g Values, T_{aw} Reference Temperatures

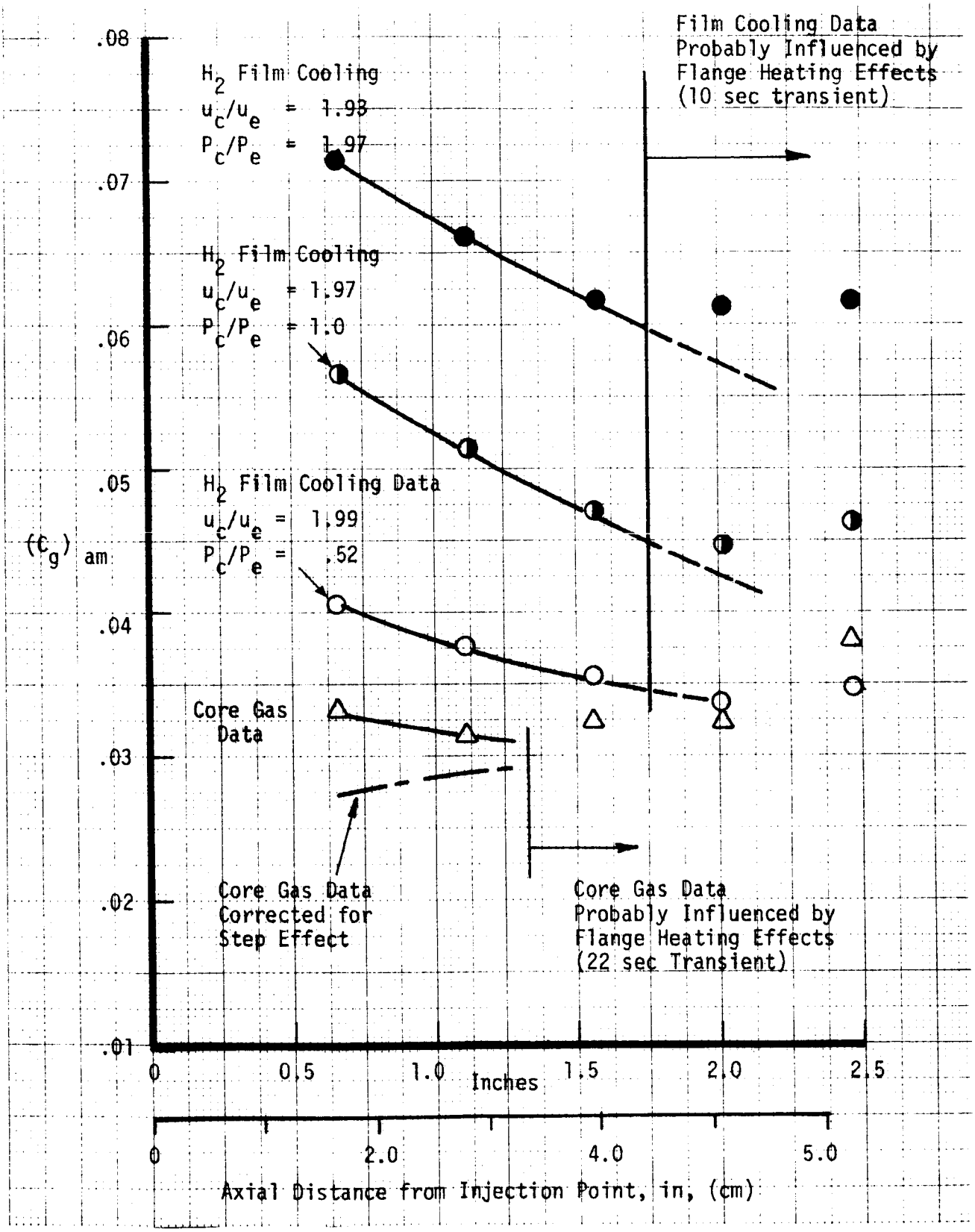

Figure 61. Variable Mach Number C_g Values

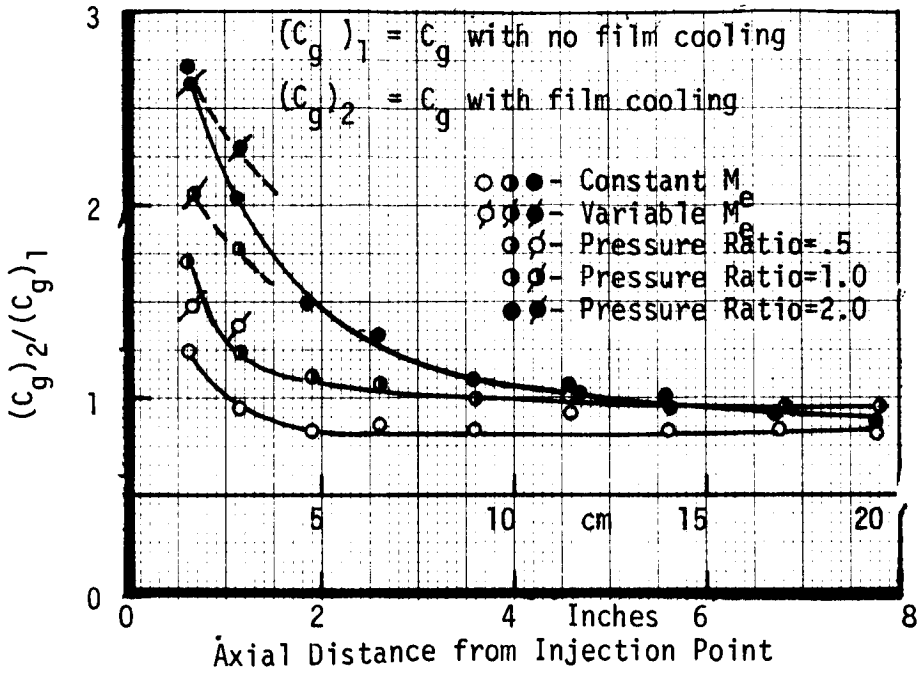

Figure 62. Injection Effect Factor Correlated with Axial Distance

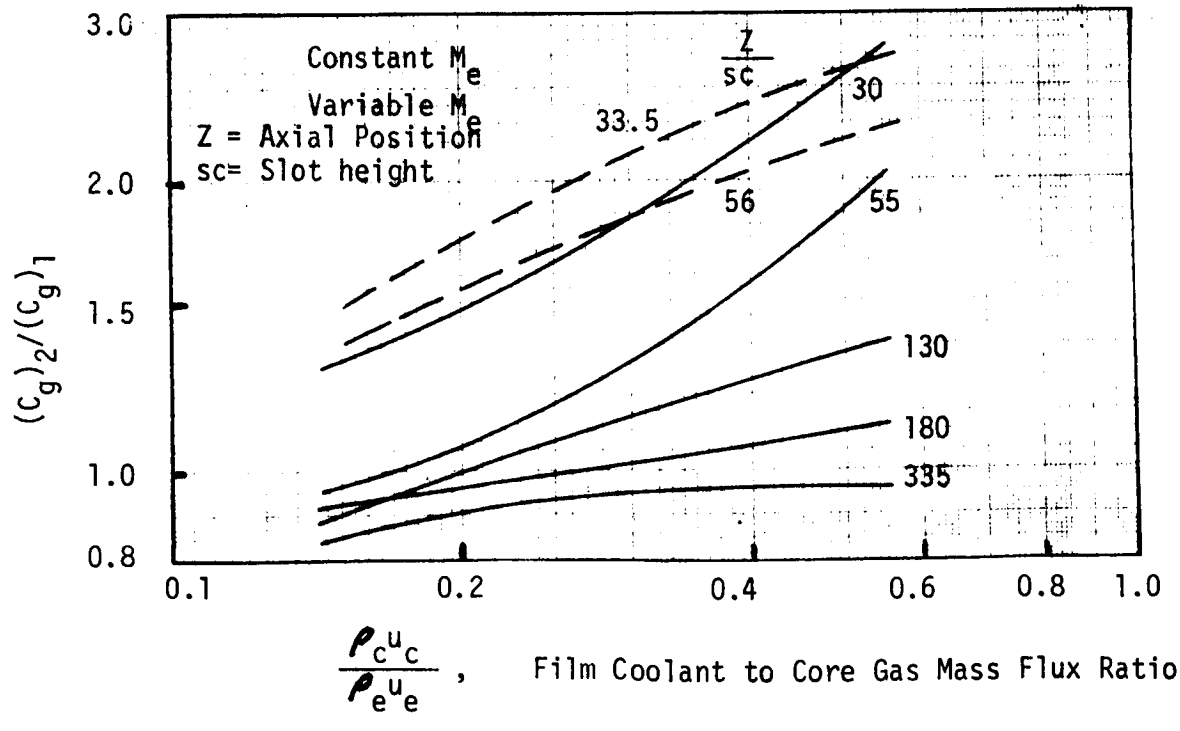

Figure 63. Injection Effect Factor Correlated with Mass Flux Ratio

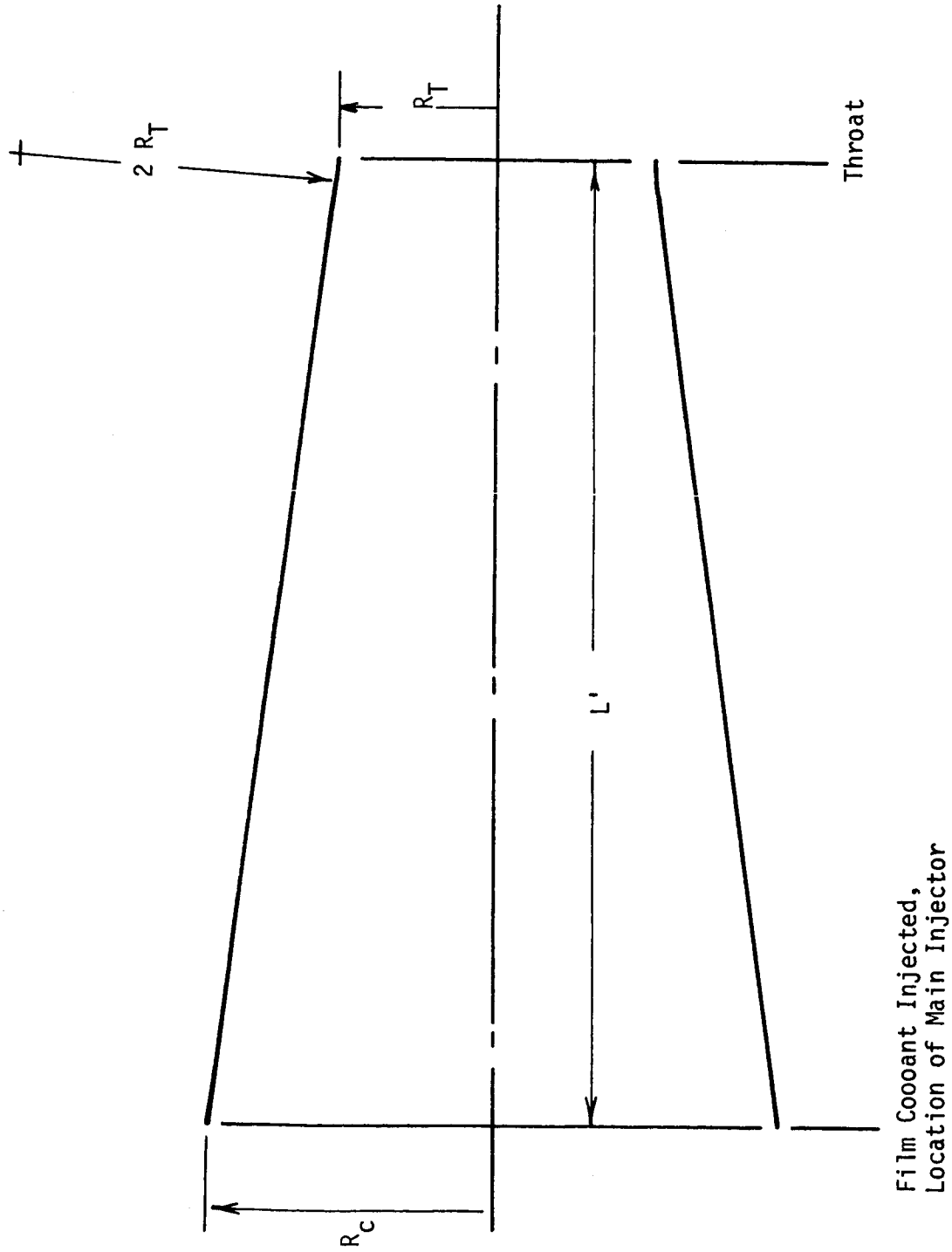

Figure 64. APS Thrust Chamber Geometry

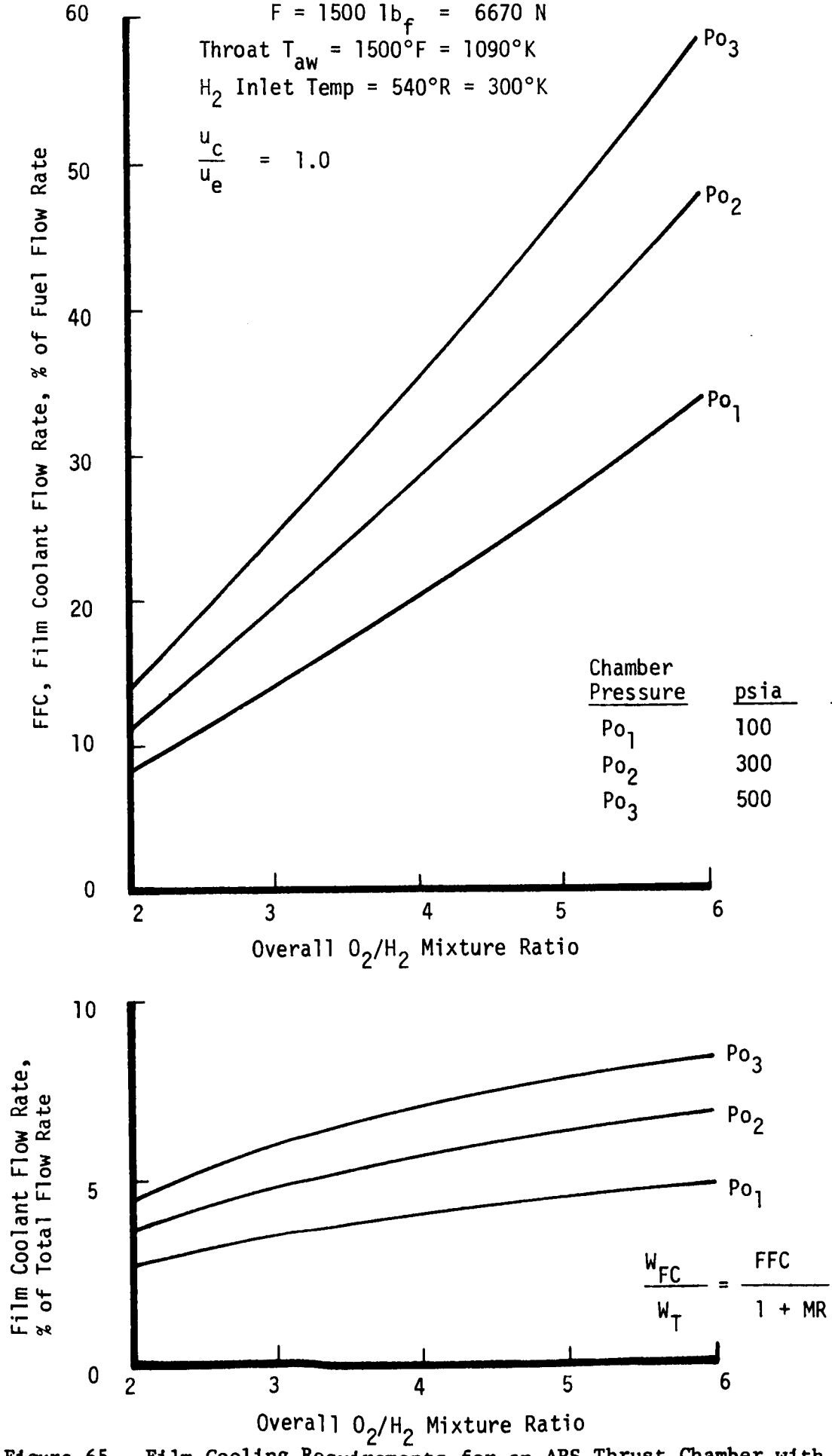

Figure 65. Film Cooling Requirements for an APS Thrust Chamber with 6670 N Thrust and 300°K Hydrogen Inlet Temperature

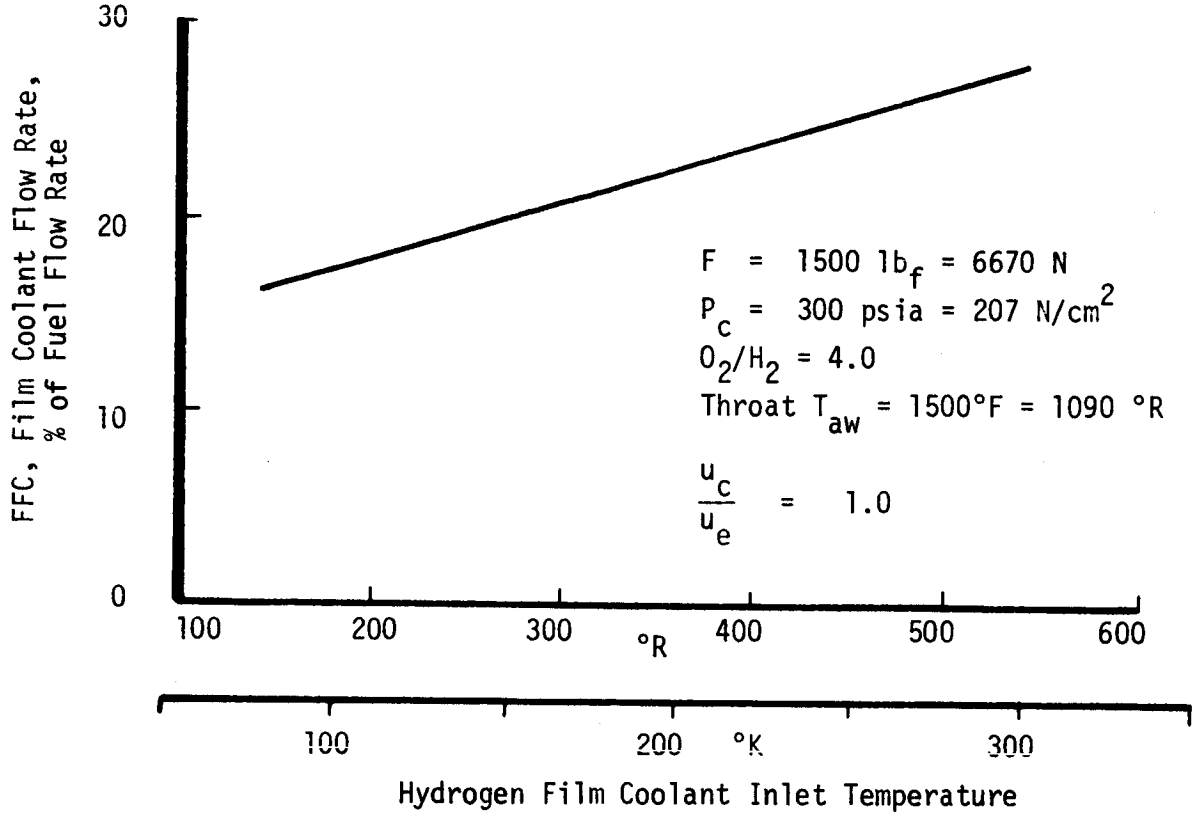

Figure 66. Effect of Inlet Temperature on Film Coolant Requirements

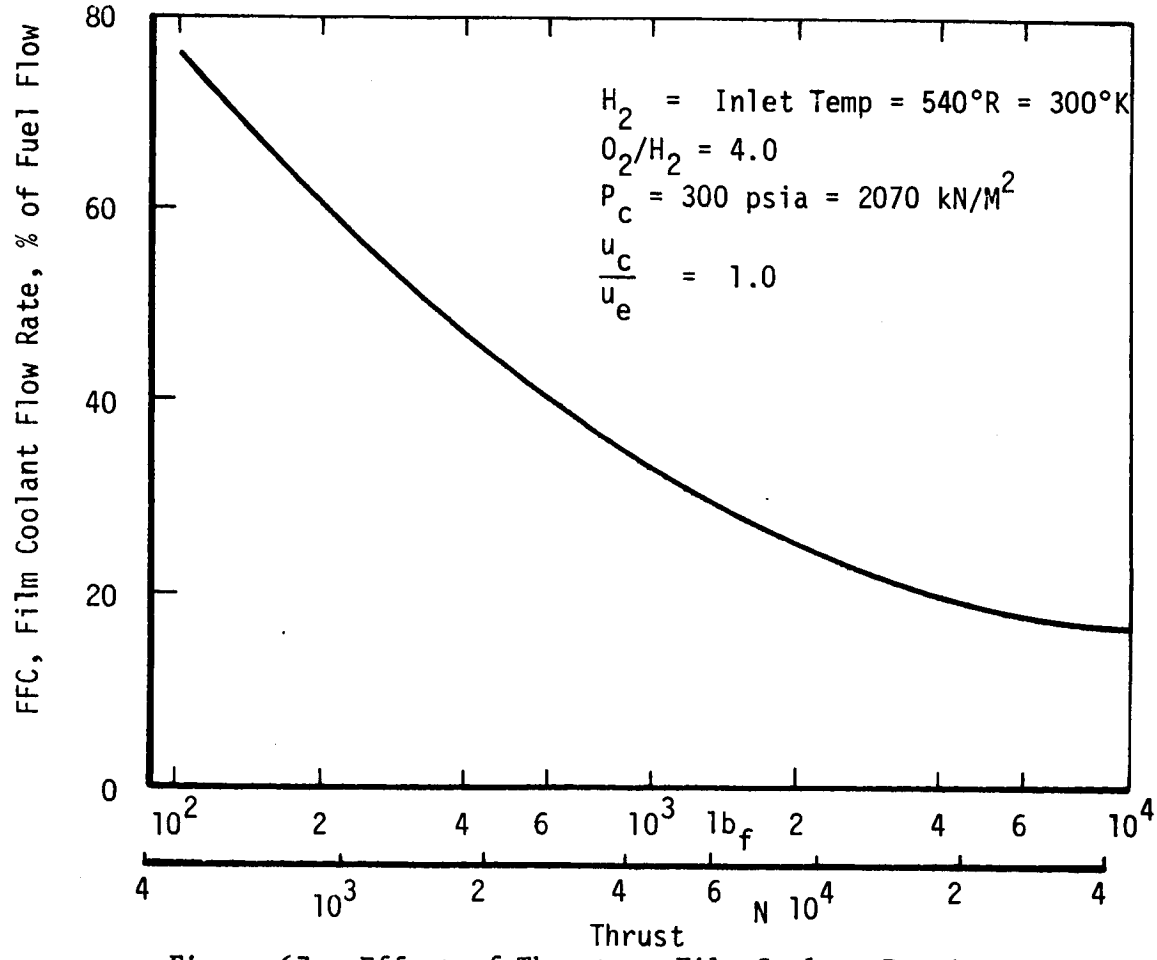

Figure 67. Effect of Thrust on Film Coolant Requirements

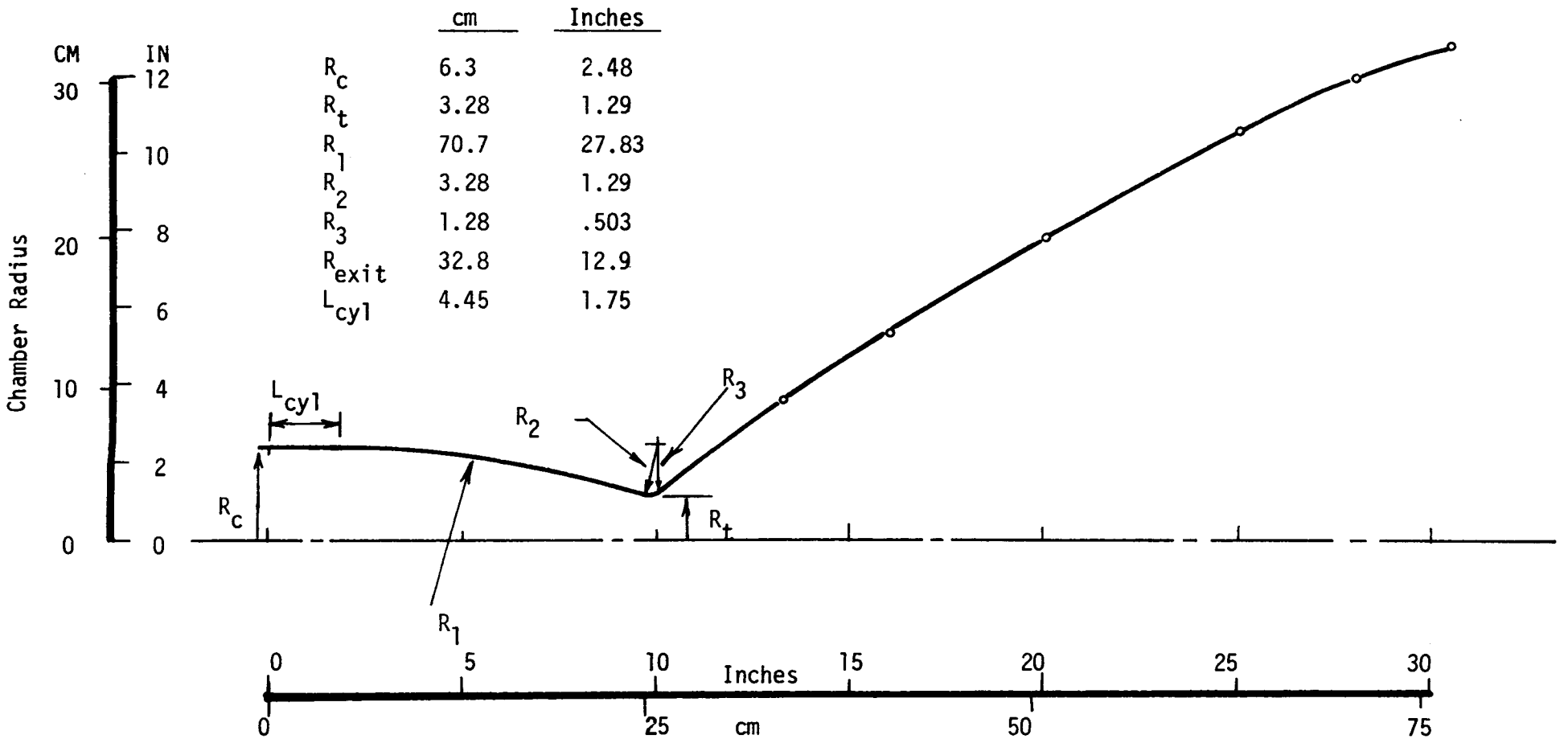

Figure 68. O_2/H_2 Space Tug Thrust Chamber Geometry

Curve	% Rated Thrust	Chamber Pressure kN/m² (psia)	O_2/H_2	Film Coolant Injection Point	Location
1	100	1310 (1900)	6.5	Injector	1.25 cm (0.5") Upstream of Throat
2	50	654 (950)	6.0	Injector	15 cm (6.0") Upstream of Throat
3	17	220 (320)	5.0	Injector	15 cm (6.0") Upstream of Throat
4	100	1310 (1900)	6.5	A/A_t = 8/1	A/A_t = 78/1
5	50	654 (950)	6.0	A/A_t = 8/1	A/A_t = 78/1
6	17	220 (320)	5.0	A/A_t = 8/1	A/A_t = 78/1

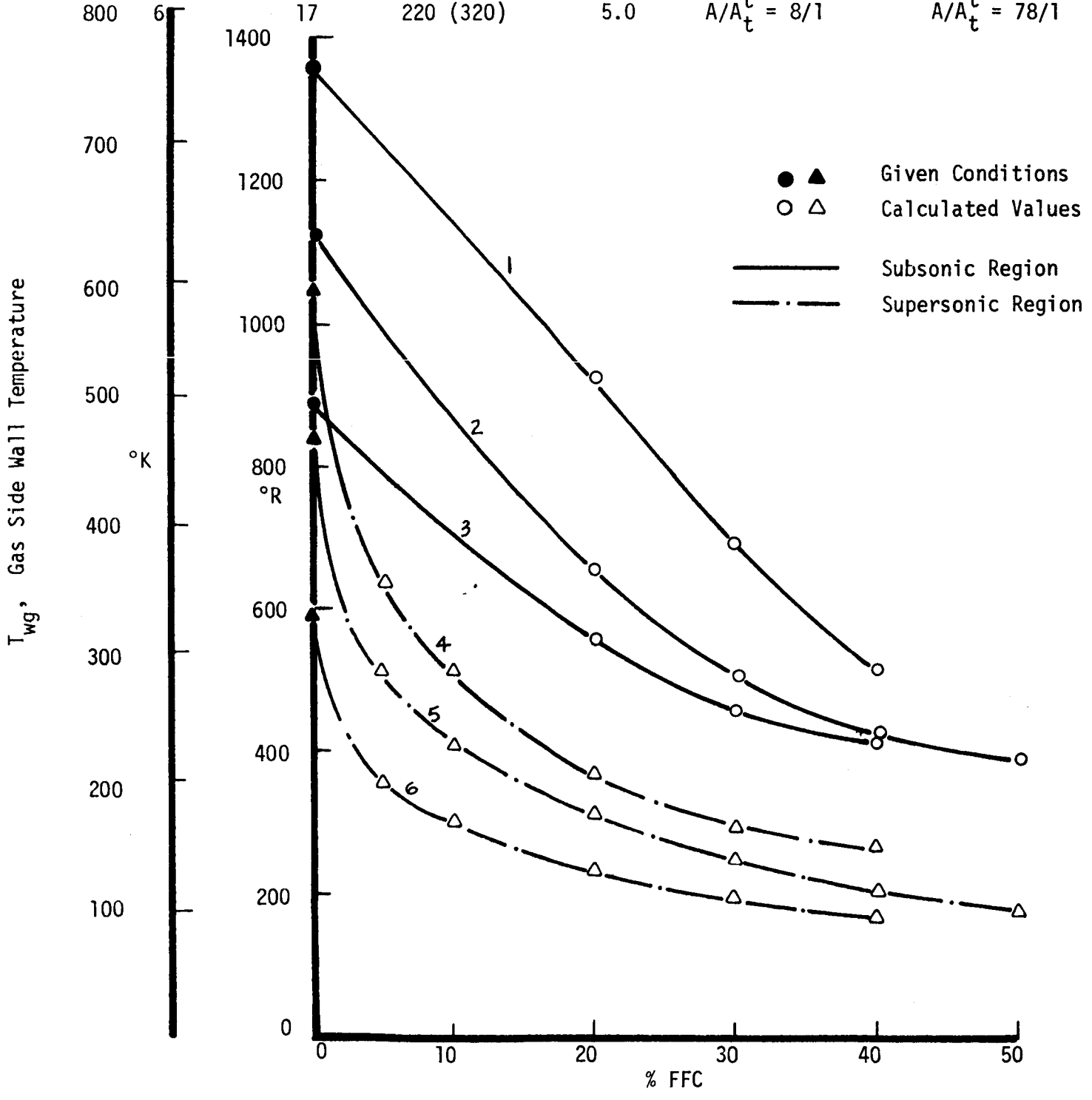

Figure 69. Estimated Wall Temperatures for a Film Cooled Space Tug Thrust Chamber

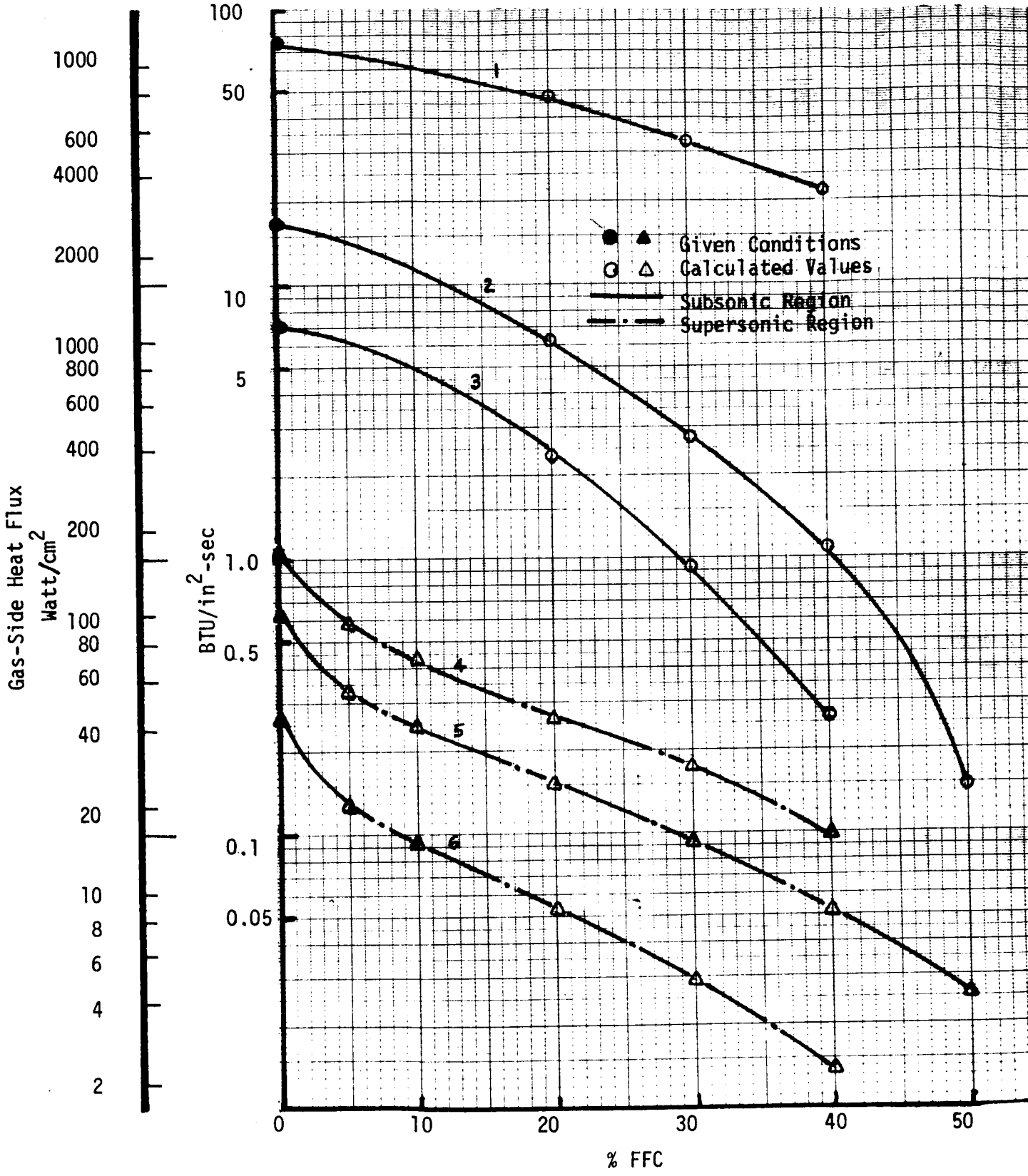

Figure 70. Estimated Heat Fluxes for a Film Cooled Space Tug Thrust Chamber

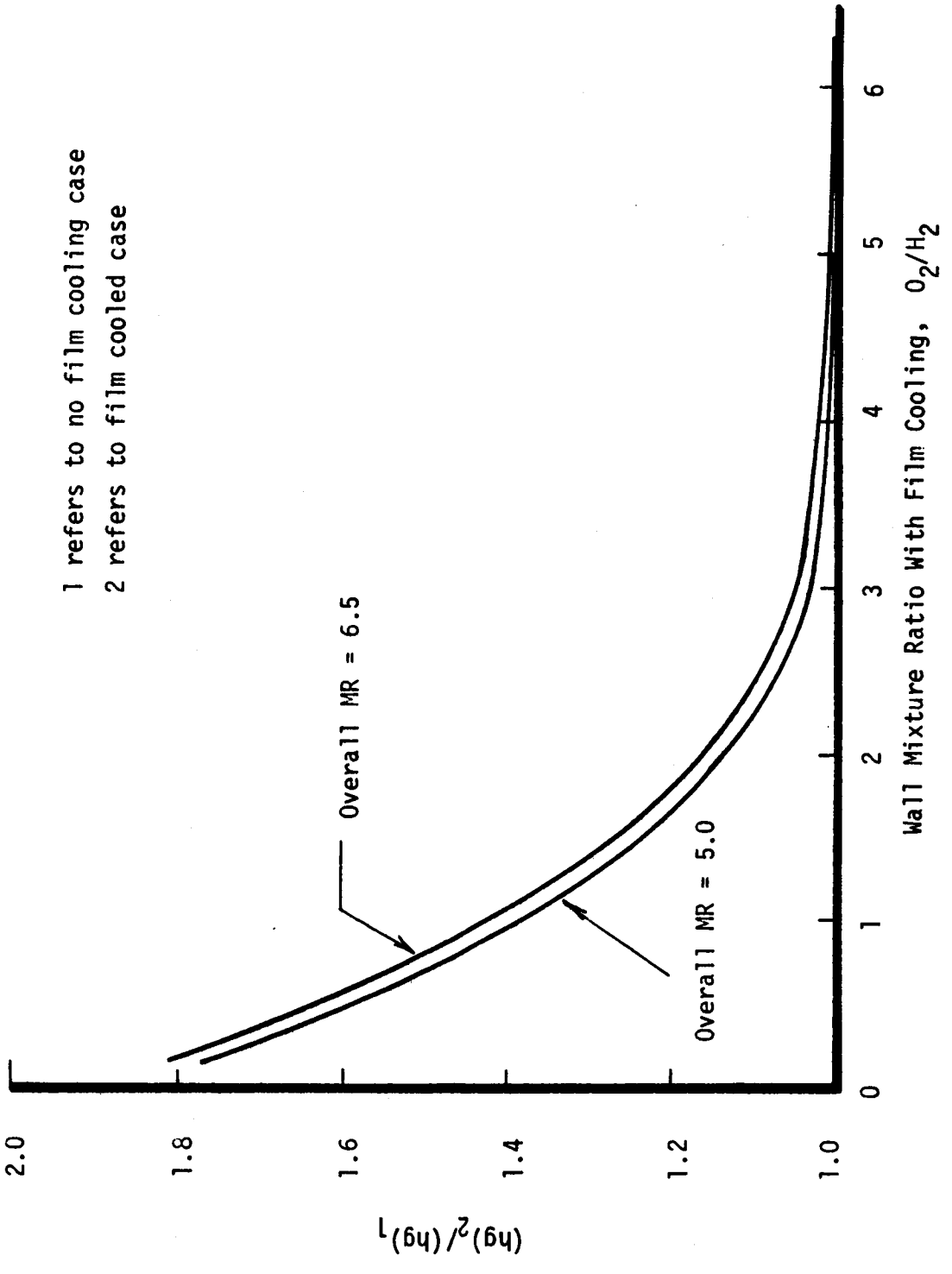

Figure 71. Effect of Wall Mixture Ratio on Heat Transfer Coefficient

APPENDIX A

DEVELOPMENT OF MODEL PARAMETERS FOR FILM COOLING IN A SUPERSONIC REGION

Appendix A

1. Shape Factor

The formulation for the profile shape factor for mixing layer flow in a supersonic region was developed from the analytical results of Reference 12, which are in excellent agreement with the adiabatic wall temperature data of Reference 10. In the downstream regime of fully-developed mixing layer profiles, the shape factor was determined from the computed concentration and velocity profiles. From its definition, Equation (10),

$$\theta = 1 - \frac{\int_0^s \left(\frac{c - c_w}{c_e - c_w}\right) \frac{u}{u_e} \, dy}{\int_0^s \frac{u}{u_e} \, dy}$$

in which s is the thickness of the mixing layer. A value of 0.485 was calculated for the fully-developed shape factor.

With this shape factor, the effectiveness in the fully-developed regime was used to establish the corresponding entrainment flow ratio W_E/W_c. For $260 \leq x/(m^{0.8} s_c) \leq 1500$, the Reference 12 effectiveness of Figure 4 is described by

$$\eta = 491 \left(\frac{X}{m^{0.8} s_c}\right)^{-1.2}$$

so that Equation (9) gives

$$W_E/W_c = \frac{1}{\eta \theta} - 1 = 0.00420 \left(\frac{X}{m^{0.8} s_c}\right)^{1.2} - 1 \qquad \text{(A1)}$$

Extrapolation of the entrainment flow ratio to zero at the coolant injection point then allowed the shape factor in the transition regime to be inferred from the effectiveness results, again using Equation (9). Figure A1 shows the above entrainment flow ratio and its extrapolation (dashed line). Figure 2 gives the resulting shape factor as a function of entrainment flow ratio; the transition

regime between Equation (11) and the fully-developed value of 0.485 is defined by $0.5 \leq W_E/W_c \leq 2.2$.

For comparison purposes and use in the $\bar{u}$ development to follow, the above procedure was also applied to the results of Reference 7. For the mass velocity ratio range of the present program, the effectiveness correlation is

$$\eta = 162 \left(\frac{x}{mh}\right)^{-1.2} \quad \frac{x}{mh} \geq 69.6$$

so that using $\theta = 0.485$ in Equation (9) gives

$$W_E/W_c = 0.0127 \left(\frac{x}{mh}\right)^{1.2} - 1 \qquad \text{(A2)}$$

in the fully-developed regime. In this case the effectiveness data indicate no transition regime, resulting in the shape factor variation with E_E/W_c shown by the dashed line in Figure 2. Extrapolation of the entrainment flow ratio back to the injection point, similar to Figure A1, was required for development of the $\bar{u}$ correlation in the next section.

Also of interest is the entrainment fraction associated with the fully-developed regime. For the configurations of References 7 and 10,

$$k = ms_c \frac{d}{dx}\left(\frac{W_E}{W_c}\right)$$

so that Equations (A1) and (A2) yield

$$k = 0.00504 \left(\frac{x}{m^{0.8} S_c}\right)^{0.2} m^{0.2} \qquad \text{Ref. 12}$$

$$k = 0.0153 \left(\frac{X}{mh}\right)^{0.2} \frac{s_c}{h} \qquad \text{Ref. 7}$$

These entrainment fractions are compared with the results of the present program in Section V,B,3.

2. Velocity Mixing Function

The velocity mixing function V (W_E/W_c) used to define the effective velocity $\bar{u}$, Equation (18), was developed from the isoenergetic wall temperature data of Reference 7 and partially confirmed by the analytical results of Reference 12. For isoenergetic injection T_{aw} differs from the freestream stagnation temperature solely due to imperfect recovery of kinetic energy, i.e.,

$$T_{o_e} - (T_{aw})_{iso} = (1 - Pr^{1/3}) (T_{o_e} - T_e) (\bar{u}/u_e)^2$$

and $\bar{u}/u_e$ is obtained directly from measurement of the isoenergetic wall temperature. Determination of the corresponding mixing function V from $\bar{u}/u_e$ by Equation (18) used the minimum $\bar{u}/u_e$ as u_c/u_e; this minimum typically occurred some distance downstream of the injection point, but well within the region of unity effectiveness. Figure A2 shows the resulting correlation of the velocity mixing function V with dimensionless axial distance; the effectiveness correlation of Reference 7 is shown for comparison and exhibits a much less rapid decay. Using the entrainment flow ratio of Equation (A2) and its extrapolation back to the injection point gave the final V (W_E/W_c) correlation shown in Figure 5.

A few values of $\bar{u}/u_e$ were also obtained from Reference 12 by solving Equation (7) using calculated values of adiabatic wall temperature and the effectiveness results of Figure 4. The corresponding mixing function values were based on u_c in the coolant slot; using the entrainment flow ratios of Figure A1 gave V (W_E/W_c). Two such points are shown on Figure 5 and agree very well with the curve developed above from Reference 7. However, $\bar{u}$ exceeded u_e at higher values of W_E/W_c, indicating negative values of V.

ENTRAINMENT FLOW RATIO AND EXTRAPOLATION FOR REF. (12)

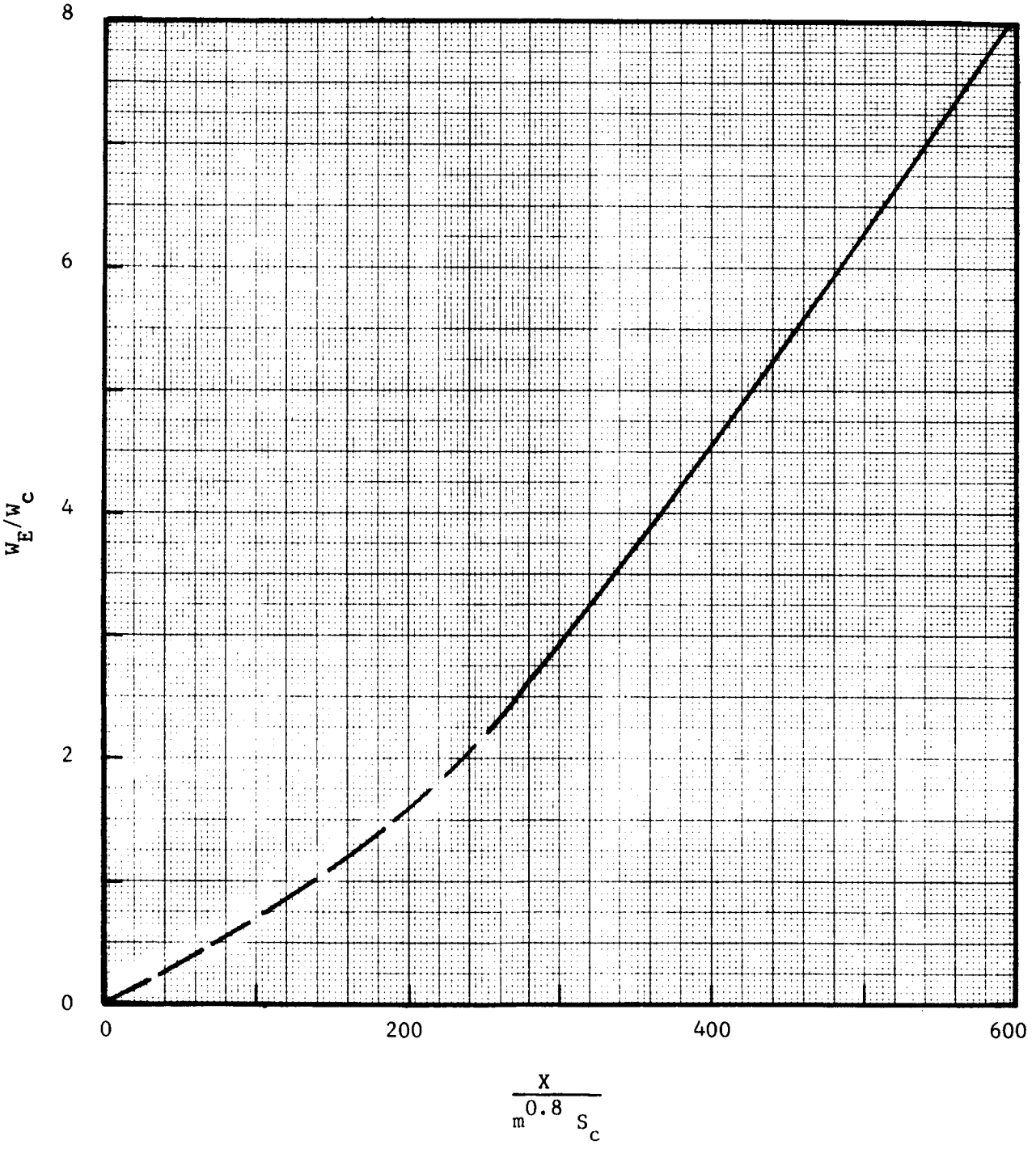

Figure A1

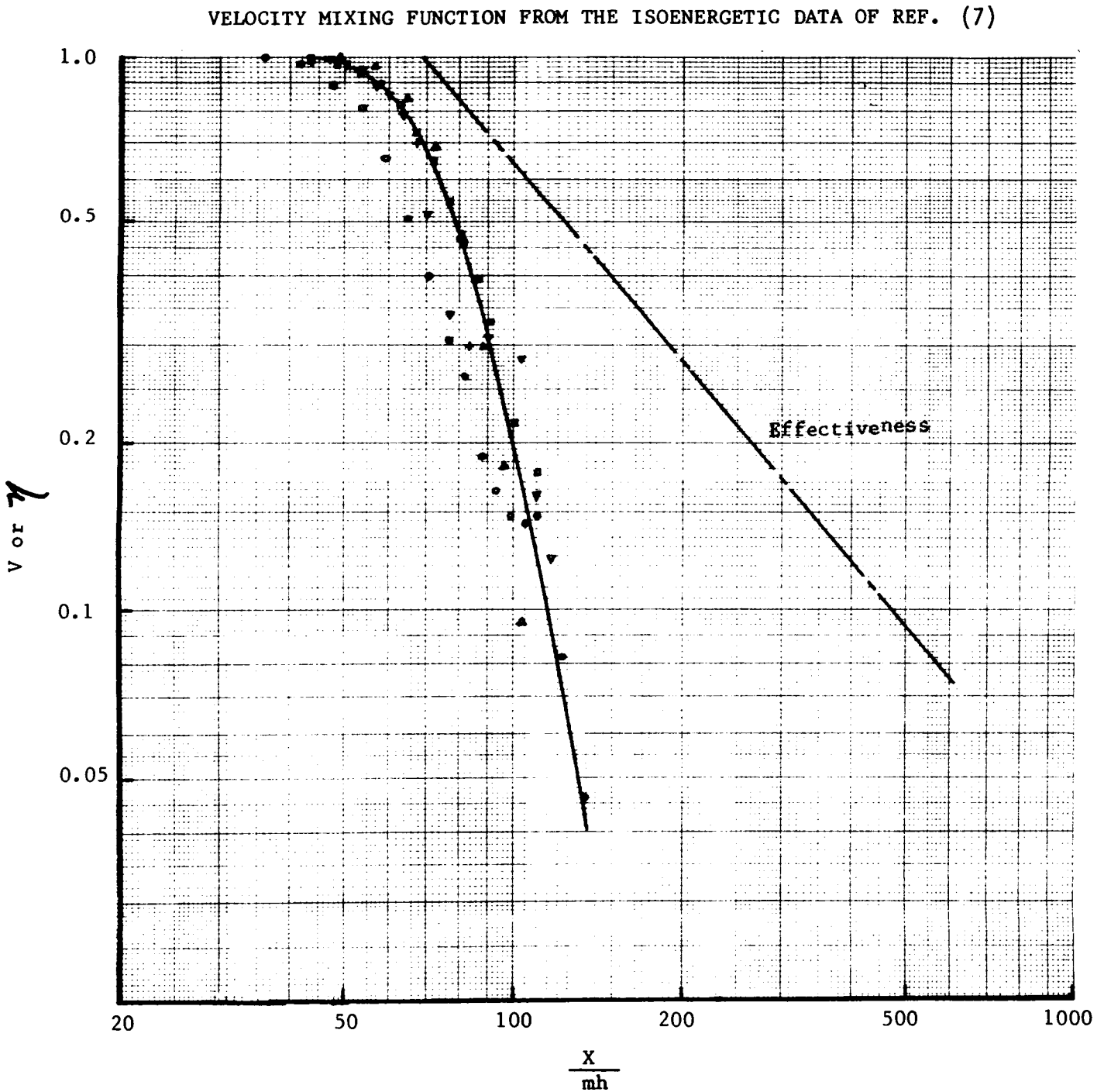
VELOCITY MIXING FUNCTION FROM THE ISOENERGETIC DATA OF REF. (7)
1.0
0.5
0.2
0.1
0.05
η or λ
Effectiveness
20
50
100
200
500
1000
X/mh

Figure A2

APPENDIX B

EXPERIMENTAL APPARATUS

Appendix B

The test components used in the film cooling tests and the film cooling test system are described in this appendix. The test components are defined as the film coolant injectors, subsonic test sections, and supersonic test sections. Other parts used in the tests are defined as part of the test system. Seals between the individual components were fabricated from Grafoil material and were crushed approximately 30% during assembly. Prior to testing, all test sections were wrapped with insulation in such a manner that a thin layer of stagnant air remained adjacent to the walls and exterior air currents could not cool the walls.

A. TEST COMPONENTS

1. Test Setup 101

The test components for Test Setup 101 consisted of the thin slot film coolant injector and the 30°-1R subsonic test section. Both of these components were residual from Contract NAS 3-14343 (Ref. 1). A sketch of the Test Setup 101 assembly is shown in Figure B1.

30°-1R Subsonic Test Section (Chamber)

Figure B2 shows the design for the 30°-1R subsonic test section (-7 configuration). The major design features are 8.9 cm (3.5-in.) cylindrical length, 30° convergence angle, and turn radii at the throat and beginning of the convergent section equal to one and two times the throat radius respectively. This component was modified slightly in that the copper electrodes used to electrically heat the cylindrical length during the Reference 1 tests were removed. The throat diameter was selected to provide a stagnation pressure of 172 N/cm^2 (250 psia) with no film cooling at the maximum available heated nitrogen flow of 0.45 kg/sec (1.0 lb/sec). A higher pressure would require smaller test sections and was, therefore, not desirable; a significantly lower pressure is not acceptable for testing with supercritical liquid film coolant as was done on Contract NAS 3-14343. The chamber diameter of 3.094 cm (1.218-in.) gives a contraction ratio of 4.0.

The test section was fabricated from Hastelloy-X tubing (all other test sections were stainless steel). The final wall thickness range was 0.048-0.051 cm (0.19-0.020 in.). Thermocouples were positioned on the test section as indicated in Table BI. The thermocouple junctions on this test section and all other test sections were formed by spot welding 0.0076 cm (0.003-in.) diameter chromel and alumel wires directly to the test section walls.

Thin Slot Subsonic Film Coolant Injector

The thin slot subsonic film coolant injector is similar to the thick slot design shown in Figures B3, B4, and B5, except that the slot height is 0.038 cm (0.015-in.) and the metering channel width is 0.058 cm (0.023-in.). Figures B6 and B7 show photographs of the inner and outer rings of the thin slot injector before final brazing. These photographs show the key internal design features of both the thin and thick slot injectors: the tapered ribs of the film coolant slot on the inner ring, and the inlet deflectors and metering channels for flow distribution control on the outer ring. The hole in the foreground of Figure 8 is the manifold instrumentation port. Figure B8 provides a closeup view of the complete injector showing the 0.038 cm (0.015-in.) slot and the ends of the tapered ribs.

2. Test Setup 102

The Test Setup 102 components were very similar to the Test Setup 101 components. They consisted of the thick slot film coolant injector, and the 30°-2R subsonic test section. A sketch of Test Setup 102 is shown in Figure B1 and a photograph of the assembly is given as Figure B9.

Thick Lip Subsonic Film Coolant Injector

The thick slot, subsonic film coolant injector design is shown in detail in Figures B3, B4, and B5. Particular care was taken to provide a uniform flow distribution to each channel through the use of deflectors at each inlet, and

0.051 cm (0.020-in.) deep metering slots for pressure drop control upstream of each channel. Tapered ribs provide a uniform coolant flow at the slot exit. Electrical discharge machining was used to fabricate the unit. The internal design is similar to the thin slot design described for Test Setup 101. A closeup view of the injection slot is shown in Figure B10.

30°-2R Subsonic Test Section

The 30°-2R subsonic test section is also depicted in Figure B2 (-9 configuration). The design of this component is identical to the 30°-1R test section design except for the turn radii at the throat and start of convergence which are twice the radii of the 30°-1R design. The material was stainless steel. The final wall thickness was 0.051-0.053 cm (0.020-0.021-in.). Thermocouple locations are indicated in Table BI.

3. Test Setups 103A and 103B

The test components for this test setup consisted of:

(a) the thick slot subsonic injector (see Test Setup 102),
(b) the 15°-2R subsonic test section,
(c) the cylindrical supersonic injector, and
(d) the cylindrical supersonic test section.

A sketch of Test Setups 103A and 103B is shown in Figure B11 and a photograph of the assembled components is shown in Figure B12.

15°-2R Subsonic Test Section

The 15°-2R subsonic test section design is shown as the -11 configuration on Figure B2. In the subsonic region, the design is similar to the 30°-2R design except that the convergence angle is 15°. The nozzle contour downstream of the

throat was designed to produce uniform core gas flow with M = 2.5 at the supersonic film coolant injection point. The final wall thickness was 0.0635 cm (0.025-in.). Thermocouple locations are noted in Table BI.

Cylindrical Supersonic Film Coolant Injector

The design of the cylindrical supersonic injector is shown in Figures B13, B14, and B15. A 0.051 cm (0.020-in.) slot height was chosen for the supersonic film coolant injectors. This value was chosen by considering two factors: (1) the relative proportions of "lip" thickness and slot height (the "lip" is the wall thickness which separates film coolant and core gas streams just upstream of the film coolant injection point), and (2) the length required in the constant Mach number test section to measure an adiabatic wall temperature increase of about 370°K (200°F). Practical fabrication considerations indicated a minimum lip thickness of about 0.051 cm (0.020-in.) and it was felt that the film coolant slot should be at least as thick as the lip.

A nozzle area ratio of 1.5 was chosen for the supersonic film coolant injector nozzles (shown in Figure B15). This is about the minimum value consistent with the desire to provide uniform outlet Mach number for the anticipated fabrication tolerances. The corresponding nominal outlet Mach number is 1.86. The injection nozzle contour was based upon the supersonic film cooling injector nozzles successfully tested at ALRC and reported in Reference 2.

Cylindrical Supersonic Test Section

The cylindrical supersonic test section design is shown in Figure B16 and the thermocouple locations are listed in Table B1. The final wall thickness was 0.051 cm (0.020-in.). The design core flow Mach number at the test section inlet was 2.5. The design goal for this unit was to maintain a nearly constant core flow Mach number. A cylindrical contour was chosen for the test section in order to simplify fabrication. Static pressure measurements indicated that the core Mach number at the downstream end of the test section ranged from 2.44

(no supersonic injection) to 2.23 (supersonic injection) at pressure ratio of 2.0. This variation is considered acceptable. The cylindrical supersonic test section was designed to discharge directly to the atmosphere since at the nominal chamber pressure of 250 psia, the flow leaving the test section had expanded to about atmospheric pressure.

Selection of the test section length was based on ALRC supersonic film cooling data (Ref. 2), since these data were obtained with a similar injection slot geometry. Several methods of generalizing these results for application to different velocity and mass velocity ratios were investigated, as shown by the predicted adiabatic wall temperature distributions of Figure B17 for hydrogen film cooling. The curve on the left uses the ALRC data in the form of entrainment fraction vs axial distance; since the selected slot height (S_c) is in the range of the Reference 2 slot, this is equivalent to correlating entrainment fraction with X/S_c. The curve on the right is based on the correlation parameter of Reference 10, while the central curve is based on al alternate correlation parameter which includes the mass velocity ratio with an exponent of unity instead of 0.8 and which discards some questionable ALRC data. The adiabatic wall temperature distributions shown on Figure B17 are based on pressure matching using a coolant injector nozzle area ratio of 1.5.

A wall temperature change of about 370°K (200°F) was considered desirable; a smaller value compromises the accuracy of the temperature distribution measurement, while a larger value results in too much effectiveness data below the range of interest for rocket engine applications. For this temperature change, Figure B17 indicates an X/S_c of 175 for the entrainment fraction correlation and 440 for the more realistic of the two effectiveness correlations. A design value of 400 was selected to assure an adequate length for the test section, and the combination of 0.051 cm (0.020-in.) slot height and 20.4 cm (8-in.) test section length was chosen as a good design compromise which maintained reasonable slot height and length values.

4. Test Setups 104A and 104B

The test components consisted of:

(a) the thin slot subsonic injector (see Test Setup 101),

(b) the 15°-2R subsonic test section (see Test Setups 103A and 103B),

(c) the cylindrical supersonic injector (see Test Setups 103A and 103B), and

(d) the cylindrical supersonic test section (see Test Setups 103A and 103B).

A photograph of Test Setups 104A and 104B is shown in Figure B18.

5. Test Setups 105A and 105B

The components which comprised this test assembly were:

(a) a conical subsonic test section,

(b) a conical subsonic film coolant injector,

(c) a conical supersonic test section,

(d) a conical supersonic film coolant injector, and

(e) a cylindrical diffuser tube.

A sketch of the Test Setups 105A and 105B assembly is shown in Figure B19 and a photograph of the test setup mounted on the film cooling test system is shown as Figure B20.

Conical Subsonic Test Section

To provide data relative to the effects of acceleration without turning, the design of the conical chamber fabricated on Contract NAS 3-14343 was modified to eliminate the short cylindrical section on its upstream end (during the previous tests, this test section was tested with the thick slot subsonic injector

Appendix B

Conical Supersonic Film Coolant Injector

The conical supersonic film coolant injector design is shown in Figure B26. This design was established by projecting the cylindrical supersonic design onto the cone angle defined by the conical supersonic test section.

Cylindrical Diffuser Tube

The conical supersonic test section was designed to discharge into a straight duct diffuser consisting of a moderate length cylinder (L/D ratio = 12) which is attached directly to the exit of the test section. The diffuser was required in order to maintain attached, shock-free flow in the conical supersonic test section. The diffuser tube design, based on the data of Reference 17, is shown in Figure B27.

B. FILM COOLING TEST SYSTEM

A schematic diagram of the film cooling test system is shown as Figure B28. This system is basically the same as the NAS 3-14343 system (Ref. 1) except that a supersonic film coolant circuit was incorporated.

TABLE BI

THERMOCOUPLE POSITIONS

Integer Values Given are Thermocouple Numbers
Z = Axial Position from Injection Point

Part 1: Test Setup 101

Thin Slot Subsonic Film Coolant Injector
30°-1R Subsonic Test Section
N_2 Inlets at 120° and 300°

Position, CW Degrees from Vertical					
0°	90°	180°	270°	Z/S_c	
1		2		37.5	
3		4		96.7	
5				143.3	
7		8		190.	
9		10		230.	(End of Cylinder)
11		12		253.3	(End of Turn)
13	25	14	26	280.	(Start of Throat Turn)
15		16		290.	(Throat)
--	27	--	28	296.7	(End of Throat Turn)
17				333.3	
Channel Centerline	Rib	Channel Centerline	Rib		

Part 2: Test Setup 102

Thick Slot Subsonic Film Coolant Injector
30°-2R Subsonic Test Section

Position, CW Degrees from Vertical					
60°	150°	240°	330°	Z/S_c	
H_2 Inlet (1)	2	H_2 Inlet (1)	1	13.3	
	4		3	25	
			5	36.7	
	8		7	48.3	
	10		9	60	(End of Cylinder)
	12		11	67.5	(End of Turn)
25	14	26	13	71.2	(Start of Throat Turn)
	16		15	75.8	(Throat)
27	--	28		77.8	(End of Throat Turn)
			17	85	
Rib	Channel Centerline	Rib	Channel Centerline		

(1) Inlets to subsonic film coolant injector

TABLE BI (cont.)

Part 3: Test Setup 103

Thin Slot Subsonic Film Coolant Injector
15°-2R Subsonic Test Section
Cylindrical Supersonic Film Coolant Injector, Cylindrical Supersonic Test Section

Position, CW Degrees from Vertical					
60°	150°	240°	330°	Z/S_c	
H_2 Inlet (1)	2	H_2 Inlet (1)	1	12.2	15°-2R Subsonic Test Section
	4		3	23.8	
	6		5	35.5	
				47.2	
	10		9	58.8 (End of cylinder)	
	12		11	64.3 (End of Turn)	
	14	25	13	78.8 (Start of Throat Turn)	
	16		15	81. (Throat)	
	--	27		83. (End of Throat Turn)	
	18		17	92.2	
	20		19	105.5	
	Channel Centerline	Rib	Channel Centerline		
	32		31	30.	Cylindrical Supersonic Test Section
49	34	50	33	55.	
			35	92.5	
	38		37	130.	
	40		39	180.	
			41	230.	
	44		43	280.	
	46			335.	
	48		47	390.	
Rib Between Channels 6, 7	Channel 2 Centerline	Rib Between Channels 15,16	Channel 11 Centerline		

(1) Inlets to subsonic film coolant injector.
(2) H_2 inlets to cylindrical supersonic injector at 0° and 180°.

TABLE BI (cont.)

Part 4: Test Setup 104

Thin Slot Subsonic Injector
Cylindrical Supersonic Injector, Cylindrical Supersonic Test Section

Position, CW Degrees from Vertical						
60°	150°	200°	240°	330°	Z/S_c	
		T_{IO}				15°-2R[1] Subsonic Test Section
	2	(Film Coolant Outlet Temp.)		1	12.2	
					23.8	
	6			5	35.5	
					47.2	
22	10		21	9	58.8	(End of Cylinder)
	12			11	64.3	(End of Turn)
	14		25	13	78.8	(Start of Throat Turn)
	16			15	81.	(Throat)
			27		83.	(End of Throat Turn)
	20			19	105.5	
Channel Centerline	Rib	Channel Centerline	Channel Centerline	Rib		
						Cylindrical[2] Supersonic Test Section
	32			31	30.	
49	34			33	55.	
				35	92.5	
	38			37	130.	
51	40			39	180.	
	42			41	230.	
	44			43	280.	
				45	335.	
	48			47	390.	
Rib Between Channels 6, 7	Channel 2 Centerline			Channel 11 Centerline		

(1) N_2 inlets to subsonic film coolant injector at 120° and 300°.

(2) N_2 inlets to supersonic film coolant injector at 0° and 180°.

TABLE BI (cont.)

Part 5: Test Setup 105

Thin Slot Conical Subsonic Injector, Conical Subsonic Test Section
Conical Supersonic Injector, Conical Supersonic Test Section

Position, CW Degrees from Vertical							
30°	40°	90°	120°	210°	300°	Z/S_c	
			H_2 Inlet		H_2 Inlet		Conical Subsonic Test Sectio
1				2		8.83	
3			13	4	14	18.8	
5				6		28.8	
7			15	8	16	38.8	
9				10		48.8	
11			17	12	18	58.8	
Channel 5			Channel 11	Channel 14	Channel 10		

Note: All above thermocouples approximately half-way between rib and channel centerline.

		H_2 Inlet	H_2 Inlet		Conical Supersonic Test Sectio
31	21	32		33.5	
33	22	34		56.	
35	23	36		78.5	
37	24	38		101.	
39	25	40		123.5	
Near CL Channel 5	Rib Between Channels 2, 3	Near CL Channel 1			

Part 6: Test Setup 106

Slot Conical Supersonic Injector
Conical Supersonic Test Section

Position, CW Degrees from Vertical				
40°	90°	120°	300°	Z/S_c
		N_2 Inlet	N_2 Inlet	
31	21	32		33.5
33	22	34		56.
35	23	36		78.5
37	24	38		101.
39	25	40		123.5
Near CL Channel 5	Rib Between Channels 2, 3	Near CL Channel 1		

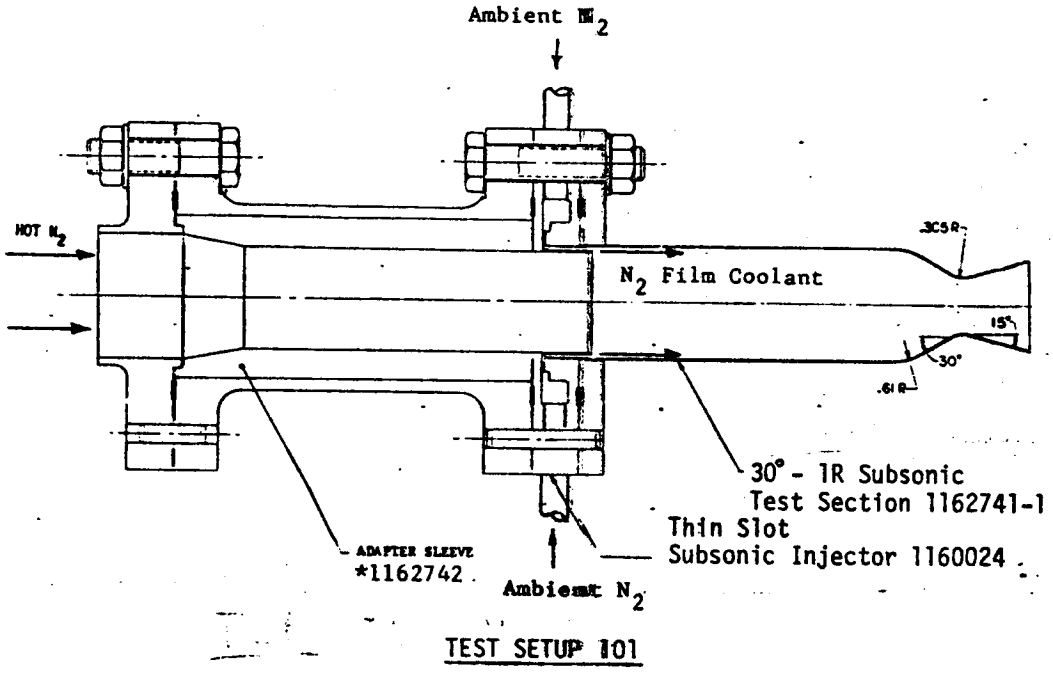

TEST SETUP 101

* Indicates ALRC Drawing Number

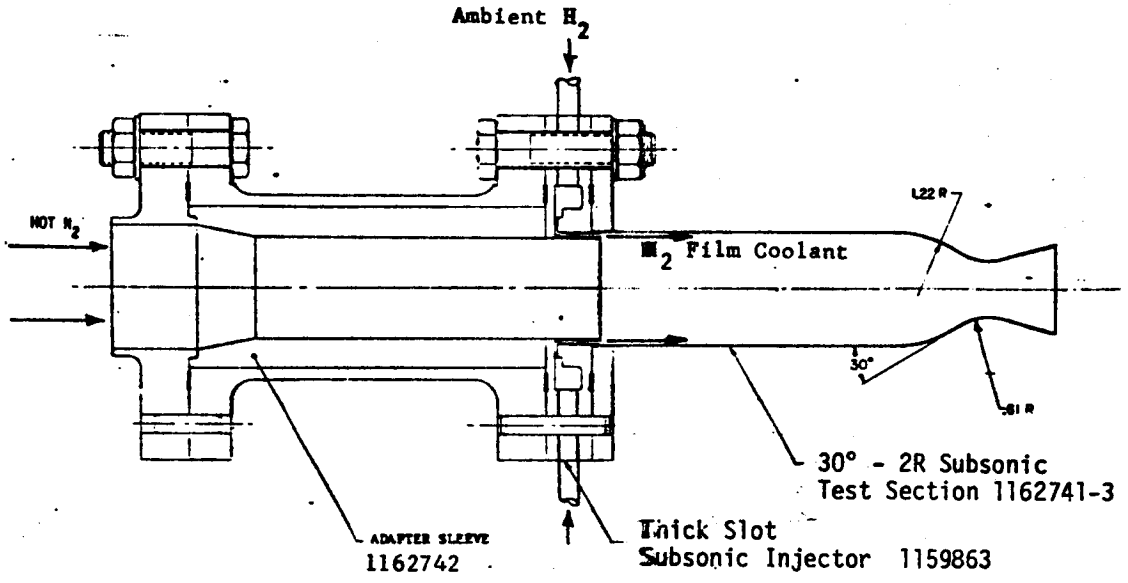

TEST SETUP 102

FIGURE B-1. SKETCHES OF HARDWARE ASSEMBLIES FOR TESTS 101 AND 102

THIS DOCUMENT AND THE DATA DISCLOSED HEREIN OR HERE
DATA IS NOT TO BE REPRODUCED, USED OR DISCLOSED IN WHOLE
OR IN PART TO ANYONE WITHOUT THE PERMISSION OF AEROJET
GENERAL CORPORATION

TABULATION BLOCK					
DASH NO.	A RADIUS	B RADIUS	C REF	D° ±0°15'	E REF
-7	.603 .610 REF	.305 REF	1.87	30°0' REF	1.10
-9	1.213 1.220	.610	2.152 2.154	30°0'	1.14
-11	SEE SHEET 2				

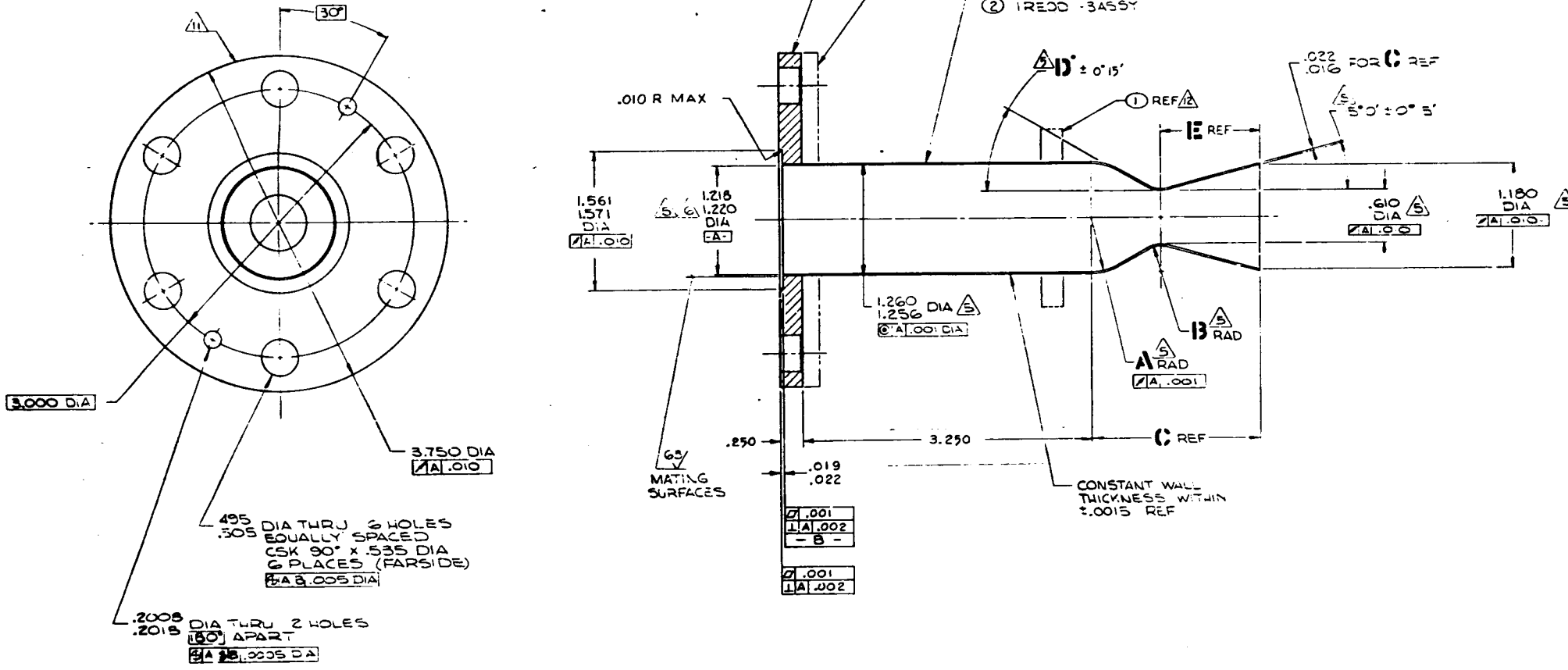

FIGURE B2. CYLINDRICAL SUBSONIC TEST SECTION DESIGNS, ALRC P/N 1162741 (Sheet 1 of 2)

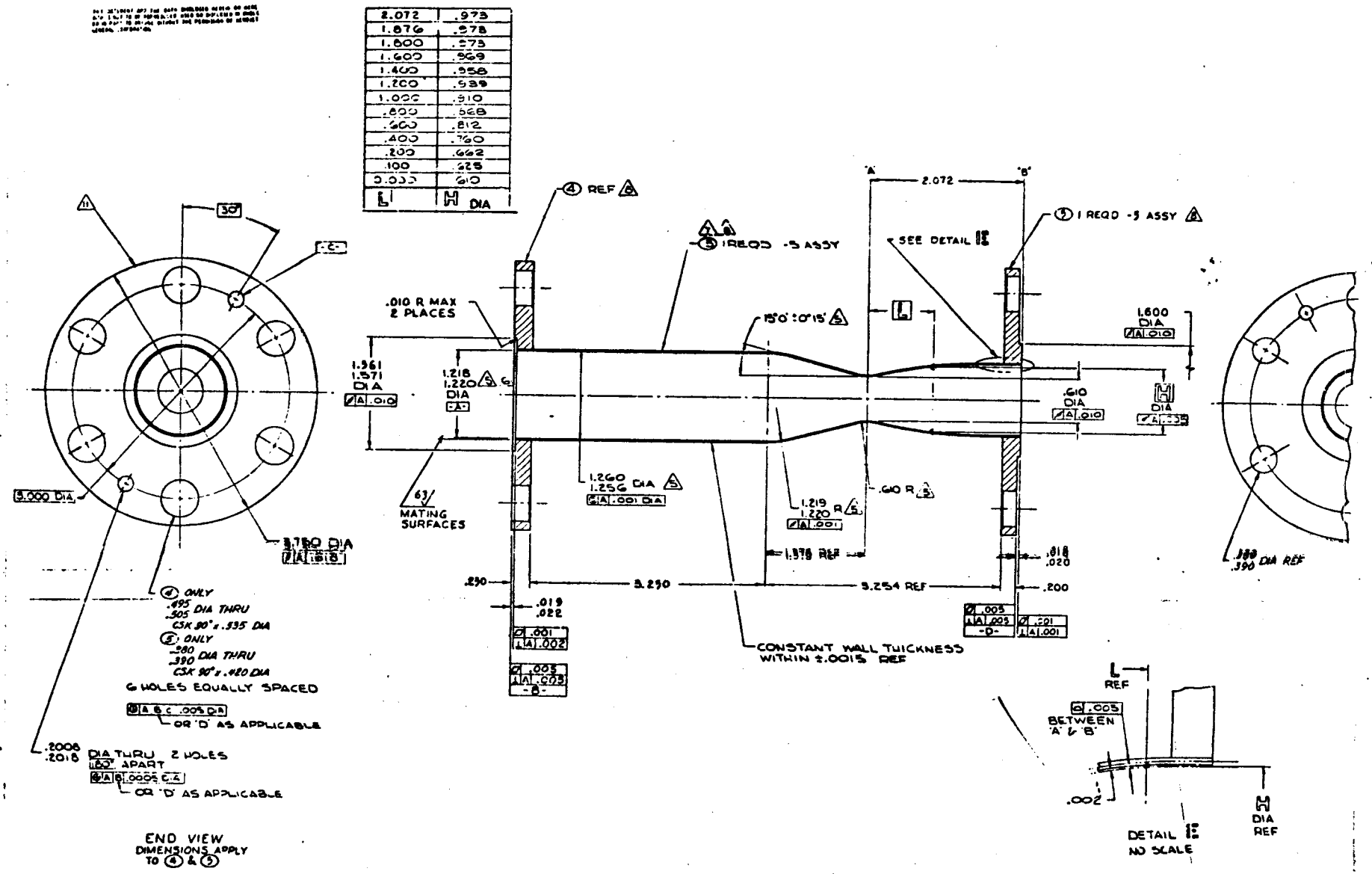

FIGURE B2. CYLINDRICAL SUBSONIC TEST SECTION DESIGNS, ALRC P/N 1102741 (Sheet 2 of 2)

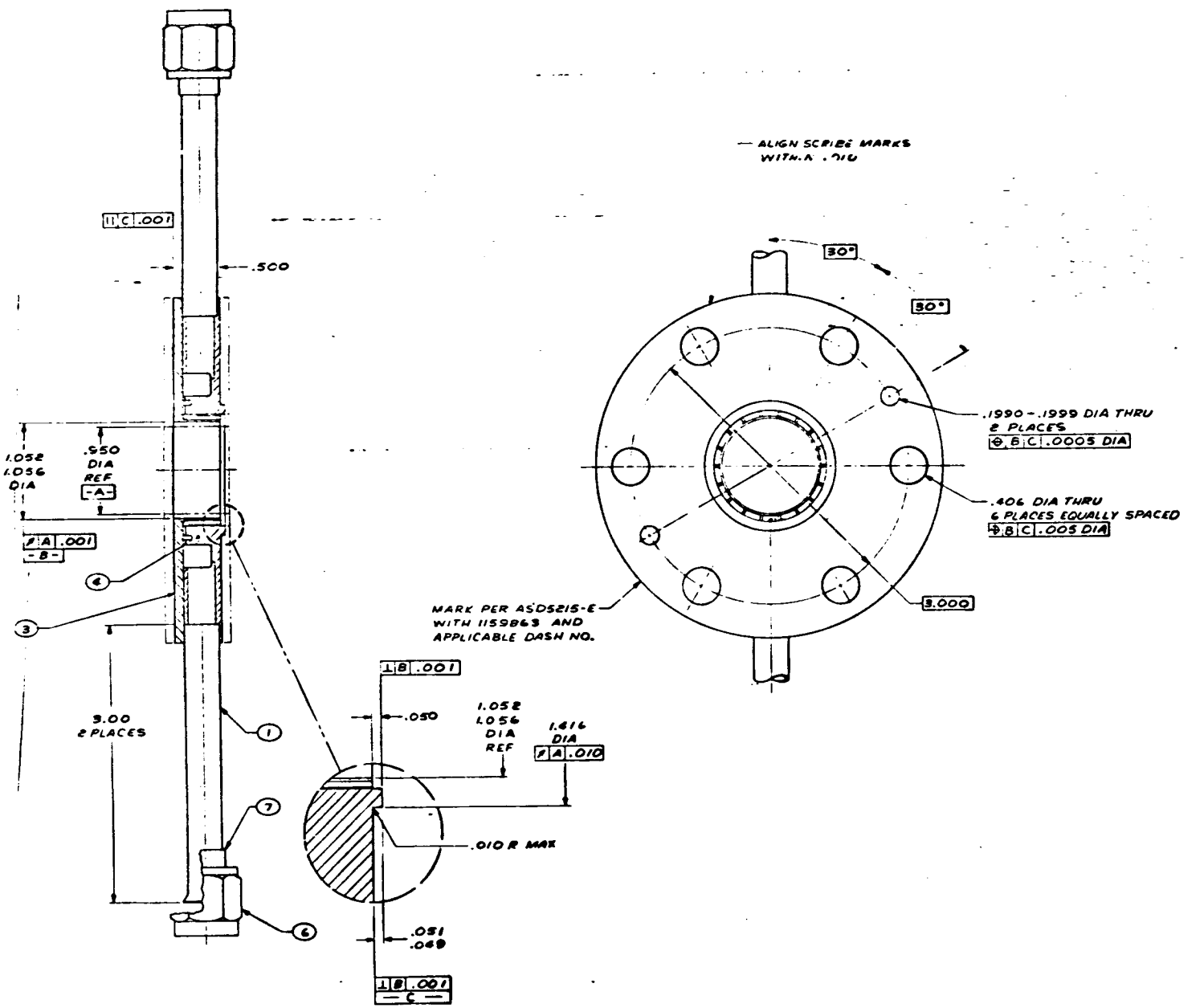

FIGURE B3. THICK SLOT FILM COOLANT INJECTOR ASSEMBLY

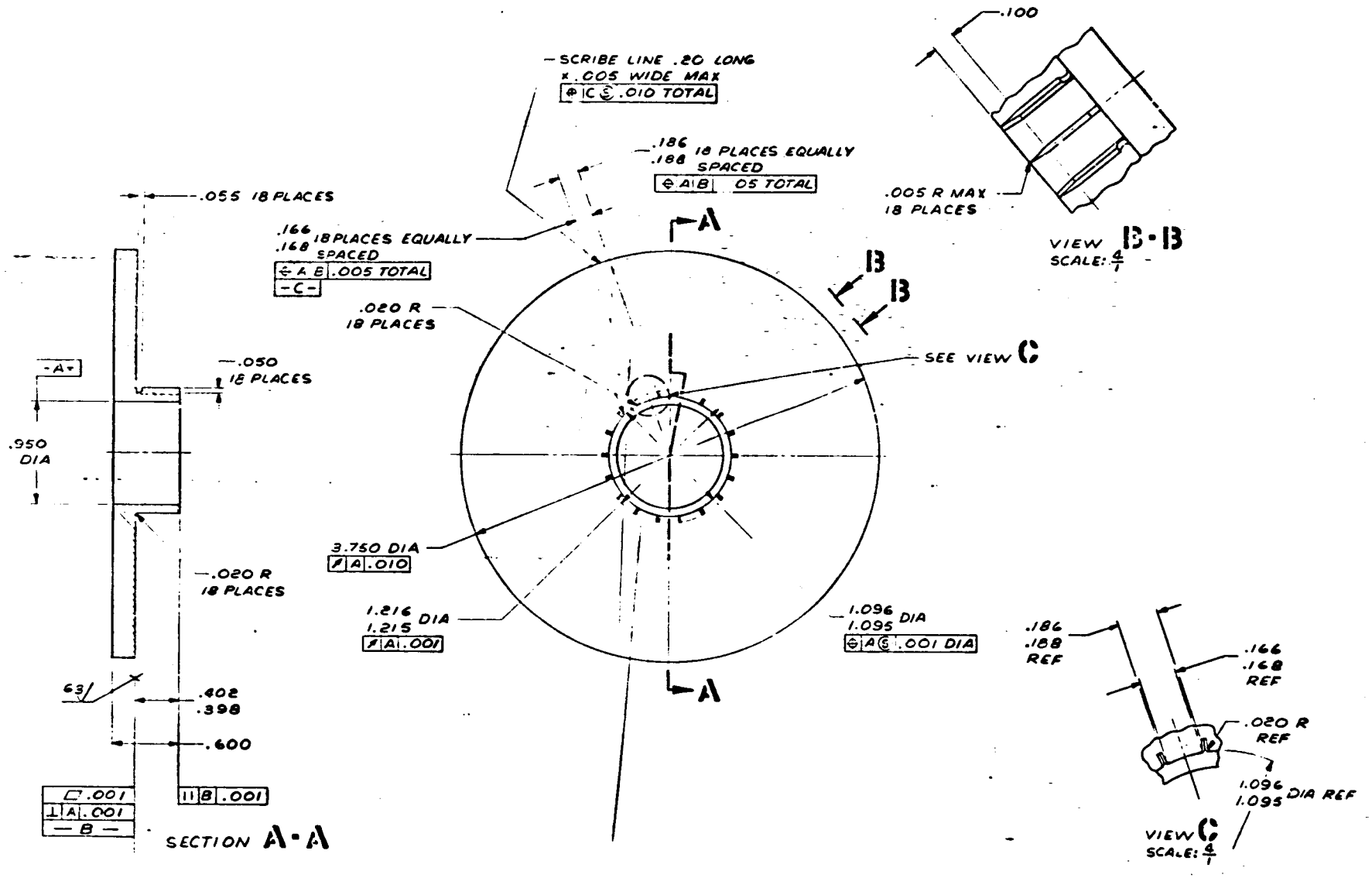

FIGURE B4. THICK SLOT FILM COOLANT INJECTOR - INNER RING

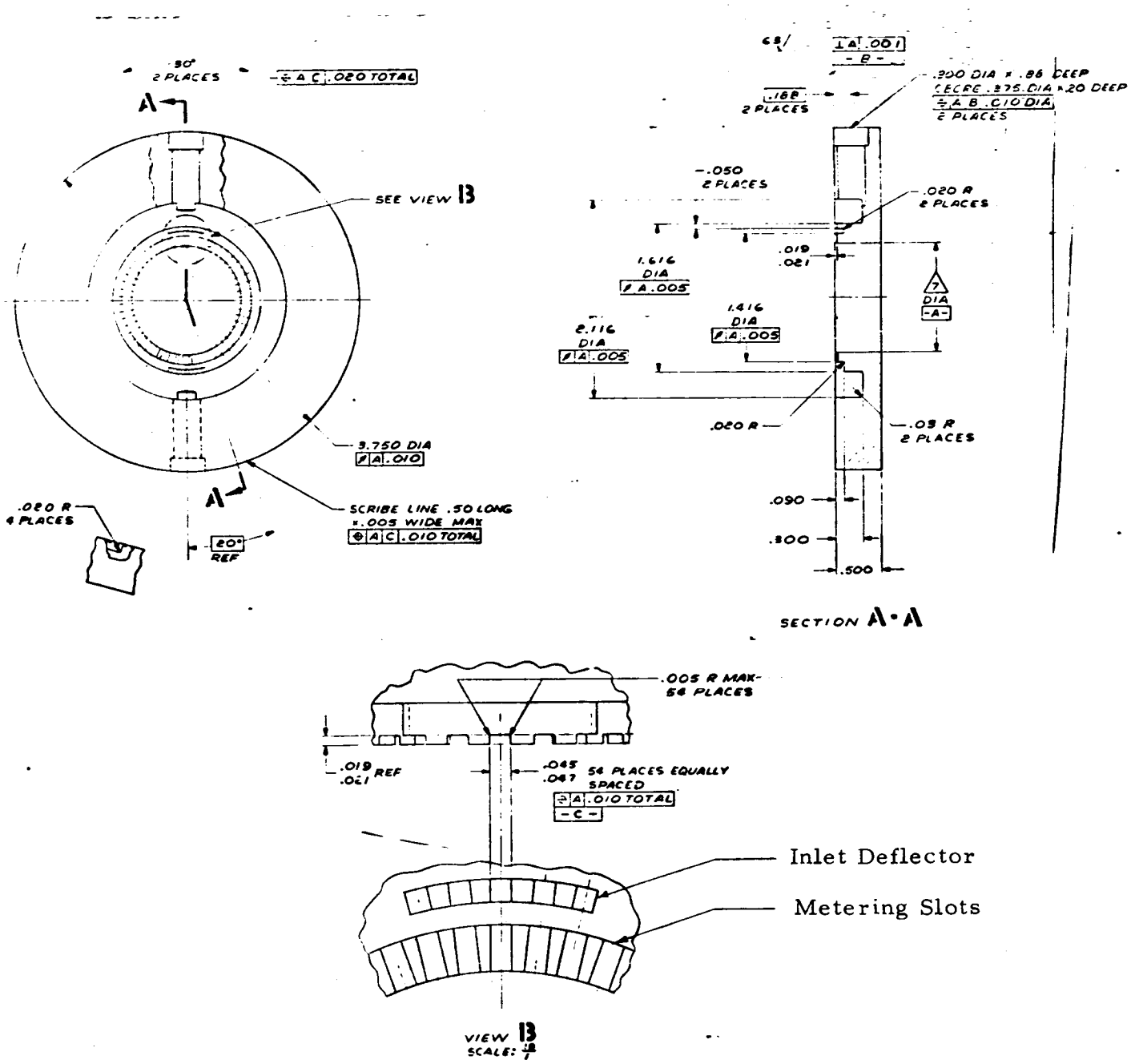

FIGURE B5 THICK SLOT FILM COOLANT INJECTOR - OUTER RING

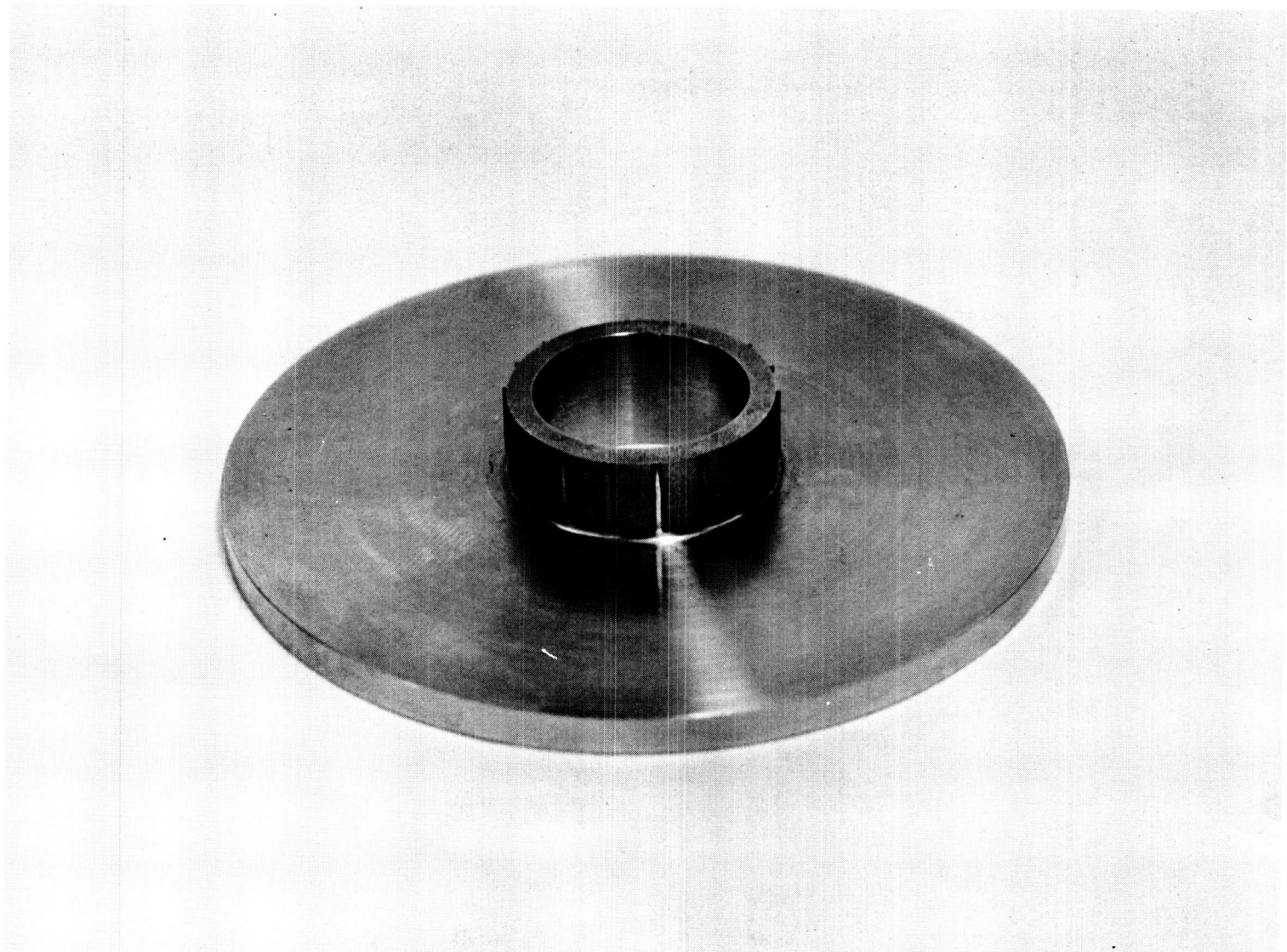

Figure B-6. Inner Ring - Thin Slot Film Coolant Injector

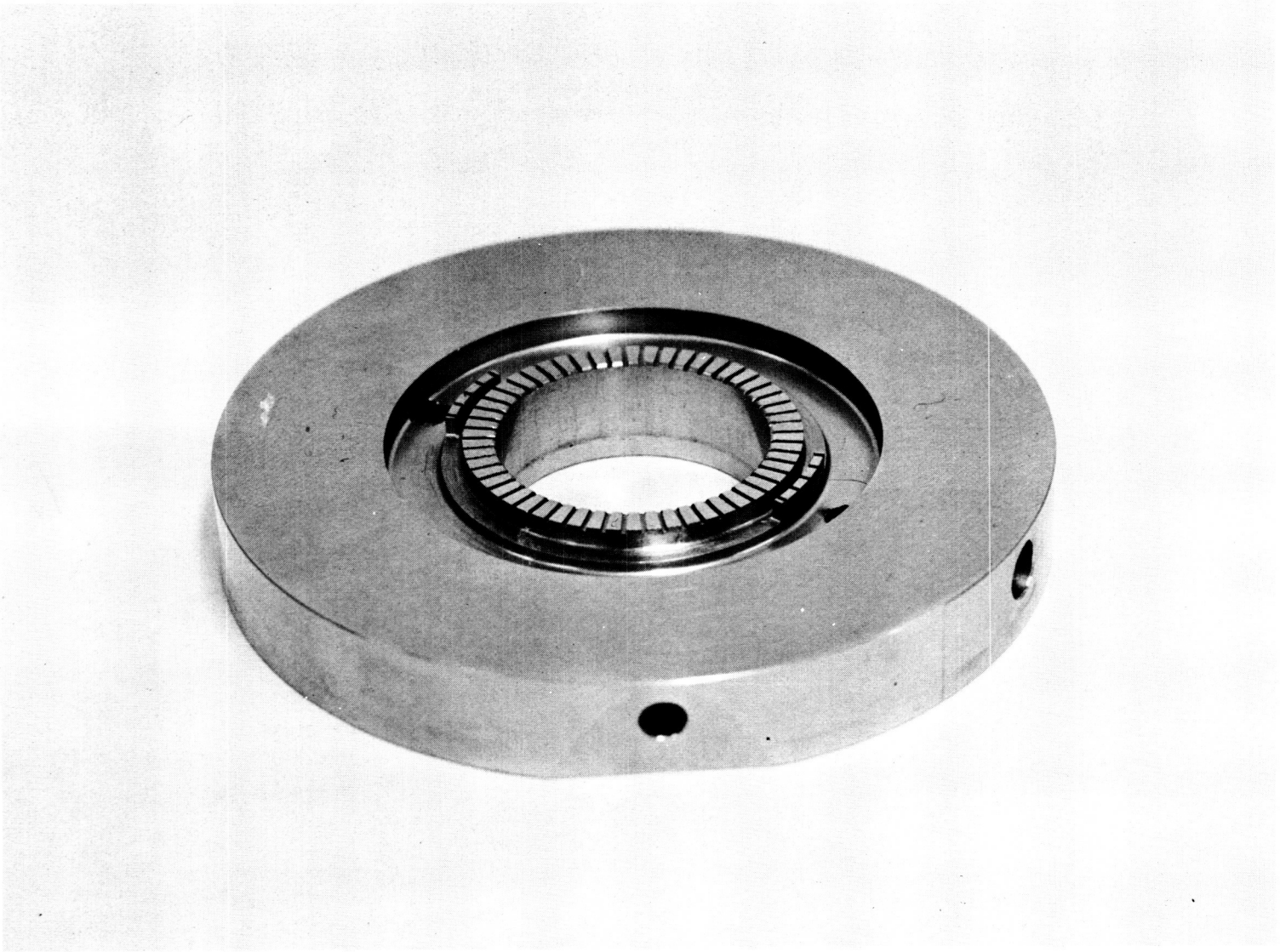

Figure B-7. Outer Ring - Thick Slot Film Coolant Injector

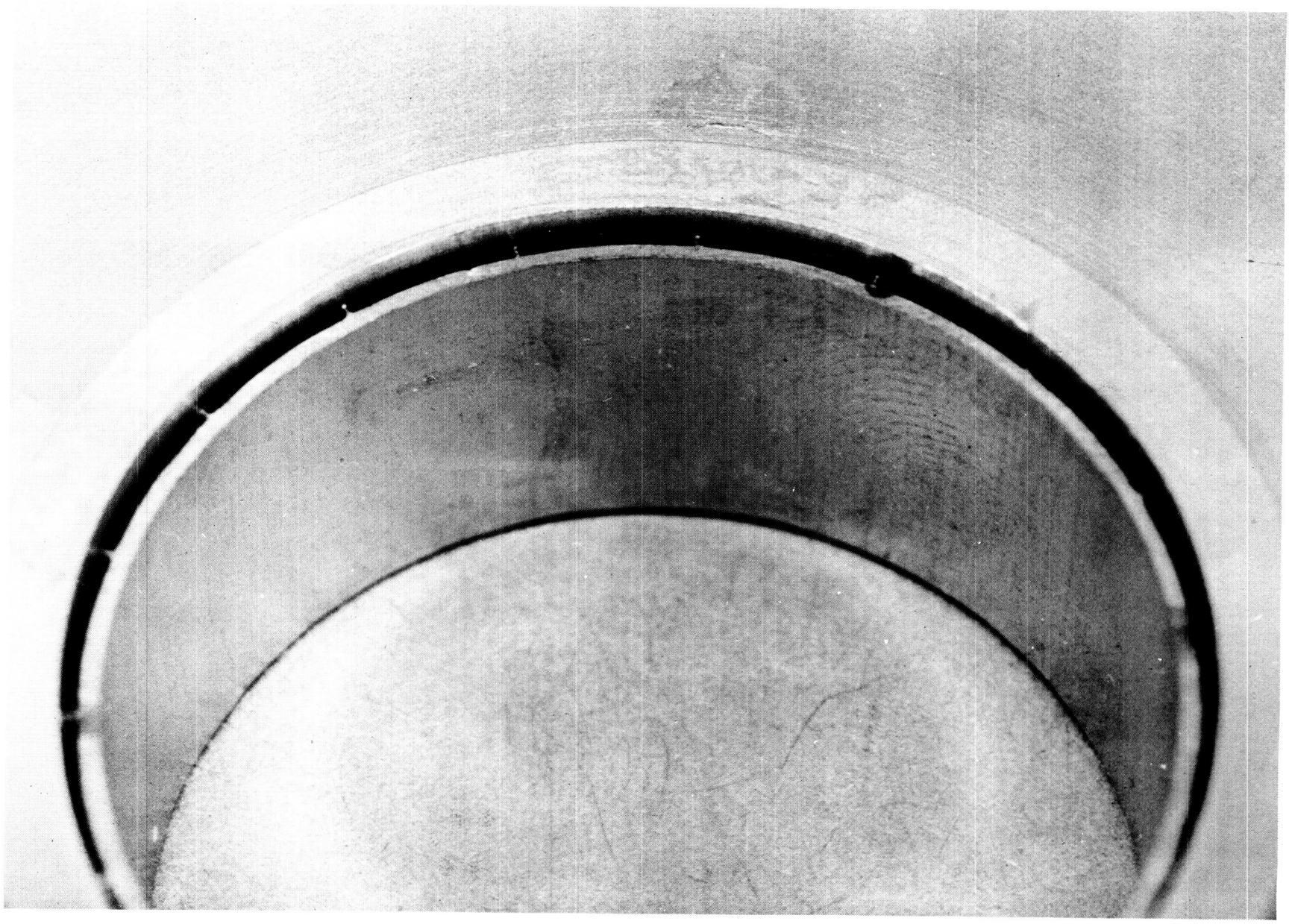

Figure B-8. Coolant Injection Slot, Thin Slot Film Coolant Injector

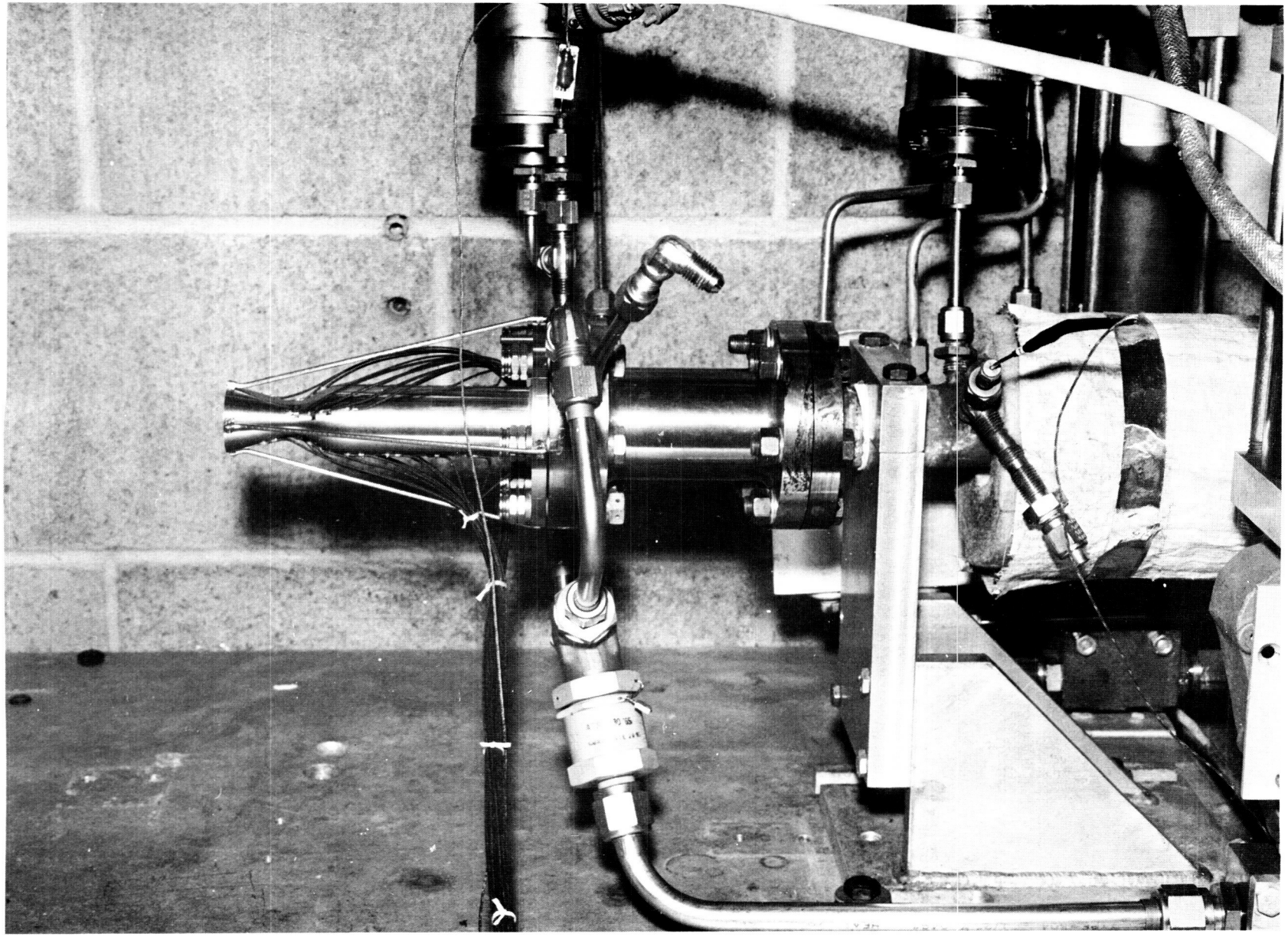

Figure B-9. Test Setup 102 Mounted on Film Cooling Test System

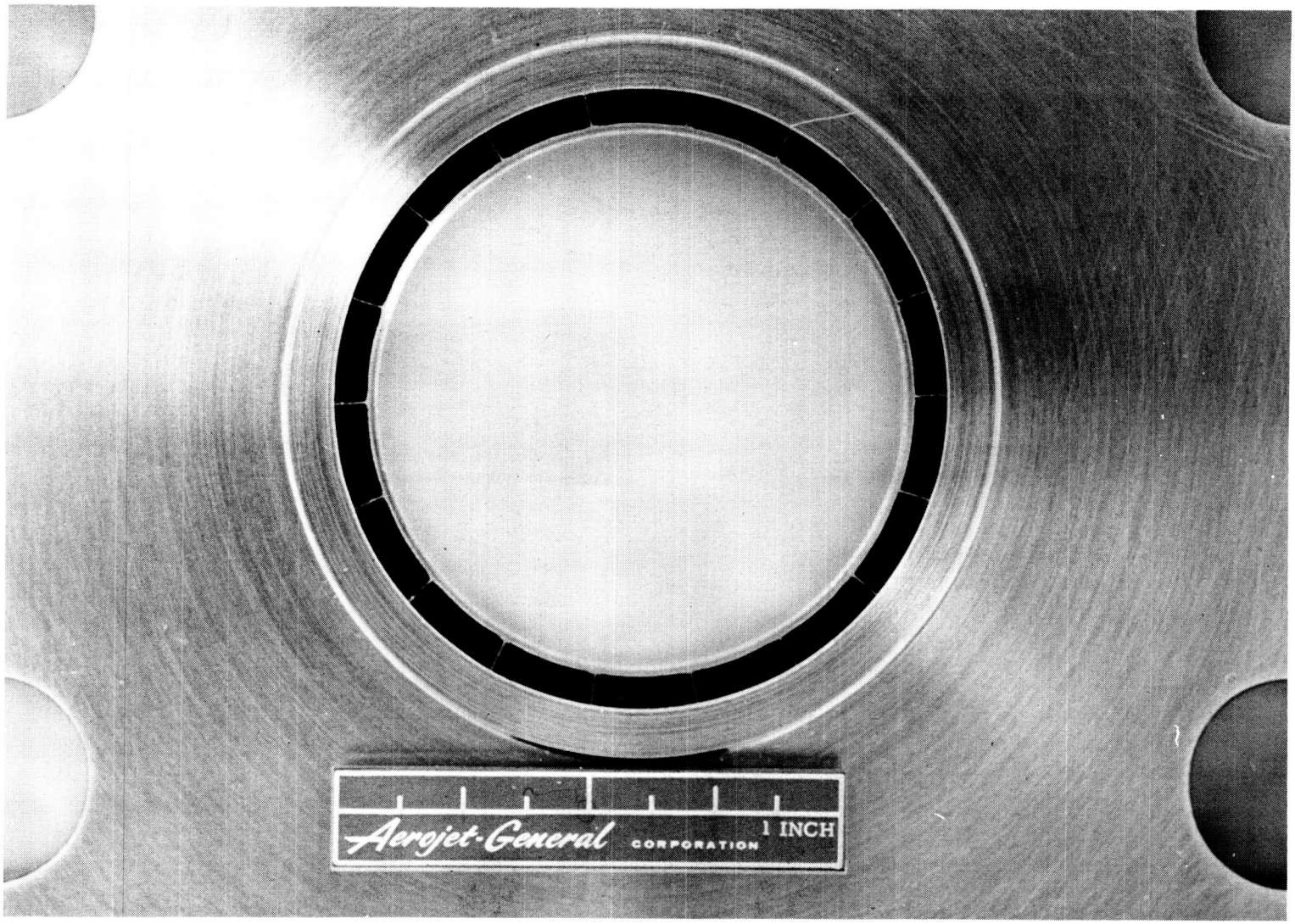

Figure B-10. Close Up View of Coolant Injection Slot, Thick Slot Film Coolant Injector

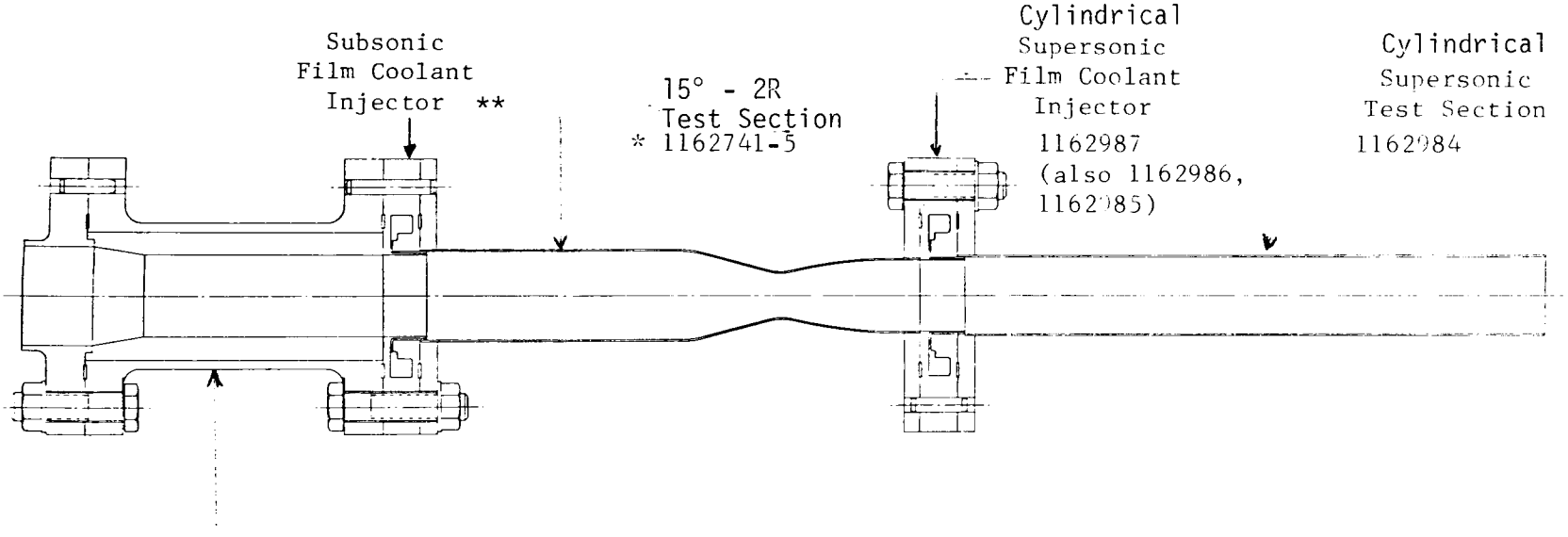

* Indicates ALRC Drawing Number

** Test Setup 103A, B: Thick Slot Subsonic Injector, 1159863
Test Setup 104A, B: Thin Slot Subsonic Injector, 1160024

FIGURE B11. SKETCH OF TEST SETUP 103A, B AND 104A, B

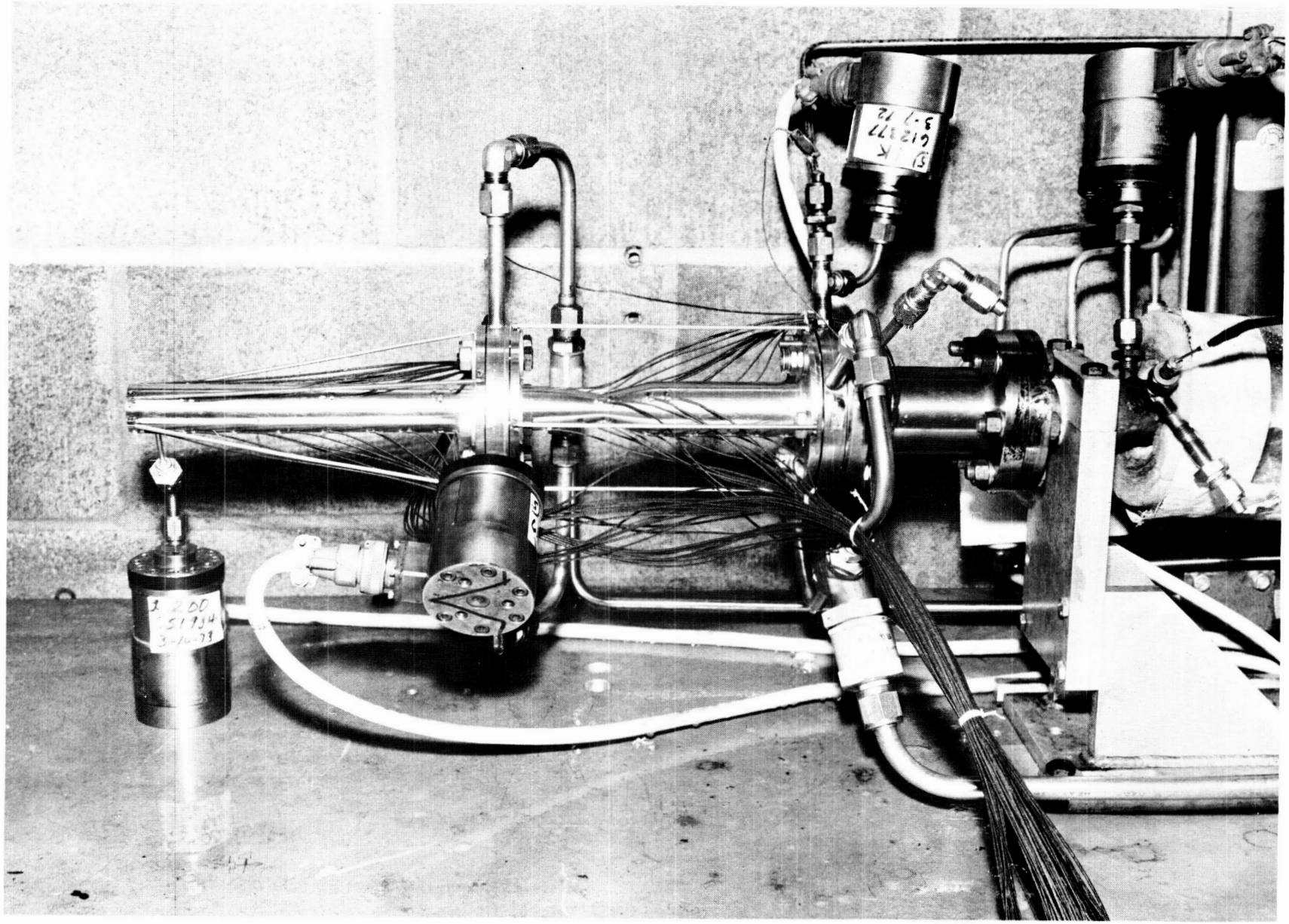

Figure B-12. Test Setup 103A,B Mounted on Film Cooling Test System

THIS DOCUMENT AND THE DATA DISCLOSED HEREIN OR HERE WITH IS NOT TO BE REPRODUCED, USED OR DISCLOSED IN WHOLE OR IN PART TO ANYONE WITHOUT THE PERMISSION OF AEROJET GENERAL CORPORATION

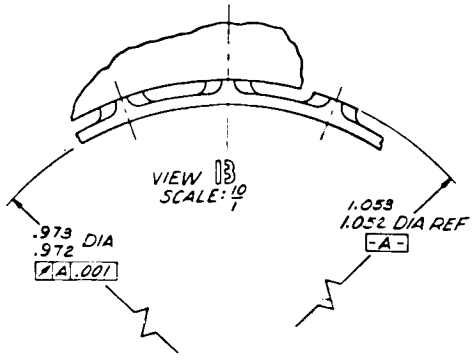

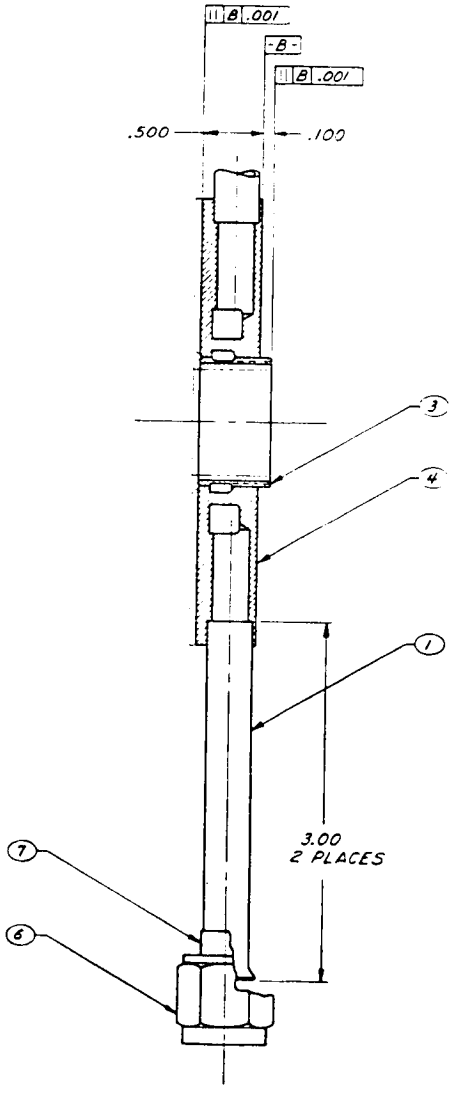

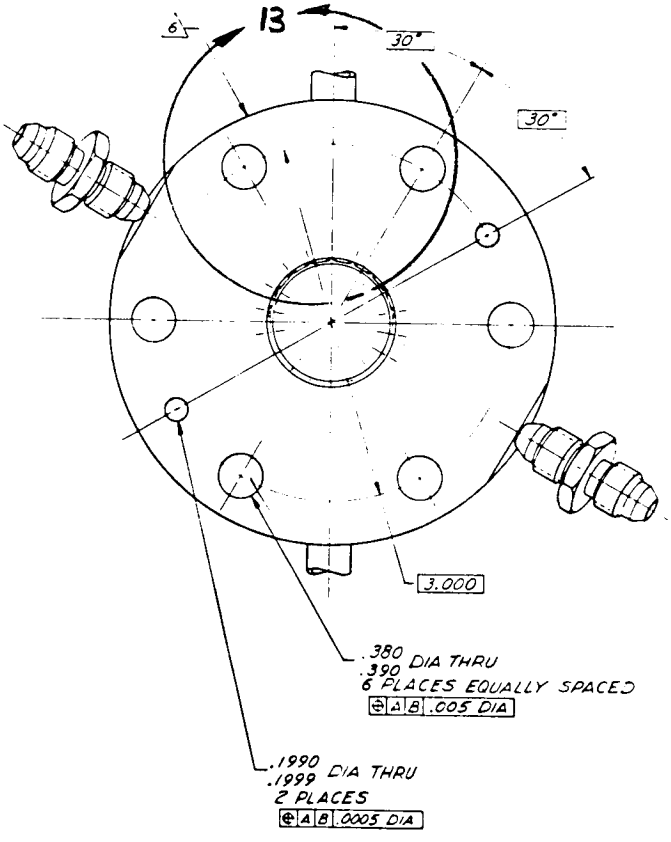

FIGURE B13. CYLINDRICAL SUPERSONIC FILM COOLANT INJECTOR ASSEMBLY, ALRC P/N 1162987

THIS DOCUMENT AND THE DATA DISCLOSED HEREIN OR MADE PART TO BE REPRODUCED USED OR DISCLOSED IN WHOLE OR IN PART TO ANYONE WITHOUT THE PERMISSION OF AEROJET GENERAL CORPORATION

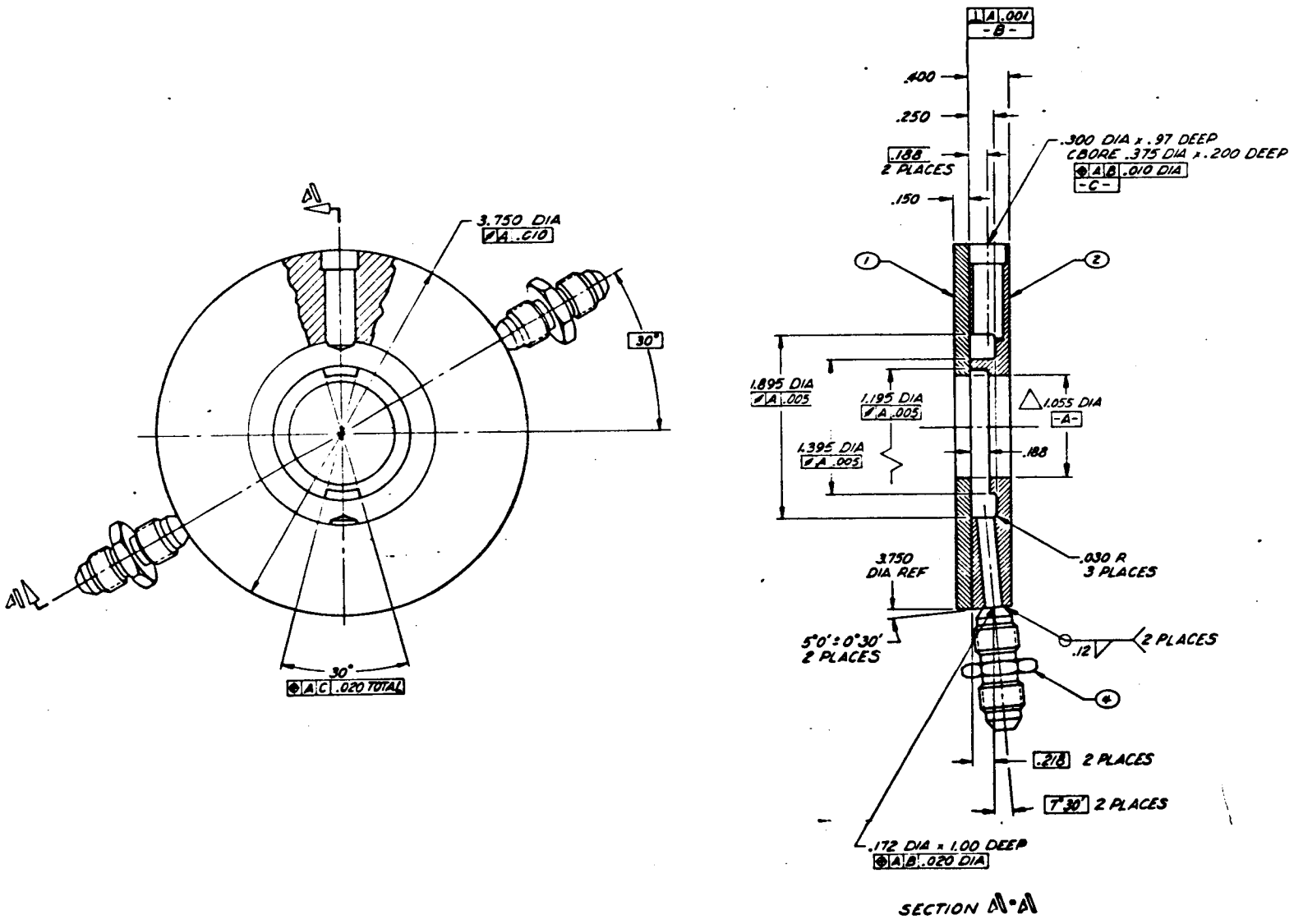

FIGURE B14. MANIFOLD DESIGN FOR THE CYLINDRICAL SUPERSONIC FILM COOLANT INJECTOR, ALRC P/N 1162986

THE EQUIPMENT AND THE DATA DISCLOSED HEREIN SO MADE
DATA IS NOT TO BE REPRODUCED USED OR DISCLOSED IN WHOLE
OR IN PART TO ANYONE WITHOUT THE PERMISSION OF AEROJET
GENERAL CORPORATION

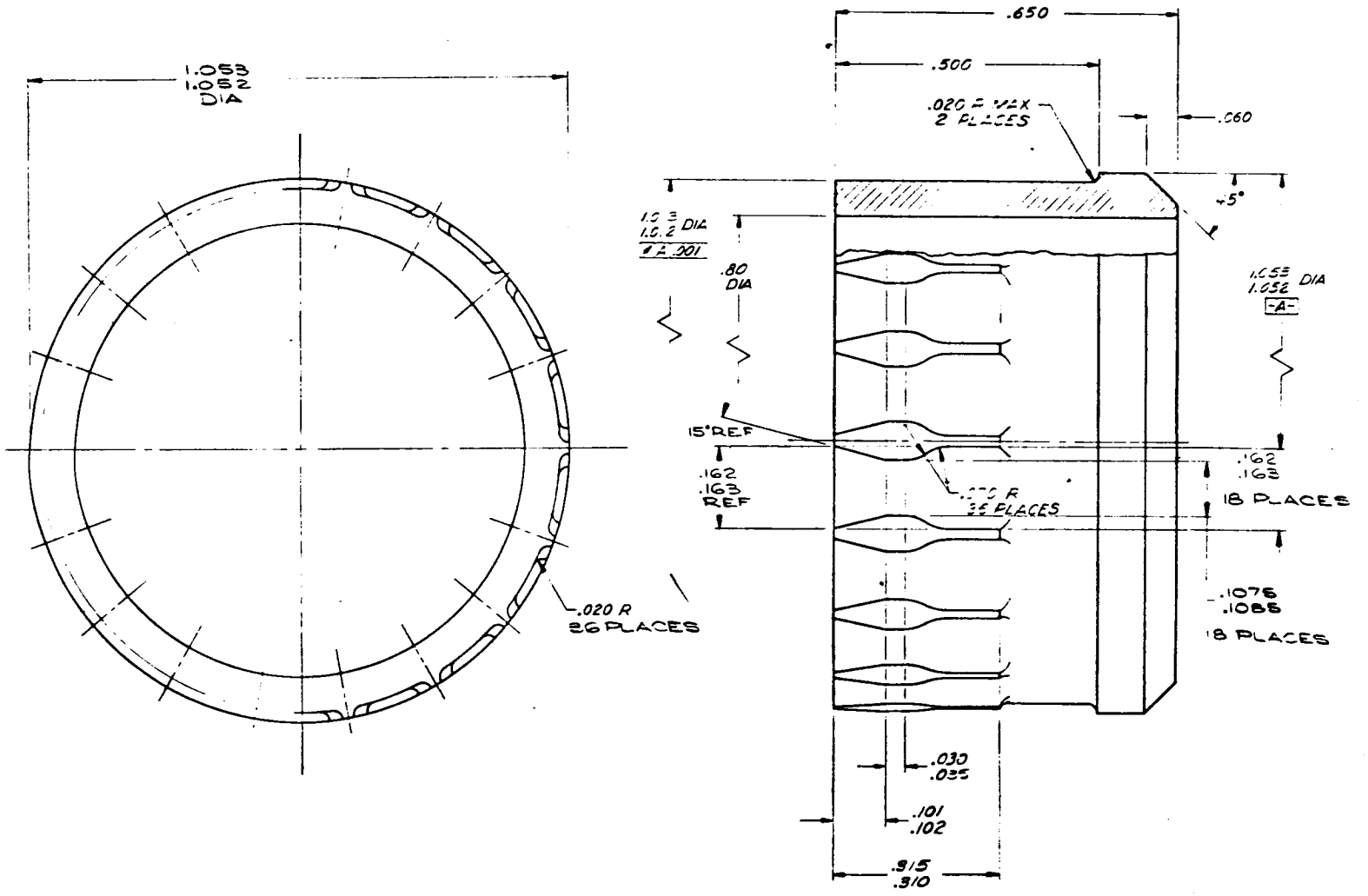

FIGURE B15. NOZZLE DESIGN FOR THE CYLINDRICAL SUPERSONIC FILM COOLANT INJECTOR, ALRC P/N 1162985

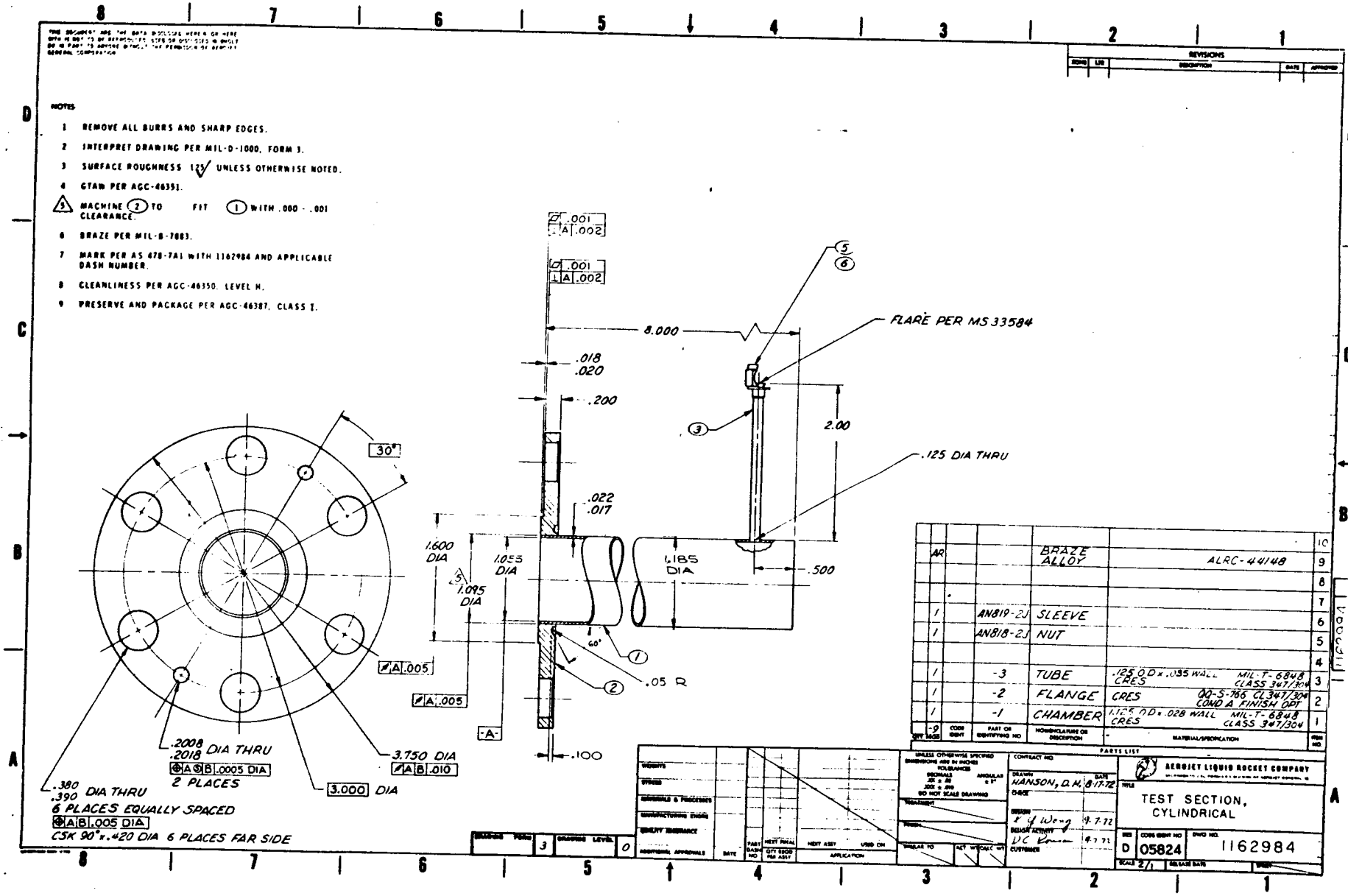

FIGURE B16. CYLINDRICAL SUPERSONIC TEST SECTION DESIGN

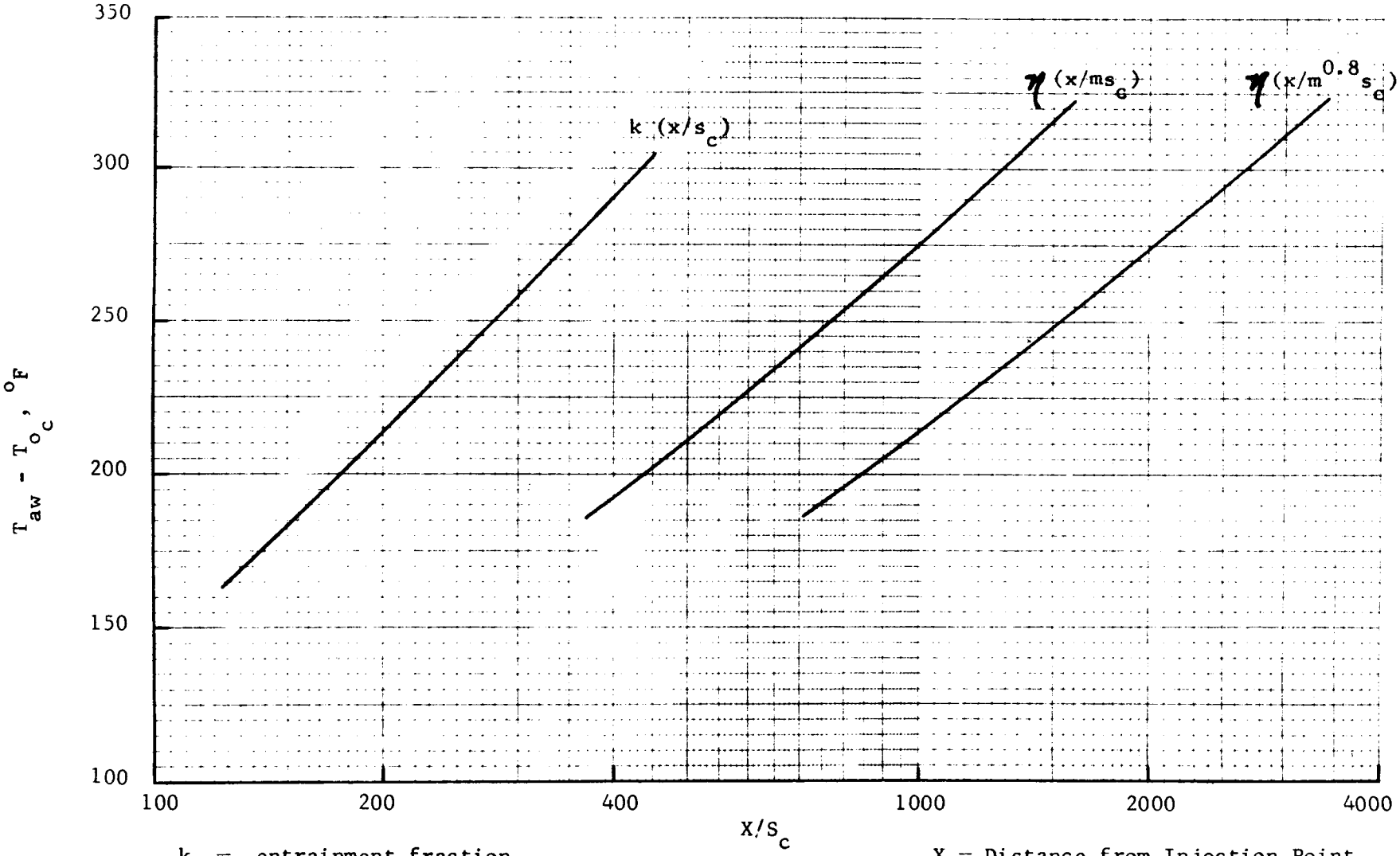

k = entrainment fraction
= effectiveness
m = film coolant-to-core gas mass velocity ratio

X = Distance from Injection Point
S_c = Injector Slot Height

FIGURE B17. PRETEST ESTIMATES OF ADIABATIC WALL TEMPERATURES FOR THE CYLINDRICAL SUPERSONIC TEST SECTION, HYDROGEN FILM COOLING

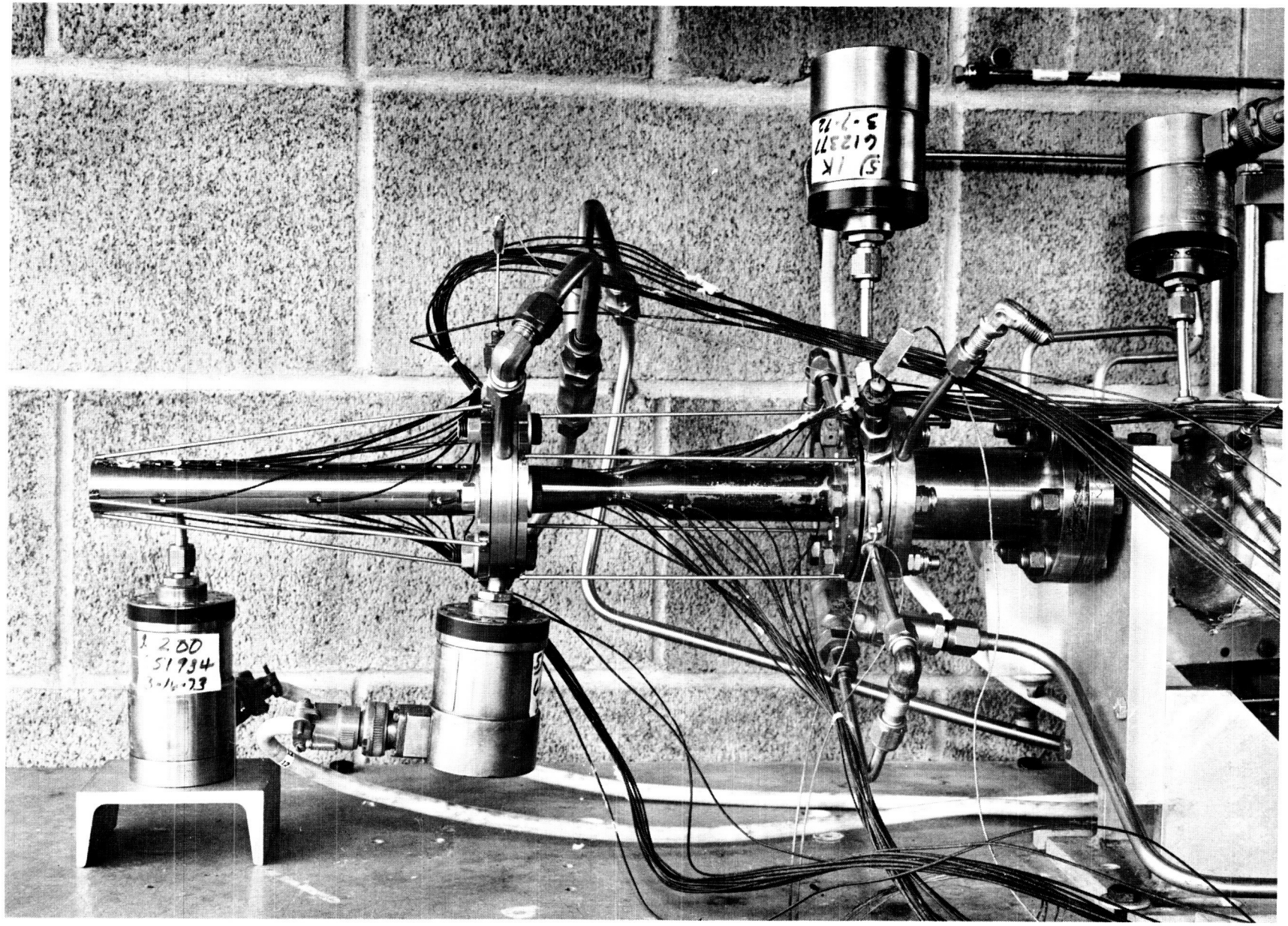

Figure B-18. Test Setup 104A,B Mounted on Film Cooling Test System

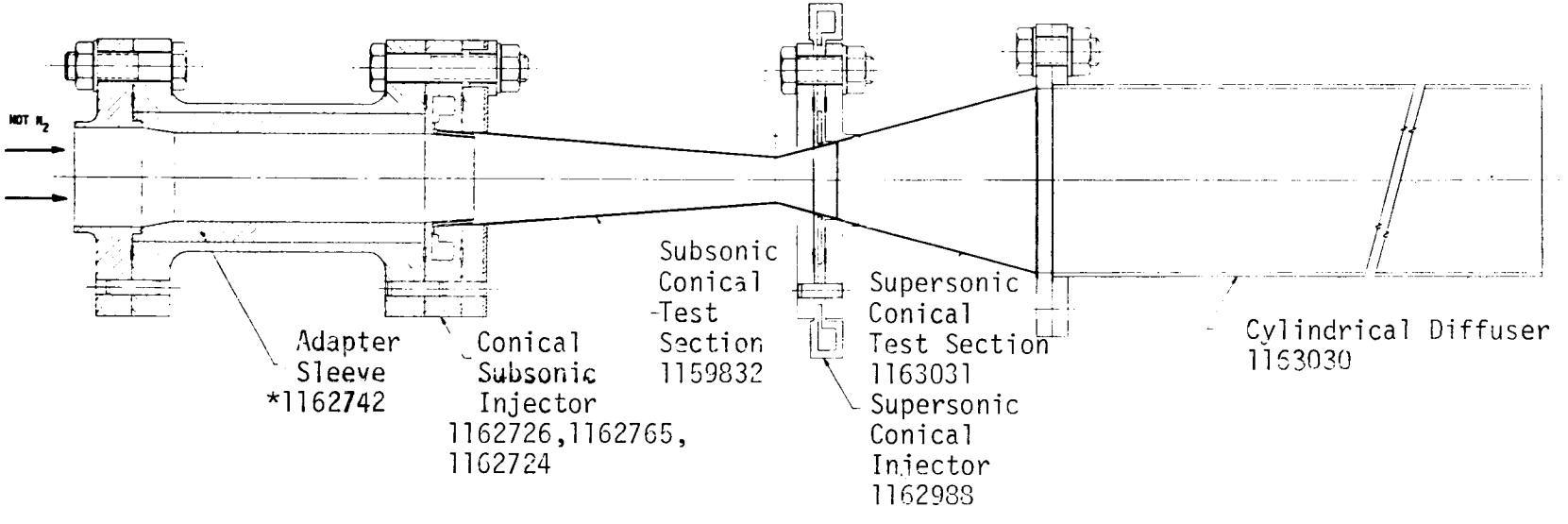

* Indicates ALRC Drawing Number

FIGURE B19. SKETCH OF TEST SETUP 105A, B and 106

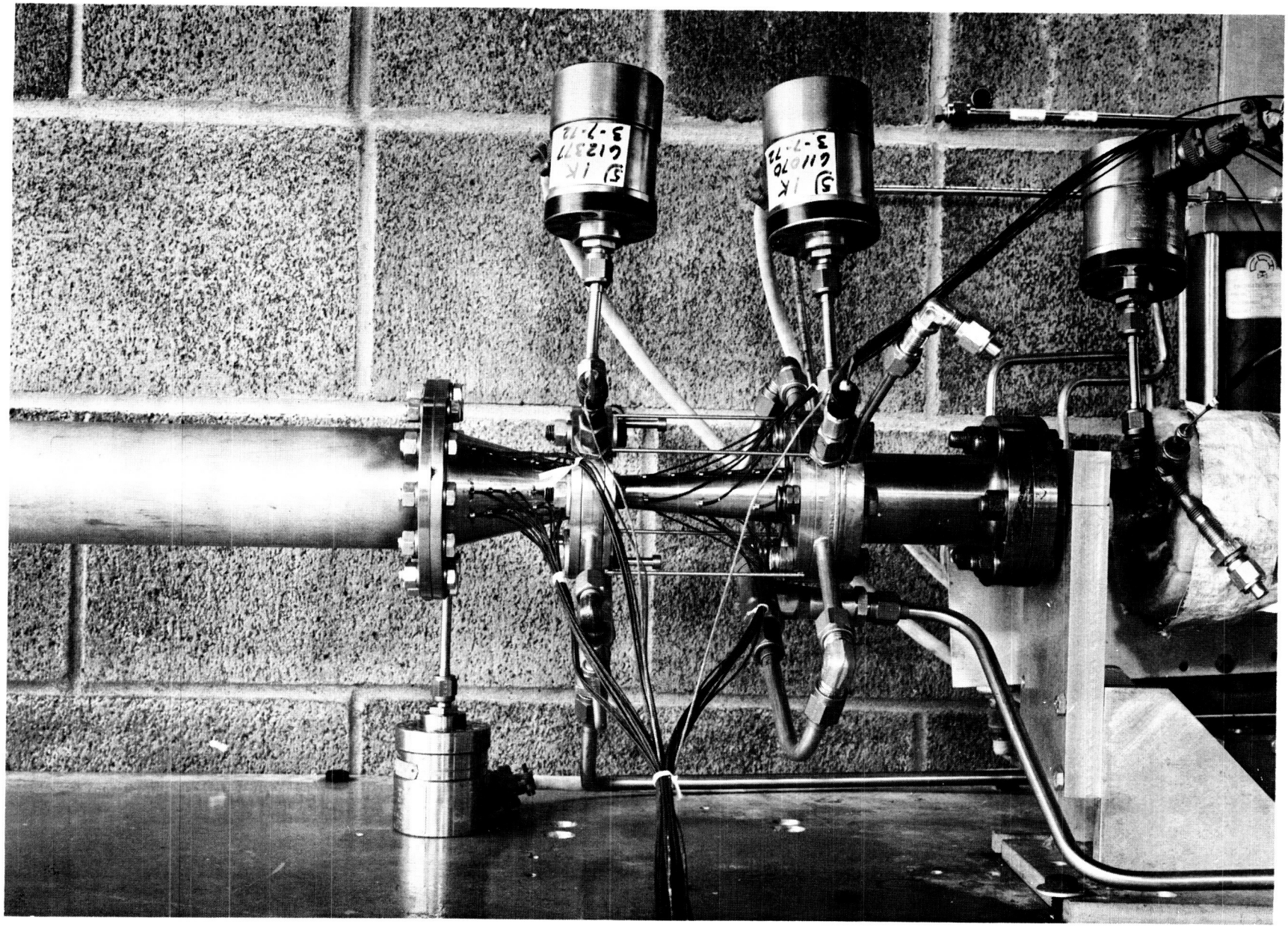

Figure B-20. Test Setup 105A,B Mounted on Film Cooling Test System

THIS DOCUMENT AND THE DATA DISCLOSED HEREIN SO MODIFIED IS NOT TO BE REPRODUCED, USED OR DISCLOSED IN WHOLE OR IN PART TO ANYONE WITHOUT THE PERMISSION OF AEROJET-GENERAL CORPORATION.

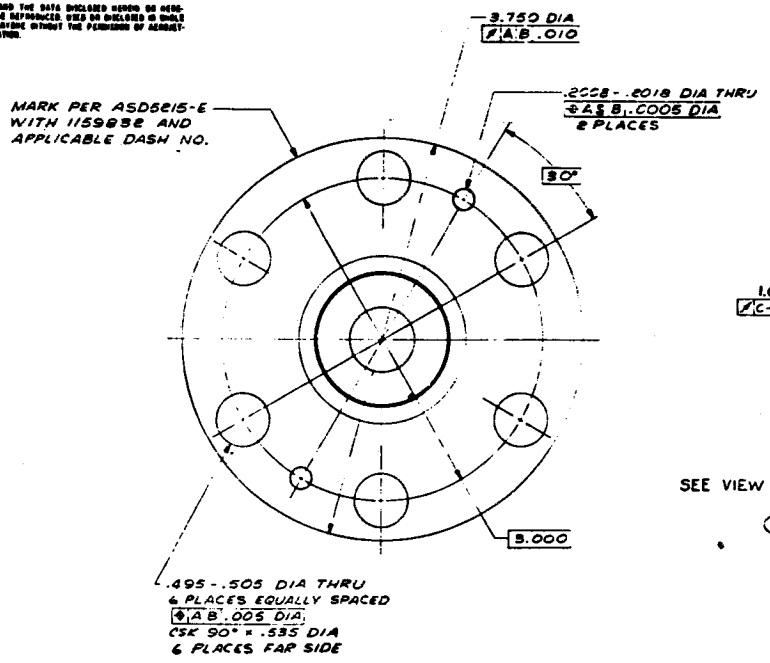

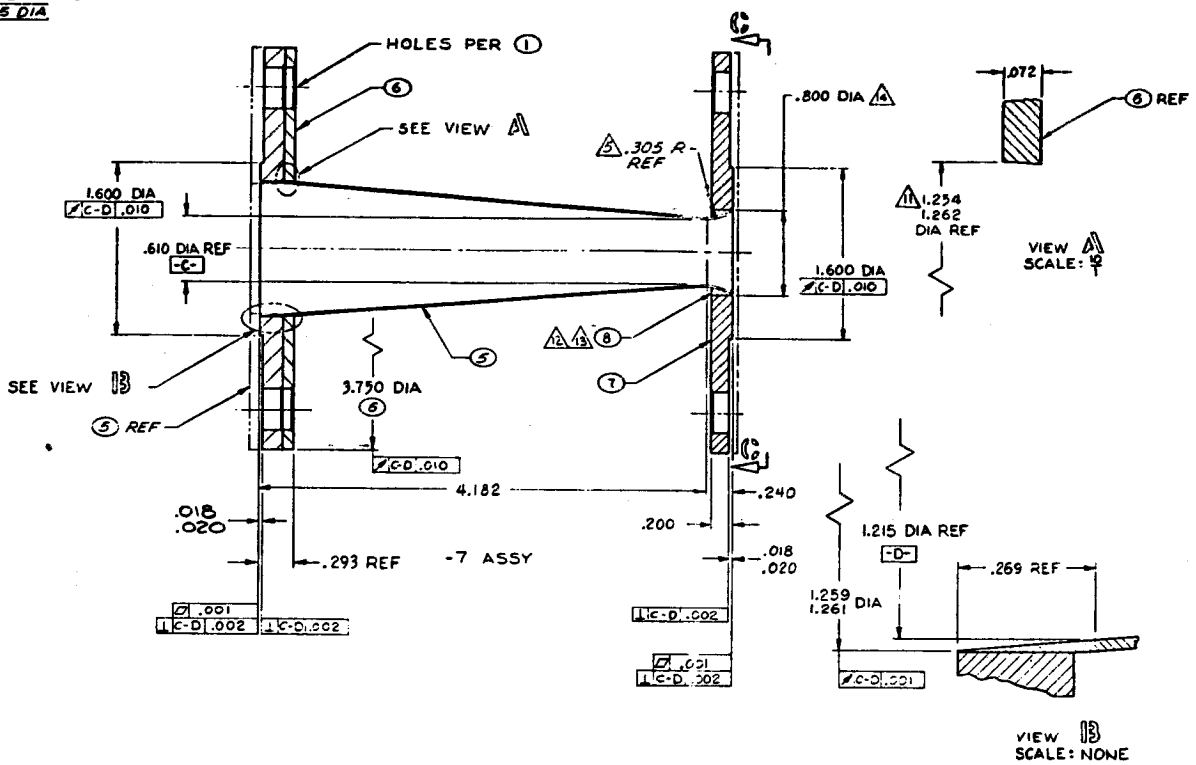

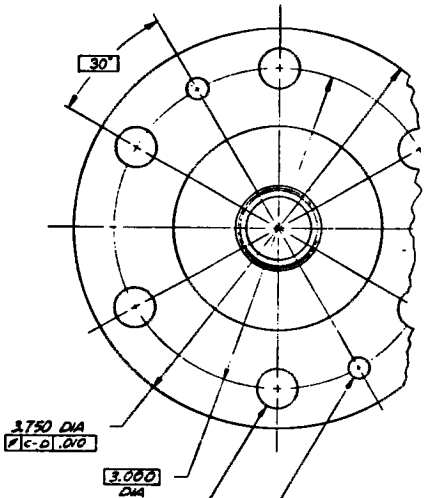

VIEW C-C

THIS DRAWING AND THE DATA CONTAINED HEREIN ARE THE PROPRIETARY PROPERTY OF GENERAL DYNAMICS CORPORATION

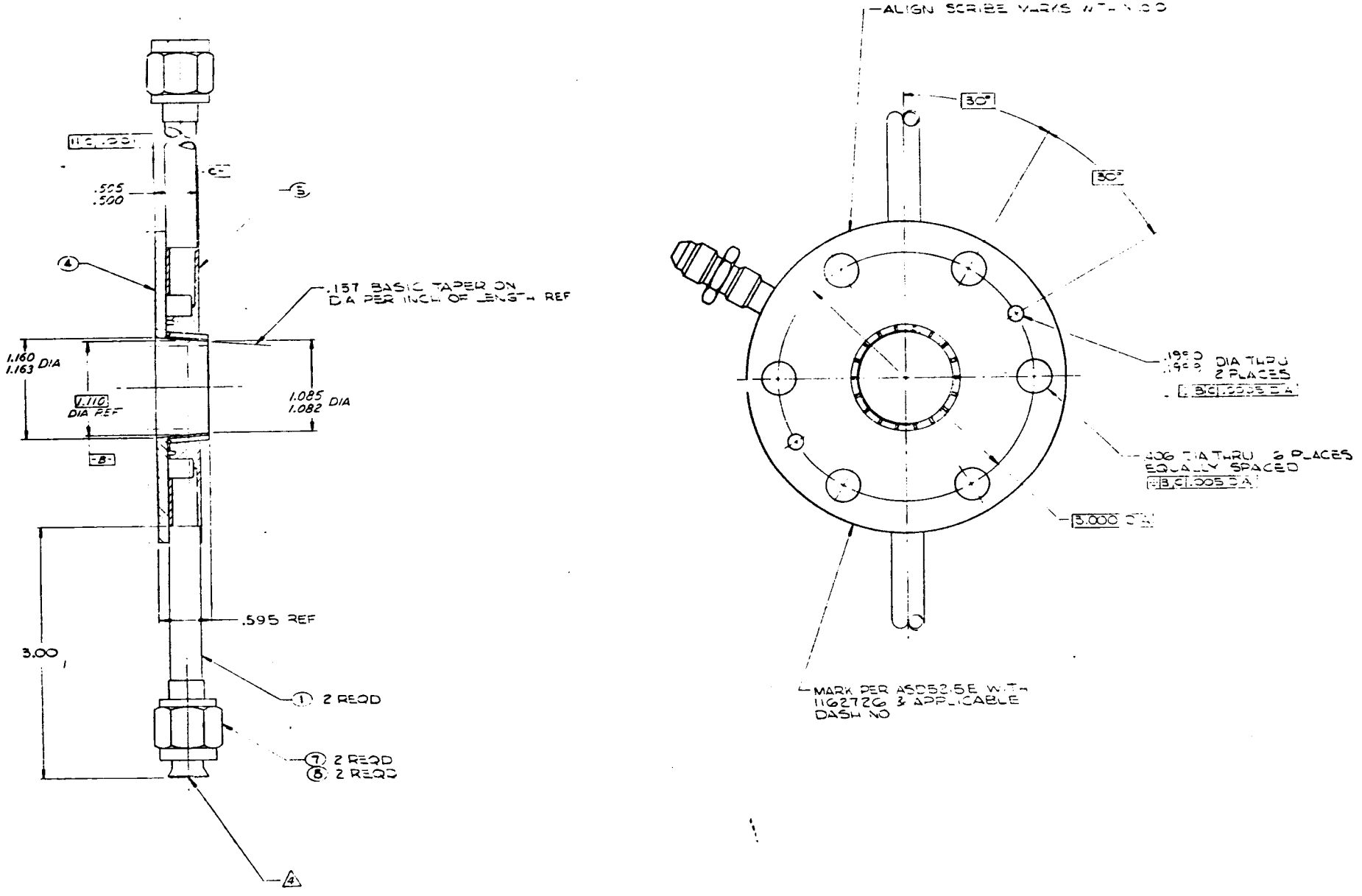

FIGURE B22. CONICAL SUBSONIC INJECTOR ASSEMBLY, ALRC P/N 1162726

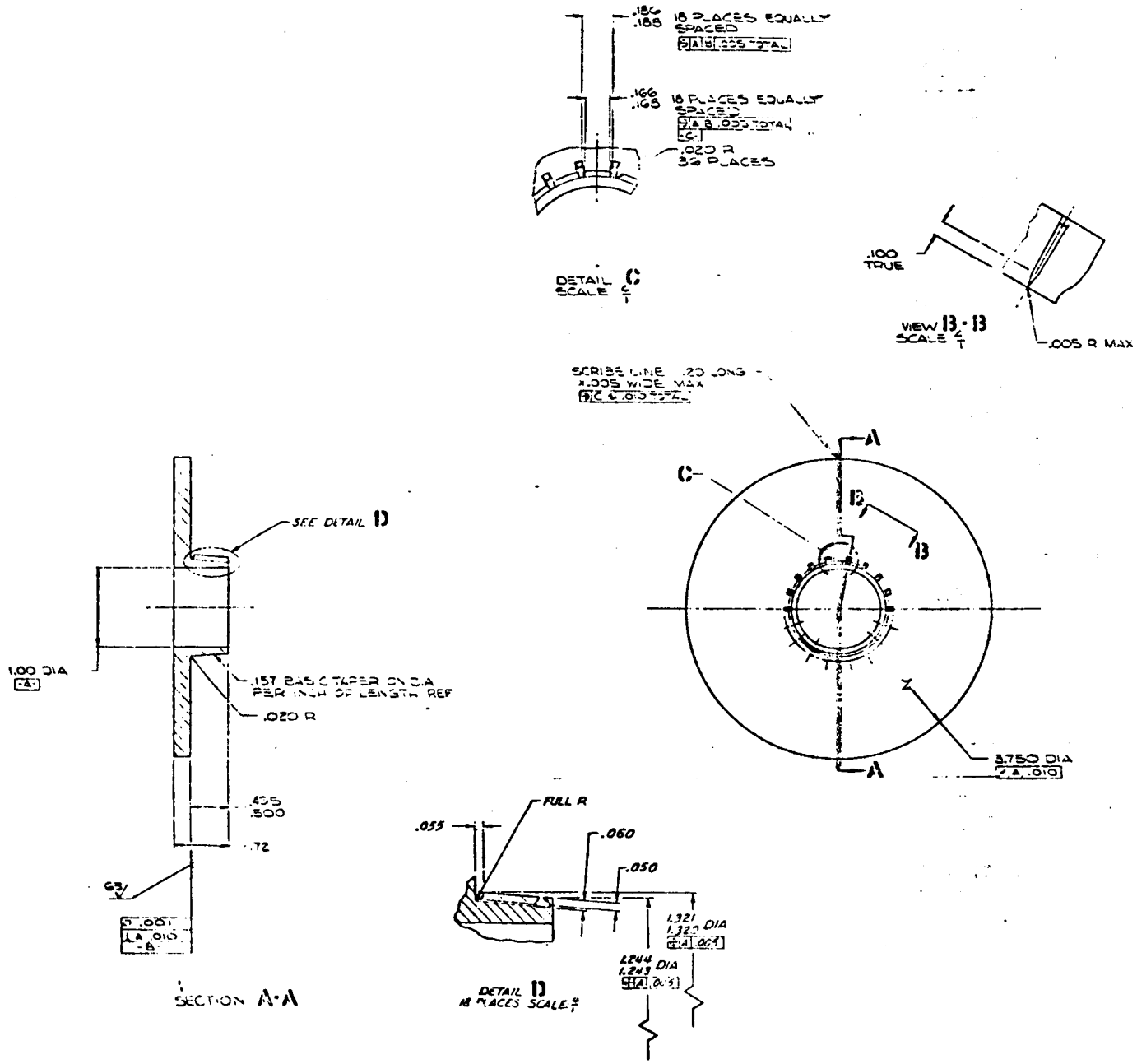

FIGURE B23: INJECTION NOZZLE DESIGN FOR THE CONICAL SUBSONIC INJECTOR, ALRC P/N 1162724

...DOCUMENT AND THE DATA DISCLOSED HEREIN OR HERE... ...NOT TO BE REPRODUCED, SOLD OR DISCLOSED IN WHOLE OR IN PART TO ANYONE WITHOUT THE PERMISSION OF AEROJET GENERAL CORPORATION

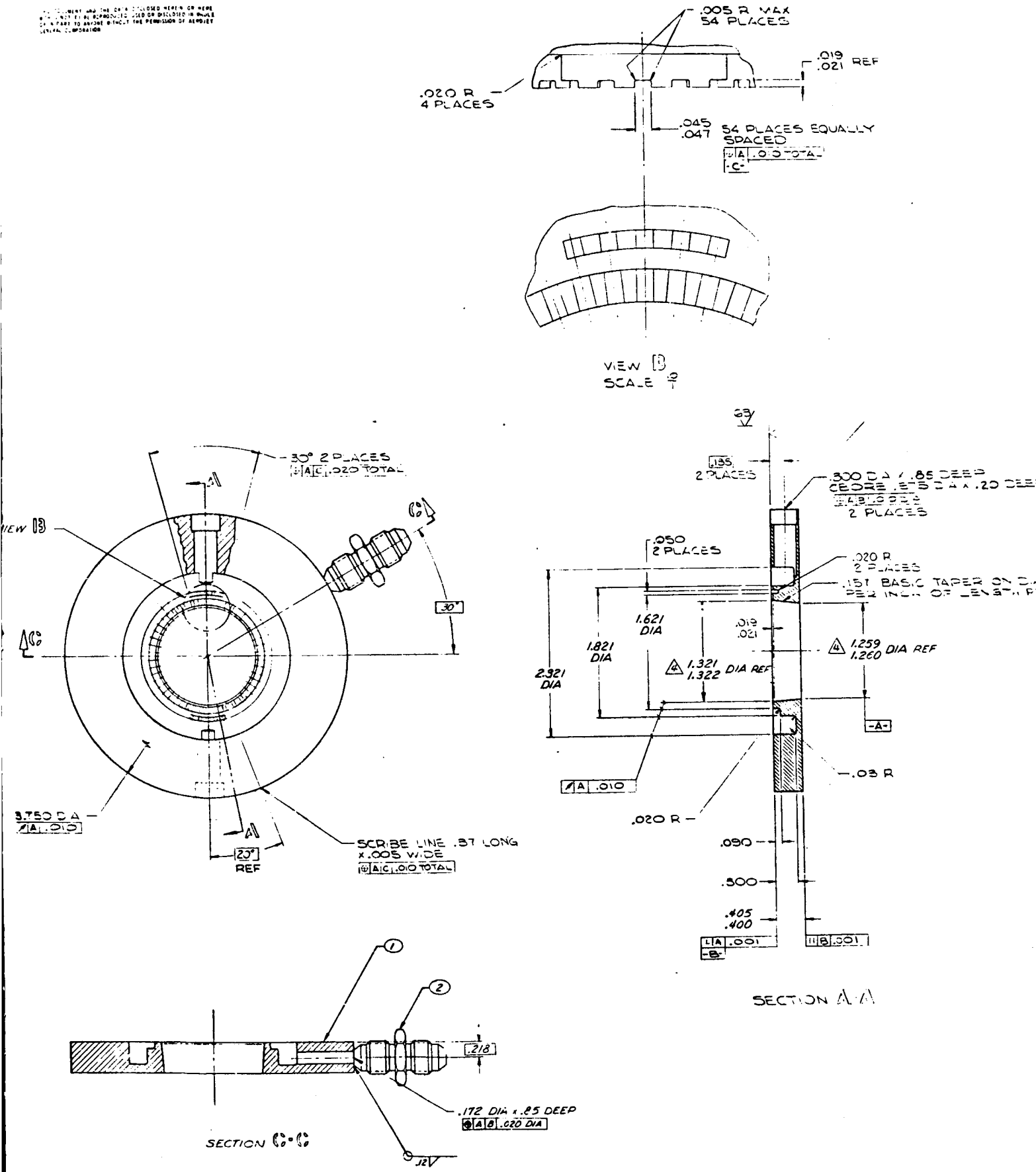

FIGURE B24: MANIFOLD DESIGN FOR THE CONICAL SUBSONIC INJECTOR, ALRC P/N 1162725

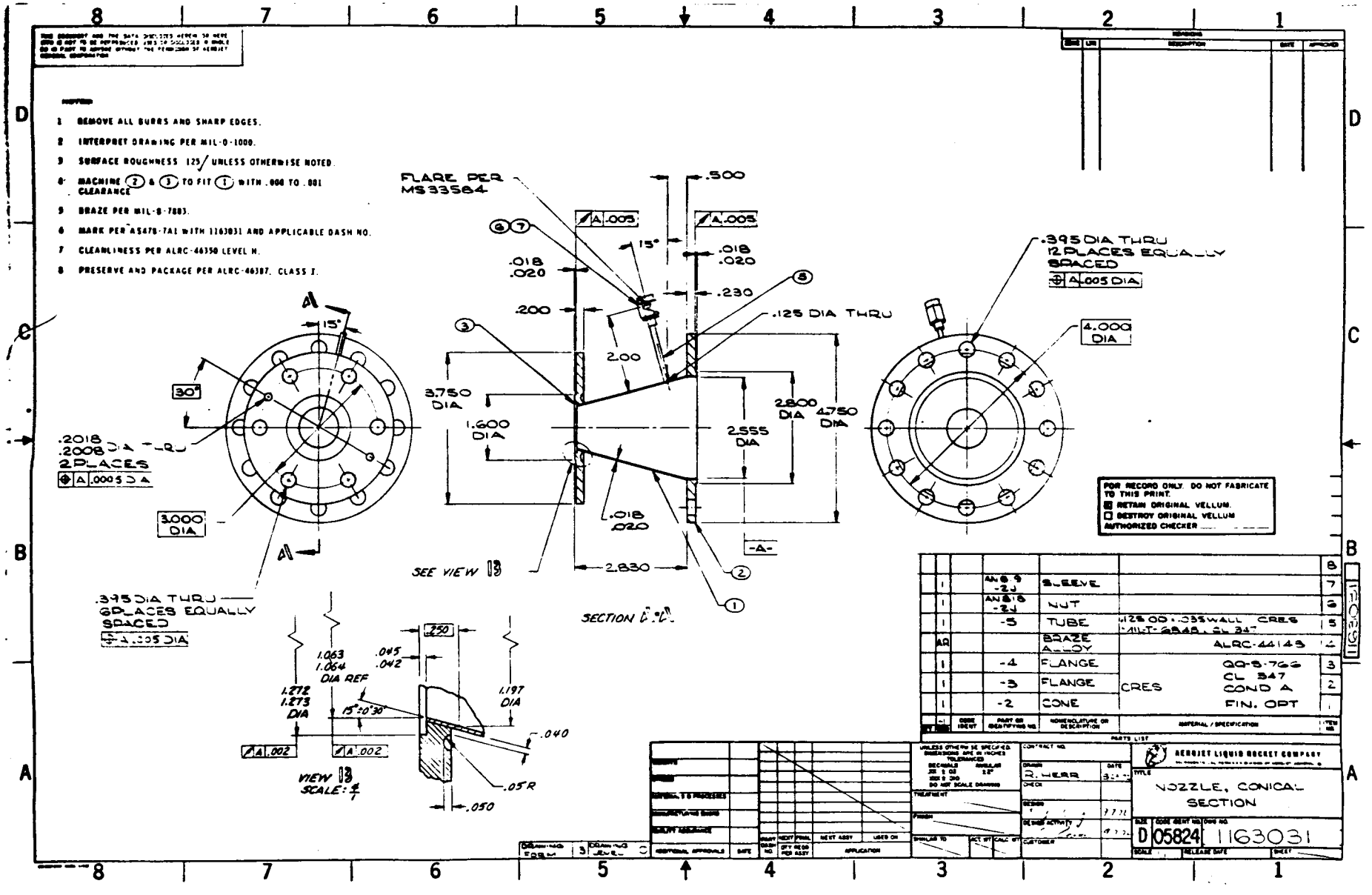

FIGURE B25. CONICAL SUPERSONIC TEST SECTION

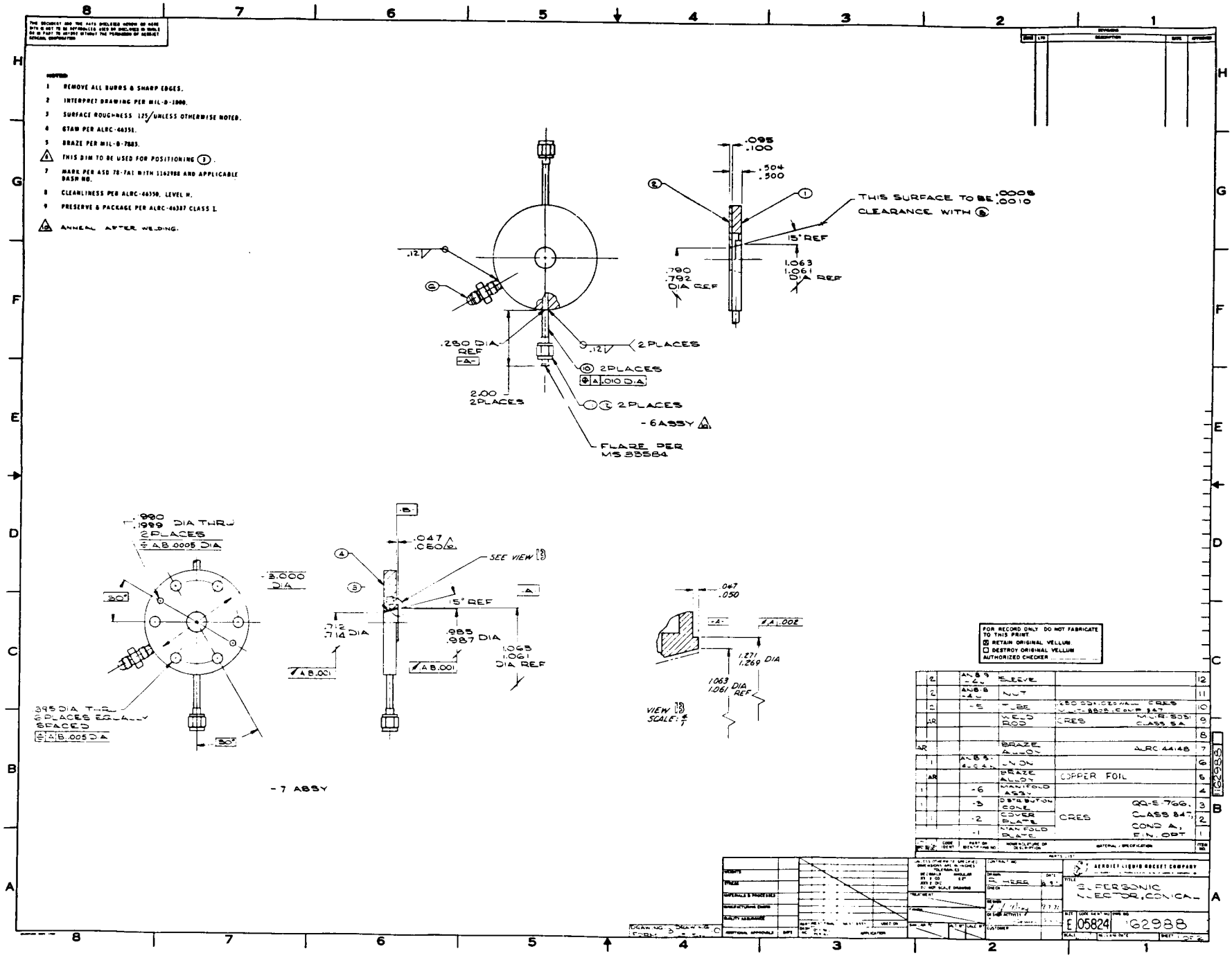

FIGURE B26. CONICAL SUPERSONIC INJECTOR DESIGN

Figure B26 (Sheet 1 of 2)

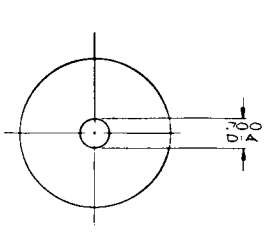

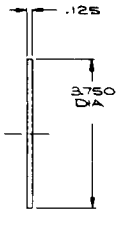

- 2 DETAIL

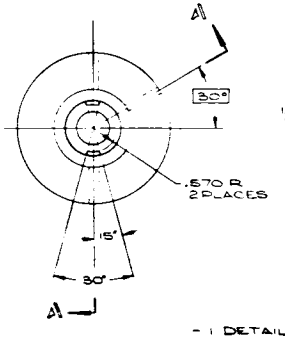

- 1 DETAIL

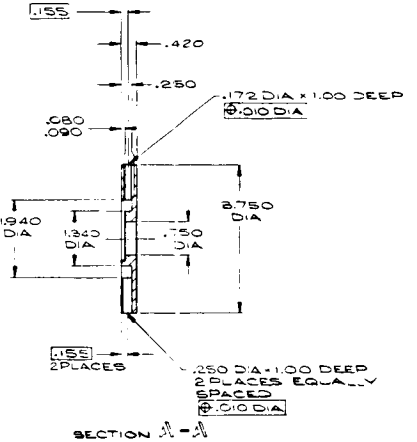

SECTION A-A

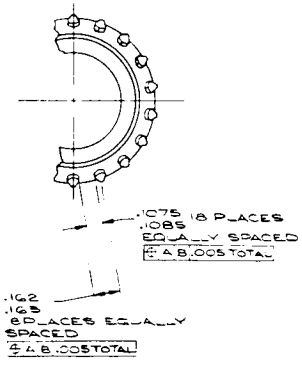

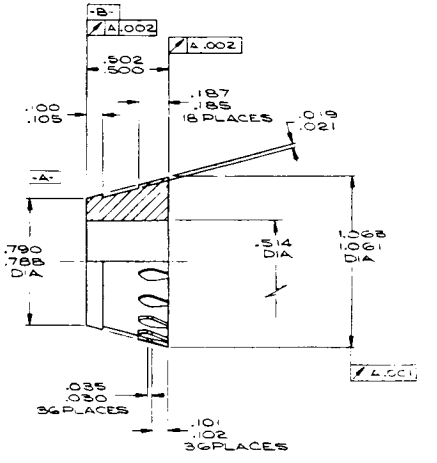

- 3 DETAIL
SCALE: 4/1

FOR RECORD ONLY DO NOT FABRICATE TO THIS PRINT
☒ RETAIN ORIGINAL VELLUM
☐ DESTROY ORIGINAL VELLUM
AUTHORIZED CHECKER

SIZE	CAGE SHEET NO.	DWG. NO.	REV
F	05824	1162988	

1162988

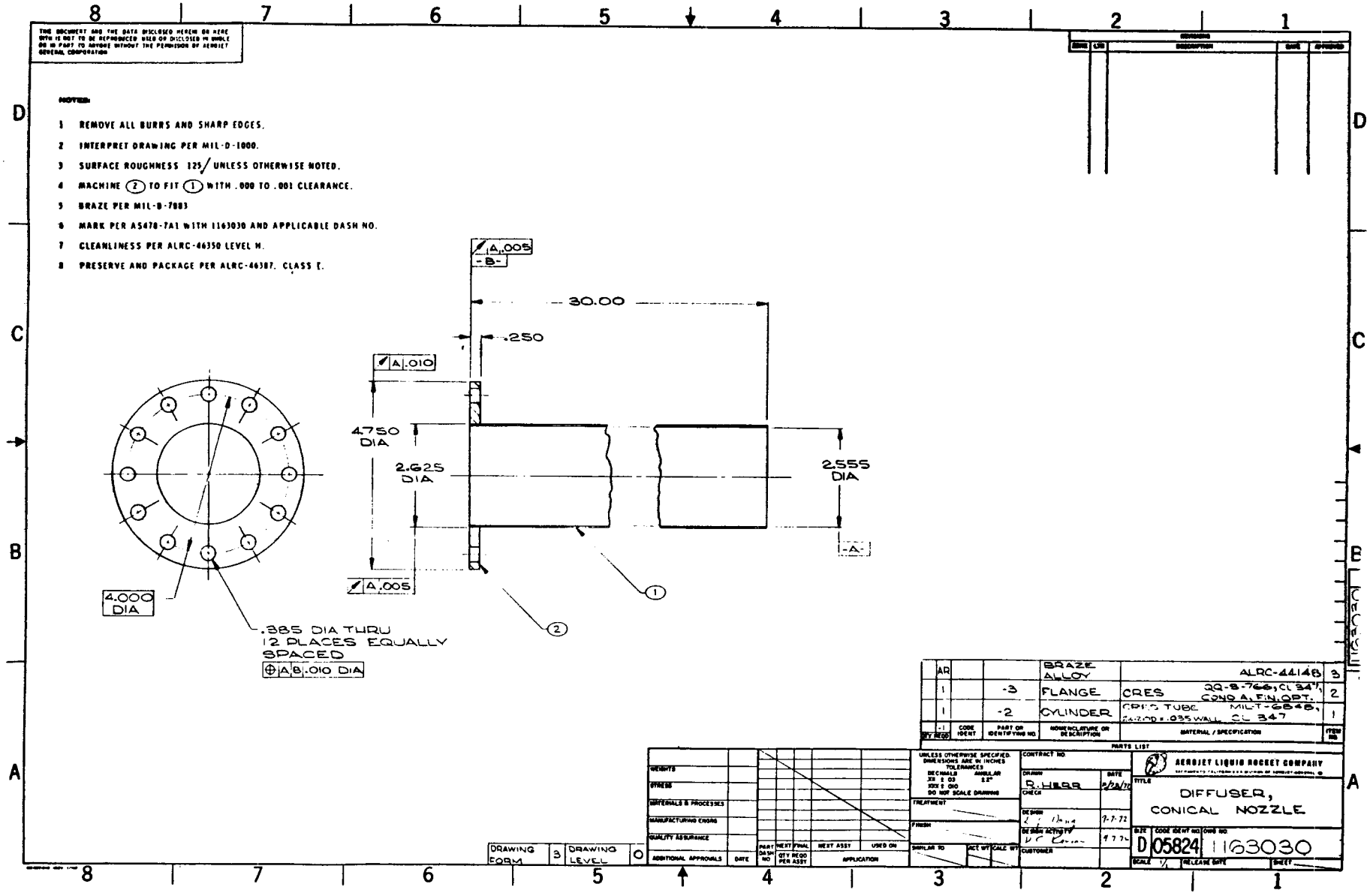

FIGURE B27. DIFFUSER TUBE DESIGN

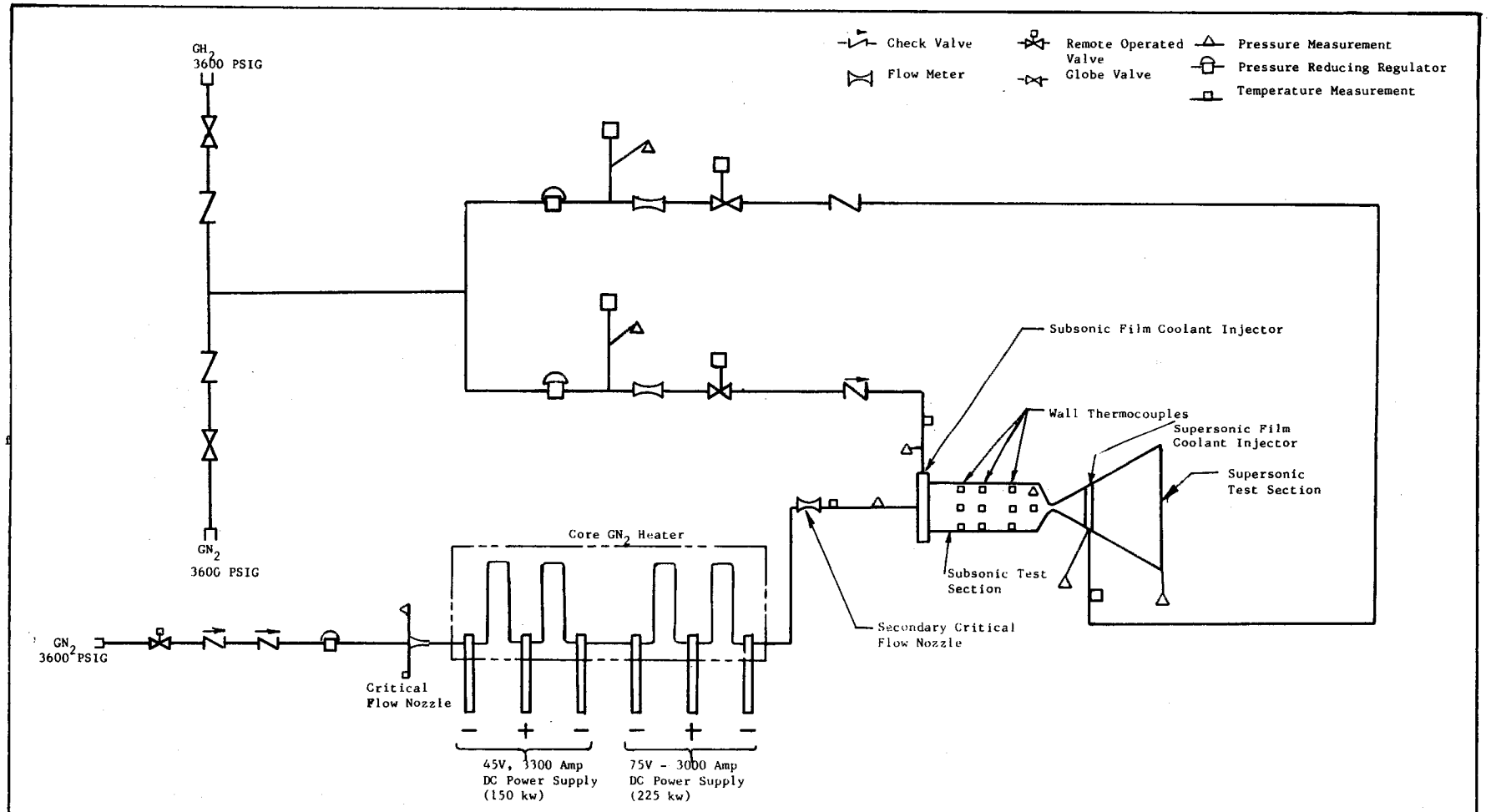

FIGURE B28. FILM COOLING TEST SYSTEM

APPENDIX C

COLD FLOW TESTS

Appendix C

Cold flow tests of the cylindrical supersonic, conical subsonic, and conical supersonic injectors were conducted. The results are summarized in this appendix. The tests were performed by flowing ambient temperature N_2 through the injection circuit to ambient pressure. There was no core flow. Film cooling test flow conditions were simulated as close as possible. A tabulated summary of the cold flow results is given in Table X.

A. SUPERSONIC INJECTORS

Two key cold flow measurements were made on the supersonic injectors: (1) total pressure upstream of the throat, and (2) total pressure at the nozzle exit. Both measurements were made with a 0.010-in. diameter probe oriented parallel to the flow and pointed upstream. The exit pressure measurement was assumed downstream of a normal shock. These measurements indicated circumferential flow distribution and injection Mach number. (The supersonic injectors are shown in Figures B15 and B26.)

The cylindrical supersonic results indicate that the total pressure measured upstream of the throat within each injection channel was uniform within 1.6%. The fabrication tolerances on this part were such that a throat area variation of $\pm$ 2.5% could occur; consequently the indicated uniformity of flow is $\pm$ 4.1%. Similar reasoning for the conical supersonic injector yields a $\pm$ 7% flow uniformity.

Exit Mach number values were calculated from normal shock tables assuming a normal shock occurs at the probe inlet when the probe is positioned in the supersonic stream at the injector nozzle outlet. The nominal exit Mach number is 1.86; however, fabrication tolerances are such that outlet Mach numbers ranging from 1.81 to 1.94 can occur at the film cooling nozzle exit in the cylindrical supersonic injector. This range is in reasonable agreement with the values determined experimentally which range from 1.83 to 2.06 for the cylindrical supersonic film coolant injector and 1.74 to 2.01 for the conical supersonic film coolant injector. The average outlet Mach numbers are 1.91 and 1.88. The static pressure ratios reported in Section V are based on these

average Mach numbers and the nozzle C_D value indicated for the film coolant nozzles by the cold flow data (0.89 for both supersonic film coolant injectors).

B. CONICAL SUBSONIC INJECTOR

The capability of the conical subsonic injector manifold design to provide an acceptable circumferential flow distribution was demonstrated during cold flow tests on Contract NAS 3-14383 with the thick slot subsonic injector. This capability was again verified during the cold flow tests on the conical subsonic injector. Velocity head measurements were made at the midpoint of each channel at the coolant slot exit using a 0.0761 cm (0.030-in.) diameter probe. The measurements agree within about $\pm$ 10%. Fabrication tolerances allow a $\pm$ 4% variation in channel flow area, therefore, the flow uniformity is $\pm$ 14%.

TABLE CI

COLD FLOW RESULTS

Film Coolant Channel Number (1)	Cylindrical Supersonic Film Coolant Injector			Conical Supersonic Film Coolant Injector		Conical Subsonic Film Coolant Injector
	$\frac{P_o}{P_{I_2}}$	$\frac{P_{ex}}{P_o}$	M_{exit}	$\frac{P_o}{P_{I_2}}$	Average M_{exit}	$U/U_{ave} = \sqrt{P_{ex}/P_{ex\ ave}}$
1	.958	.769	1.90	.963	1.91	1.012
2	.963	.769	1.90	.943	1.93	.991
3	.972	.781	1.87	.960	1.85	.945
4	.974	.747	1.94	.958	1.74	.963
5	.9177	.739	1.96	.960	1.76	.916
6	.981	.763	1.91	.965	1.87	.909
7	.972	.692	2.06	.972	1.88	.945
8	.972	.789	1.86	.956	1.82	.900
9	.958	.774	1.89	.950	1.80	.927
10	.965	.756	1.93	.947	1.88	.962
11	.936	.751	1.93	.956	1.86	1.021
12	.967	.750	1.93	.973	1.87	1.004
13	.967	.756	1.92	.975	1.91	1.052
14	.967	.727	1.99	.971	1.89	1.079
15	.972	.774	1.89	.971	1.98	1.12
16	.967	.8	1.83	.971	1.99	1.091
17	.961	.783	1.87	.971	2.01	1.091
18	.951	.771	1.89	.942	1.96	1.029
	ave=.966±1.6%		ave=$1.915^{+7.6\%}_{-4.5\%}$	ave=$.961^{+1.5\%}_{-2.0\%}$	ave=$1.88^{+7.0\%}_{-7.5\%}$	

P_o = Total pressure in film cooling nozzle upstream of nozzle throat.

P_{I_2} = Film coolant injector manifold pressure.

P_{ex} = Total pressure at film coolant nozzle exit.

M_{exit} = Mach number at nozzle exit (assuming P_{ex} downstream of normal shock).

(1) - Related to thermocouple locations in Table BI.

APPENDIX D

SYMBOLS

Appendix D

1. ENGLISH LETTERS

A/A_T	Thrust chamber area ratio
c	Elemental hydrogen mass fraction
C_P	Specific heat
C_g	Heat transfer correlation coefficient
D	Chamber or nozzle flow diameter
F	Thrust
FFC	Fraction of fuel used as film coolant
G	Axial mass velocity based on total flow
h	Step height (slot height plus lip thickness)
h_g	Gas-side convective heat transfer coefficient
H	Static enthalpy
H_o	Total enthalpy
k	Entrainment fraction
k_o	Laboratory entrainment fraction for straight, unaccelerated flow with continuous slot injection
k_m	Entrainment fraction multiplier; k'_m is for n = 0
L'	Combustion chamber axial length
m	Mass velocity ratio, $\rho_c u_c / \rho_e u_e$
M	Mach Number
MR	Mixture ratio
MW	Molecular weight
n	Acceleration exponent
P	Static pressure
P_o	Total pressure
Pr	Prandtl number
q/A	Heat flux
r	Local chamber or nozzle radius
R	Radius or curvature; positive when the wall turns into the flow
R_c	Thrust chamber radius at main injector location

1, English Letters (cont.)

Re_c	Coolant Reynolds number based on slot height, $\rho_c \mu_c s_c / \mu_c$
Re_D	Overall Reynolds number, $\rho_{ref}\ GD/\rho_e \mu_{ref}$
R_t	Throat radius
R_{th}	Thermal resistance
s	Mixing layer thickness
s_c	Coolant slot height
s_o	Initial mixing layer thickness
St	Stanton number = hg/G
t	Time
T	Static temperature
T_o	Total temperature
T_{wg}	Gas side wall temperature
u	Axial velocity
$\bar{u}$	Effective velocity for recovery term, Equation (3)
V	Velocity Mixing Function, defined by Equation (18)
W	Total flow rate
W_c	Film coolant flow rate
W_E	Entrainment flow rate
x	Contour distance from the film coolant injection point
$\bar{x}$	Contour integral defined by Equation (14)
$\bar{x}_1$	Value of $\bar{x}$ when k is unity
y	Distance in direction perpendicular to wall
Z	Distance along test section axis

2. GREEK LETTERS

α	Angle between the nozzle centerline and the wall tangent
η	Film cooling effectiveness, defined by Equation (1)
θ	Enthalpy and elemental mass fraction profile shape factor for the mixing layer
μ	Viscosity
ρ	Density; $\bar{\rho}$ is defined as $0.5\ (\rho_e + \rho_w)$
ϕ	Ratio of two-dimensional to one-dimensional mass velocity

3. SUBSCRIPTS

o	Film coolant injection location (except H_o, T_o, k_o)
aw	Adiabatic wall condition
b	Bulk value for the mixing layer
c	Coolant inlet
e	Mainstream or core
ref	Gas composition at the wall at the reference temperature
v	Edge of the viscous sublayer
w	At the chamber wall

APPENDIX E

DISTRIBUTION LIST

Appendix E

National Aeronautics and Space Administration
Lewis Research Center
21000 Brookpark Road
Cleveland, Ohio 44135

1 Attn: Contracting Officer, MS 500-313
5 E. A. Bourke, MS 500-205
1 Technical Utilization Office, MS 3-16
1 Technical Report Control Office, MS 5-5
2 AFSC Liaison Office, MS 501-3
2 Library MS 60-3
1 Office of Reliability and Quality Assurance, MS 500-211
1 N. T. Musial, MS 500-113
20 D. E. Sokolowski, Project Manager, MS 500-204

1 Director, Manned Space Technology, RS
Office of Aeronautics and Space Technology
NASA Headquarters
Washington, D. C. 20546

2 Director Space Prop. and Power, RP
Office of Aeronautics and Space Technology
NASA Headquarters
Washington, D.C. 20546

1 Director, Launch Vehicles and Propulsion, SV
Office of Space Science
NASA Headquarters
Washington, D.C. 20546

1 Director, Materials and Structures Division, RW
Office of Aeronautics and Space Technology
NASA Headquarters
Washington, D.C. 20546

1 Director, Advanced Missions, MT
Office of Manned Space Flight
NASA Headquarters
Washington, D.C. 20546

1 National Aeronautics and Space Administration
Ames Research Center
Moffett Field, California 94035
Attn: Library

1 National Aeronautics and Space Administration
Flight Research Center
P.O. Box 273
Edwards, California 93523
Attn: Library

1 Director, Technology Utilization Division
Office of Technology Utilization
NASA Headquarters
Washington, D.C. 20546

1 Office of the Director of Defense
Research and Engineering
Washington, D.C. 20301
Attn: Office of Assistant Director (Chem. Technology)

10 NASA Scientific and Technology Information Facility
P.O. Box 33
College Park, Maryland 20740
Attn: NASA Representative

1 National Aeronautics and Space Administration
Goddard Space Flight Center
Greenbelt, Maryland 20771
Attn: Library

1 National Aeronautics and Space Administration
John F. Kennedy Space Center
Cocoa Beach, Florida 32931
Attn: Library

1 National Aeronautics and Space Administration
Langley Research Center
Langley Station
Hampton, Virginia 23365
Attn: Library

1 National Aeronautics and Space Administration
Manned Spacecraft Center
Houston, Texas 77001
Attn: Library

1 National Aeronautics and Space Administration
George C. Marshall Space Flight Center
Huntsville, Alabama 35912
Attn: Library

2 Jet Propulsion Laboratory
4800 Oak Grove Drive
Pasadena, California 91103
Attn: Library
R. Kushida

1 Defense Documentation Center
Cameron Station
Building 5
5010 Duke Street
Alexandria, Virginia 22314
Attn: TISIA

1 RTD (RTNP)
Bolling Air Force Base
Washington, D.C. 20332

1 Arnold Engineering Development Center
Air Force Systems Command
Tullahoma, Tennessee 37389
Attn: Library

1 Advanced Research Projects Agency
Washington, D.C. 20525
Attn: Library

1 Aeronautical Systems Division
Air Force Systems Command
Wright-Patterson Air Force Base
Dayton, Ohio
Attn: Library

1 Air Force Missile Test Center
Patrick Air Force Base, Florida
Attn: Library

1 Air Force Systems Command
Andrews Air Force Base
Washington, D.C. 20332
Attn: Library

1 Air Force Rocket Propulsion Laboratory (RPR)
Edwards, California 93523
Attn: Library

1 Air Force Rocket Propulsion Laboratory (RPM)
Edwards, California 93523
Attn: Library

1 Air Force FTC (FTAT-2)
Edwards Air Force Base,
California 93523
Attn: Library

1 Air Force Office of Scientific Research
Washington, D.C. 20333
Attn: Library

1 Space and Missile Systems Organization
Air Force Unit Post Office
Los Angeles, California 90045
Attn: Technical Data Center

Appendix E

1 Office of Research Analyses (OAR)
Holloman Air Force Base,
New Mexico 88339
Attn: Library
RRRD

1 U.S. Air Force
Washington, D.C.
Attn: Library

1 Commanding Officer
U.S. Army Research Office (Durham)
Box CM, Duke Station
Durham, North Carolina 27706
Attn: Library

1 U.S. Army Missile Command
Redstone Scientific Information Center
Redstone Arsenal, Alabama 35808
Attn: Document Section

1 Bureau of Naval Weapons
Department of the Navy
Washington, D.C.
Attn: Library

1 Commander
U.S. Naval Missile Center
Point Mugu, California 93041
Attn: Technical Library

1 Commander
U.S. Naval Weapons Center
China Lake, California 93557
Attn: Library

1 Commanding Officer
Naval Research Branch Office
1030 E. Green Street
Pasadena, California 91101
Attn: Library

1 Director (Code 6180)
U.S. Naval Research Laboratory
Washington, D.C. 20390
Attn: Library

1 Picatinny Arsenal
Dover, New Jersey 07801
Attn: Library

1 Air Force Aero Propulsion Laboratory
Research and Technology Division
Air Force Systems Command
United States Air Force
Wright-Patterson AFB, Ohio 45433
Attn: APRP (Library)

1 Electronics Division
Aerojet-General Corporation
P.O. Box 296
Azusa, California 91703
Attn: Library

1 Space Division
Aerojet-General Corporation
9200 East Flair Drive
El Monte, California 91734
Attn: Library

1 Aerojet Ordnance and Manufacturing
Aerojet-General Corporation
11711 South Woodruff Avenue
Fullerton, California 90241
Attn: Library

4 Rocketdyne, Division of
Rockwell International
6633 Canoga Avenue
Canoga Park, California
Attn: Library
D. Campbell
A. Y. Falk
R. J. Burick

1 Aeronutrionic Division of
Philco Ford Corporation
Ford Road
Newport Beach, California 92663
Attn: Technical Information Department

1 Aerospace Corporation
2400 E. El Segundo Blvd.
Los Angeles, California 90045
Attn: Library-Documents

1 Arthur D. Little, Inc.
20 Acorn Park
Cambridge, Massachusetts 02140
Attn: Library

1 Astropower Laboratory
McDonnel-Douglas Aircraft Company
2121 Paularino
Newport Beach, California 92163
Attn: Library

1 ARO, Incorporated
Arnold Engineering Development Center
Arnold AF Station, Tennessee 37389
Attn: Library

1 Susquehanna Corporation
Atlantic Research Division
Shirley Highway and Edsall Road
Alexandria, Virginia 22314
Attn: Library

1 Beech Aircraft Corporation
Boulder Facility
Box 631
Boulder, Colorado
Attn: Library

2 Bell Aerosystems, Inc.
Box 1
Buffalo, New York 14240
Attn: Library
J. M. Senneff

1 Instruments and Life Support Division
Bendix Corporation
P.O. Box 4508
Davenport, Iowa 52808
Attn: Library

1 Boeing Company
Space Division
P.O. Box 868
Seattle, Washington 98124
Attn: Library

1 Chemical Propulsion Information Agency
Applied Physics Laboratory
8621 Georgia Avenue
Silver Spring, Maryland 20910

1 Chrysler Corporation
Missile Division
P.O. Box 2628
Detroit, Michigan
Attn: Library

1 Chrysler Corporation
Space Division
P.O. Box 29200
New Orleans, Louisiana 70129
Attn: Librarian

1 Curtiss-Wright Corporation
Wright Aeronautical Division
Woodridge, New Jersey
Attn: Library

1 University of Denver
Denver Research Institute
P.O. Box 10127
Denver, Colorado 80210
Attn: Security Office

1 Fairchild Stratos Corporation
Aircraft Missiles Division
Hagerstown, Maryland
Attn: Library

1 Research Center
Fairchild Hiller Corporation
Germantown, Maryland
Attn: Library

Appendix E

1 General Dynamics/Convair
P.O. Box 1128
San Diego, California 92112
Attn: Library

1 Missiles and Space Systems Center
General Electric Company
Valley Forge Space Technology Center
P.O. Box 8555
Philadelphia, Pennsylvania 19101
Attn: Library

1 General Electric Company
Flight Propulsion Lab Department
Cincinnati, Ohio
Attn: Library

1 Grumman Aircraft Engineering Corporation
Bethpage, Long Island, New York
Attn: Library

1 Hercules Powder Company
Allegheny Ballistics Laboratory
P.O. Box 210
Cumberland, Maryland 21501
Attn: Library

1 IIT Research Institute
Technology Center
Chicago, Illinois 60616
Attn: Library

1 Kidde Aero-Space Division
Walter Kidde and Company, Inc.
567 Main Street
Belleville, New Jersey 07109

1 Ling-Temco-Vought Corporation
P.O. Box 5907
Dallas, Texas 75222
Attn: Library

1 Lockheed Missiles and Space Company
P.O. Box 504
Sunnyvale, California 94087
Attn: Library

1 Lockheed Propulsion Company
P.O. Box 111
Redlands, California 92374
Attn: Library, Thackwell

1 Marquardt Corporation
16555 Saticoy Street
Box 2013 - South Annex
Van Nuys, California 91409
Attn: L. R. Bell, Jr.

1 Denver Division
Martin-Marietta Corporation
P.O. Box 179
Denver, Colorado 80201
Attn: Library

1 Western Division
McDonnell Douglas Astronautics
5301 Bolsa Avenue
Huntington Beach, California 92647
Attn: Library

1 McDonnell Douglas Aircraft Corporation
P.O. Box 516
Lambert Field, Missouri 63166
Attn: Library

1 Space and Information Systems Division
Rocketdyne International
12214 Lakewood Blvd.
Downey, California
Attn: Library

1 Northrop Space Laboratories
3401 West Broadway
Hawthorne, California
Attn: Library

1 Purdue University
Lafayette, Indiana 47907
Attn: Library (Technical)

1 Rocket Research Corporation
Willow Road at 116th Street
Redmond, Washington 98052
Attn: Library

1 Stanford Research Institute
333 Ravenswood Avenue
Menlo Park, California 94023
Attn: Library

3 TRW Systems, Inc.
1 Space Park
Redondo Beach, California 90278
Attn: Technical Library
Doc. Acquisitions
H. Burge
W. A. Carter

1 United Aircraft Corporation
Corporation Library
400 Main Street
East Hartford, Connecticut 06108

2 United Aircraft Corporation
Pratt and Whitney Division
Florida Research and Development Center
P.O. Box 2691
West Palm Beach, Florida 33402
Attn: Library
G. B. Cox

1 United Aircraft Corporation
United Technology Center
P.O. Box 358
Sunnyvale, California 94038
Attn: Library

1 Garret Corporation
AiResearch Division
Phoenix, Arizona 85036
Attn: Library